STIMULI RESPONSIVE FLUORESCENT MATERIALS

A thesis submitted to the department of chemistry, Jadavpur University in fulfilment of the requirements for the degree of doctor of philosophy (Science)

Submitted by

Dibyendu Dey

DEPARTMENT OF CHEMISTRY

JADAVPUR UNIVERSITY

KOLKATA-700032

INDIA

2025

যাদবপুর বিশ্ববিদ্যালয়
কলকাতা-৭০০০৩২, ভারত

*JADAVPUR UNIVERSITY
KOLKATA-700 032, INDIA

Dr. Manas Kumar Panda
Assistant professor, Faculty of science
Department of Chemistry: Inorganic section
Email: **manaspanda.chemistry@jadavpuruniversity.in**

CERTIFICATE FROM THE SUPERVISOR

This is to certify that the thesis entitled **"Stimuli responsive fluorescent materials"** submitted by Mr. **Dibyendu Dey**, who got his name registered on 18th November, 2020 for the award of Ph.D. (Science) degree of Jadavpur University, is absolutely based upon his own work under the supervision of Dr. Manas Kumar Panda and that neither this thesis nor any part of it has been submitted for either any degree/diploma or any other academic award anywhere before.

06/8/2025

Dr. Manas Kumar Panda

Dr. Manas Panda
Assistant Professor
Department of Chemistry
Jadavpur University
Kolkata-700 032

(Signature of supervisor with date and official seal)

DEDICATION

Every challenging work needs self-effort and support from those connected by heart. I dedicate this thesis to those who are part and parcel in every stage of my life, my loving & caring Mother, Father and brother Who made me feel that "I can do", who's Love, affection and prayers for days & night gave me strength to come to this stage and move on further in future days.

Acknowledgements

Firstly, I would like to thank Almighty for giving me good health, strength, knowledge and opportunity to carry undertake this research and to complete it successfully. Without his blessings, it would not have been possible to achieve this goal.

Completing this PhD thesis has been a long and challenging journey, and I could not have done it without the support and guidance of many individuals.

I would like to express my deepest gratitude to my supervisor, Dr. Manas Kumar Panda. His invaluable advice, constant encouragement, and insightful feedback have been instrumental in shaping this research. I am profoundly grateful for his patience and unwavering support throughout this process.

I would also like to thank the members of my thesis committee, Prof. Kajal Krishna Rajak (HOD dept of chemistry), and Dr. Manas Kumar Panda (Supervisor), for their constructive criticism and suggestions, which have greatly improved the quality of this work.

My heartfelt thanks go to my colleagues and friends in the SFML research group at Jadavpur University, especially Mr. Prasenjit Giri, Ms. Diotima Bhattacharjee, Mr. Mainak Bose, Mr. Ranajit Mondal, Mr. Souvik Garani, and, neighbouring lab colleagues Anupam, Aruntima di, Arijit, Osman, Uday for their camaraderie, stimulating discussions, and for making the lab a wonderful place to work. Special thanks to the MSc project students for their technical support and assistance, especially Prasita, Shippy and Ankita for their enthusiasm, consistency and great scientific ideas.

I am also grateful to the funding bodies, CSIR New Delhi and Jadavpur University, for their financial support, which made this research possible.

On a personal note, I would like to thank my family for their unconditional love and support. To my parents, Dilip Kumar Dey and Mrs. Chaina Dey, thank you for believing in me and for your endless encouragement. To my Grandparents Nemai Dey and late Mrs. Madhuri Dey for raising, nurturing and keeping me smiling. My home tutor, mr. Mahadev Dey and my School teachers, especially PET sir Indrajit Poddar and Gautam Chatterjee for teaching me Discipline and mathematics respectively...My College teachers Dr Chandan Kumar Pal, Dr Debjani Ghosh, Dr Partha Haldar, Dr Rana Sen in my college time journey, and my senior mentors, Dr Rajdeep Mukherjee, Dr. Koushik Bera and Prof Mintu Halder at my lab project supervisor iit Kgp for their patience, understanding, and unwavering support have been my anchor throughout this journey.

Lastly, I would like to acknowledge the countless sacrifices made by my friends and family, who have been a constant source of motivation and strength. This thesis is as much yours as it is mine.

Thank you all.

Dibyendu Dey 06.08.2025

Dibyendu Dey (senior research fellow)

Dept of Chemistry, Jadavpur University, Kolkata -32

Contents

Chapter 5: Influence of Polymorphism and Substituent Variation on the Thermoresponsive and Luminescent Characteristics of Organic Molecular Crystals.

Abstract

The work in this thesis is five folds consisting of an introduction cum literature survey chapter and four chapters based on my Ph.D. work. In the first chapter we studied the Aggregation induced emission (AIE) and mechanochromic properties of newly synthesized donor-acceptor (D-A) type molecules abbreviated as **1CF$_3$** &**1F$_2$**. These structurally simple donor-acceptor (D-A) type cyanostilbene-based molecules were synthesized in one step Knoevenagel condensation reaction that display AIE and fluorescence switching in presence of various stimuli. We demonstrated their application in inkless mechano-writing and vapo-erasing. With the aid of X-ray single crystal structure and other analytical techniques, we have investigated the mechanism of stimuli-responsive behaviour and their structure function correlation.

In the second chapter, a diphenylamine-acylhydrazone based derivatives namely **DPAHydZOH** was synthesized which exhibit remarkable multi-stimuli responsive properties, encompassing mechanochromic luminescence (MCL), thermochromic luminescence, and photomechanical effects in presence of external stimulus like mechanical stress and light. Such materials that respond to multiple stimuli are incredibly important for developing advanced technologies like strain sensors, photo sensors, and actuators.

The third chapter focusses on photo-switchable solid fluorescent materials, a phenomenon in which the luminescence properties of the solid crystal or films can be tuned using light of specific wavelength. Compared to other stimuli-switching materials, photo-switching fluorophores are comparatively rare and thus need special attention to be explored in much detail. With this aim, we have synthesized two new cyanovinyl-based molecules named as **ArF$_2$** and **ArCF$_3$**, show diametrically opposite photo-switching behavior in their solid state due to substitutional effect. By simply changing the substitution from **-F** to **-CF$_3$,** we can achieve completely opposite luminescence switching behaviour in the solid state. Such smart optical switching materials have immense potential in optoelectronics and other technological applications.

The content of the last chapter (4) is slightly different compared to the previous chapters. In this chapter, we introduce a novel class of D-A type acylhydrazone derivatives named as **NMe$_2$OH**, **NEt$_2$OH-FL & NFL** that display thermos-responsive actuation (Thermosalient effect) due to thermal phase transition and fluorescence modulation using polymorphism and substitutional effect. We have demonstrated that polymorphism and alkyl group substitution can be used as an efficient tool for manipulating both thermal actuation and optical property.

List of Publications:

Significant number of interesting results were obtained on Stimuli-responsive materials and their possible applications. We have published several papers in some mainstream journals such as Crystal Growth and design, ACS Applied Bio-materials, CrystEngComm etc. The references of these papers are listed below---

1. Aggregation induced emission and mechanochromic luminescence by cyanostilbene-based organic luminophores. **Dibyendu Dey**, Prasenjit Giri, Nayim Sepay, Ahmad Hussain, Manas K. Panda*, ***Journal of Photochemistry & Photobiology, A: Chemistry***. 2023, **437**, 114480.

2. Light-fueled rapid macroscopic motion of a green fluorescent organic crystal. Prasenjit Giri, Abhrojyoti Mazumder, **Dibyendu Dey**, Souvik Garani, Anju Raveendran and Manas K. Panda*. ***CrystEngComm.*** 2021**, 23**, 5876.

3. Rapid Visual Detection of Amines by Pyrylium Salts for Food Spoilage Taggant. Basavaraja D, **Dibyendu Dey**, Varsha T. L, Chettiyan Thodi F. Salfeena, Manas K. Panda* and Sasidhar B. Somappa*, ***ACS Appl. Bio Mater***. 2020, **3**, 772−778.

4. Multi-stimuli responsive behavior by a simple donor-acceptor type acylhydrazone based crystal, **Dibyendu Dey**, Prasita Mazumder, Ahmad Husain, Manas K. Panda*, ***Inorganica Chimica Acta.***, 2024, **568**, 122110.

5. Polymorphism and Substitutional Effect on the Thermoresponsive and Luminescence Properties of Organic Molecular Crystals, Prasita Mazumder, **Dibyendu Dey**, Prasenjit Giri, Souvik Garani, Ranajit Mandal, Ahmad Husain, Manas K. Panda*, ***Crystal Growth and Design***., 2024 ,**24**, 7925-7935.

6. Solid-State Fluorescence Switching by Functionalized Cyanovinyl Molecules: Syntheses, Computational Study and Application for Authentic Data Encryption and Tagging, **Dibyendu Dey**, Prasita Mazumder, Prasenjit Giri, Antonio Prlj, Luca Grisanti, Manas K. Panda. ***Manuscript submitted.***

7. Tunable Synaptic Memory Response and Solid-State Luminescence by Regio-Isomeric Donor-Acceptor-Donor Type Conjugated Organic Materials**,** Mainak Bose, Manoj Kangsabanik, **Dibyendu Dey**, Rabindra Nath Gayen, Manas K. Panda (***Manuscript under preparation***).

Introduction

Stimuli-responsive materials are the kind of materials which shows behaviours and properties in response to specific stimuli like pressure, temperature, light, Chemicals, PH etc. These materials, particularly fluorescent ones are in the scope of our discussion. These materials found applications in vast majority of fields which includes sensors, bio-imaging, memory media and displays etc.

Fluorescent materials[1] have gained much exposure recently due to their potential applications as sensors, bio-imaging, memory media and displays. Chemical substances, temperature, light, pH, electricity and mechanical forces are the typical stimuli utilized to change the fluorescent behaviours of these materials Examples range from simple luminescent materials to three-dimensional cages and polymers for the diverse applications in the development of materials that require specific responses to the external stimuli.[2] The design and control of stimuli-responsive behaviour where the stimulus induces a complex response, such as structural rearrangement, changes in colour in visible and UV regions, and changes in fluorescence properties. In most examples, the stimulus has a linear effect on the system such that one stimulus causes one response, stoichiometrically. A single luminophore cannot achieve a multi-emission colour using external stimuli for organic and organometallic materials. One exception is crystalline compound, which leads to new applications of stimuli-responsive luminescent materials that are flexible, sophisticated, and highly functional. For example, pyrene, anthracene, and naphthalene-based liquid crystals show piezo (mechano) chromic luminescence and thermochromic luminescence in liquid as well as crystalline states. However, multiluminescent colours have not been achieved for these LC materials.[1-3]

Stimuli can induce responses such as structural rearrangements, color changes (visible or UV), and alterations in fluorescence properties, often in a linear manner. While single Luminophores in organic and organometallic materials typically can't achieve multi-emission colors, crystalline compounds offer new possibilities for advanced, interdisciplinary area to develop and exploit some luminescent (visible or UV) materials for the generation of versatile responses with response to different types of stimuli.[3]

1.1 Background of the study: Literature Survey

Solid-state crystalline fluorescent materials that may or may not be transition metal complexes which would be able to produce colour or change colour concerning external stimuli like sensors for ammonia gas, formalin sensors for endangered fishes in the market, preparing OLEDs[3] for modern electronic gadgets displays which exclude blue light which is harmful to eyes, we also tried to prepare some security based writing systems like our previous work i.e. sunlight mediated inkless printing.[26]

1.1.1 Stimuli Responsive Fluorescence

Fluorescence is a multistep process, the molecule starts at the ground state (S_0). - It absorbs light and transitions to an excited state (S_1 or S_2): It loses some energy through vibrational relaxation. - It also returns to the ground state (S_0) by emitting a photon, which we observe as fluorescence. Fluorescence is characterized by the emission of light at a longer wavelength than the absorbed light, following Stokes' Law. This process is crucial in various fields, including chemistry, biology, and medical diagnostics.

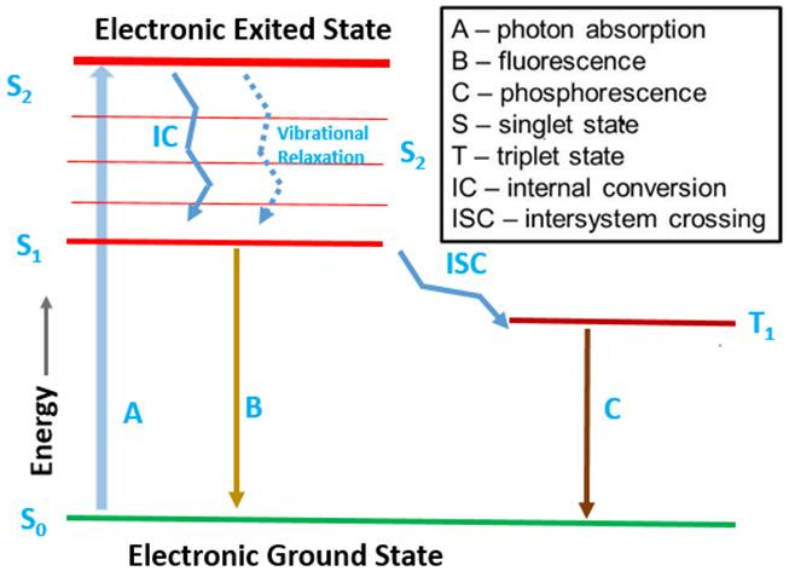

Figure 1. Jablonski diagram for transitions in different electronic exited states.

A Jablonski diagram is a graphical representation of the electronic states of a molecule and the transitions between them. Here are the key components of the Jablonski diagram and the process of fluorescence: A molecule in its lowest energy state, known as the ground state (S_0),

typically remains stable under normal conditions. However, when it absorbs a photon of light, it transitions from the ground state to an excited singlet state (S_1, S_2, etc.), represented by an upward vertical arrow in the Jablonski diagram. Once in the excited state, the molecule quickly undergoes vibrational relaxation, where it loses some energy and moves to the lowest vibrational level of the excited state through rapid energy dissipation, depicted by wavy lines. Following this, the molecule returns to its ground state by emitting a photon, a process known as fluorescence, represented by a downward vertical arrow. The emitted photon possesses lower energy, or a longer wavelength, due to the energy lost during vibrational relaxation. In certain cases, instead of immediately returning to the ground state, the molecule may undergo intersystem crossing to a triplet state (T_1), a transition where its spin state changes. If the molecule eventually emits light from this triplet state, the process is known as phosphorescence, which occurs more slowly than fluorescence due to the forbidden nature of the transition. This sequence of events illustrates the key processes involved in the absorption and emission of light, providing insight into the dynamics of molecular photophysics.

The ability of certain materials to change their light emission properties when exposed to external stimuli, such as mechanical force, temperature, pH, light, or chemical interactions. This phenomenon is particularly useful in applications like sensors, security inks, memory storage, and display technologies. One notable example is mechanochromic luminescence (ML), where the emission color shifts when mechanical force—such as grinding, stretching, or smearing—is applied. This change occurs due to alterations in molecular interactions, aggregation states, or crystalline structures within the material. Some materials also exhibit luminescence quenching upon mechanical perturbation, meaning their fluorescence intensity diminishes due to enhanced crossover to non-radiative excited states. Other types include thermochromic luminescence, in which emission changes with temperature, and solvatochromic luminescence, where fluorescence varies depending on the surrounding solvent environment. Many of these materials belong to aggregation-induced emission (AIE) or aggregation-enhanced emission (AIE)[5] families, making them valuable for organic light-emitting diodes (OLEDs)[4] and drug delivery tracking. Stimuli-responsive luminescent materials provide dynamic and reversible optical responses, paving the way for innovative applications in scientific and industrial fields. Their development remains an exciting and challenging area of materials science, driven by the need for adaptable and functional optoelectronic technologies.

Fluorophores, or fluorescent dyes, are molecules or parts of molecules that exhibit fluorescence in either solid or solution states. The fluorophore is responsible for both the absorption and emission of light. Although fluorophores are sometimes referred to as chromophores, there's a distinction: chromophores absorb light, whereas fluorophores emit it. Essentially, fluorophores give compounds their color.

Stable and bright fluorophores typically absorb and emit light within the 300–700 nm wavelength range. While there are fluorophores with longer wavelengths (in the near-infrared range), these tend to have shorter thermal and photochemical stability compared to those in the 300–700 nm range.[4]

Certain solid-state fluorescent materials have the ability to responds to external or environmental cues, such as thermal, mechanical, electrical, optical, magnetic, chemical or biological stimuli. This is due to their ability to undergo stimuli induced structural rearrangement driven by change in weak intermolecular interactions such as hydrogen bonding interaction, van der Waals interactions, π-π interaction or halogen bonding interactions. Any change in the fluorophore packing results in a change in the fluorescence intensity and emission maxima (λ_{max}). The photoexcitation of d electrons in the metal complexes or π-π* transitions in organic compounds is the main reason for this fluorescence change. Moreover, the mode of molecular interaction in excited state largely depends on the supramolecular packing. The change in fluorescence is the indicator of sensing. Thus, one can tune the fluorescence of the materials by inducing supramolecular structural change which can be triggered by external stimuli. These materials have many important applications as sensors or as solid-state light emitter. For example, vapoluminescent materials can be used as sensors of detecting hazardous and toxic chemicals or gases. There are many stimuli responsive materials have been synthesized and can be classified under the following titles, mechanochromic luminescence, vapochromism, pH- dependent fluorescence, thermal fluorescence, electroluminescence etc (Figure 2). Majority of the chromic materials are responsive to single stimuli. However, multi-stimuli responsive solid-state emitters are also reported but rare. Considering the importance and diversity of the application of these materials, we became interested to synthesize multi-stimuli responsive fluorescent material.

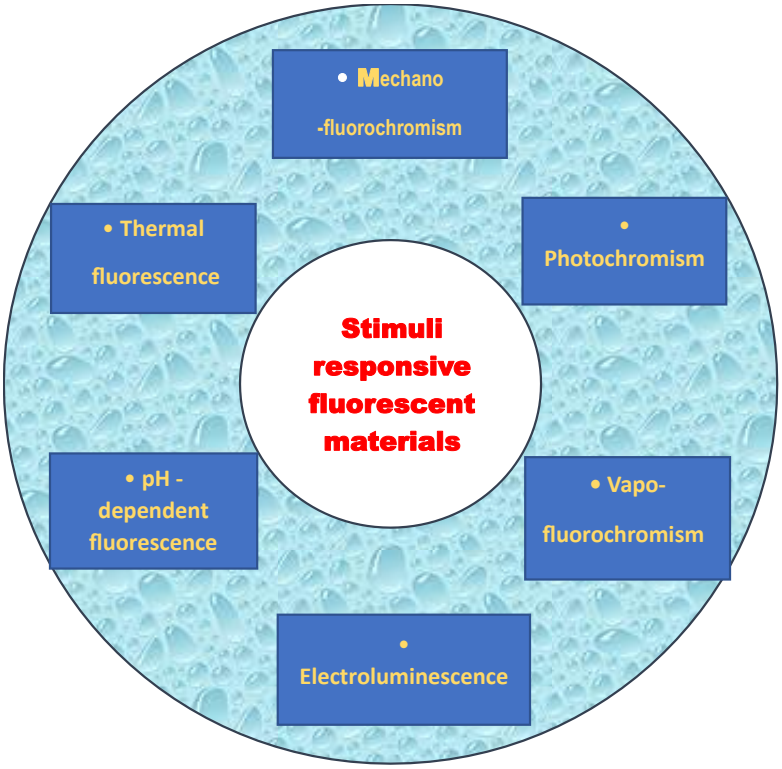

Figure 2. Types of stimuli responsive fluorescence materials

1.1.2 Solvatochromic Luminescence

Solvatochromic luminescence refers to the phenomenon where a compound's emission wavelength shifts depending on the polarity of the surrounding solvent. This effect is particularly pronounced in molecules with intramolecular charge transfer (ICT) character—typically those possessing donor–acceptor architectures. When such a molecule is excited, its electron distribution becomes more polarized. In polar solvents, this excited state is more stabilized than the ground state, resulting in a red shift (longer wavelength) of the luminescence. In less polar environments, the excited state is less stabilized, leading to blue-shifted emission. This sensitivity to microenvironment polarity makes solvatochromic luminophores excellent candidates for sensing applications and molecular probes, especially in coordination polymers, where their framework environments can amplify such effects. Solvent vapour induced reversible changes in the fluorescent properties of certain materials are known as solvatochromism (Figure 3). Vapochromic sensor materials are employed for detecting volatile organic compounds (VOCs). When exposed to VOCs, these materials exhibit reversible changes in their luminescence, allowing them to sense volatile impurities effectively. In everyday life, significant amounts of VOCs are released into the atmosphere by various

sources, including industries, agricultural insecticides, and vehicle emissions. Therefore, there is a high demand for suitable sensing materials that can efficiently detect these volatile compounds.[20]

For instance, in 2006, Boens and colleagues reported a fluorescent BODIPY-derived dye (Boron-dipyrromethene) whose fluorescence properties are highly dependent on the solvent. As the polarity of the solvent increases, both the fluorescent quantum yield and the fluorescence lifetime decrease, while the wavelength of the fluorescence shifts to the red region. This indicates that such materials can also be practically applied for vapor sensing.

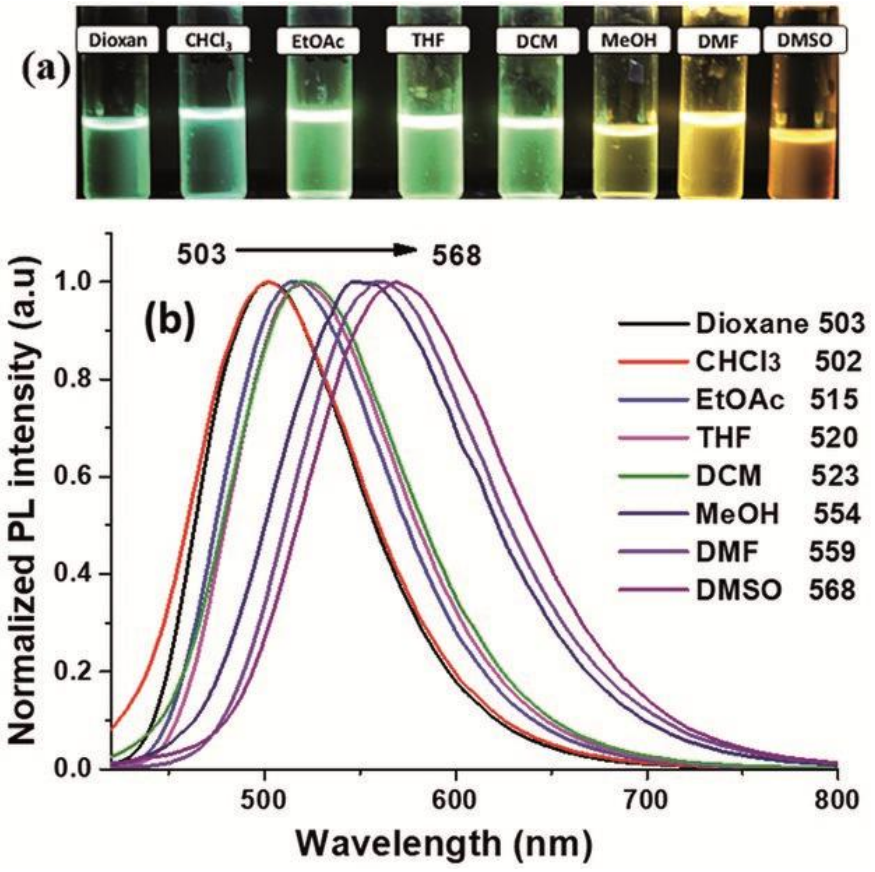

Figure 3. (a) Solvatochromism (b) normalized emission spectra of compound 2 in several solvents. Figures were taken from reference 20 and reprinted with copyright permission from RSC.

1.1.3 Solution and Solid-State Emission

In general, most organic luminophores exhibit fluorescence in solution, but lose their fluorescence in the solid state. This phenomenon, known as aggregation-induced quenching (ACQ), results from the photoexcited energetic state being quenched by non-radiative processes. When luminophores come into close proximity and aggregate, the aromatic rings of

adjacent luminophores experience strong intermolecular π–π stacking interactions. In this state, the excited states of the aggregates decay or relax back to the ground state via non-radiative channels, leading to quenching of fluorescence. This is a drawback of solution state emitters that limits their practical applications in devices. In contrast, solid state fluorescent materials are more limited but can overcome the practical limitations of solution state fluorescence. Solid state fluorescent compounds are easier to handle and free from concentration-related issues. However, there are only a few solid-state fluorescent compounds with high efficiency, reproducibility, and reversibility.[5, 37] To achieve solid state fluorescent materials, it is necessary to design molecules with fluorophore units and other functional groups that engage in intermolecular interactions. Modifications in the molecular packing or conformation of the luminophore can affect the HOMO-LUMO energy levels and thus the fluorescence. Polymorphism, the ability of a single compound to exist in more than one solid crystalline structure, is a suitable approach to achieve tunable solid-state fluorescence. This phenomenon provides insights into the structure-property relationship of the compound. Different polymorphs of the same organic or inorganic compound can exhibit different solid-state luminescence.[6-9] Recently, Mutai et al. reported reproducible on-off switching of solid-state luminescence by controlling molecular packing through heat mode interconversion. Das and coworkers found reversible thermally induced fluorescence switching of polymorphs based on alkoxy-cyano substituted diphenylbutadienes. Tang and coworkers revealed thermally driven emission switching between crystal and amorphous phases of (4-biphenylyl) phenyldibenzofulvene. Thus, achieving tunable solid-state fluorescence by tailoring molecular substitution and supramolecular packing is a challenging problem in this research area.[5]

Solid-state emitters have garnered significant attention in recent years due to their diverse applications in optoelectronics, OLED devices, and sensing technologies. Emitters that can alter their fluorescence color under mechanical pressure are particularly intriguing for their potential use in mechanosensors and related devices. Notably In 2016, Ito and colleagues reported a mechanoluminescent gold (I) isocyanide complex. When subjected to grinding (mechanical pressure stimuli), this complex exhibited a fluorescence change from blue to yellow to green due to transitions from crystalline to amorphous phases. This material holds potential for developing imaging techniques that can store information invisible under normal light but visible under UV illumination.

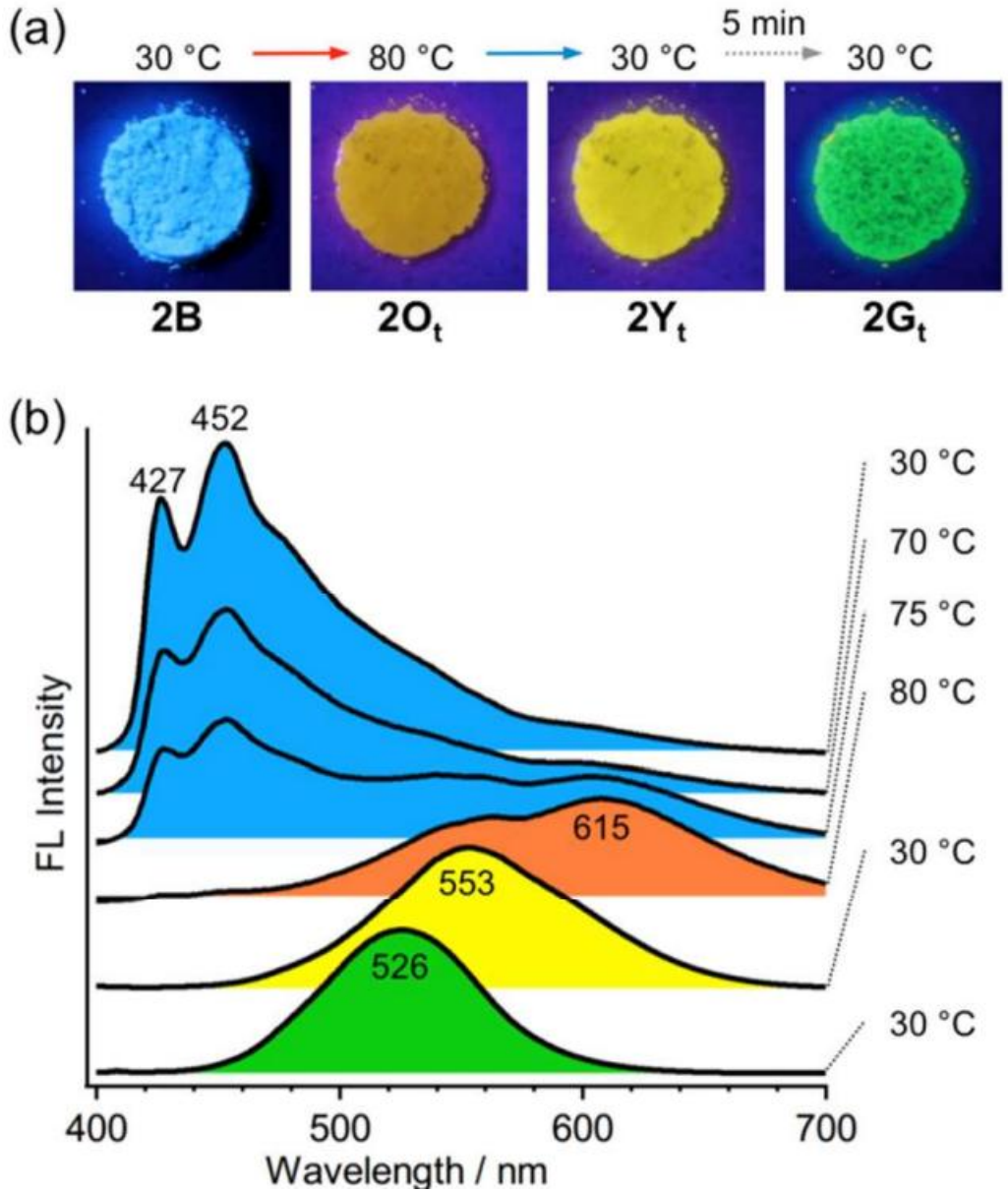

Figure 4. (a) Photographs showing the luminescent color change induced by changing temperature. (b) Temperature-dependent fluorescence spectra upon heating from 30 to 80 °C and subsequent cooling to 30 °C. Figures were taken from reference 21 and reprinted with copyright permission from ACS.

1.1.4 Aggregation-induced emission (AIE)

The phenomenon of enhancing fluorescence efficiency in solid-state by inhibiting non-fluorescent processes is known as aggregation-induced emission enhancement (AIE)[22] or crystallization-induced emission (CIE) ,[35-36] depending on the context. Typically, most organic compounds exhibit fluorescence in their solution state but lose it in their solid state (figure 4). However, certain compounds display increased fluorescence upon aggregation or

crystallization. AIE refers to the former, while CIE describes the later. Polymorphic compounds are usually non-emissive in solution but highly emissive in aggregate or solid-state. This effect results from the restriction of intramolecular rotations, which prevents non-radiative relaxations. The AIE effect was first observed by Tang et al. in 2001 when they synthesized 1-methyl-1,2,3,4,5-pentaphenylsilole (MPPS). MPPS is non-fluorescent in solution but exhibits significant fluorescence in solid-state. A unique feature of AIE materials is the absence of closely packed π-π interactions or the formation of excimers, both known to negatively impact fluorescence.[2,6]

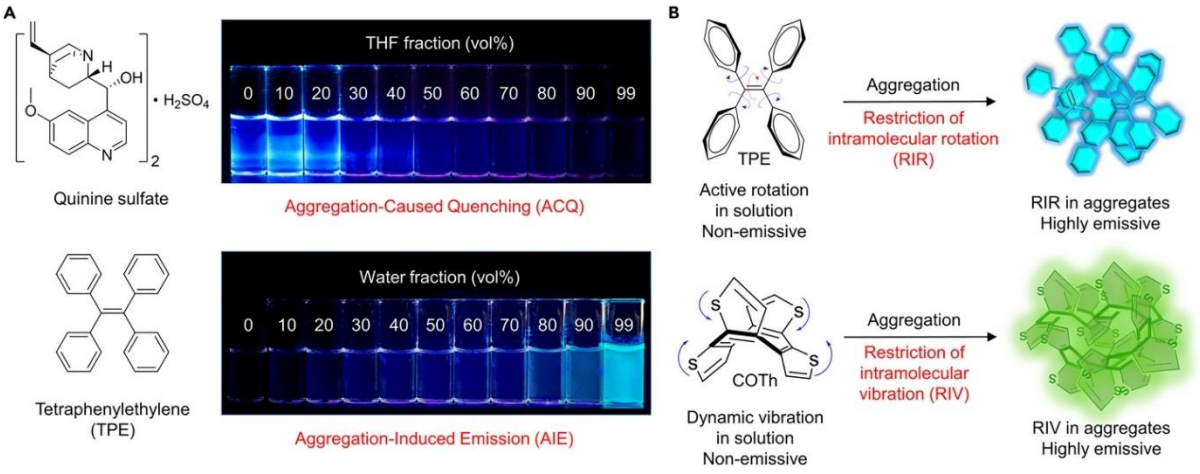

Figure 5. Aggregation caused quenching (above) and aggregation induced emission (AIE) (below) Figures were taken from reference 22 and reprinted with copyright permission Cell Press.

Due to their simple molecular design yet excellent solid-state fluorescence properties, AIE materials are widely used in chemo-sensors, biosensors, cell imaging, and smart materials. These materials demonstrate how the inhibition of non-radiative processes and specific molecular interactions can lead to highly efficient solid-state fluorescence, opening up a range of practical applications.

Tang et al in 2011, showed that Molecules whose emissions can be repeatedly switched between different colors or between dark and bright states by external stimuli in the solid state hold great potential for applications in sensors, memories, and security inks. Although modifying molecular structures is a common approach to tune dye emissions (figure 6), success has been limited in switching the luminescence of solid-state materials with high efficiency and reproducibility due to insufficient conversion or irreversible reactions. Some dyes exhibit

morphology-dependent emission, meaning their emission can be repeatedly switched in the solid state if the molecular arrangement can be reversibly tuned

Most reported materials respond to stimuli such as chemicals, heat, and vapor. However, the mechanochromic fluorescence of organic materials is rarely reported, and a molecular-level understanding of these mechanisms remains unclear. While the switching of emission colors is frequently reported, the tuning of fluorescence efficiency is rarely examined. Although some copper, gold, and platinum complexes, derivatives of oligo (p-phenylene vinylene) with cyano groups and long alkyl chains, pyrene and anthracene-based liquid crystals, and other dyes have been reported to exhibit mechanochromic luminescence, there is still no clear design strategy for constructing such molecules.

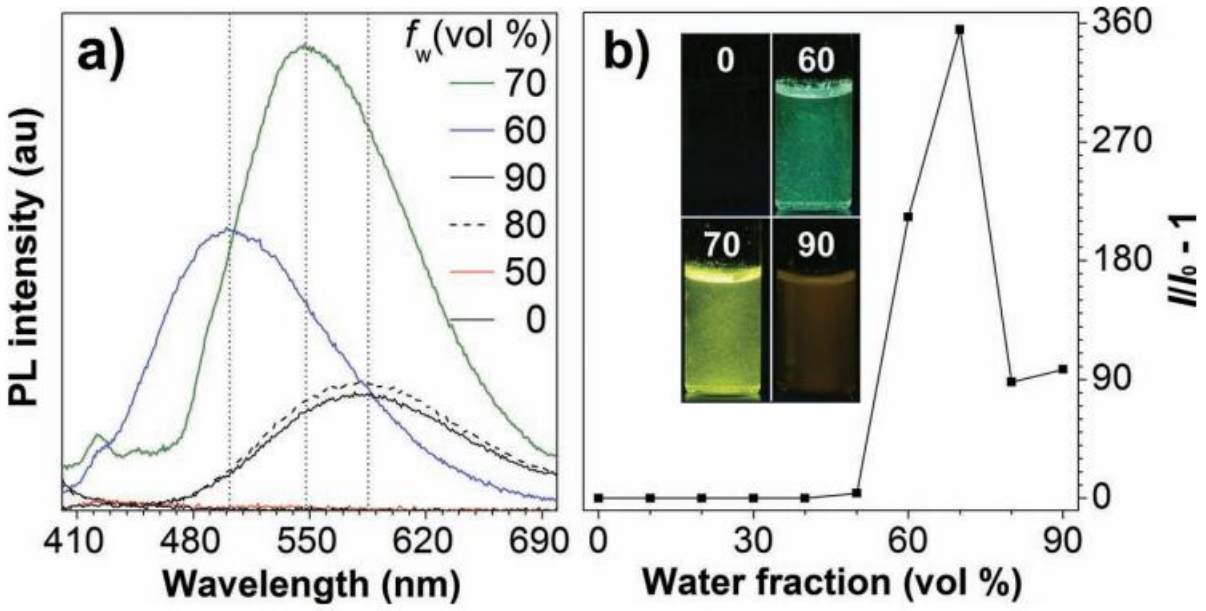

Figure 6. a) PL spectra of the dye in acetonitrile and acetonitrile/water mixtures. b) Plot of PL peak intensity vs water fraction (fw) of the aqueous mixture. Luminogen concentration: 50 × 10 − 6 M; excitation wavelength: 370 nm. Photographs of 1 in acetonitrile and its suspension in acetonitrile/water mixtures with fw = 60%, 70%, and 90% under UV illumination. Figures were taken from reference 23 and reprinted with copyright permission from Wiley.

1.1.5 Crystallization induced emission (CIE)

Crystallization-induced emission (CIE) is a captivating photophysical phenomenon where compounds emit light more efficiently in their crystalline state compared to their amorphous state. This phenomenon can also be referred to as crystallization-induced emission

enhancement (CIEE). In an amorphous or disordered solid state, compounds tend to emit light weakly or moderately. However, upon crystallization, the emission intensity significantly increases. This can occur due to the formation of through-space charge-transfer complexes, which facilitate stronger emission.

CIE has a range of promising applications across various fields like Optical Waveguides, anisotropic Light-Emitting Diodes (LEDs), Polarized Organic Lasers, Optical Sensors, Bioimaging, Organic Light-Emitting Diodes (OLEDs). CIE is closely associated with other phenomena such as: Crystallization-Induced Emission Enhancement (CIEE), Mechanochromic Luminescence, Mechanochromic Fluorescence (Mechanofluorochromism, MFC).[6]

CIE opens up exciting possibilities for advanced material science, contributing to innovations in optoelectronics, sensors, and imaging technologies. Several compounds exhibit CIE, including: Azobenzene Derivatives**,** F-Doped Carbon Dots**,** Various Organic Materials: Pyrrolidinylvinylquinoxaline derivatives, 1,2-Diphenyl-3,4-bis(diphenylmethylene)-1-cyclobutene, (4-Biphenylyl) phenyldibenzofulvene.

1.1.6 Mechanochromic Luminescence (MCL)

Mechanoresponsive Compounds are a special class of smart materials that exhibit a change in their fluorescence color when subjected to mechanical forces. Fluorescence in the solid state is influenced by interactions between neighbouring molecules, which are dictated by their supramolecular packing[36] and molecular conformation. Supramolecular packing is governed by weak intermolecular interactions,[7] such as hydrogen bonding and π-π interactions, which require minimal energy (stimulus) to reconfigure. When pressure is applied to these materials, it alters the supramolecular packing and the interactions between excited state molecules, leading to changes in fluorescence emission. In some cases, this process can be reversed through thermal annealing or exposure to solvent vapor. These materials have significant applications (Figure 7).

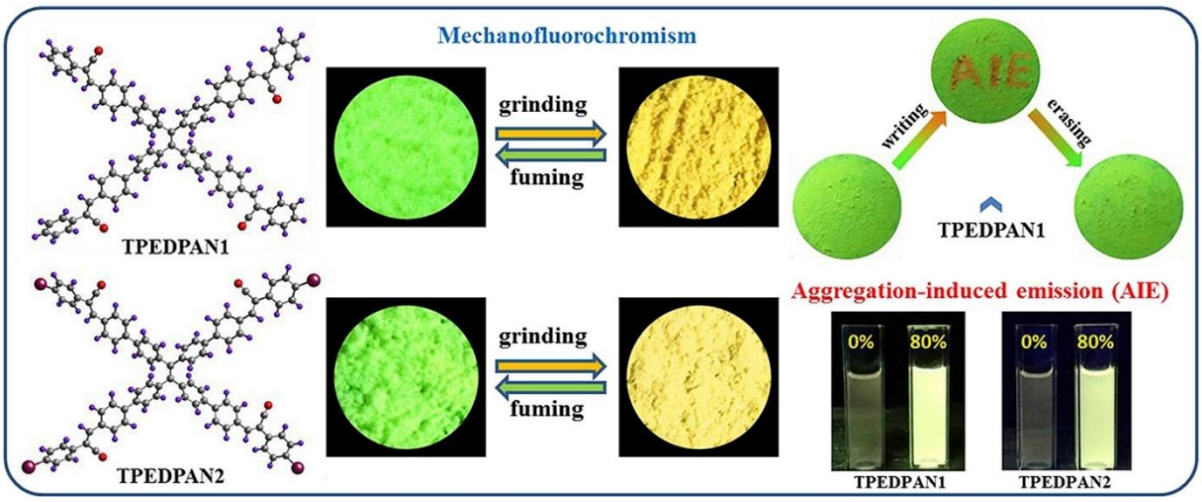

Figure 7. Change of photoluminescence color Green to yellow transformation under uv light upon grinding and surprisingly back to green upon vapour fuming. Figures were taken from reference 24 and reprinted with copyright permission from ELSEVIER**.**

Mechano-sensors, Optical Pressure Meters, Tunable Solid State Emitters. Mechanochromism: This phenomenon has been observed in liquid crystalline and crystalline solids and in dye-doped polymers. Examples includes**:** Diphenylflavanene, a typical piezofluorochromic compound[35-39], displays emission shifts due to intramolecular conformational changes or alterations in intermolecular interactions under mechanical pressure. Crystal to Amorphous phase: Grinding these materials can result in changes in mechanochromic luminescence. For example, the compound 4,4'-(acenaphtho[1,2-b]quinoxaline-8,11-diyl)bis (N, N-diphenylaniline), a donor-acceptor-donor type molecule, undergoes a luminescent change from green to orange color upon mechanical grinding. X-ray studies have shown that this color switching is due to the transformation from the crystalline phase to the amorphous phase. In summary, mechanoresponsive compounds are innovative materials that respond to mechanical forces by altering their fluorescence properties, offering potential uses in various sensing and optoelectronic applications.[8]

Recently jia et al showed that a novel single crystal, PyB, is synthesized in high yield by simply connecting a pyrene unit with a rhodamine B moiety. PyB exhibits multiple functions, including aggregation-induced emission, low-loss optical waveguiding, and tricolored mechanochromism. The key to fabricating such a multifunctional single crystal lies in selecting the C=N group as a spacer,[26] This choice simplifies the synthetic process, confines the molecular conformation to develop single crystals, and enables the dynamic observation of color variation in situ, as well as the quantitative analysis of applied pressure effects. This

straightforward approach can be extended to other fluorophores, thus offering new opportunities for the real-world application of mechanochromic materials in mechanical sensors, optical encoding, and optoelectronic devices.

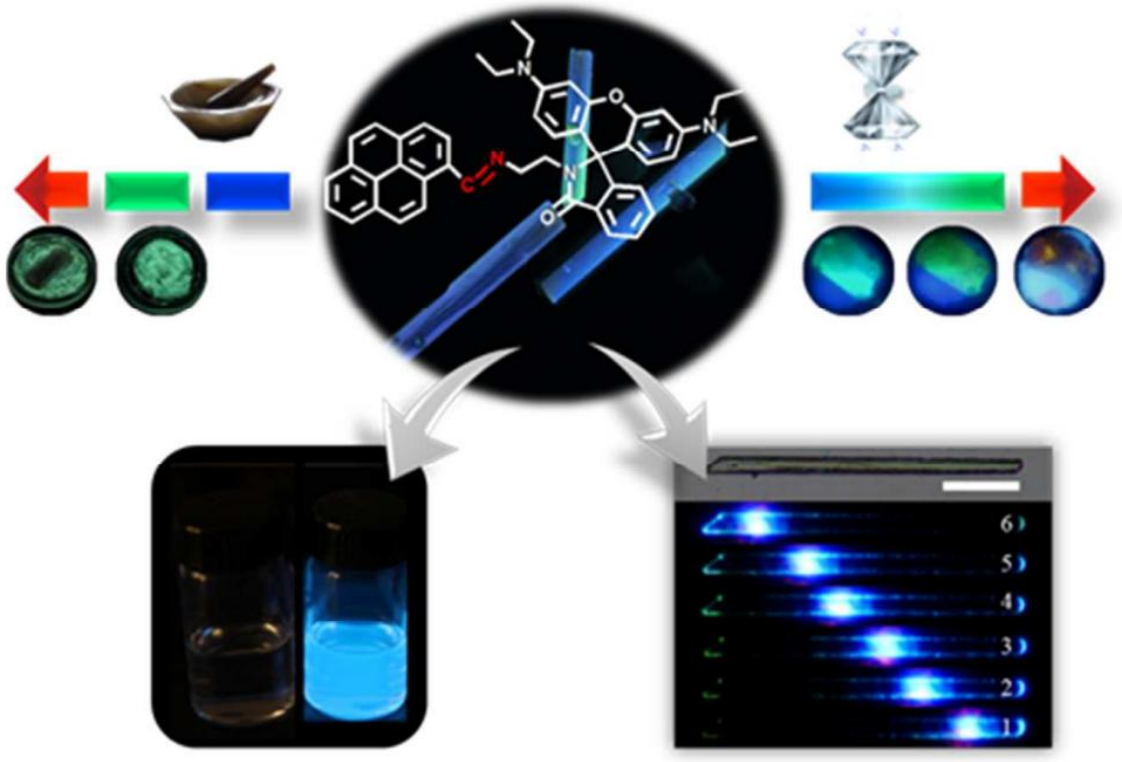

Figure 8. AIE, Mechanochromism and optical waveguiding. Figures were taken from reference 25 and reprinted with copyright permission from ACS.

1.1.7 Vapochromic Luminescence (VCL)

In the field of chemistry, vapochromism often intersects with solvatochromism, as vapochromic systems involve dyes that change color in response to the vapor of an organic compound or gas. Vapochromic devices serve as the optical equivalent of electronic noses.

They are primarily used in sensors designed to detect volatile organic compounds (VOCs) across various environments, such as industrial, domestic, and medical settings. Vapochromism is a fascinating and unique chromatic phenomenon where materials change color in response to the exposure of vapors of organic compounds or gases. It stands out from other chromatic phenomena due to its specificity in response to vapor stimuli. While vapochromism involves a color change in response to vapor, solvatochromism refers to a change in color due to the solvent environment. The color change occurs because the dye

interacts differently with various solvents, causing shifts in the absorption or emission spectra. Vapochromic materials are particularly useful in sensing applications, especially for detecting volatile organic compounds (VOCs), because of their sensitivity to vapor stimuli.

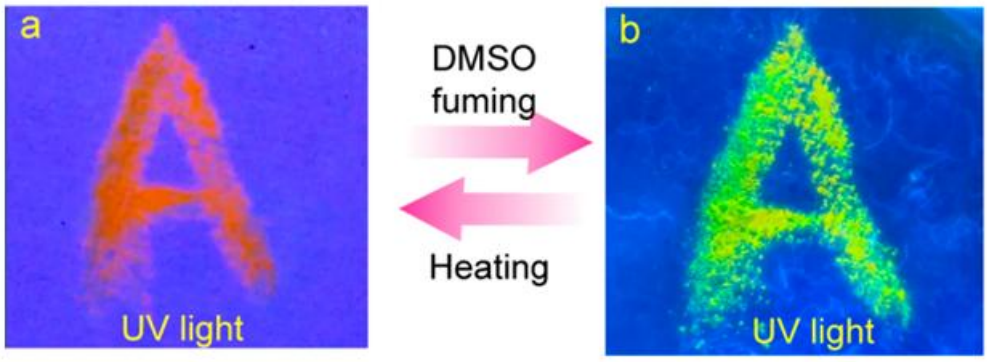

Figure 9. Reversible writing of 1R (a) "A" written by mechanical pressing. (b) DMSO fuming to green emissive "A" Figures were taken from reference 26 and reprinted with copyright permission from ACS.

The mechanism behind these behaviours are still illusive but it possible due to the arrangement of molecules within a crystal lattice can be sensitive to vapor exposure. Vapors can induce structural changes in the crystal, such as phase transitions or reorganisation of molecules, leading to color changes. Some vapochromic [9,26] materials exhibit color changes due to charge transfer processes. When exposed to vapors, the transfer of electrons between donor and acceptor molecules can be influenced, resulting in a change in the absorption or emission spectra.

Panda et al in 2018 showed that inkless writing, and self-erasing application is a remarkable solution to reduce paper waste, recycling cost in the printing industry. These innovative materials present an opportunity to reduce global warming by lowering the consumption of plant-based paper. Reported the design, synthesis, and fabrication of a donor-acceptor type (Z)-1,2-diarylacrylonitrile (1) compound. This compound exhibits highly contrasting and reversible Vapochromism under both visible and UV light in its solid state. Observed a unique multiphase luminescence switching from green (λ_{max} = 535 nm) to yellow (λ_{max} = 566 nm) and finally to orange-red (λ = 580, 640 nm), triggered by the gradual exclusion of entrapped DMSO molecules from the crystalline rod-like materials (figure 9). Utilising this purely organic material, demonstrated reversible inkless writing and printing on a cellulose strip by harnessing the photothermal effect of sunlight, which acts as an "inkless pen" (Figure 10). Successfully printed complex designs that are invisible in ambient light but become more visible under UV

light. Impressively, the writing is self-erasable when exposed to sunlight for prolonged periods, kept at ambient temperature, or instantly warmed. This smart functionality provides a cost-effective and environmentally friendly method for secure data communication and confidential data printing. An unprecedented, high-contrast vapochromic system that efficiently switches its visible and fluorescence colors. This system exhibits a unique multiphase fluorescence response, transitioning from green to orange-yellow through a yellow emissive state. The application of this material in a smart inkless writing process using environmentally abundant and benign sunlight stimuli. The written content can be self-erased in multiple ways, including exposure to sunlight, ambient temperature, vapor fuming, or warming. The results presented here have significant implications for developing cost-effective and environmentally friendly printing and writing technology for temporary, confidential communication with multiphase luminochromic behavior for security and anti-counterfeiting applications (Figure 10).

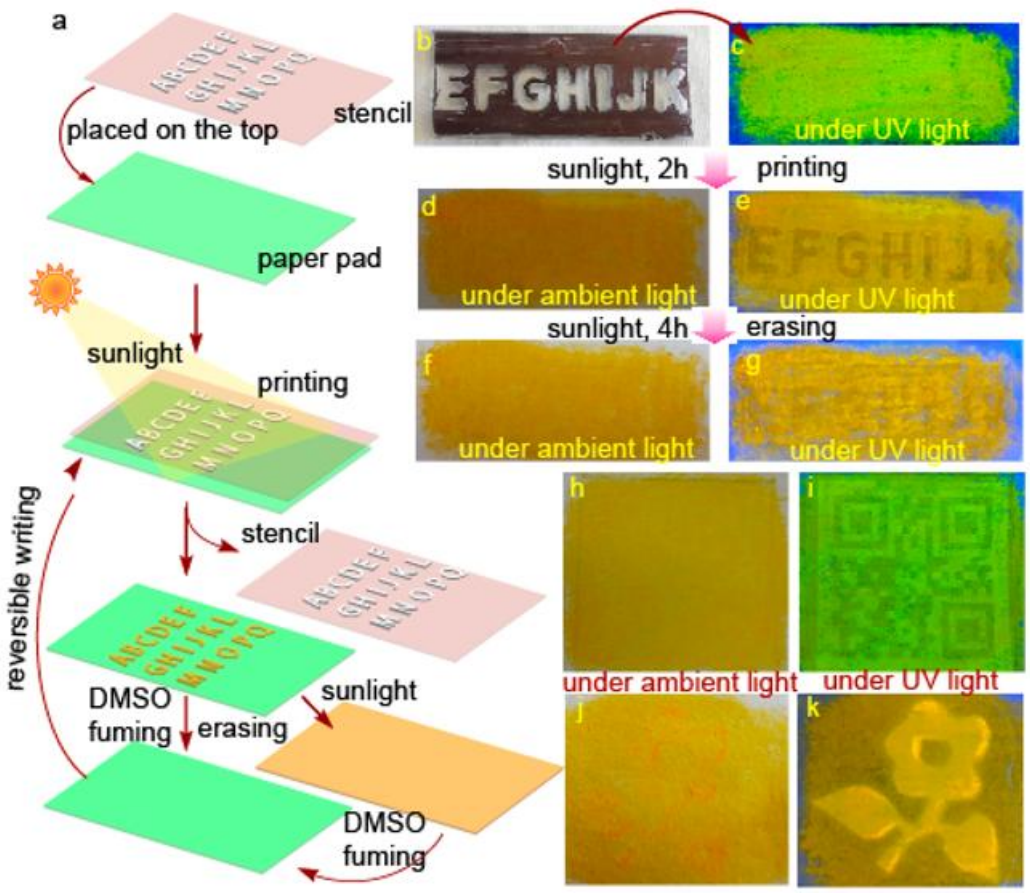

Figure 10. (a) Schematic diagram of the sunlight mediated printing. (b, c) Printing pad made from 1G. (d, e) Printing pad under sunlight and UV light. (f, g) Self-erasing under sunlight and UV light. (h–k) Printing of QR codes. Figures were taken from reference 26 and reprinted with copyright permission from ACS.

1.1.8 Thermochromic Luminescence

Thermo-fluorescence offers versatile applications in creating temperature monitoring and controlling devices. These devices find utility in diverse fields such as information recording, counterfeit prevention and detection, dynamic temperature measurement, and writing-erasing tools. Generally, for most organic compounds, luminescence intensity decreases with an increase in temperature due to thermal vibrations of molecules causing the loss of excited state energy through non-radiative processes.

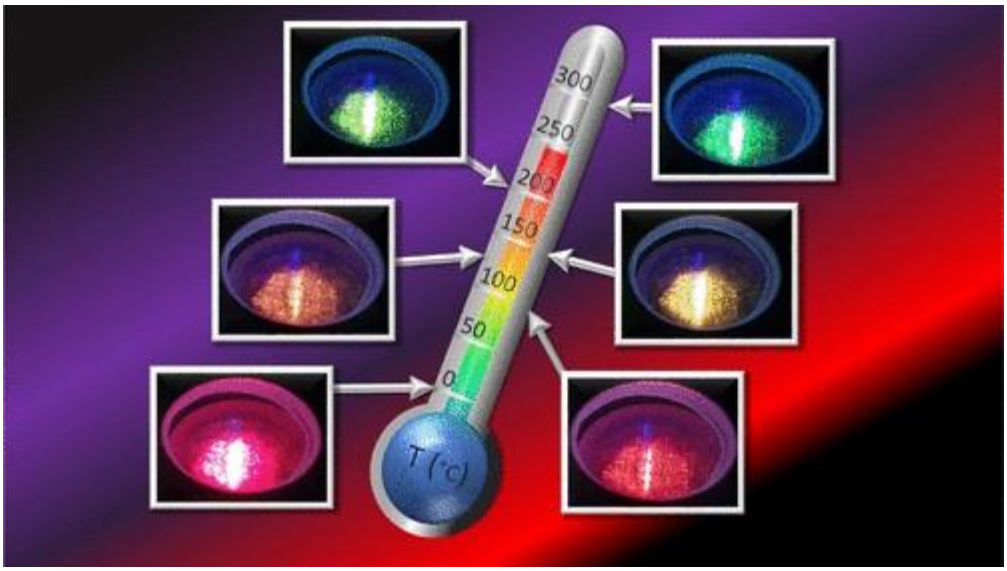

Figure 11. Change of photoluminescence color upon heating. Figures were taken from reference 27 and reprinted with copyright permission from ACS.

However, a particular class of charge transfer fluorescent compounds exhibits enhanced fluorescence intensity with increasing temperature due to twisted intramolecular charge transfer (TICT) interactions in the solid state. This unique behavior underscores the potential of temperature-sensitive luminescent materials for various applications, including marine research, underground geochemistry, wind tunnels, the automobile industry, and the aircraft industry, where conventional thermometers face significant challenges.[10]

In these scenarios, optical thermometers, such as infrared thermometers or fluorescent thermometers, offer major advantages, though their application is primarily limited to surface measurements. Nonetheless, luminescence-based temperature sensors are gaining attention in these applications due to their rapid response, high spatial resolution, and safe remote handling

capabilities. Consequently, there is a growing need for increased research activity in this area to harness these benefits fully.

Kato and co-workers presented a new type of stimuli-responsive luminescent liquid crystal that shows three distinct luminescent colors reddish-orange, yellow, and green—which can be switched by mechanical and thermal stimuli. The liquid crystal is composed of two dumbbell-shaped compounds and contains only one type of luminophore, 9, 10-bis(phenylethynyl)anthracene. When heated, the mixture forms a micellar cubic phase that emits reddish-orange photoluminescence under UV light. Mechanical shearing of the mixture in this phase at 90°C changes the luminescent color to green due to a phase transition to a columnar phase. Further mechanical shearing at room temperature results in an unidentified mesomorphic phase with yellow emission. This mesomorphic phase can transition back to the isotropic phase upon heating and subsequently cool to exhibit the original reddish-orange emission.

The liquid crystal's ability to switch between three different luminescent colors (Figure 12) in the condensed state, depending on the molecularly assembled structures, offers promising applications in mechano-sensors, security papers, optoelectronic devices, and data storage. This study highlights the potential of using a single luminophore to achieve multicolor luminescent displays and sophisticated stimuli-responsive luminescent materials.

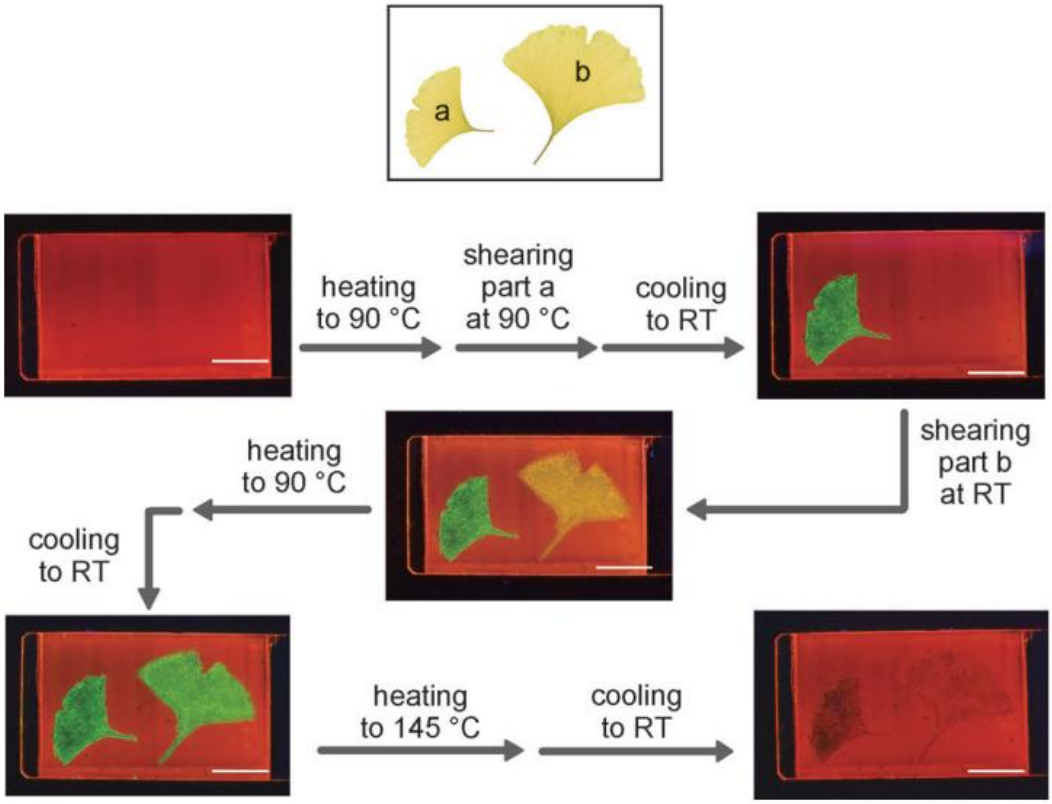

Figure 12. Procedures of writing and erasing tricolored luminescent images. Photoluminescent images were taken for the mixtures on a glass substrate under UV irradiation at 365 nm. Scale bar: 1 cm. Top panel shows two mechanically sheared sections a and b. Figures were taken from reference 28 and reprinted with copyright permission Wiley.

Zhao et al have demonstrated effective strategies to achieve rewritable and multi-level security printing using ionic Mn(II) complexes such as $[MnBr_4]_2[etpp]^{+2}$ and $[MnX_2Y_2]_2[tppt]^{+2}$ (X and Y = Cl, Br, or I). By leveraging reversible ionic coordination between the sensitizer and the emitter in these Mn(II) complexes, they dynamically controlled emission intensity and lifetime, enabling two types of confidential information printing (Figure 13). First, delicate images can be recorded on security paper composed of $[MnCl_4]_2[etpp]^{+2}$ and a PEG-PPG-PEG matrix using water as ink and then erased by heating multiple times. These printed patterns are invisible under ambient light but become clearly visible under UV illumination. The cost per print for this water-jet rewritable security printing, based on a conservative estimate of 30 uses per sheet, was calculated. The cost per print of the water-jet rewritable security printing system was estimated to be 0.014 Yuan, indicating its low cost. Additionally, cytotoxicity measurements of the etpp ligand and the $[MnCl_4]_2[etpp]^{+2}$complex were conducted using standard MTT (methyl thiazolyl tetrazolium) assays demonstrating the low toxicity of the

materials used. Consequently, this proposed strategy for security printing features multiple usages, easy operation, and low cost, suggesting great potential for daily routine encryption.

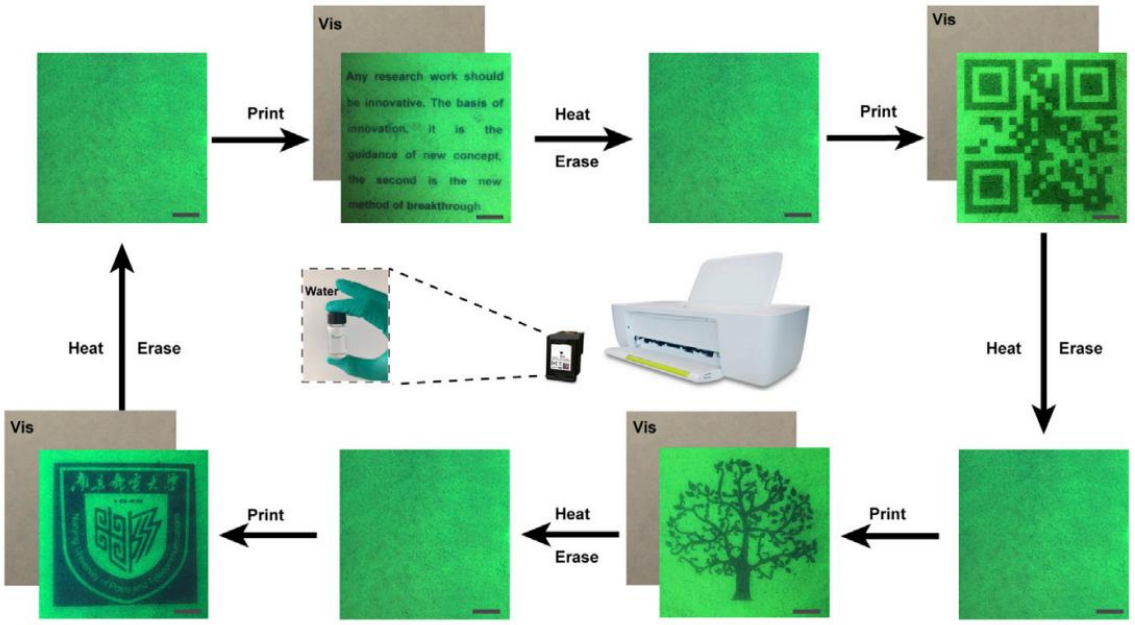

Figure 13. Water-Jet Rewritable Security Printing Photographs of sentences and patterns printed on security paper by using pure water as ink under ambient light and UV light. Scale bars, 1 cm. Figures were taken from reference 29 and reprinted with copyright permission from cell Press.

1.1.9 pH Dependent fluorescence

pH-dependent fluorescence refers to the change in a molecule's fluorescence intensity or emission wavelength as the pH of its environment varies. This behavior is typically observed in fluorophores that undergo protonation or deprotonation, altering their electronic structure and, consequently, their photophysical properties. pH is one of the important factors that have an influence in the day to day life. Measurement of pH is required in different situations. There are variety of methods for pH measurement. For example, Ikeda et al. reported the neutral and charged benzothiazole-based dyes that showed distinct fluorescence response in different pH condition in the presence of DNA.[8]

1.1.10 Photoswitching Materials

Photoswitching refers to the reversible transformation of a molecule between two distinct isomeric forms upon exposure to light. These molecules called photoswitches which undergo

structural changes such as cis–trans isomerization, ring opening/closing, or bond rearrangements, which alter their optical, electronic, or chemical properties. Molecular materials that exhibit photo-switchable optical properties in the solid state are of significant research interest due to their broad range of applications in optoelectronics, data storage, erasable and rewritable memory devices, anti-counterfeiting coding, and super-resolution imaging. Specifically, these photo-switching[50-52] optical materials have emerged as competitors to existing magneto-optical switching materials, which are commonly used in erasable and rewritable memory devices such as CD-ROMs and light-switchable optical fibers.[11]

These molecular materials can modulate their optical properties, such as visible or fluorescence color, through light irradiation of a specific wavelength or waveband. Typically, the underlying mechanism behind this optical switching involves changes in electronic excited states due to reversible or irreversible conversion between stable and metastable geometric (cis-trans) isomers, conformational isomers, or supramolecular packing changes triggered by light. The reverse transformation to the initial thermodynamically stable isomer is generally initiated using different wavelengths of light or thermal energy[12] (Figure 14).

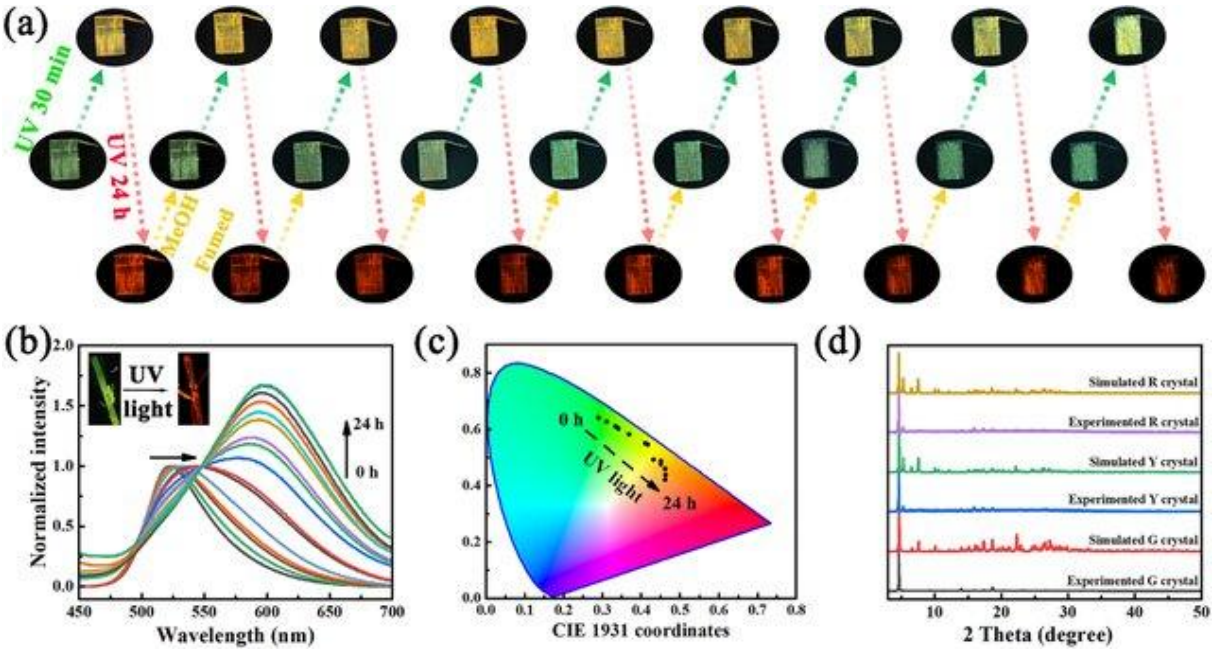

Figure 14. Reversible Switching of Photoluminescence color by using UV light. Figures were taken from reference 30 and reprinted with copyright permission from ELSEVIER**.**

These capabilities make photo-switchable molecular materials highly attractive for various advanced technological applications

Our extensive literature survey has revealed that the primary photo-fluorochromic systems reported consist mainly of diarylethenes, azobenzenes, fulgides, and spiropyrans. While compounds containing these molecular units exhibit excellent photochromic or photo-fluorochromic properties, they also have various drawbacks or limitations. For instance, diarylethene systems have good photochromic properties and fatigue resistance but are synthetically very challenging, raising concerns about their cost-effectiveness and viability for practical applications. Spiropyran (SP)–merocyanine (MC) systems show good photochromism in the solid state; however, in most cases, they are poorly photoactive in the solid crystalline state because the tight packing of the crystal impedes the geometric isomerization (cis-trans isomerization) that occurs during photochemical reactions between the SP and MC forms.[13]

Fulgide systems suffer from low photostability of the photoconverted state and poor fatigue resistance. Additionally, undesired spectral absorption and concomitant reverse reactions causing inefficient photoconversion are common drawbacks of these systems. Moreover, a majority of the molecular systems exhibit photo-triggered fluorochromism only in solution state, not in solid state, thus limiting their practical application. This limitation may be due to the difficulty in achieving solid-state optical properties, especially fluorescence, due to the phenomenon known as aggregation-caused quenching (ACQ).[14] particularly switchable fluorescence properties in the solid state. Therefore, design and synthetic efforts should be aimed at creating novel molecules with new photo-responsive units. In fact, reports of solid-state photo-switching luminescence materials are very limited, making the development of efficient solid-state luminescence switches significantly challenging yet increasingly imperative for numerous practical applications.

1.1.11 Thermosalient Crystals

Dynamic molecular crystals are a newly researched class of engineering materials with significant promise due to their responsiveness, lightweight, flexibility, and potential biocompatibility as energy-converting materials. These crystals demonstrate remarkable dynamic effects, including bending, twisting, jumping, fracturing, shape-memory, and self-

healing. Such properties make them suitable for use in actuators, flexible electronics, optical waveguides, sensors, and various other applications [15].

The energy transduction process in these materials typically involves the input of energy, such as heat, light, or mechanical force, and the output in the form of kinetic energy capable of performing mechanical work. This process depends on the amplification of molecular-scale changes, leading to reshaping or autonomous propulsion at a macroscopic level.[53-54] Organic crystalline materials have the added advantage of low densities, making them lightweight. They are also amenable to chemical alteration of their physicochemical properties and can maintain mechanical stability across a wide range of temperatures, enhancing their potential for future applications [16].

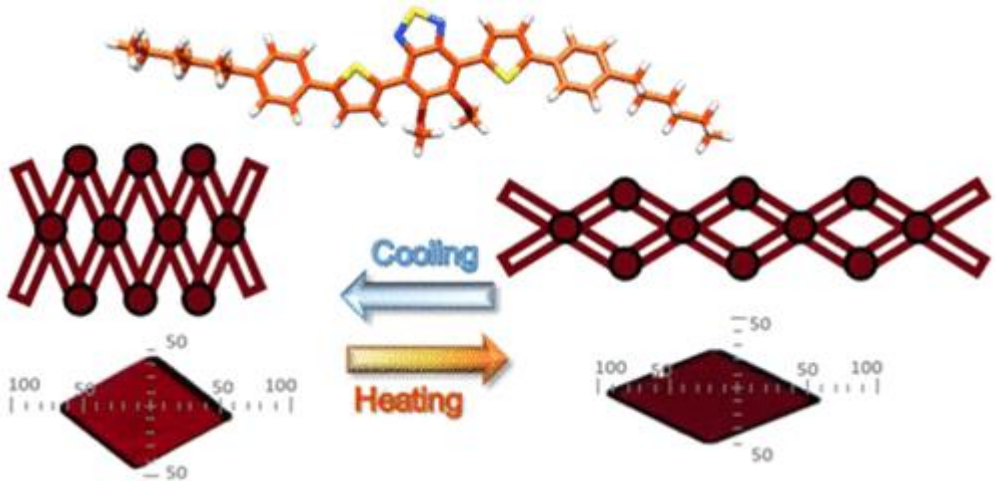

Figure 15. Change in the shape of a crystal due to packing change during reversible cycle of heating and cooling. Figures were taken from reference 31 and reprinted with copyright permission from ACS.

Current research efforts are focused on understanding intermolecular interactions and establishing predictive approaches for their physicochemical properties. Mechanically flexible crystals are generally categorized as either plastic or elastic, based on their response and ability to recover shape after applying mechanical force. Despite significant efforts, a reliable design of mechanical properties, such as flexibility, remains challenging for molecular crystals, as the role of molecular movement and intermolecular interactions in dissipating strain is intricately linked to crystal packing (figure 15).

Various mechanical effects have been reported with molecular materials, yet organic crystals capable of multiple dynamic effects are rare, and at present, their performance is worse than some of the common actuators. Gong et al reported a confluence of different mechanical effects

across three polymorphs of an organic crystal that can efficiently convert light into work. Upon photo dimerization, acicular crystals of polymorph I display output work densities of about 0.06–3.94 kJ m^{-3}, comparable to ceramic piezoelectric actuators. Prismatic crystals of the same form exhibit very high work densities of about 1.5–28.5 kJ m^{-3}, values that are comparable to thermal actuators. Moreover, while crystals of polymorph II roll under the same conditions, crystals of polymorph III are not photochemically reactive; however, they are mechanically flexible. The results demonstrate that multiple and possibly combined mechanical effects can be anticipated even for a simple organic crystal.[17]

Compared to mechanical or temperature-driven control over macroscopic shape, light-driven actuation offers distinct advantages, including the ability for remote control and precise energy input. Light-triggered movements or deformations of molecular crystals have been established through several photochemical reactions, such as trans-cis photoisomerization, photocyclization, and photocycloaddition.

However, two significant challenges in this field are low efficiency and a lack of multifunctionality—both highly desired yet difficult to achieve. Predicting actuation efficiency is challenging, and for small objects like organic crystals, measuring it is practically difficult. Additionally, achieving multiple mechanical motions from the same compound is particularly challenging due to the complexities in predicting crystal packing, intermolecular interactions, and crystal habits. To address these challenges, the well-established dimerization reaction, known for its reliable relation with geometric criteria, is employed in solid-state chemistry research.[18-19]

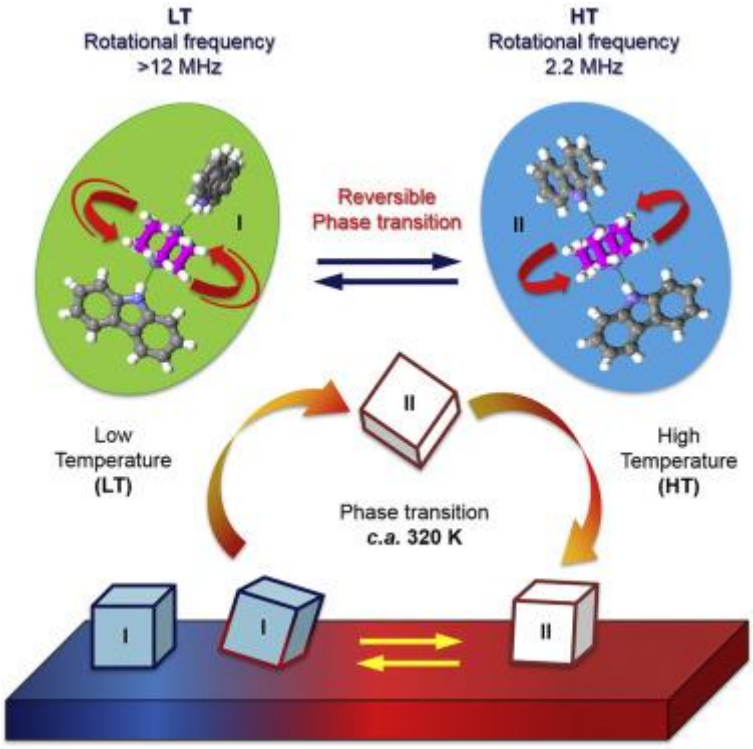

Figure 16. Responsiveness to heat stimuli, jumping from the hot plate due to thermosalient phase transition. Figure was taken from reference 32 and reprinted with copyright permission from ELSEVIER.

Jumping crystals[32] are a class of thermosalient crystals, exhibit sudden and dramatic movements such as jumping, bending, or twisting in response to external stimuli like heat or light. This behavior arises from the rapid release of internal stress accumulated within the crystal structure during a phase transition. The mechanism behind this phenomenon involves phase transitions, where molecular rearrangements lead to the abrupt release of stored elastic energy, causing the crystal to move. Additionally, anisotropic thermal expansion, in which different parts of the crystal expand at varying rates, generates internal stress that, when released, results in jumping.[32] Some crystals also undergo photochemical reactions, such as cis-trans isomerization or photocyclization, in response to light, leading to structural changes that induce mechanical motion. Notable examples include tetrabromobenzene crystals, which jump, split, and spin when gently heated, oxitropium bromide crystals, which exhibit jumping behavior due to the thermosalient effect first observed in the 1980s, and (phenylazophenyl) palladium hexafluoroacetylacetonate (PHA), which undergoes a phase transition upon heating, causing the crystals to leap off the hot stage (figure 16). These dynamic materials have promising applications in actuators that convert energy into motion, artificial muscles that mimic biological movement, and sensors that detect environmental changes and respond with

mechanical motion. As an emerging field, the study of jumping crystals continues to reveal new insights into their underlying mechanisms and potential technological applications.[25-33]

1.2 Scope of this study

While numerous stimuli-responsive fluorescent materials have been documented in literature, the potential for developing new materials with unique properties is always welcomed. Recent reviews have developed a fascinating combination of different mechanical effects across three polymorphs of an organic crystal capable of efficiently converting light into work. Dynamic molecular crystals represent an exciting and newly researched class of engineering materials with the potential to be responsive, lightweight, flexible, and biocompatible. These materials are known for their remarkable dynamic effects, which can be restorative or disintegrative. These effects include bending, twisting, jumping, fracturing, shape-memory, and self-healing. Such properties make them promising for use in actuators, flexible electronics, optical waveguides, sensors, and many other potential applications. These materials typically transduce energy by converting inputs like heat, light, or mechanical force into kinetic energy, which can be used for mechanical work. The efficiency of this process relies on amplifying molecular-scale changes to achieve macroscopic reshaping or autonomous propulsion. Additionally, their low densities make them lightweight, and their physicochemical properties can be chemically altered. These materials also remain mechanically stable over a wide range of temperatures, making them suitable for high or low-temperature applications.

Most current research efforts aim to better understand the role of intermolecular interactions and develop predictive approaches to their physicochemical properties. Mechanically flexible crystals are generally classified as plastic or elastic, based on their response and ability to recover shape after mechanical force is applied. However, designing reliable mechanical properties like flexibility for molecular crystals remains challenging due to the complex relationship between molecular movement, intermolecular interactions, and crystal packing. Compared to mechanical or temperature-driven control, light actuation offers advantages like remote control and precise energy input. Light-triggered motions or deformations have been demonstrated for several photochemical reactions, including trans-cis photoisomerization, photocyclization, and photocycloaddition.

Despite the existence of several such materials, a systematic study and understanding of structure-function correlation remain unexplored. This thesis aims to highlight our recent

advancements in solid-state emitters and investigate their stimuli-sensing behavior for practical applications. We present several organic molecular system that exhibiting unique fluorescence properties due to charge transfer interactions. Furthermore, we have studied the impact of various stimuli on the fluorescence behavior of these solid crystals.

■ REFERENCES

1. J. C. deMello, H. F. Wittmann, R. H. Friend, *Adv. Mater.*,1997, **9**, 230−232.
2. T. Mutai, H. Satou and K. Araki, *Nature Mater.* 2005, **4**, 685−687.
3. R. Davis, N. P. Rath and S. Das, *Chem. Commun.*, 2004, 74–75.
4. Y. Dong, J. W. Y. Lam, A. Qin, Z. Li, J. Sun, H. H. Y. Sung, I. D. Williamsa and B. Z. Tang, *Chem Commun.*, 2007, 40–42.
5. H. Tanaka, K. Shizu, H. Nakanotani, and C. Adachi, *Chem. Mater*, 2013, **25**, 3766–3771.
6. C. Cao, X. Liu, Q. Qiao, M. Zhao, W. Yin. D. Mao, H. Zhang and Z. Xu. *Chem. Commun*. 2014, **50**, 15811-15814.
7. M. Baruah, W. Qin, C. Flors, J. Hofkens, R. A. L. Valle´e, D. Beljonne, M. V. Auweraer, W. M. De Borggraeve, and N. Boens, *J. Phys. Chem. A*, 2006, **110**, 5998-6009.
8. S. Ikeda, A. Okamoto, *Photochem. Photobiol. Sci.*, 2007, **6**, 1197–1201.
9. L. Bai, P. Bose, Q. Gao, Y. Li, R. Ganguly, Y. Zhao, *J. Am. Chem. Soc.* 2017, **139**, 436−441.
10. J. Wu, J. Tang, H. Wang, Q. Qi, X. Fang, Y. Liu, S. Xu, S. X. Zhang, H. Zhang, and W. Xu, *J. Phys. Chem. A*, 2015, **119**, 9218−9224.
11. J. Luo, Z. Xie, J. W. Y. Lam, L. Cheng, H. Chen, C. Qiu, H.S. Kwok, X. Zhan, Y. Liu, D. Zhu and B. Z. Tang, *Chem. Commun.*, 2001, 1740–1741.
12. Z. Chi, X. Zhang, B. Xu, X. Zhou, C. Ma, Y. Zhang, S. Liu and J. Xu, Chem. Soc. Rev., 2012, **41**, 3878–3896.
13. S. Yagai, T. Seki, H. Aonuma, K. Kawaguchi, T. Karatsu, T. Okura, A. Sakon, H. Uekusa, H. Ito, *Chem. Mater.*, 2016, **28**, 234−241.
14. B. R. Crenshaw, M. Burnworth, D. Khariwala, A. Hiltner, P.T. Mather, R. Simha, and C. Weder, *Macromolecules.*, 2007, **40**, 2400-2408.
15. S. Hirata, K. Lee, and T. Watanabe, *Adv. Funct. Mater.*, 2008, **18**, 2869–2879
16. Y. Zhao, H. Gao, Y. Fan, T. Zhou, Z. Su, Y. Liu, Y. Wang. *Adv. Mater.*, 2009, **21**, 3165-3169.
17. Q. Zhu, W. Yang, S. Zheng, H. H. Y. Sung, I. D. Williams, S. Liu and B. Z. Tang, *J. Mater. Chem. C.*, 2016, **4**, 7383-7386.
18. P. Minei, M. Koenig, A. Battisti, M. Ahmad, V. Barone, T. Torres, D. M. Guldi, G. Brancato, G. Bottari and A. Pucci, *J. Mater. Chem. C.*, 2014, **2**, 9224–9232.
19. K. Nagura, S. Saito, H.Yusa, H. Yamawaki, H. Fujihisa, H. Sato, Y. Shimoikeda, and S. Yamaguchi, *J. Am. Chem. Soc.*, 2013, **135,** 10322−10325.

20. K. Anandhan, M. Cerón, V. Perumal, P.Ceballos, P. Gordillo-Guerra, E Pérez Gutiérrez, A. E. Castillo, S. Thamotharan, M. J. Percino , *RSC Adv*., 2019, **9**, 12085-12096.
21. S. Yagai, T. Seki, H. Aonuma, K. Kawaguchi, T. Karatsu, T. Okura, A. Sakon, H. Uekusa, H. Ito, *Chem. Mater*., 2016, **28,** 234–241.
22. C. Xu, H. Shen, T. M. Liu , R. T. K. Kwok , J. W. Y. Lam , B.Z. Tang, *iScience*., 2023, **26,** 106568.
23. X. Luo, J. Li, C. Li, L. H, Yong, Q. Dong, Z. Liu, Z. Bo, B. Z. Tang. *Advanced Materials.*, 2011, **23**, 3261-3265.
24. S. Gundu, M. Kim, N. Mergu, Y.A. Son. *Dyes and Pigments.*, 2017, **146**, 7-13.
25. Y. Li, Z. Ma, A. Li, W. Xu, Y. Wang, H. Jiang, O. K. Wang, Y. Zhao, O. X. Jia, *ACS Appl. Mater. Interfaces.*, 2017, **9**, 8910–8918.
26. T. Panda, D.K. Maity, M. Panda. *ACS Appl. Mater. Interfaces.*, 2018, **10**, 29100−29106.
27. W. P. Karolina, T. Kamila, M. Karolina, L. Benoit, F. L. Marciniak, *ACS Appl. Mater. Interfaces.*, 2020, **12,** 44039–44048.
28. Y. Sagara, T. Kato, *Angew. Chem. Int. Ed*., 2011, **50**, 9128–9132.
29. P. She, Y. Ma, Y. Qin, M. Xie, F. Li, S. Liu, W. Huang, Q. Zhao, *Matter*., 2019, **1**, 1644–1655.
30. E. Procházková, J.Filo, L.M. Čechová, M. Dračínský, I. Císařová, Z. Janeba, I. Kawamura, A. Naito, I. Kubena, P. Nádaždy, P. Šiffalovič , M. cigan, *Dyes and Pigments.*, 2022, **199**, 110066.
31. M. Afsar U. Raúl M. Sergio, G.V. Marcelo, E. M. Carmen, R. Delgado, E. Gutiérrez, P. A. Monge, B. G. Lor. *J. Am. Chem. Soc*. 2024, **146**, 40, 27690–27700.
32. A. C. Molina, D. P. Karothu, M. J. Jellen, R. A. Toscano, M. A. G. Garibay, P. Naumov, B. R. Molina, *Matter*, 2019, **1,** 1033-1046.
33. Hong, J.W.Y. Lam, B. Z. Tang, *Chem. Commun***.**, 2009, **29**, 4332-4353.
34. P. Naumov, S. Chizhik, M. K. Panda, N. K. Nath, E. Boldyreva. *Chem. Rev.* 2015, **115**, 12440–12490.
35. G. Bae, M. Seo, S. Lee, D. Bae, M. Lee, *Adv. Mater. Technol*., 2021, **6**, 2100479.
36. S. Zeng, H. Sun, C. Park, M. Zhang, M. Zhu, M. Yan, N. Chov, S. Li, A.T. Li, G. Smith, S. Xu, Z. Li, Y. Hou, B. Li, D. Z. Wang, L. Sun, *Mater. Horiz.*, 2020, **7**, 164.
37. S. Ito, *CrystEngComm.*, 2022, **24**, 1112.
38. G. Giordano, M. Gagliardi, Y. Huan, M. Carlotti, A. Mariani, A. Menciassi, E.

Sinibaldi, B. Mazzolai. *Adv. Sci.*, 2021, **8**, 2100418.

39. T. Butler, A.S. Mathew, M. Sabat, C.L. Fraser, *A.C.S. Appl, Mater. Interfaces.*, 2017, **9** 17603.
40. G. Gogoi, D. Kashyap, R.J. Sarma, *Cryst. Growth Des*., 2018, **18,** 4963.
41. J. Luo, Z. Xie, J.W.Y. Lam, L. Cheng, H. Chen, H.S.K. Qiu, X. Zhan, Y. Liu, D. Zhu, B. Z. Tang, *Chem. Commun.*, 2001, 1740.
42. P. Shi, R. Zhao, M. Zhang, M. Lin, Y. Duan, T. Han, *Mater. Lett.*, 2019, **243**, 38.
43. S. Nakamura, K. Okubo, Y. Nishii, K. Hirano, N. Tohnai, M. Miura. *J. Mater. Chem. C.*, 2024, **12**, 2370–2378.
44. Z. Li, X. Wang, L. Han, C. Zhu, H. Xin, Y. Yin, *Adv. Mater*., 2022, **34**, 2107398.
45. J. J. Liu, S.B. Xia, T. Liu, J.M. Liub, F.X. Cheng, *CrystEngComm*., 2021, **23**, 4320.
46. C. L Sun, C. Wang, R. Boulatov. *Chem photo chem.*, 2019, **3**, 268.
47. J. W. Leem, H-J Jeon, Y. Ji, S. M. Park, Y. Kwak, J. Park, K-Y Kim, S-W Kim, Y L. Kim, *ACS Cent. Sci.*, 2022, **8**, 513.
48. H. Zhang, X. Ji, *ACS Cent. Sci.*, 2022, **8**, 507.
49. D. Hu, W. Xu, G. Wang, K. Liu, Z. Wang, Q. Shi, S. Lin, Z. Liu, and Y Fang, *Adv. Funct. Mater*.,2022, **32,** 2207895.
50. Z. Yu and S. Hecht, *Chem. Commun.*, 2016, **52**, 6639.
51. Y. Zhang, K. Zhang, J. Wang, Z. Tian, and A. Q. Li, *Nanoscale.*, 2015, **7**, 19342.
52. M. Kathan and S. Hecht *Chem. Soc. Rev.*, 2017, **46**, 5536.
53. D. Das, T. Jacobs, L. J. Barbour, *Nat. Mater*., 2010, **9**, 36−39.
54. I. E. Claassens, L. J. Barbour, D. A. Haynes, *J. Am. Chem. Soc*., 2019, **141,** 11425−11429.

CHAPTER-2

Cyanostilbene-based organic luminophores exhibiting aggregation-induced emission and mechanochromic luminescence.

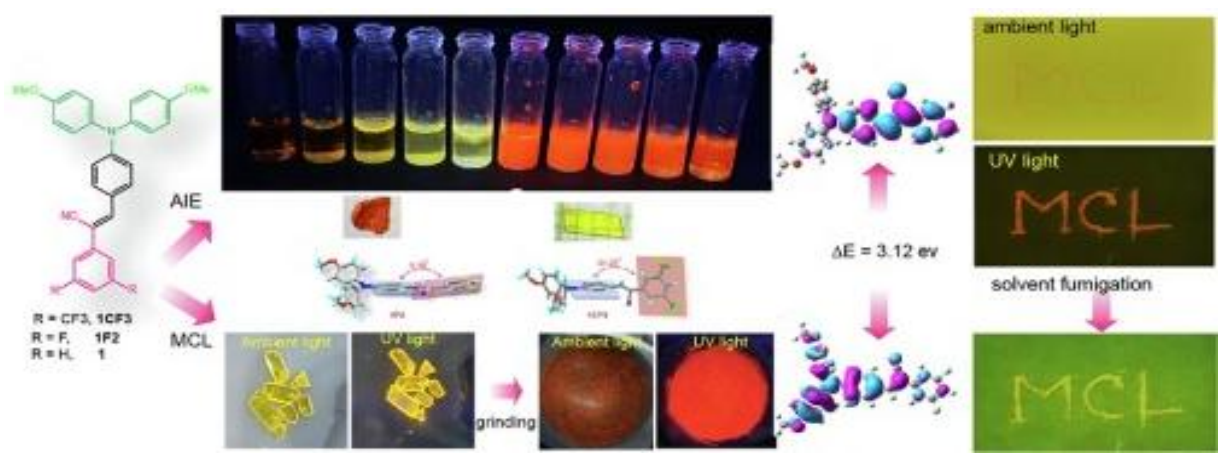

Cyanostilbene-based organic luminophores exhibiting aggregation-induced emission and mechanochromic luminescence.

2.1 Introduction

This chapter discussees about novel cyanostilbene-based luminogens, **1CF$_3$** and **1F$_2$**, which exhibit pronounced "aggregation-induced emission" (AIE) characteristics and mechanochromic luminescence (MCL) switching in the solid state. A poorly emissive methanol solution of **1CF$_3$** or **1F$_2$** becomes highly emissive after the addition of a poor solvent. Our morphological study reveals that during the AIE process, the molecules self-assemble into a higher crystalline state. When the single crystals of **1CF$_3$** or **1F$_2$** were subjected to mechanical pressure, a prominent mechanochromic switch from greenish-yellow emission to red emission was observed. The red emissive material can revert to its initial greenish-yellow emission through solvent vapor fumigation. Powder X-ray diffraction and single crystal X-ray diffraction studies revealed that the mechanochromic color switching is due to packing changes induced by mechanical pressure. The practical applicability of these MCL materials was demonstrated through ink-free writing and solvent vapor erasing.

In recent years, organic solid-state photoluminescent materials have garnered significant attention due to their wide range of technological applications, including light-emitting diodes, sensors, optical waveguiding materials, and biological applications.[1–10] Achieving solid-state emissive materials is challenging compared to their solution-phase counterparts because the emission of typical organic fluorophores rapidly quenches with increasing solution concentration due to molecular aggregation, which favors detrimental π-π stacking interactions. Since the discovery of Aggregation Induced Emission (AIE) by Tang et al.[11–15] solid-state emitters can now be developed by strategically designing AIE-gen molecules that facilitate non-planar packing in aggregation, thereby enhancing fluorescence emission in the solid aggregated state.[16–24]

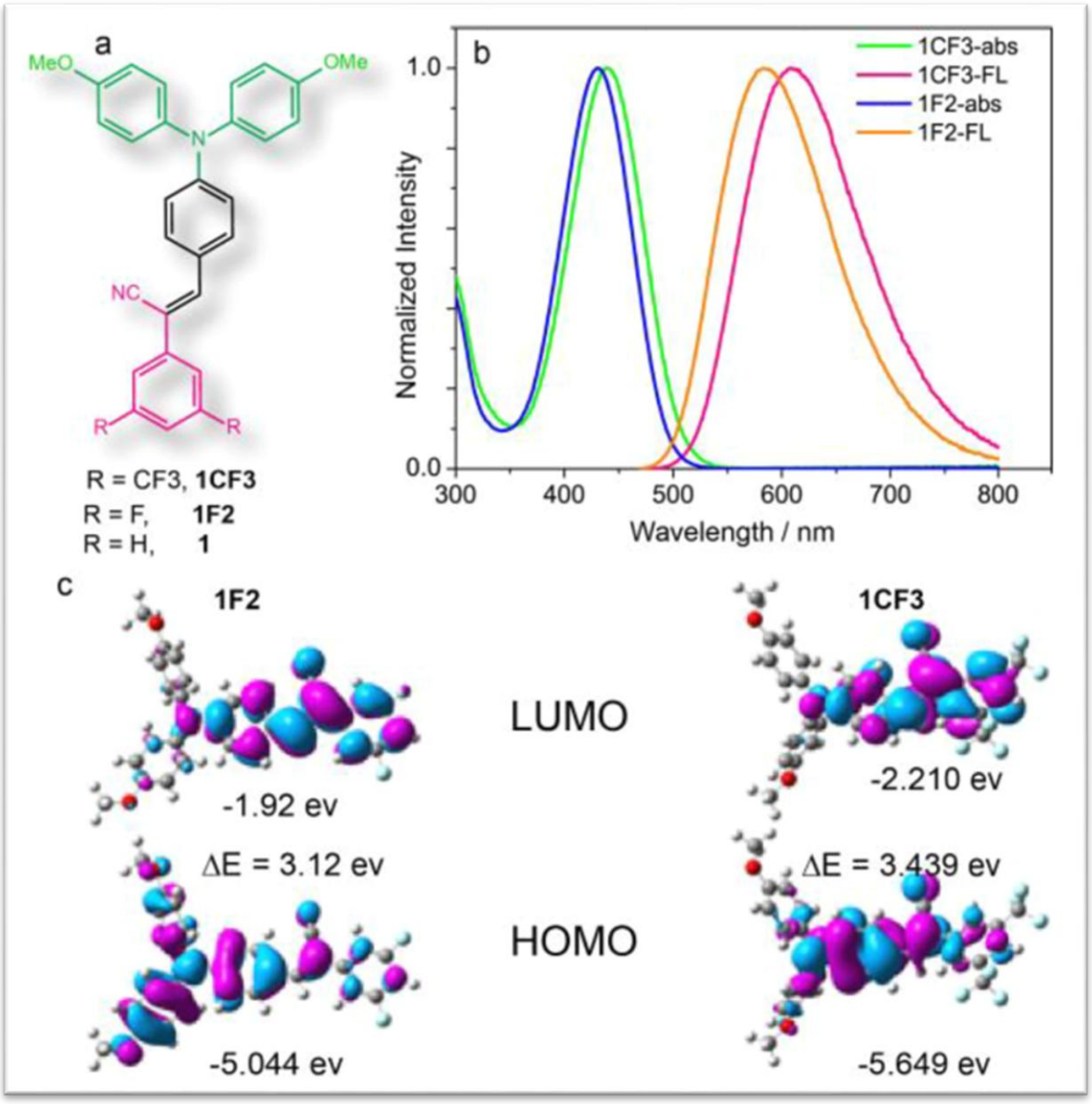

Figure. 1 (a) Molecular structure and (b) absorption/emission data of **1F$_2$** and **1CF$_3$** in toluene solution. (c) DFT calculated HOMO-LUMO profiles of **1F$_2$** and **1CF$_3$**.

Stimuli-responsive fluorescence switching materials, capable of reversibly switching their emission color in response to various external stimuli such as light, mechanical/shear force, heat and chemical vapour,[25–32] are of particular importance due to their utility in various technological applications. Among the various stimuli, mechanical force is an environmentally benign and easily accessible energy source that can be used to manipulate the emission properties of solid-state luminescent materials. MCL materials can switch their emission wavelength and intensity in response to different mechanical forces such as crushing, grinding, or directional rubbing.[33–42] In condensed media such as crystals, polymers, or amorphous states, color changes can be attributed to molecular tautomerization, isomerization, or supramolecular

packing changes, although the exact mechanism of chromogenic switching associated with excited-electronic state variations remains elusive. Moreover, the synthesis of most MCL dyes involves tedious multistep processes, undermining their viability and cost-effectiveness for practical applications.

Thus, it is always desirable to design and synthesize new MCL molecules with novel optical properties. Herein, we report synthetically simple, donor-acceptor (D-A) type cyanostilbene-based molecules (**1CF$_3$** and **1F$_2$**) that display pronounced AIE behavior as well as MCL in the solid state. These molecules are designed with bulky methoxy-substituted diphenylamine donor groups, which facilitate non-planar packing arrangements during aggregation, while the **F/CF$_3$** and –CN functional groups facilitate the reconfiguration of intermolecular interactions during packing changes. To observe the influence of substituents in the acceptor moiety, we also synthesized a reference molecule **1** without any **-F** or **-CF$_3$** groups.

2.2 Experimental

2.2.1. Materials & methods

4-[Bis(4-methoxyphenyl)-amino]benzaldehyde and 3,5-Bis(trifluoromethyl)-phenyl acetonitrile were purchased from TCI India and used as received without further purifications. Tetrabutyl ammonium hydroxide (TBAH), acquired from Merck Chemicals, was also used in its commercially available form. For synthesis, Merck ACS-grade solvents were employed, while spectroscopy-grade solvents facilitated crystallization and spectroscopic studies to ensure high-quality results. Several Analytical Techniques Utilized as follows,

NMR Spectroscopy: Both ^{1}H NMR (300 MHz) and ^{13}C NMR spectra were recorded on a Bruker AVANCE 300 spectrometer using $CDCl_3$ or DMSO-d_6 as the solvent. The chemical shifts (δ) are reported in ppm for precision.

Scanning Electron Microscopy (SEM): SEM images of the samples were captured using a FEI INSPECT F50 instrument with an operating voltage of 5 kV. The samples were coated with a thin layer of gold to enhance conductivity and image clarity.

High-Resolution Mass Spectrometry (HRMS): The HRMS of compounds **1F$_2$** and **1CF$_3$** were acquired using a QTOF Micro YA263 mass spectrometer operated in electrospray ionization (ESI) mode.

UV-Vis and Fluorescence Spectroscopy: UV-Vis absorption spectra were recorded with a Shimadzu UV-2401C spectrophotometer in solution and solid-state configurations. For fluorescence studies in the solid state, a HORIBA Jobin Yvon Fluorolomax-4 spectrofluorimeter was employed. Additionally, lifetime measurements were performed on a Modular Time-Correlated Single Photon Counting (TCSPC) system equipped with a Delta Flex detector (PPD850).

Infrared Spectroscopy (IR): IR spectra were recorded using a PerkinElmer LX-1 FT-IR spectrometer to examine functional group characteristics and molecular interactions.

Powder X-ray Diffraction (PXRD): PXRD patterns were obtained using a Bruker D8 Advanced Diffractometer with Cu Kα radiation (λ = 1.5418 Å), operating at 40 kV and 40 mA. The Lynxeye detector was utilized for data acquisition with a scanning rate of 0.2 seconds per step over a 2θ range of 0° to 50°.

Single Crystal X-ray Diffraction

High-quality single-crystal X-ray diffraction data for **1F$_2$** and **1CF$_3$** were collected using a Bruker D8 Venture APEX 3 diffractometer equipped with a CCD area detector and MoKα radiation (λ = 0.71069 Å). The SAINT program (version 8.38A) was used for data reduction, and XPREP (within the APEX 3 suite, version 2017.3–0) ensured structural agreement. Absorption corrections were performed with SADABS, and the structures were solved using SHELXT (version 2018/2) and refined with SHELXL-2014. Non-hydrogen atoms were refined anisotropically, while hydrogen atoms were calculated and refined isotropically. Crystallographic data for **1CF$_3$** and **1F$_2$** have been deposited at the Cambridge Crystallographic Data Centre (CCDC) under deposition no, 2154811 and 2154774.

2.2.2 Synthesis & Characterizations:

In a 100 mL round-bottom flask equipped with a magnetic stirrer and a reflux condenser, 4-[Bis(4-methoxyphenyl)-amino]benzaldehyde (0.167 g, 0.5 mmol) and 2-(3,5-difluorophenyl)acetonitrile (0.076 g, 0.5 mmol) were added. Potassium tert-butoxide (0.126 g, 1.13 mmol) and tetrabutyl ammonium hydroxide (1 mL, 1.0 mmol, 25% w/v methanol solution) were introduced to the reaction mixture to serve as a base and a phase transfer catalyst, respectively. The reaction mixture was heated at 60°C for 4 hours with continuous stirring to

promote the Knoevenagel condensation process. After the reaction was complete, the mixture was cooled and left undisturbed for crystallization over 3 days. This resulted in the formation of orange, block-shaped crystals. The crystals were isolated by filtration, yielding 188 mg of the product, corresponding to 80% yield.

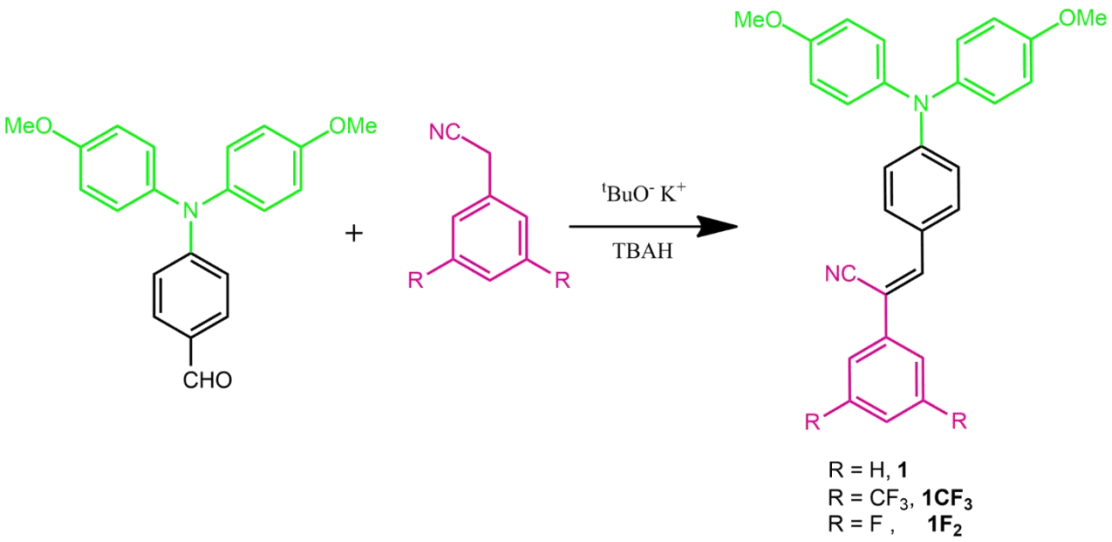

Scheme S1. General synthetic scheme for **1, 1F$_2$** and **1CF$_3$.**

The synthesis of compound **1CF$_3$** was carried out using the Knoevenagel condensation reaction, a commonly employed method to form carbon-carbon double bonds by combining aldehydes and activated methylene compounds. Below is the detailed elaboration of the synthesis process:

4-(Bis(4-methoxyphenyl)amino)benzaldehyde (0.188 g, 0.56 mmol) was used as the aldehyde source.3,5-Bis(trifluoromethyl)phenylacetonitrile (0.1 mL, 0.56 mmol) was used as the methylene compound. 30 mL of methanol was chosen as the reaction medium due to its ability to dissolve reactants effectively and facilitate the condensation reaction. To the methanolic solution containing the two reactants, potassium tert-butoxide (0.126 g, 1.13 mmol) was added as a strong base to deprotonate the methylene compound, activating it for nucleophilic attack on the aldehyde. Additionally, tetrabutyl ammonium hydroxide (1 mL, 1.0 mmol, 25% w/v methanol solution) was introduced to enhance the reaction rate and yield by acting as a phase transfer catalyst. The reaction mixture was heated to 60°C under constant stirring for 4 hours. This temperature was carefully controlled to facilitate the condensation reaction while preventing side reactions. After completion, the reaction mixture was allowed to cool to room temperature. The solution was then set aside to facilitate slow crystallization over a period of

2 days. Slow crystallization helped in forming high-purity crystals of the product. The resultant product was obtained as cuboidal yellow crystals of compound **1CF$_3$**, which were separated from the mother liquor using filtration. The yield of the purified compound was 220 mg (78%), indicating an efficient and high-yield synthesis.

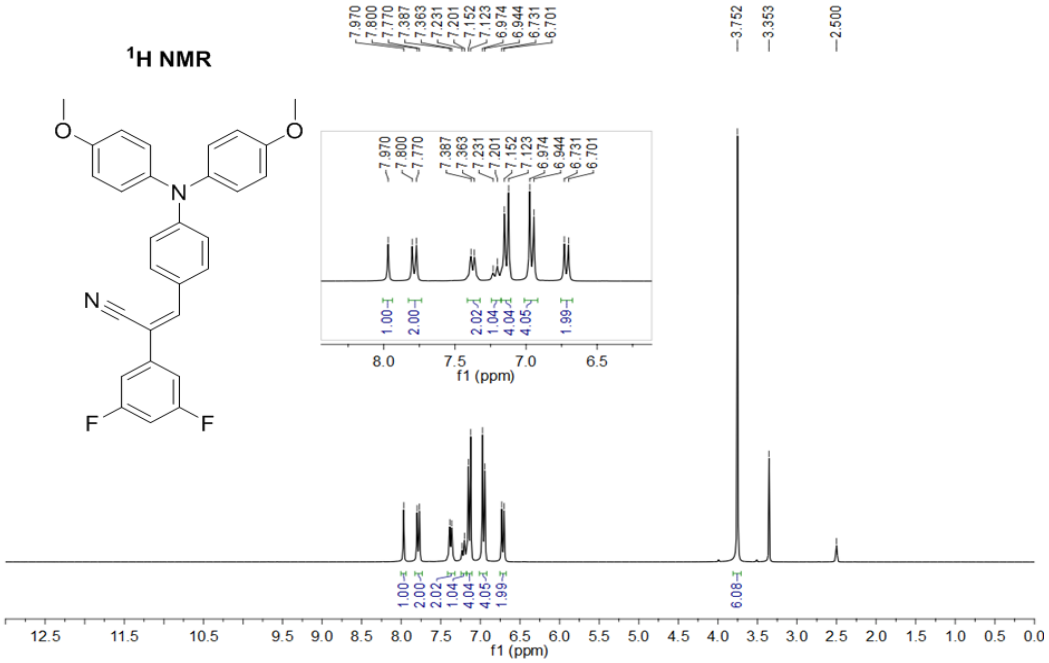

Figure 2. ^{1}H NMR spectra (in DMSO-d$_6$) of synthesized compound **1F$_2$** .

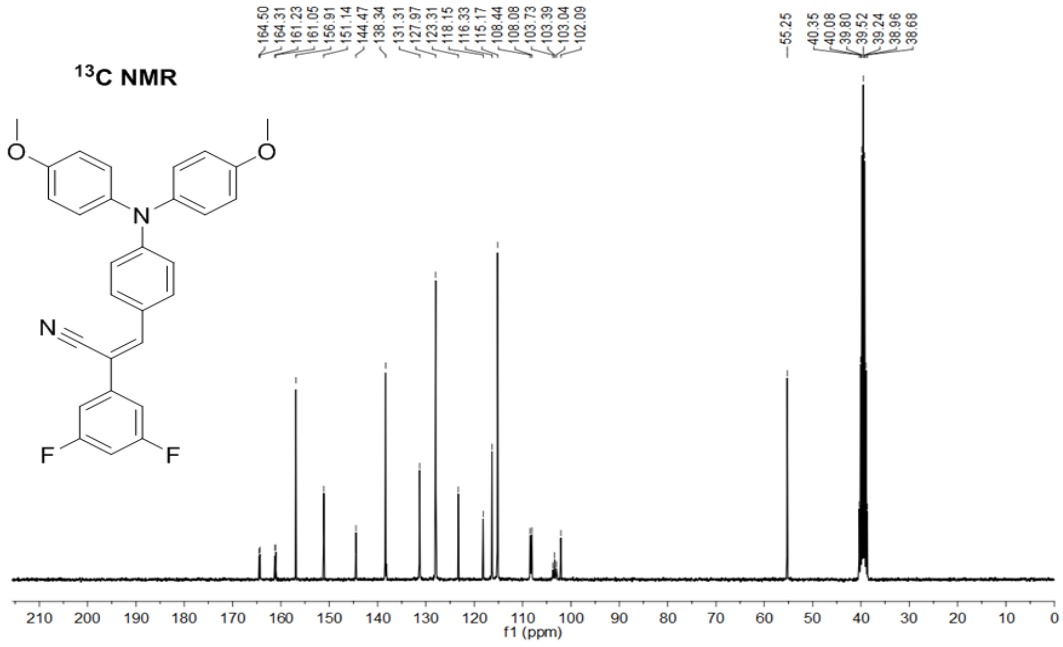

Figure 3. ^{13}C NMR spectra of synthesized compound **1F$_2$** (in DMSO-d$_6$) solvent.

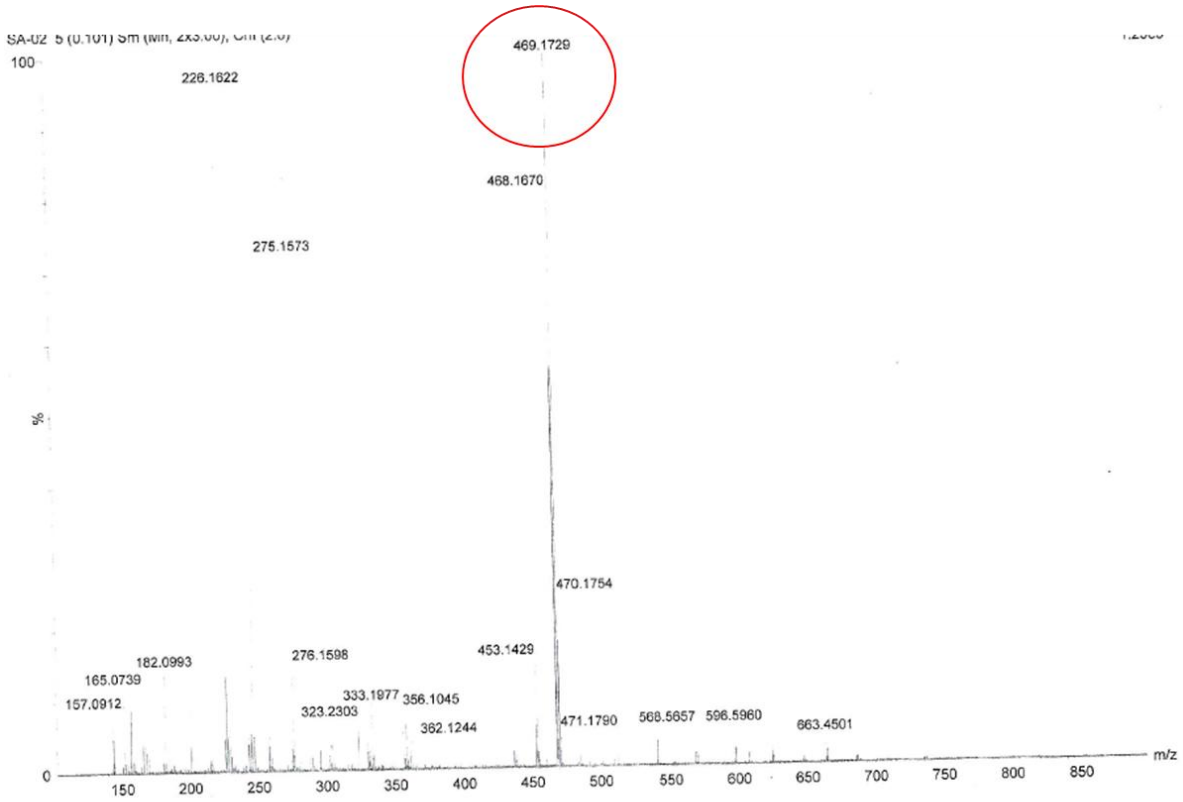

Figure 4. High-resolution mass spectra(HRMS) of the compound **1F$_2$.**

^{1}H NMR (300 MHz, DMSO-d$_6$): 1F$_2$ Chemical shifts (δ): 7.97 (s, 1H), 7.79 (d, J = 9.0 Hz, 2H), 7.38 (d, J = 7.2 Hz, 2H), 7.22 (d, J = 9.0 Hz, 1H), 7.14 (d, J = 8.7 Hz, 4H), 6.96 (d, J = 9.0 Hz, 4H), 6.72 (d, J = 9.0 Hz, 2H), 3.75 (s, 6H).

^{13}C NMR (75 MHz, DMSO-d$_6$): 1F$_2$ Chemical shifts (δ): 164.5, 164.3, 161.2, 161.1, 156.9, 151.1, 144.5, 138.3, 131.3, 128.0, 123.3, 118.2, 116.3, 115.2, 108.4, 108.1, 103.7, 103.4, 103.0, 102.1, and 55.3.

HRMS: 1F$_2$ Calculated for $C_{39}H_{22}F_2N_2O_2$ (M + H): 468.16. Observed mass (m/z): 469.17.

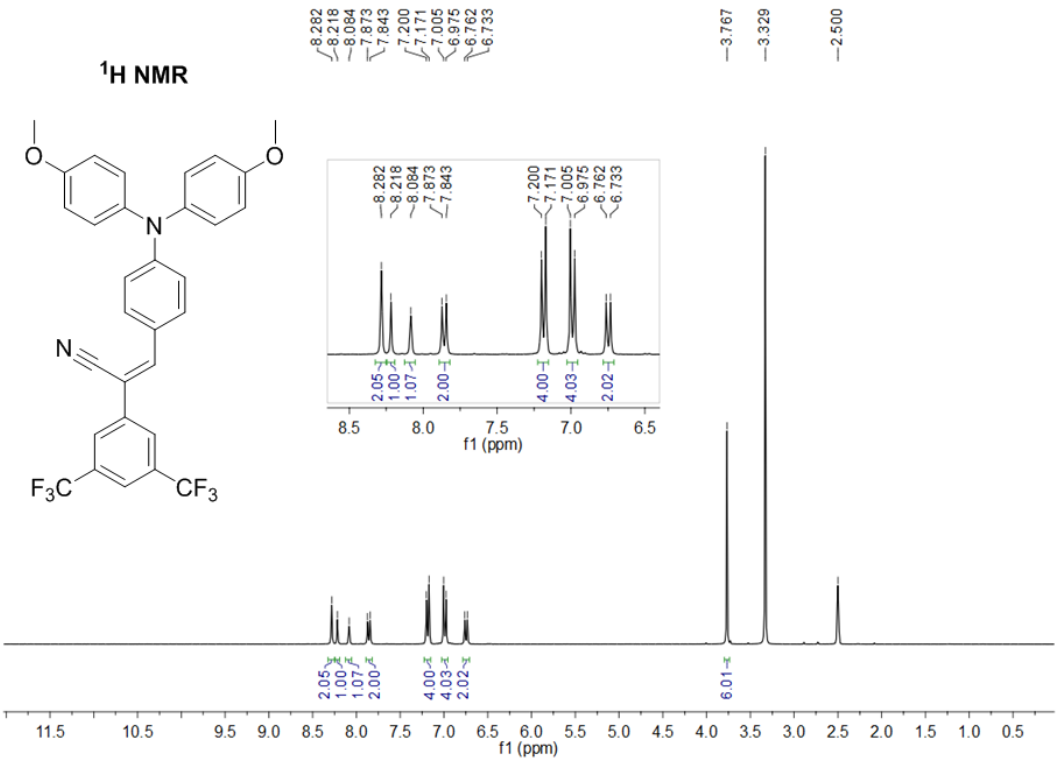

Figure 5. ^{1}H NMR spectra (in DMSO-d_6) of synthesized compound **1CF$_3$.**

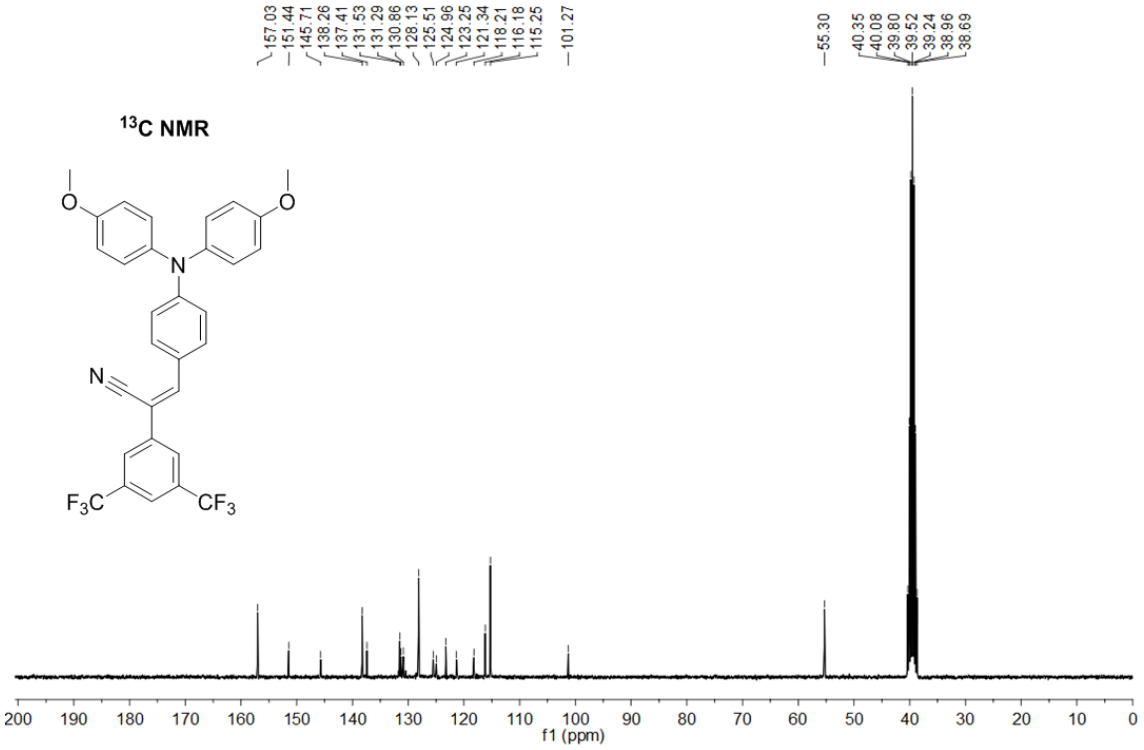

Figure 6. ^{13}C NMR spectra of synthesized compound **1CF$_3$** in DMSO-d_6 solvent.

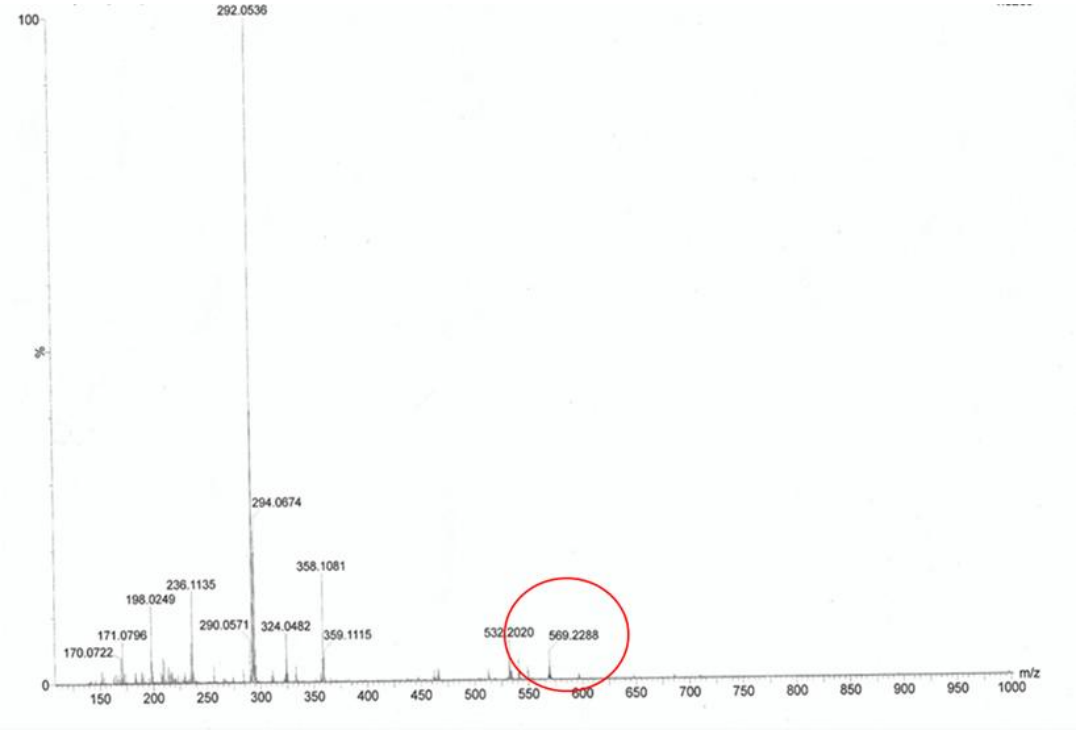

Figure 7. High-resolution mass spectra(HRMS) of the compound **1CF$_3$.**

^{1}H NMR (300 MHz, DMSO-d$_6$): 1CF$_3$ δ 8.28 (singlet, 2H), δ 8.22 (singlet, 1H), δ 8.08 (singlet, 1H), δ 7.86 (doublet, J = 9.0 Hz, 2H), δ 7.19 (doublet, J = 8.7 Hz, 4H), δ 6.99 (doublet, J = 9.0 Hz, 2H), δ 6.75 (doublet, J = 8.7 Hz, 2H), δ 3.77 (singlet, 6H)

^{13}C NMR Analysis (75 MHz, DMSO-d$_6$): Peaks and chemical shifts (δ 157.0, 151.4, 145.7, 138.3, 137.4, 131.5, 131.3, 130.9, 128.1, 125.5, 125.0, 123.3, 121.3, 118.2, 116.2, 115.3, 101.3, 55.3.

HRMS Analysis: Calculated mass for **C$_{31}$H$_{22}$F$_6$N$_2$O$_2$** (M+H): 569.22. Observed mass (m/z): 569.22.

Synthesis of Reference Molecule 1

For comparison, compound **1** was synthesized by reacting 4-[Bis(4-methoxyphenyl)-amino]benzaldehyde (0.167 g, 0.5 mmol) with 2-phenylacetonitrile (0.06 mL, 0.5 mmol) under conditions similar to the synthesis of **1F$_2$** and **1CF$_3$**. The reaction yielded a 71% product.

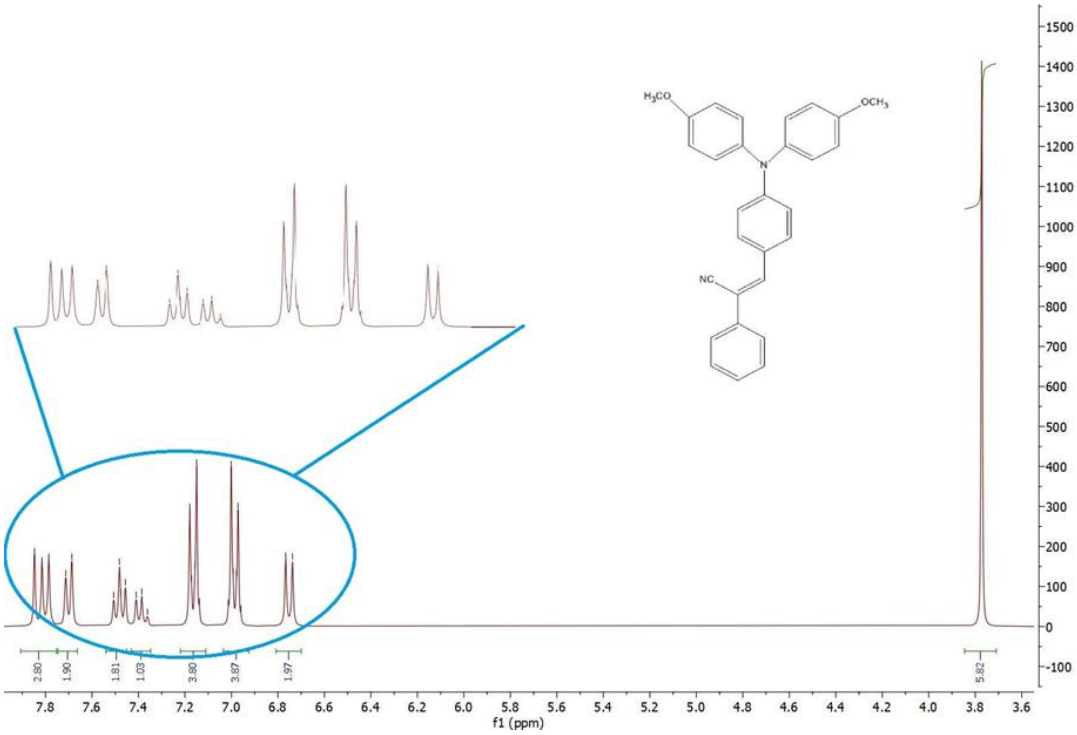

Figure 8. ^{1}H NMR spectra of reference compound **1** in DMSO-d_6.

^{1}H NMR (300 MHz, DMSO-d_6): Chemical shifts (δ): 7.02 (d, J = 9 Hz, 4H), 7.16 (d, J = 9 Hz, 4H), 3.77 (s, 6H), 6.75 (d, J = 9 Hz, 2H), 7.5 (t, 2H), 7.38 (m, 1H), 7.81 (m, 3H), 7.7 (d, J = 5.0 Hz, 2H).

2.3 Result and Discussion

The compounds **1CF$_3$**, **1F$_2$**, and **1** were synthesized using the Knoevenagel condensation reaction, a well-known method for forming carbon-carbon double bonds. The reactions were catalyzed using potassium tert-butoxide as the base, as illustrated in Scheme 1. The synthesis involved the reaction of 4-[Bis(4-methoxyphenyl)-amino]benzaldehyde with the following reactants, respectively: 3,5-Bis(trifluoromethyl)-phenyl acetonitrile for compound **1CF$_3$.** 3,5-Difluorobenzyl cyanide for compound **1F$_2$**. Benzyl cyanide for the reference compound **1**.

The synthesized compounds were subjected to rigorous characterization using ^{1}H NMR**,** ^{13}C NMR**,** and mass spectrometry**,** with detailed data and spectral results provided in figures 1-8. This confirmed the successful synthesis and purity of the compounds.

2.3.1 **Photophysical Studies:**

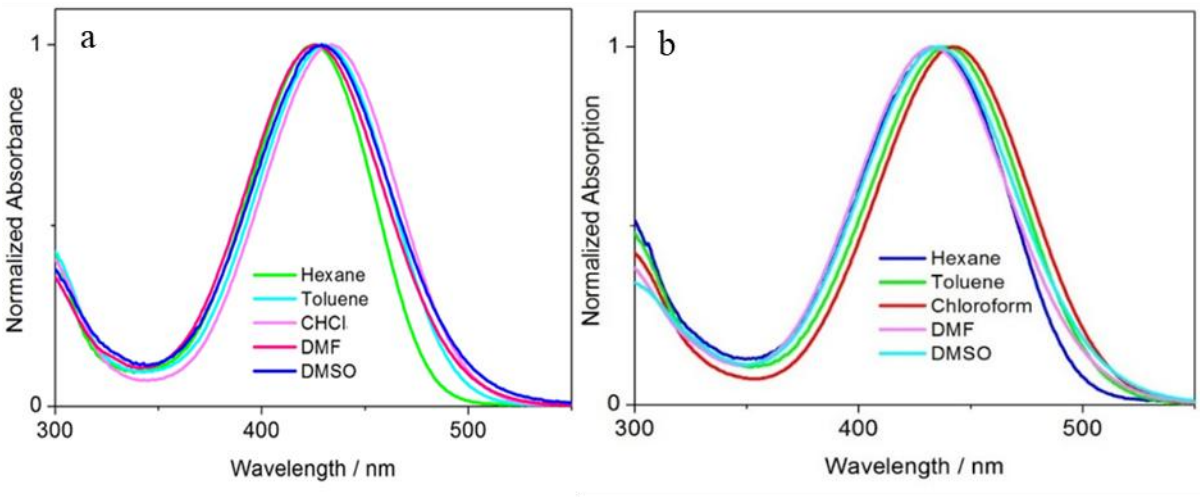

Figure 9. (a) Absorbance spectra of **1F$_2$** (b) **1CF$_3$** in different solvents.

The UV-visible absorption spectra for compounds **1F$_2$** and **1CF$_3$** were recorded in a toluene solution with a concentration of 1×10^{-5} M**. 1F$_2$** exhibited an absorption maximum (λ_{max}) at 431 nm, (Figure. 9) while **1CF$_3$** showed λ_{max} at 439 nm. These absorption bands are attributed to the intramolecular charge transfer (ICT) transitions, which result from the interaction between the donor methoxy-substituted diphenylamine (OMeDPA) group and the –**CN/CF$_3$** acceptor group present in the molecules. A slight shift in the absorption maximum (λ_{max}) was observed when the solvent polarity was varied, indicating the characteristic ICT behaviour of the compounds (Figure 9). The reference compound **1**, studied in methanol at a concentration of 2×10^{-6} M, displayed a blue-shifted absorption band at λ_{max} = 412 nm and emitted light with a peak at 575 nm (Figure. 10).

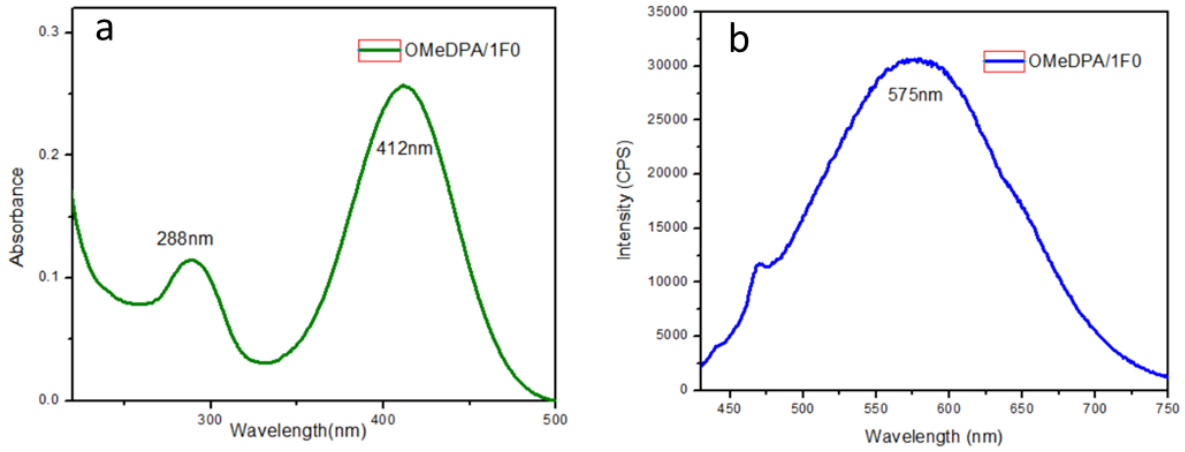

Figure 10. (a) Absorption and (b) emission spectra of **1** in 2 x 10^{-6} M methanol solution.

Density Functional Theory (DFT) Analysis:

To gain a deeper understanding of the ICT process, DFT calculations were carried out. The results revealed that the HOMO (Highest Occupied Molecular Orbital) electron density is primarily localized on the OMeDPA donor fragment, while the LUMO (Lowest Unoccupied Molecular Orbital) is concentrated on the phenyl ring bearing fluorine or –**CF_3** substituents**.**

The calculated HOMO-LUMO energy gaps are: 3.44 eV for compound **1CF_3**. 3.12 eV for compound **1F_2**.These values highlight the electronic transitions involved in ICT process. **1F_2** exhibited a strong emission band with λ_{max} = 583 nm **1CF_3** displayed an emission band at λ_{max} = 610 nm, both attributed to the ICT fluorescence, involving a ^{1}CT → S_0 transition (Figure 11). The steady-state fluorescence spectra of the compounds, recorded in toluene at a concentration of 1×10^{-6} M, displayed distinct emission features: Both **1F_2** and **1CF_3** exhibited typical solvatochromic fluorescence shifts when the polarity of the solvent was changed (Figures 12). As the solvent polarity increased, dipole-dipole interactions between the solvent and solute molecules strengthened, leading to significant differences in dipole moments between the excited and ground states.

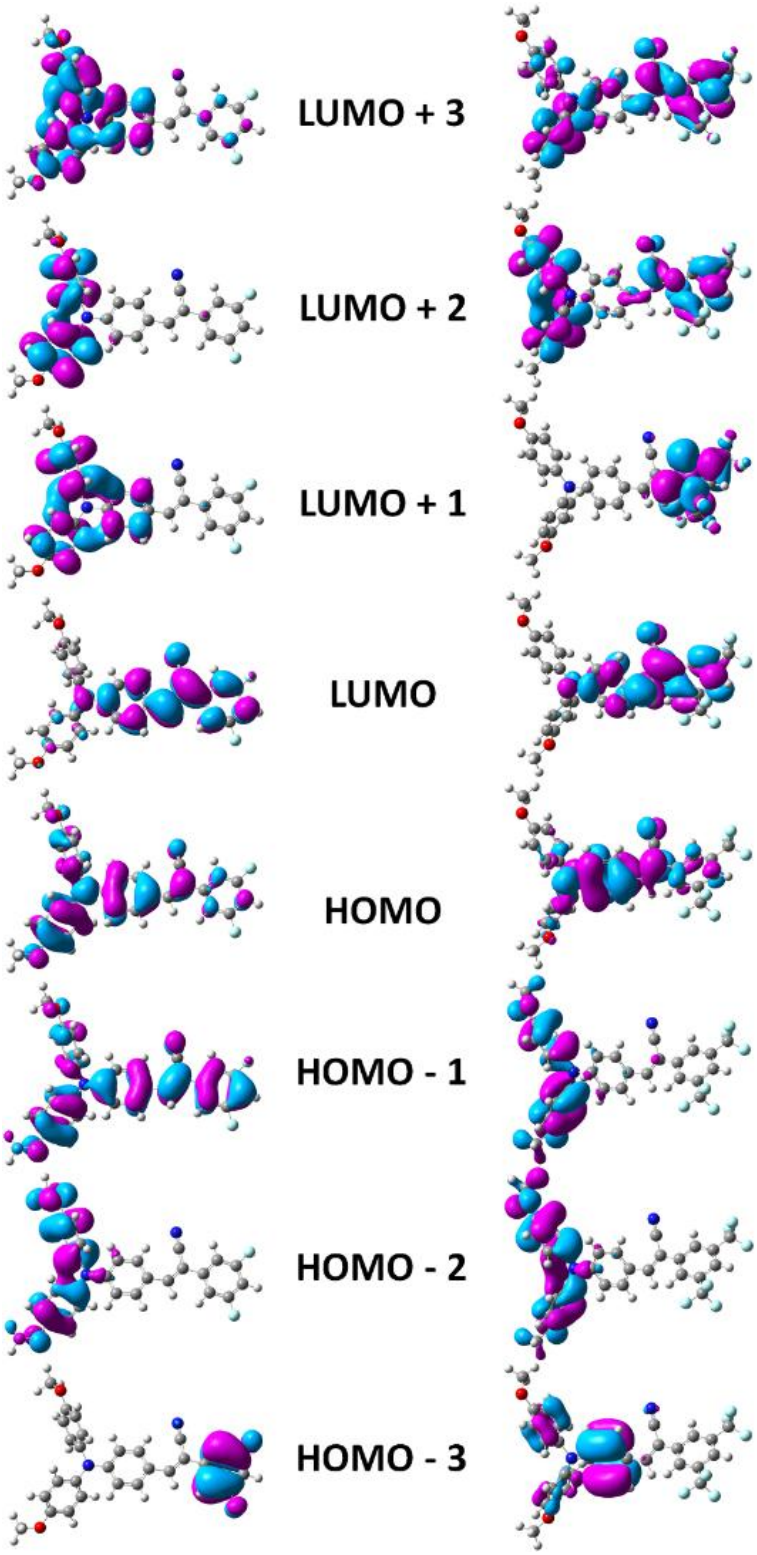

Figure 11: Frontier Molecular Orbitals of **1F$_2$** (left) and **1CF$_3$** (right).

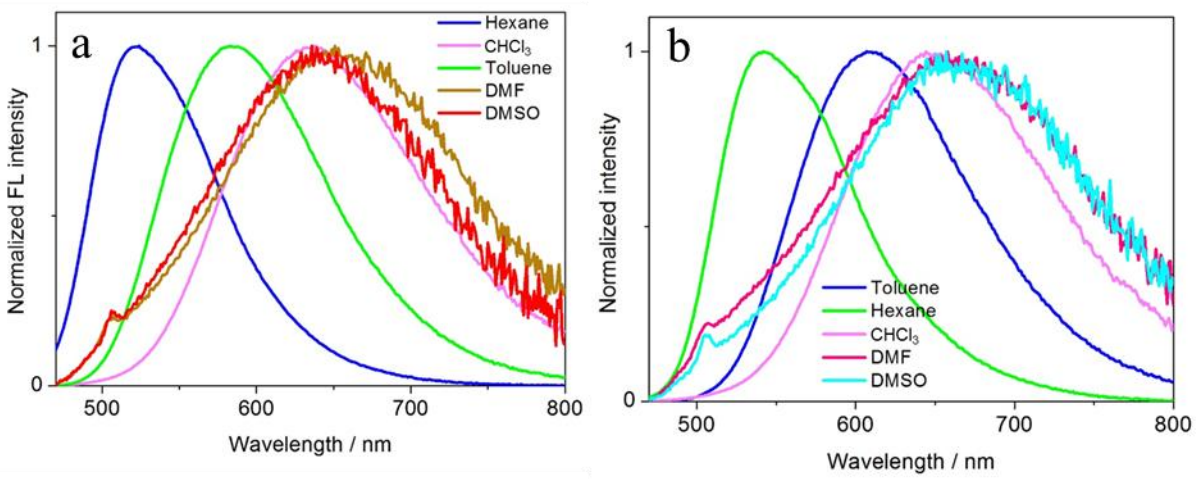

Figure 12. (a) Solvatochromic fluorescence of **1F₂** (b) **1CF₃** in different solvents.

This solvatochromic shift is a hallmark feature of ICT compounds. The unique optical properties, including ICT absorption and emission, as well as solvatochromic behavior, highlight the significance of **1CF₃**, **1F₂**, and reference compound **1**. The strategic incorporation of electron-donating and electron-accepting groups ensures the modulation of their photophysical characteristics, making them promising candidates for various practical applications.

Aggregation-Induced Emission (AIE)

Both compounds **1F₂** and **1CF₃** demonstrate significant Aggregation-Induced Emission (AIE) behavior. Below is an elaboration and rephrased overview of their photophysical properties:

Emission Enhancement with Water Addition:

In pure methanol (water fraction, f_w = 0%), both compounds exhibit weak emissions: **1F₂**: $\lambda_{em,max}$ = 650 nm, with low quantum efficiency ($\phi < 1$). **1CF₃**: $\lambda_{em,max}$ = 667 nm, also with low quantum efficiency ($\phi < 1$).These weak emissions are attributed to increased non-radiative decay ($K_{nr} \uparrow$) caused by the free rotational motion of phenyl rings in their isolated states. As the water fraction (f_w) is increased, the emission intensity of both compounds improves significantly due to molecular aggregation. **1F₂**: At f_w = 70%, the emission intensity reaches its maximum with λ_{em} = 615 nm.

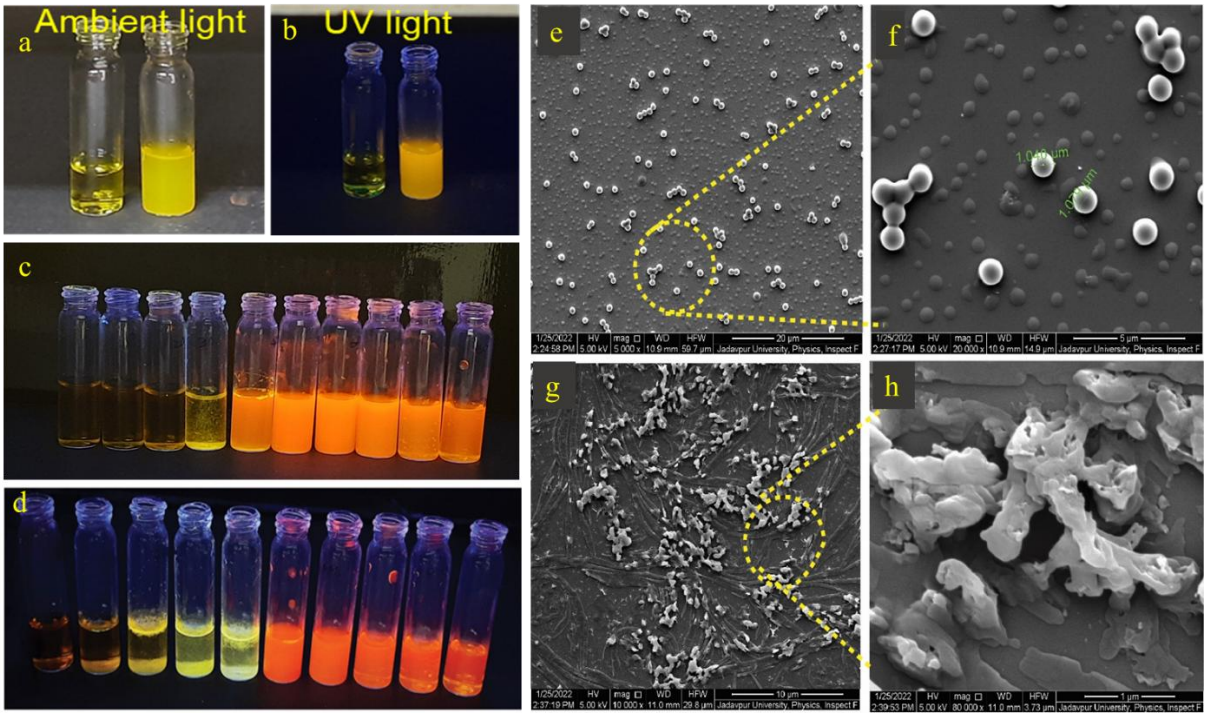

Figure 13. (a, b) AIE behavior of the reference compound **1** in Methanol -water mixture (70:30) under ambient and UV light respectively. (c, d) Images of AIE solution of **$1F_2$** and **$1CF_3$** at different methanol-water ratio. (e, f) SEM picture of the $1F_2$ in methanol-water mixture 9:1 and (g, h) in methanol-water mixture 4:6.

There is a 94-fold enhancement in emission intensity compared to the initial value. A blue shift in emission maxima is observed, from 650 nm (f_w = 0%) to 617 nm (f_w = 50%), with a $\Delta\lambda$ of 33 nm. Beyond f_w = 50%, the emission maxima remain nearly constant. **$1CF_3$**: At f_w = 70%, the intensity enhancement is more rapid, reaching 118-fold compared to the initial value. The emission maxima shift from 667 nm (f_w = 0%) to 628 nm (f_w = 50%), with a $\Delta\lambda$ of 39 nm. This significant increase in emission intensity upon aggregation is due to the suppression of non-radiative decay ($K_{nr}\downarrow$) and enhanced radiative emission ($K_r\uparrow$). The molecules aggregate in a manner that restricts free rotation of the phenyl rings, locking them into a more stable conformation.

Mechanism of AIE:

In the aggregated state, the molecules adopt a non-planar orientation of their triphenylamine rings, which prevents π-π stacking interactions. Intermolecular interactions such as hydrogen bonding and CH…π interactions create a conformational locking effect. This suppresses non-

radiative decay pathways ($K_{nr}\downarrow$) and promotes higher radiative emission ($K_r\uparrow$). A blue shift in emission upon aggregation is attributed to the conformational twisting of aryl rings into sterically constrained zones, forming a different molecular conformer. The reference molecule **1** also exhibits AIE behavior when subjected to a methanol-water mixture. This behavior is likely due to its non-planar packing in the aggregated state, which prevents detrimental π-π stacking interactions (Figure 14).

To observe structural changes during the AIE process**,** Scanning Electron Microscopy (SEM) was conducted on aggregated particles of **1F₂** and **1CF₃** at different water fractions, At a 9:1 methanol-water mixture**,** rose-petal-like particles (~500 nm in diameter) were formed. These structures reflect the initial stages of aggregation. With increasing water fraction to 60% where fluorescence intensity is maximized, block-like crystalline structures were observed, indicating a transition to a more ordered arrangement. Similar morphological trends were observed for compound **1F₂** (Figure.13). These results indicate that both **1F₂** and **1CF₃** self-assemble into long-range, orderly arrangements during the aggregation process, driven by a range of intermolecular interactions such as hydrogen bonding and CH…π interactions.

The unique molecular design of **1F₂** and **1CF₃**, particularly the incorporation of bulky triphenylamine rings with methoxy substituents, plays a pivotal role in Encouraging non-planar packing, preventing detrimental π-π stacking interactions and also Promoting the AIE process effectively. This careful structural design provides insight into developing new AIE-active materials (AIEgens) for various technological applications.

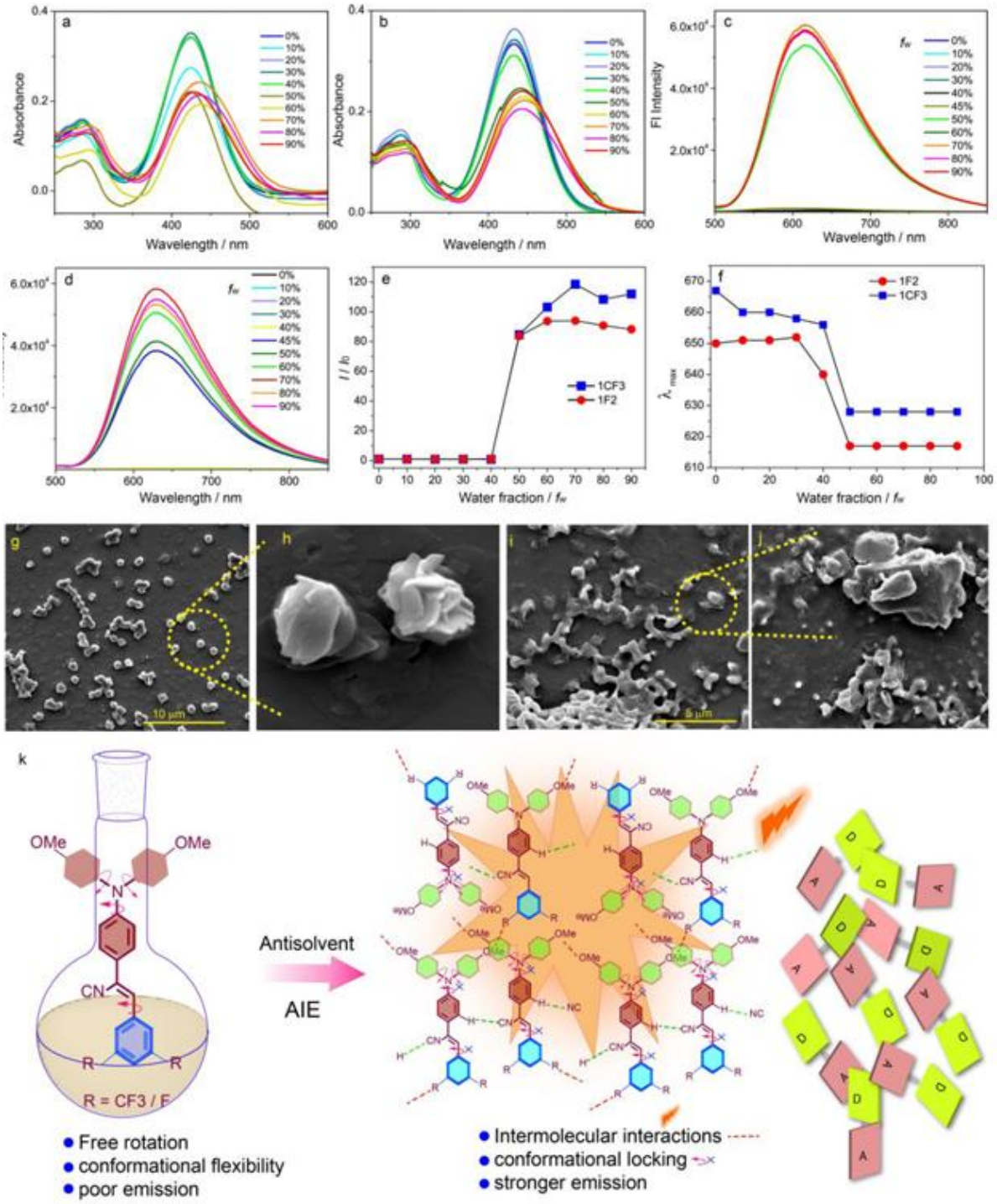

Figure 14. Aggregation induced emission of **1F₂** and **1CF₃**. (a, b) absorption profiles **1F₂** and **1CF₃** respectively with gradual increase of water fraction, (c, d) emission profiles of **1F₂** and **1CF₃** respectively with gradual increase of water fraction, (e) Intensity vs f_w plot, (f) Plot of λ_{max} vs water fraction (f_w) , (g, h) SEM picture of the **1CF₃** in methanol-water mixture 9:1 (i, j) SEM picture of the **1CF₃** in methanol-water mixture 4:6, (k) schematic mechanism of AIE for **1CF₃** and **1F₂**.

3.2.2 Solid-State Luminescence and Mechanochromic colour Switching

The solid-state fluorescence and mechanochromic luminescence (MCL) behavior of compounds **1CF$_3$** and **1F$_2$** were investigated in detail (Figure 16). Revealing unique photophysical characteristics, **1CF$_3$**: The crystalline form of **1CF$_3$** displayed a greenish-yellow emission with a broad, structureless band peaking at 522 nm**,** attributed to intramolecular charge transfer (ICT) fluorescence. In contrast, the difluoro-substituted **1F$_2$** exhibited two distinct emission bands**:** A high-energy band at 516 nm**,** attributed to an n→π* transition. A low-energy band at 628 nm, corresponding to ICT fluorescence.

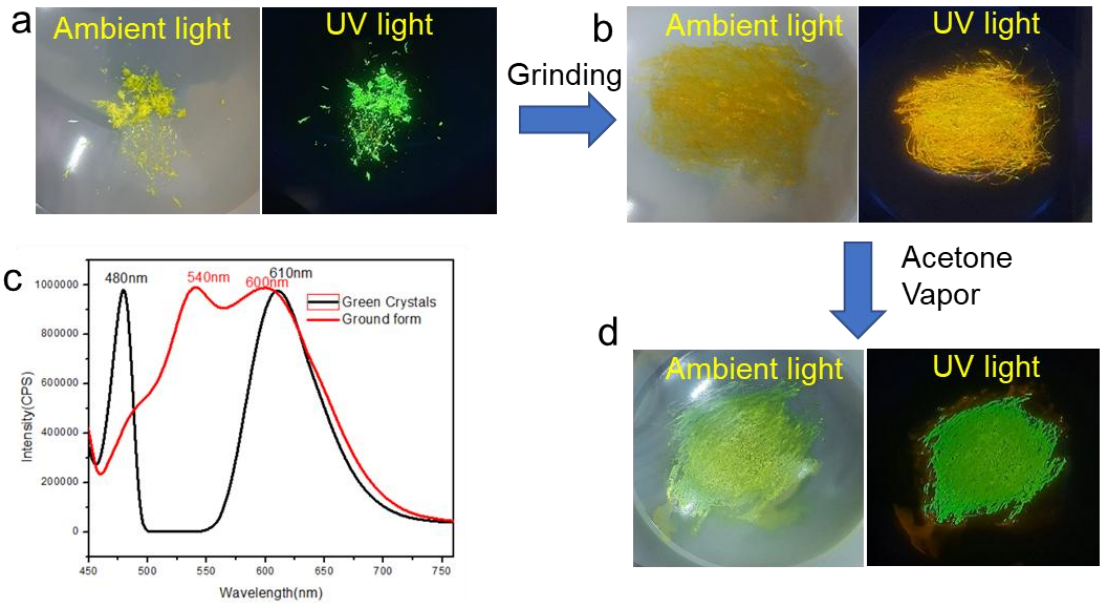

Figure 15. (a, b) Compound **1** before and after grinding in ambient and under UV light (c) Fluorescence spectra of **1** in pristine and ground forms (d) Picture of the ground Compound **1** after solvent fumigation.

Mechanochromic Luminescence (MCL):

To investigate the mechanochromic behavior, experiments were conducted by applying mechanical pressure to the crystals, such as grinding, which resulted in significant fluorescence color changes.

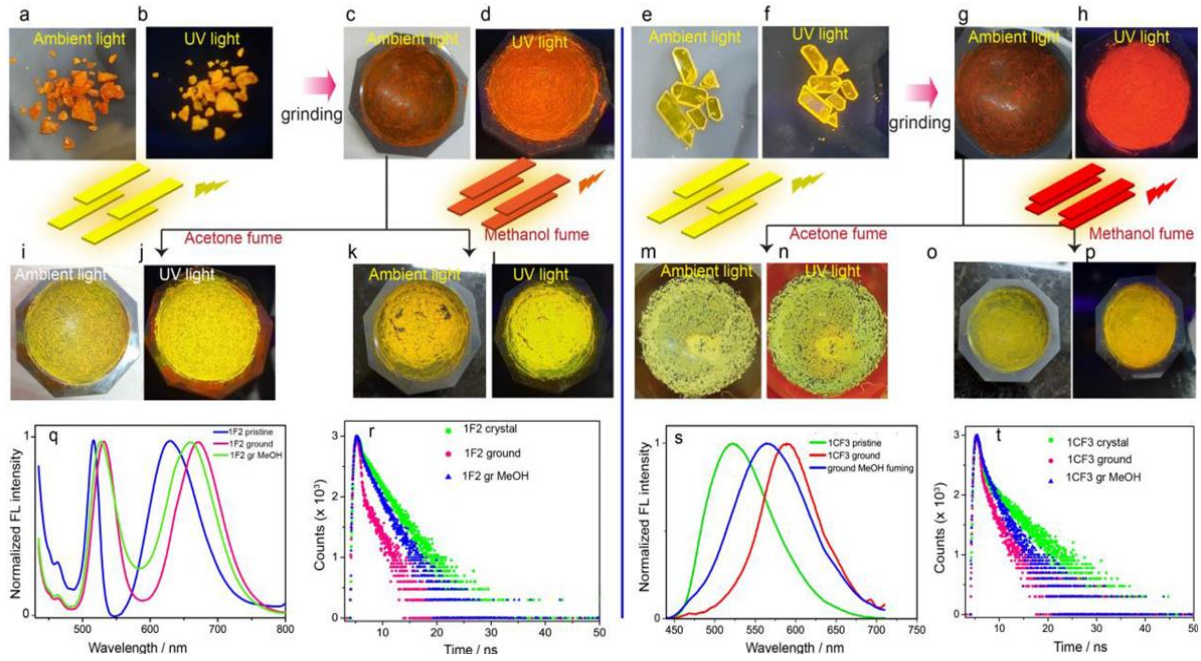

Figure 16. MCL behavior of **1F₂** (a-d, i-l, q, r) and **1CF₃** (e-h, m-p, s, t). (a-d) MCL behavior of **1F₂**, (i-l) colour after solvent vapour fuming, (e-h) MCL switching of **1CF₃**, (m-p) colour after solvent fuming, (q, r) emission profiles and fluorescence life time plots of **1F₂** during mechano and vapochromic switching, (s, t) emission profiles and fluorescence life time plots of **1CF₃** during mechano and vapochromic switching.

Table 1 Solid state fluorescence life time and Lifetime values in solution before and after AIE

Compound	**Life time of pristine sample (ns)**	**Life time of ground sample (ns)**	**Life time of methanol fumed sample (ns)**
1F₂	τ_1 = 3.167 ± 0.0217 (95.7%) τ_2 = 0.3035 ± 0.0345 (4.3 %) χ^2 = 1.097 λ_{ex} = 437 nm, λ_{em} = 628 nm	τ_1 = 2.4159± 0.0431(78.54 %) τ_2 = 0.223 ± 0.0093(21.5%) χ^2 = 1.0243 λ_{ex} = 437 nm, λ_{em} = 671 nm	τ_1 = 2.63 ns (72 %) τ_2 = 0.68 ns (28 %) χ^2 = 1.04
1CF₃	τ_1 = 0.386±0.011 (16.68%) τ_2 = 5.001 ± 0.0473 (83.32 %) χ^2 = 1.110812 λ_{ex} = 434 nm, λ_{em} =522 nm	τ_1 = 0.543 ± 0.01 (49.58%) τ_2 = 2.947 ± 0.0419 (50.42 %) χ^2 = 1.096 λ_{ex} = 424 nm, λ_{em} = 599 nm	τ_1 = 0.77 ns (38 %) τ_2 = 2.58 ns (62 %) χ^2 = 1.03

Samples	Fluorescence Life time values, τ (ns)
AIE mixture, **$1CF_3$: water =40:60** λ_{ex} = 424 nm, λ_{em} = 522 nm	τ_1 = 6.0997 ±0.0641 (48.74%) τ_2 = 1.5679 ± 0.0315 (51.26 %) χ^2 = 1.071
AIE mixture, **$1F_2$: water =40:60** λ_{ex} = 437 nm, λ_{em} = 628nm	τ_1 = 0.16379 ±0.0105 (87.01%) τ_2 = 1.5853 ± 0.05719 (12.99 %) χ^2 = 1.07744

Table 2. Quantum yield of **$1F_2$** and **$1CF_3$**.

	Before grinding	After grinding
$1F_2$	0.08	0.03
$1CF_3$	0.21	0.09

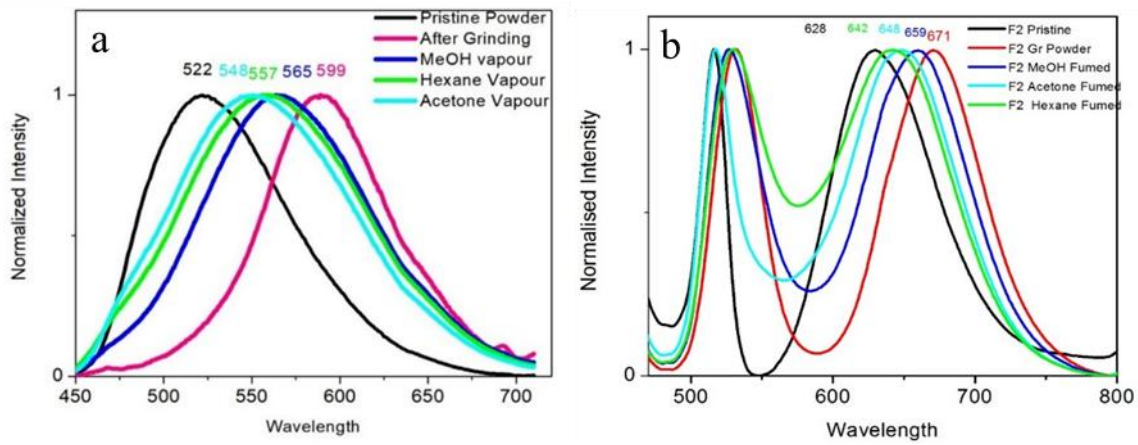

Figure 17. Mechanochromic redshift and solvent fume induced blue-shift of luminescence of (a) **$1CF_3$** (b) **$1F_2$**

Observations of Structural Rearrangement reveals that time-resolved fluorescence measurements revealed that the lifetime values of **$1CF_3$** and **$1F_2$** crystals changed after grinding. These alterations indicate a rearrangement of supramolecular packing and intermolecular non-covalent interactions, which modified the excited-state electronic levels and relaxation pathways. Mechanism of Luminescence Shifts: The red-shifting of luminescence upon grinding is attributed to: Planarization of the molecular structure, aligning the molecular framework more effectively. The formation of an excimer-like coupling in the excited state, driven by stronger intermolecular π-π stacking interactions induced by the applied pressure. Reversibility of MCL: The pressure-induced color change from grinding was found

to be reversible. The red-emissive ground powder could revert to its pristine greenish-yellow emission upon exposure to solvent vapors: **1CF$_3$**: The emission maximum ($\lambda_{em,max}$ = 599 nm) shifted to 565, 557, and 548 nm when exposed to methanol, hexane, and acetone vapors, respectively. A similar trend was observed for **1F$_2$**. Comparison with Reference Compound: Unlike **1CF$_3$** and **1F$_2$**, the reference compound (without **-F** or **-CF$_3$** substituents) exhibited only a slight hypsochromic shift upon grinding, underscoring the importance of fluorinated substituents in facilitating molecular planarization and red-shifted emission. The MCL behavior of **1CF$_3$** and **1F$_2$** highlights the crucial role of the **-F** and **-CF$_3$** substituents in the acceptor phenyl ring. These groups aid in molecular planarization under mechanical pressure, leading to enhanced intermolecular π-π stacking and the formation of excimer-like states responsible for the red-shifted luminescence. This study reveals the potential of such materials for applications in reversible, pressure-responsive luminescent systems, which could be leveraged in areas such as security writing, stress sensing, or optical data storage.

2.3.3 X-ray Structure and Intermolecular Interactions

The solid-state physical properties of compounds **1F$_2$** and **1CF$_3$** are closely tied to their molecular packing and intermolecular interactions. Detailed structural analysis using single crystal X-ray diffraction provided key insights into the mechanism behind their color-switching behavior.

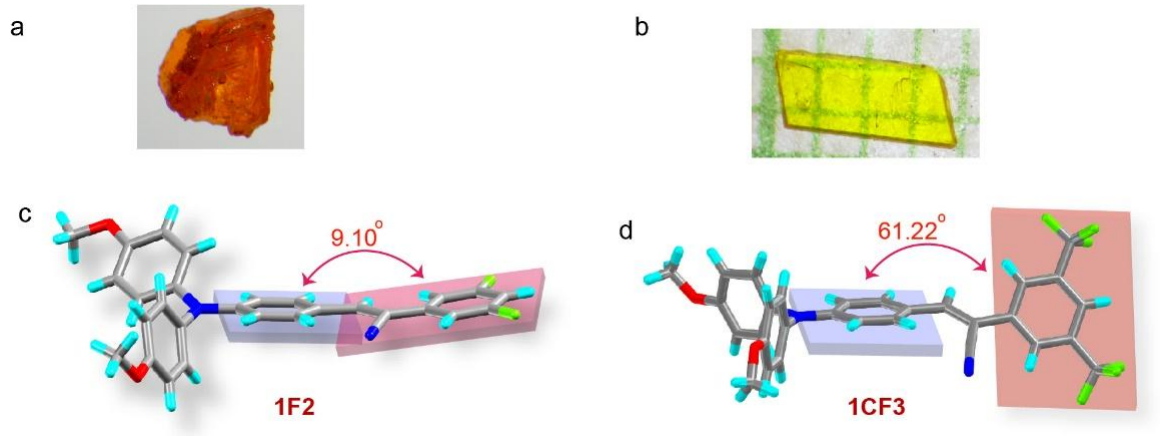

Figure 18. (a) **1F$_2$** crystal (b) **1CF$_3$** crystal (c, d) Molecular conformations of **1F$_2$** and **1CF$_3$** respectively, observed in single crystal X-ray structure.

Crystal Formation **1F$_2$**: Slow evaporation of a DMF solution yielded orange block-shaped crystals of **1F$_2$** belonging to the monoclinic system with a P2$_1$/n space group (Table 4,).

Conformational analysis revealed that the angle between the C_6H group and the π-phenyl plane is 9.10°, making the phenyl rings nearly coplanar (Figure 18). This coplanarity facilitates a high degree of charge transfer interaction, which is crucial for the photophysical properties of **1F₂**. Packing and Intermolecular Interactions: The crystal lattice of **1F₂** is held together by several intermolecular interactions, forming an extended supramolecular network. These include: C–H•••N interactions: C56–H56•••N4 = 3.419 Å, C37–H37•••N4 = 3.440 Å, C6–H•••N7 = 3.309 Å, C26–H26•••N7 = 3.564 Å. These involve the nitrogen atom of the –CN group interacting with both aromatic and aliphatic protons, forming a zigzag pattern along the a-axis of the crystal. C–H•••F interactions: C40–H40•••F_2 = 3.340 Å, involving the fluorine atom of the $C_6H_4F_2$ ring. C–H•••π interactions One interaction involves an aromatic proton (H55•••ring centroid = 2.597 Å) extending along the b-axis. The other involves an aliphatic OCH_3 proton (H15B•••ring centroid = 3.439 Å) extending along the c-axis. Although π•••π stacking interactions are absent in the initial crystal structure, the application of mechanical pressure induces structural rearrangements such as: Planarization of phenyl rings. Formation of excimeric-type coupling due to enhanced π•••π stacking interactions. These changes result in a bathochromic shift (red-shifted luminescence) to orange-red emission. Crystal Formation **CF₃**: Crystallization of **1CF₃** from acetonitrile yielded crystals belonging to the monoclinic system with a $P2_1/n$ space group. In contrast to **1F₂**, the molecular conformation of **1CF₃** is non-planar. The $C_6H_4(CF_3)_2$-phenyl ring is twisted by 61.22° relative to the central ring (Fig. 19). Packing and Intermolecular Interactions: The molecular packing in **1CF₃** is stabilized by: C–H•••N interactions: C9–H9•••N2 = 3.629 Å C–H•••π interactions: C3B–H3B•••ring centroid = 3.133 Å π•••π stacking interactions: A strong stacking interaction (centroid•••centroid = 3.845 Å) is observed between the $C_6H_4(OMe)$ ring and $C_6H_3(CF_3)_2$ ring, extending along the c-axis. Behavior under External Stimuli: Upon application of shear pressure, the π•••π stacking interactions become stronger, leading to molecular planarization. This induces excimeric-type coupling, which is responsible for the observed red-shifted fluorescence in the ground powder of **1CF₃**. The distinct intermolecular interactions and molecular arrangements in **1F₂** and **1CF₃** play a pivotal role in their mechanochromic luminescence (MCL) properties. External stimuli such as thermal energy, mechanical pressure, or solvent vapor induce structural reconfigurations that alter non-covalent interactions, including Hydrogen bonding (e.g., C–H•••N, C–H•••O, C–H•••F). π•••π stacking .C–H•••π interactions (Figures 20, 21).

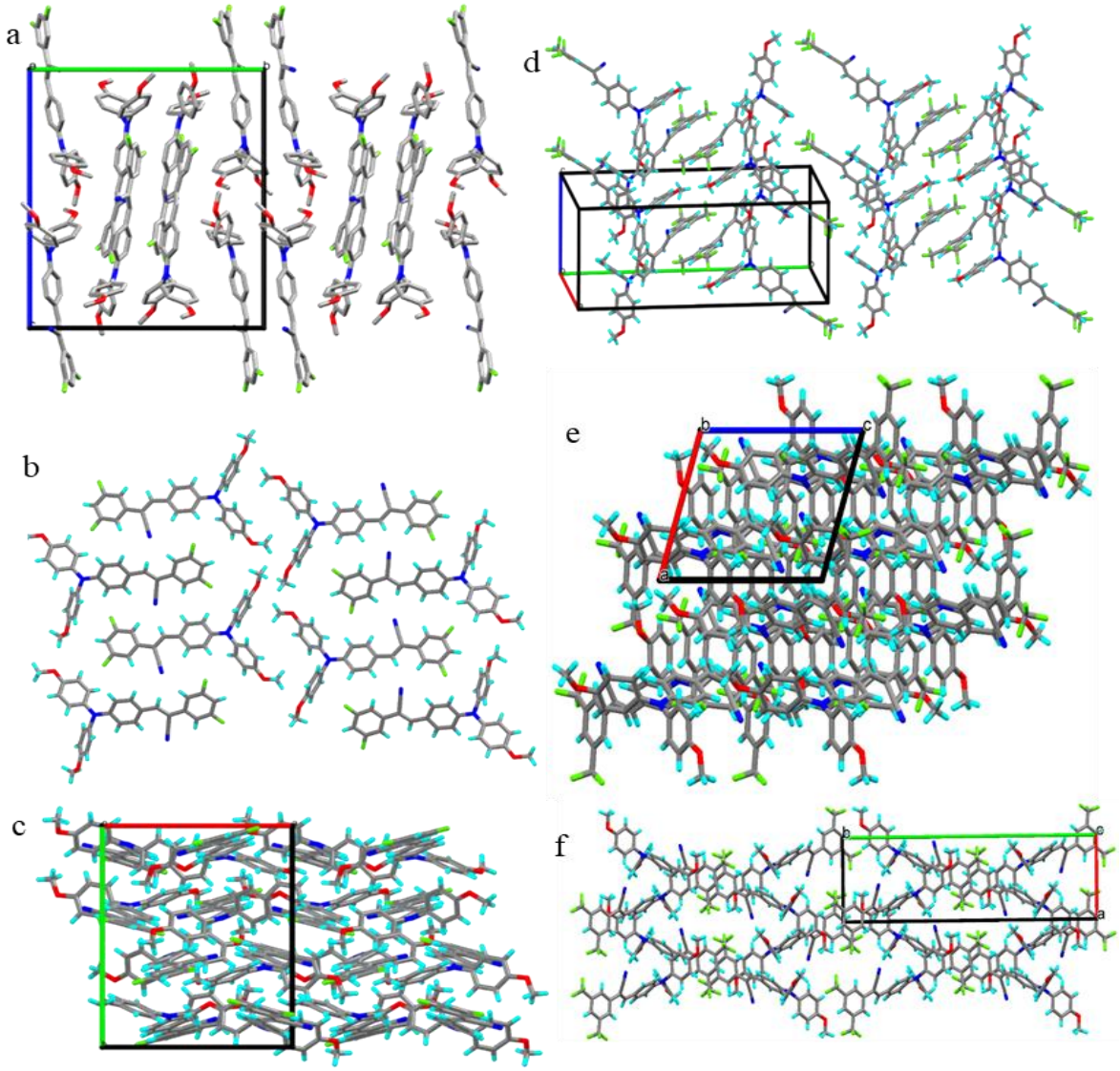

Figure 19. (a) Packing view of **1F$_2$** along a-axis, (b) along b-axis (c) along c-axis respectively (d) Packing view of **1CF$_3$** along a-axis (e) along b-axis and (f) along c-axis respectively.

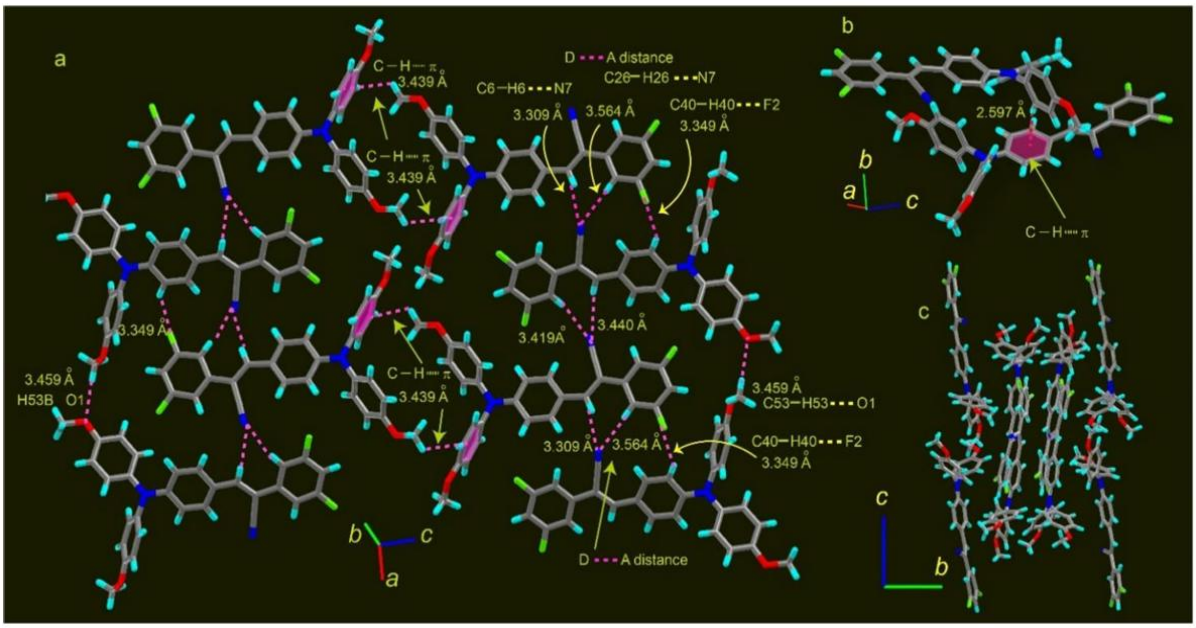

Figure 20. Different modes of hydrogen bonding interactions and C-H••• π interactions in **1F$_2$** crystal lattice.

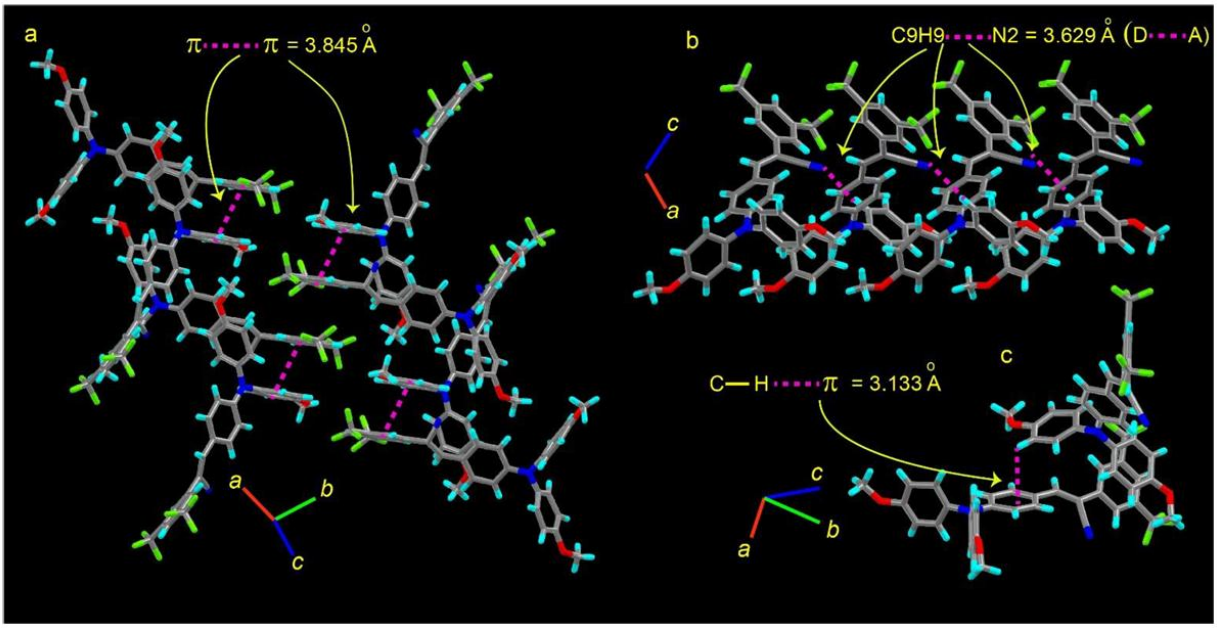

Figure 21. Intermolecular interactions in **1CF$_3$** crystal lattice.

These structural changes impact the excited electronic states and relaxation pathways, resulting in fluorescence color shifts. While **1F$_2$** lacks π•••π stacking in its pristine form, mechanical pressure induces planarization and enhanced π•••π interactions, resulting in red luminescence. In contrast, **1CF$_3$** already exhibits strong π•••π stacking interactions in its crystalline state, which are further intensified under pressure. The combination of structural analysis and mechanochromic behavior in **1F$_2$** and **1CF$_3$** emphasizes the importance of molecular conformation and non-covalent interactions in determining photophysical properties. These

findings provide valuable insights for designing advanced functional materials for applications such as pressure sensors, optical storage devices, and security systems.

Table 3. Single crystal X-ray parameters of **1F$_2$** and **1CF$_3$** at 298 K.

Compound	**1F$_2$**	**1CF$_3$**
CCDC deposit No.	2154774	2154811
Chemical formula	$C_{29}H_{22}F_2N_2O_2$	$C_{31}H_{22}F_6N_2O_2$
M_r	468.49	568.51
Crystal system	Monoclinic	Monoclinic
Space group	$P2_1/n$	$P2_1/n$
a / Å	13.2742(11)	9.2421(7)
b / Å	17.4500(15)	29.261(2)
c / Å	20.9236(17)	10.5202(9)
α / ° β / ° γ / °	90 92.771(3) 90	90 106.728(2) 90
V / Å^3	4841.0(7)	2724.7(4)
Zs	8	4
ρ_{calc} / (g cm^{-3})	1.286	1.386
μ / mm^{-1}	0.092	0.115
F_{000}	1952	1168
θ_{min} / °	1.929	2.19
θ_{max} / °	27.165	28.39
Reflections collected	10671	5902
Independent reflections	9106	5048
GoF	1.038	1.027
Final R indices [$I > 2\sigma(I)$]	R_1 = 0.0683 wR_2 = 0.1991	R_1 = 0.0587 wR_2 = 0.1374
R indices (all data)	R_2 = 0.0785 wR_2 = 0.2120	R_2 = 0.0672, wR_2 = 0.1436

2.3.4 PXRD and IR Analysis: Insights into Mechanochromic Luminescence:

The Powder X-ray Diffraction (PXRD) and Infrared (IR) Spectroscopy analyses were conducted to understand the changes in molecular packing and intermolecular interactions associated with mechanochromic luminescence (MCL) of compounds **$1F_2$** and **$1CF_3$.** These methods provided valuable insights into the structural reorganization processes during mechanical and vapor-induced stimuli.

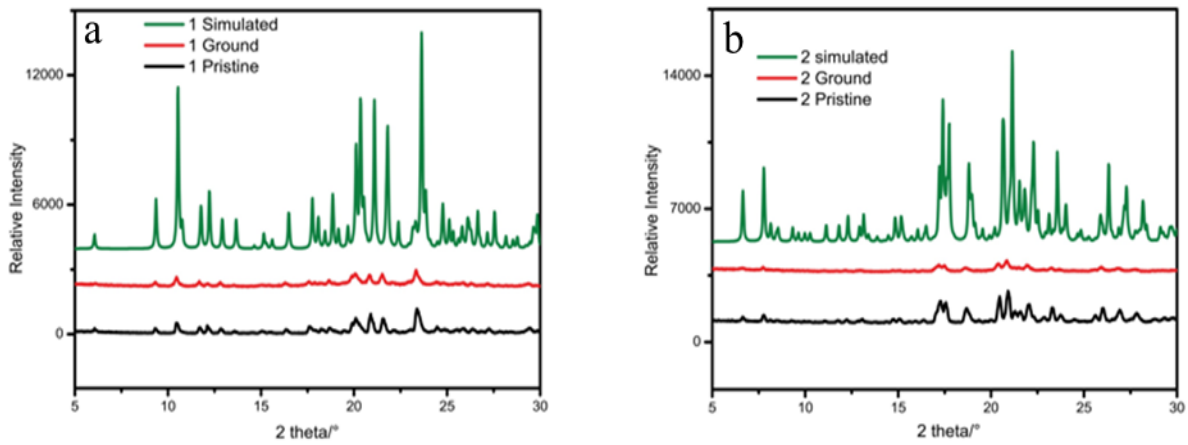

Figure 22. PXRD plot of the (a) **$1F_2$** and (b) **$1CF_3$** crystal in pristine and ground forms.

Pristine versus Ground Samples: PXRD patterns of the pristine samples of **$1F_2$** and **$1CF_3$** closely match the simulated diffraction patterns derived from the respective crystal structure CIF files, indicating a well-ordered molecular packing in the unaltered samples. Upon grinding the samples (application of mechanical pressure): The diffraction peak intensities of **$1CF_3$** (ground form) were significantly reduced, and the peaks became broader. This suggests a reorganization of the molecular packing, resulting in a loss of long-range crystallinity and order. A similar trend was observed for **$1F_2$** (Figure 22).

Impact on Mechanochromic Luminescence: The observed changes in the PXRD patterns highlight that mechanical pressure alters the supramolecular interactions**,** including hydrogen bonding and π•••π stacking. These changes are directly linked to shifts in electronic levels, which are responsible for fluorescence switching from yellow to red emission.

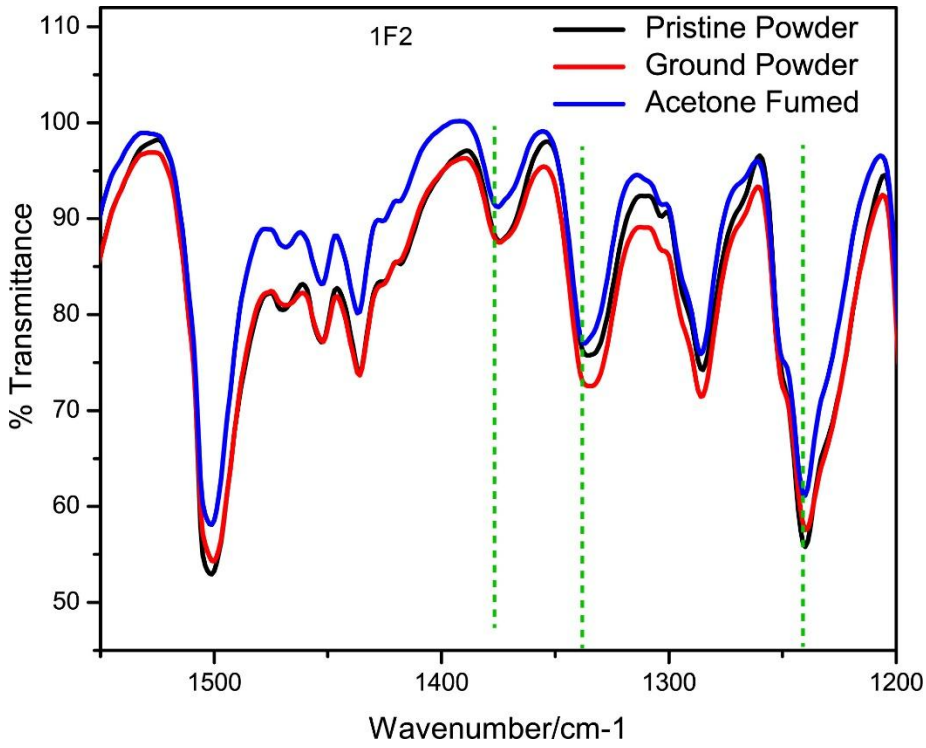

Figure 23. Infrared (ATR) spectra of the **1F$_2$** crystal in pristine, ground and acetone fumed forms.

Spectral Changes: The IR spectra of **1F$_2$** and **1CF$_3$** were recorded for three states: pristine, ground, and after solvent fumigation. Prominent spectral changes were observed, indicating molecular rearrangement: For **1CF$_3$**: The C–H bending frequency shifted to 1504 cm^{-1}. A noticeable shift in the C–F stretching frequency to 1342 cm^{-1}. For **1F$_2$**: The C–H bending frequency shifted to 1502 cm^{-1}. These shifts provide evidence of pressure-induced reorganization of intermolecular interactions, such as hydrogen bonding and π•••π stacking. Mechanochromic switching from yellow to red fluorescence can be attributed to the pressure-induced planarization of molecules, which promotes stronger π•••π stacking interactions in the excited state. This enhanced interaction stabilizes excimeric states, resulting in red-shifted emission.

2.4 Applications in Mechano-Writing and Vapo-Erasing

Leveraging the mechanochromic and vapochromic luminescent properties of **1CF$_3$** and **1F$_2$**, innovative applications for inkless writing and solvent vapor erasing were demonstrated:

Inkless Mechano-Writing: A thin layer of **1CF$_3$** powder was uniformly coated onto a glass slide to create a writable surface. Using a glass rod as a stylus, the word "RED" was inscribed by applying pressure to the surface. The resulting fluorescence: Clearly visible under both ambient and UV light. Exhibited a red emission due to pressure-induced molecular rearrangement. The red fluorescent writing was legible to the naked eye (Figure 24).

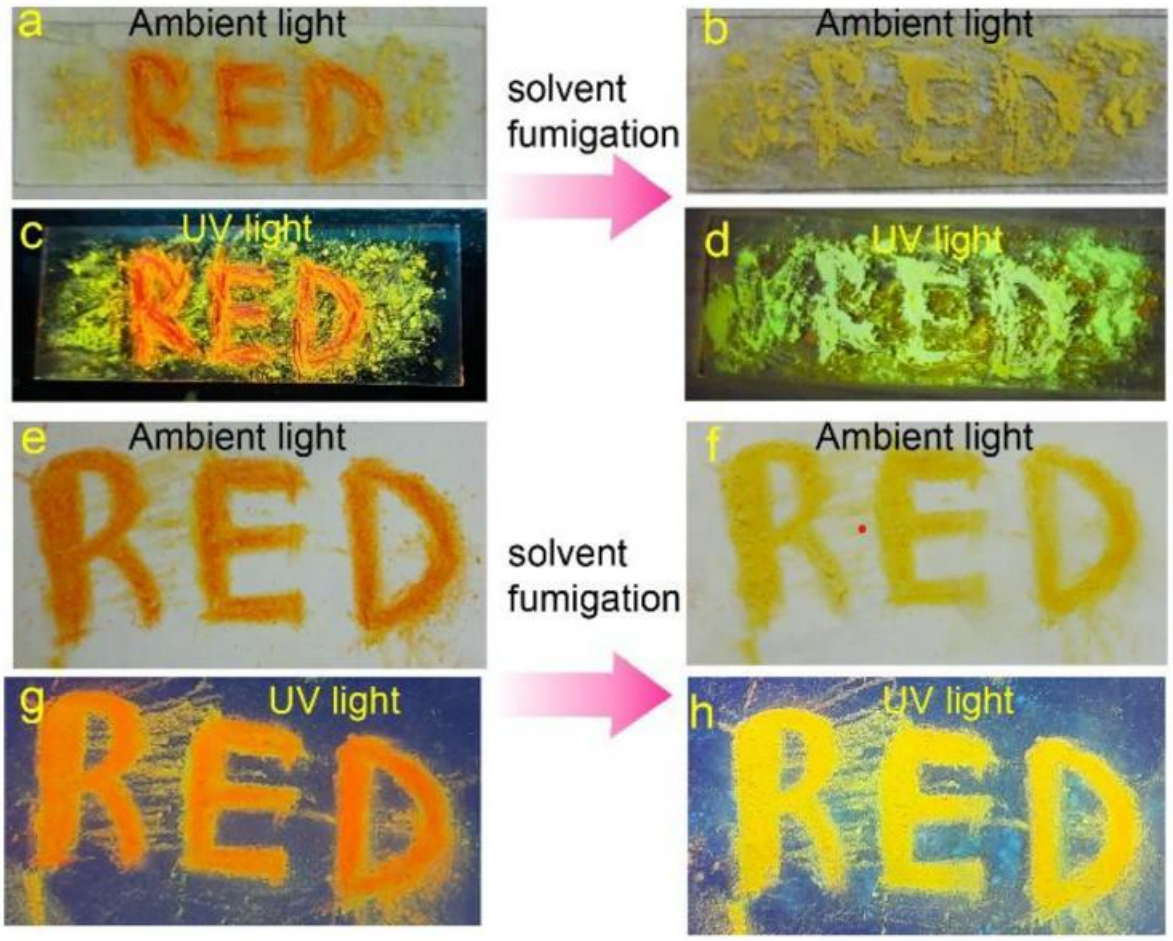

Figure 24. Mechanochromic inkless writing and vapour induced erasing using **1CF$_3$** compound (a,b,c,d) The word “RED” written on a glass plate (e,f,g,h) written on a filter paper by using same glass rod as stylus.

Vapo-Erasing: The red fluorescent writing was subjected to solvent vapor fumigation using acetone or methanol: The fluorescence switched from red to greenish-yellow, closely resembling the background color and reducing the writing's visibility. This reversibility demonstrates the practical utility of these materials for dynamic luminescent applications. Writing on cellulose paper: The same experiment was conducted on cellulose filter paper, where the mechanochromic transition of the word "RED" (Figure 24) was successfully

demonstrated. The process was reversible for up to three cycles, after which the filter paper started to degrade. The unique properties of these materials make them suitable for various practical applications, including security and confidential writing. Reversible writing on surfaces for temporary, secure information storage. Applications in erasable and reusable notepads or message boards. Potential for use in strain sensors that change fluorescence color under mechanical stress. Vapochromic color changes could aid in sensing volatile or harmful solvents. This study underscores the versatility of **1F$_2$** and **1CF$_3$,** offering a foundation for future advancements in luminescent materials for innovative technologies.

2.5 Conclusion

In summary, we successfully developed synthetically simple, donor-acceptor (D-A) cyanostilbene-based molecules as high-contrast mechanochromic materials that also exhibit prominent Aggregation-Induced Emission (AIE) behavior. Our findings revealed that during aggregation, these molecules self-assemble into highly ordered structures, enhancing their emission intensity. The inclusion of non-planar bulky diphenylamine groups was particularly advantageous, as it facilitated non-planar packing and effectively prevented π-π stacking interactions during the aggregation process. This emphasizes the critical role of molecular design in crafting AIE-active materials (AIEgens).

In addition to their AIE properties, the molecules demonstrated mechanochromic luminescence (MCL) characteristics. A thorough structure-property relationship analysis, utilizing single crystal X-ray diffraction (SCXRD), powder X-ray diffraction (PXRD), and infrared spectroscopy (IR), revealed that MCL behavior arises from mechanical shear pressure-induced packing changes. These structural rearrangements reconfigure non-covalent interactions, such as π•••π stacking, resulting in fluorescence color switching. Specifically, pressure-induced molecular planarization and enhanced π•••π stacking interactions in the excimeric state were responsible for the red-shifted fluorescence. Leveraging the mechanochromic and vapochromic switching properties of these materials, we demonstrated their application in inkless mechano-writing and vapo-erasing. These capabilities highlight their potential as: Security inks for secret data encoding and decoding. Sensing materials for detecting harmful solvents or volatile chemicals. Strain sensors capable of identifying specific load or stress limits through luminescence color changes.

Overall, this study not only establishes the utility of cyanostilbene-based materials in advanced applications but also opens new avenues for designing multifunctional luminescent systems with practical significance. These materials hold promise for innovations in confidential writing, solvent sensing, and stress detection technologies.

■ REFERENCES

1. H. Zhu, S. Zhang, J. Yang, M. Wu, Q. Wu, J. Liu, J. Zhang, L. Kong, J. Yang, *Solid State Chem.*, 2022, **305**, 122706.
2. Z. Wen, T. Yang, D. Zhang, Z. Wang, S. Dong, H. Xu, Y. Miao, B. Zhao, H. Wang, *J. Mater. Chem. C.*, 2022, **10**, 1833-1838.
3. G. Bae, M. Seo, S. Lee, D. Bae, M. Lee, *Adv. Mater. Technol.*, 2021, **6**, 2100479.
4. S. Zeng, H. Sun, C. Park, M. Zhang, M. Zhu, M. Yan, N. Chov, S. Li, A.T. Li, G. Smith, S. Xu, Z. Li, Y. Hou, B. Li, D.Z. Wang, L. Sun, *Mater. Horiz*., 2020, **7**, 164.
5. S. Ito, CrystEngComm., 2022, **24**, 1112-1126.
6. G. Giordano, M. Gagliardi, Y. Huan, M. Carlotti, A. Mariani, A. Menciassi, E. Sinibaldi, B. Mazzolai, *Adv. Sci*. 2021, **8**, 2100418.
7. Y. Li, Z. Ma, A. Li, W. Xu, Y. Wang, H. Jiang, K. Wang, Y. Zhao, X. Jia, A.C.S. Appl, Mater. Interfaces., 2017, **9**, 8910.
8. H. Yang, Z. Fu, S. Wang, H. Liu, J. Zhou, K. Wang, X. Wu, B. Yang, B. Zou, W. Zhu, *Mater. Adv*., 2021, **2**, 4859-4866.
9. T. Butler, A.S. Mathew, M. Sabat, C.L. Fraser, *A.C.S. Appl, Mater. Interfaces.*, 2017, **9**, 17603.
10. G. Gogoi, D. Kashyap, R.J. Sarma, *Cryst. Growth Des*., 2018, **18**, 4963.
11. J. Luo, Z. Xie, J.W.Y. Lam, L. Cheng, H. Chen, H.S.K. Qiu, X. Zhan, Y. Liu, D. Zhu, B. Z. Tang, *Chem. Commun*., 2001, 1740.
12. J. Mei, N.L.C. Leung, R.T.K. Kwok, J.W.Y. Lam, B.Z. Tang, *Chem. Rev.*, 2015, **115**, 11718.
13. X. Wang, C. Qi, Z. Fu, H. Zhang, J. Wang, H.-T. Feng, K. Wang, B. Zou, J.W.Y. Lam, B.Z. Tang, *Mater. Horiz*., 2021, **8**, 630.
14. Y. Wang, G. Zhang, M. Gao, Y. Cai, C. Zhan, Z. Zhao, D. Zhang, B.Z. Tang, *Faraday Discuss.*, 2017, **196**, 9-30.
15. Z. He, C. Ke, B.Z. Tang, *ACS Omega*., 2018, **3**, 3267.
16. F. Panahi, A. Mahmoodi, S. Ghodrati, A.A. Abdi, F. Eshghi, *Sci. Rep.*, 2022, **12,** 2385.
17. W. Yang, C. Liu, S. Lu, J. Du, Q. Gao, R. Zhang, Y. Liub, C. Yang, *J. Mater. Chem. C.*, 2018, **6**, 290.
18. S. Liu, G. Feng, B.Z. Tang, B. Liu, *Chem. Sci.*, 2021, **12,** 6488.
19. M. Wang, Y. Wang, R. Hu, R. Li, Z. Shuai, Y. Wei, *Dyes Pigm*., 2021, **198**, 109939.

20. X. Lu, W. Li, N.R. Sottos, J.S. Moore, *A.C.S. Appl, Mater. Interfaces*., 2018, **10**, 40361.
21. Y. Pei, J. Xie, D. Cui, S. Liu, G. Li, D. Zhu, Z. Su, *Dalton Trans.*, 2020, **49**, 13066.
22. J. Shi, Q. Deng, C. Wan, M. Zheng, F. Hunag, B. Tang, Chem. Sci., 2017, **8**, 6188.
23. B. Ma, W. Zhuang, H. Xu, G. Li, Y. Wang, *A.C.S. Appl, Mater. Interfaces*., 2019, **11**, 47259.
24. L. Mao, Y. Liu, S. Yang, Y. Li, X. Zhang, Y. Wei, *Dyes Pigm*., 2019, **162**, 611.
25. S. Ito, *J. Photochem. Photobiol. C: Photochem. Rev*., 2022, **51**, 100481.
26. S. Nagai, M. Yamashita, T. Tachikawa, T. Ubukata, M. Asami, S. Ito, *J. Mater. Chem. C*., 2019, **7**, 4988.
27. Y. Lv, Y. Liu, X. Ye, G. Liu, X. Tao, *CrystEngComm*., 2015, **17** , 526.
28. Y. Lv, Y. Liu, D. Guo, X. Ye, G. Liu, X. Tao, *Chem. Asian J*., 2014, **9**, 2885.
29. S. Yagai, T. Seki, H. Aonuma, K. Kawaguchi, T. Karatsu, T. Okura, A. Sakon, H. Uekusa, H. Ito, *Chem. Mater*., 2016, **28**, 234.
30. Y. Sagara, T. Kato, *Angew. Chem*., 2011, **123,** 9294.
31. P. Xue, J. Ding, P. Wang, R. Lu, *J. Mater. Chem. C.*, 2016, **4**, 6688.
32. G. Zhang, J. Sun, P. Xue, Z. Zhang, P. Gong, J. Peng, R. Lu, *J. Mater. Chem. C*., 2015, **3**, 2925.
33. Z. Lv, Z. Man, Z. Xu, L. Fu, S. Li, Y. Zhang, H. Fu, *Adv. Optical Mater*., 2021, **9**, 2100598.
34. J. Zhao, L. Li, W. Wang, X. Guan, J. Rong, C. Zhang, *J. Lumin.*, 2021, **241**, 118495.
35. L. Wen, J. Sun, C. Li, C. Zhu, X. Zhang, Z. Wang, Q. Song, C. Lv, Y. Zhang, *New J. Chem.*, 2021, **45**, 11530.
36. P. Shi, R. Zhao, M. Zhang, M. Lin, Y. Duan, T. Han, *Mater. Lett.* 2019, **243**, 38.
37. Z. Li, X. Wang, L. Han, C. Zhu, H. Xin, Y. Yin, *Adv. Mater*., 2022, **34**, 2107398.
38. K. Zheng, F. Ni, Z. Chen, C. Zhong, C. Yang, A*ngew. Chem. Int. Ed*., 2020, **59**, 9972.
39. J. J. Liu, S.B. Xia, T. Liu, J.M. Liub, F.X. Cheng, *CrystEngComm.*, 2021, **23**, 4320.
40. C. Duan, Y. Zhou, G.G. Shan, Y. Chen, W. Zhao, D. Yuan, L. Zeng, X. Huang, G. Niu, *J. Mater. Chem. C*., 2019, **7**, 3471.
41. L. Yu, C. Yang, *J. Mater. Chem. C*., 2021**, 9**, 17265.
42. Z. Wan, Y. Zan, B. Wang, W. Fang, S. Cui, Y. Teng, F. Zhang, Y. Li, L. Chen, G. Bai, *J. Lumin*., 2021, **242**, 118555.
43. APEX3, version 2017.3-0, and SAINT, version 8.38A, Bruker AXS Inc., Madison, WI, 2012, URL: https://www.bruker.com.

44. G. M. Sheldrick, SADABS, University of G¨ oettingen, G¨ oettingen, Germany, 1996 (Part of Bruker APEX3 software package (version 2017.3-0): Bruker AXS, 2017).
45. G. M, Sheldrick, SHELXTL XT – Crystal Structure Solution, version 2014/4, Bruker AXS, 2010-2014.
46. G.M. Sheldrick, SHELXL2014, University of G¨oettingen, Germany, 2014.
47. G.M. Sheldrick, *Acta Crystallogr. A*., 2015, **71**, 3–8.
48. G.M. Sheldrick, *Acta Crystallogr. A*, 2008, **64**, 112–122.

CHAPTER-3

Multi-stimuli responsive characteristics exhibited by a structurally simple acylhydrazone-based crystal featuring a donor–acceptor architecture

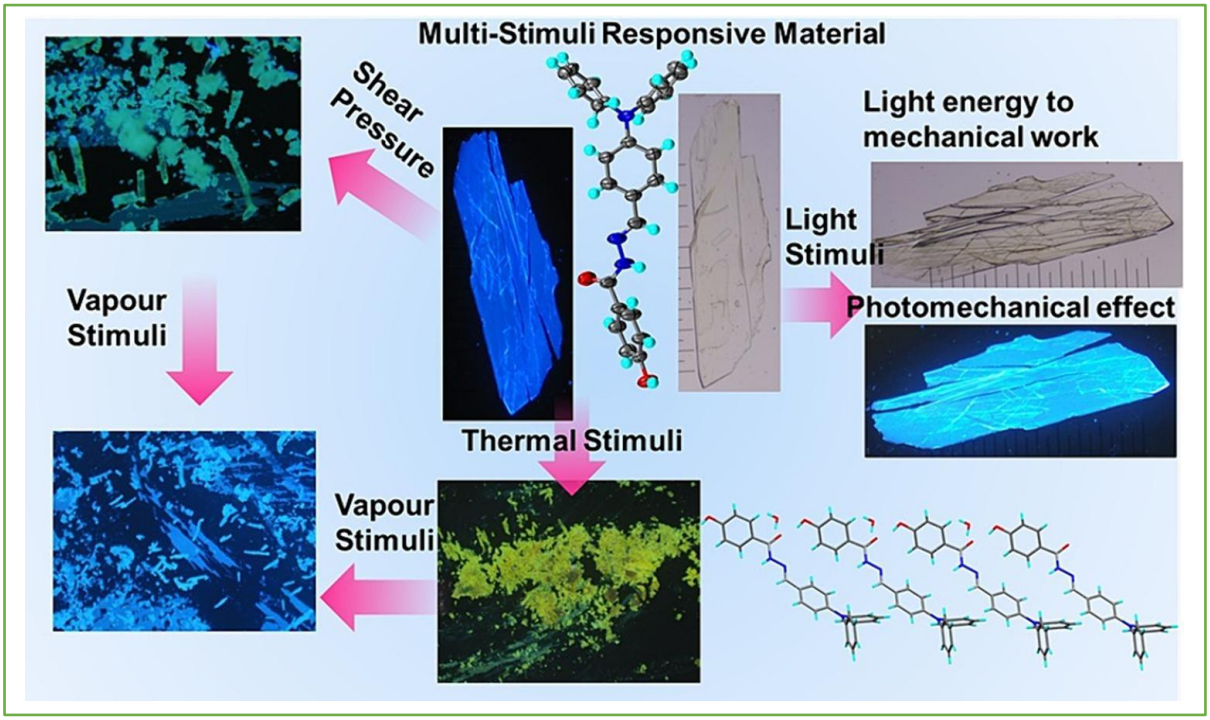

Multi-stimuli-responsive characteristics exhibited by a structurally simple acylhydrazone-based crystal featuring a donor–acceptor architecture.

3.1 Introduction

This study introduces a novel compound, (E)-N'-(4-(diphenylamino)benzylidene)-4-hydroxybenzohydrazide (**DPAhydrzOH)**, which belongs to the class of diphenylamine-acylhydrazone derivatives. The compound exhibits remarkable multi-stimuli responsive properties, encompassing mechanochromic luminescence (MCL),[1-9] thermochromic luminescence, and an intriguing photomechanical effect when in its solid crystalline state. The detailed single-crystal structure analysis reveals that the molecule is stabilized through diverse hydrogen-bonding interactions, which play a critical role in its structural and functional properties. A thorough mechanistic investigation indicates that the pronounced MCL behavior is driven by structural rearrangement induced by shear pressure, leading to changes in the molecular packing. This reconfiguration is responsible for the observed switching in luminescent properties. Furthermore, the compound displays a captivating photomechanical effect, manifested as surface cracking and minor movements of the crystal when exposed to 365 nm ultraviolet light. This phenomenon is attributed to photoinduced isomerization from the Trans to cis form within the crystalline lattice.

This multi-faceted response to external stimuli underscores the potential of **DPAhydrzOH** as a material for innovative applications in fields such as optoelectronics and sensory devices, where such versatile and responsive behavior could be effectively utilised. In recent years, stimuli-responsive materials have gained considerable attention for their ability to alter physical properties, such as shape, size, or optical behavior, in response to external stimuli like light, heat, pressure, or chemical vapors. These materials hold immense promise for applications in sensors, actuators, and optoelectronic technologies.[10-15] The responsiveness of a material is influenced by key parameters, including functional groups in the molecule, supramolecular packing, and non-covalent intermolecular interactions. Among all stimuli, light stands out as a ubiquitous and clean source of energy, capable of modifying the physical and optical properties of materials without generating harmful by-products. This capability to convert light energy into macroscopic mechanical work has emerged as a captivating research avenue, offering a sustainable framework for mechanical operations without reliance on fossil fuels.[15-25] On a molecular scale, light-induced processes—such as rearrangement,

isomerization, or photochemical reactions—affect supramolecular interactions and packing arrangements, leading to amplified macroscopic effects like shape change, cracking, bending, jumping, and surface alterations. The role of reconfigurable weak non-covalent interactions is especially crucial in magnifying these molecular motions to the bulk scale. Research in this domain has seen exponential growth, showcasing numerous light-responsive crystalline and polymeric materials that possess vast technological potential.

Stimuli-responsive luminescence switching is another intriguing property that solid-state materials exhibit, and it serves as a foundation for developing advanced optoelectronic devices. These materials are capable of reversible or irreversible shifts in emission color when exposed to external stimuli such as light, shear force, heat, or chemical vapors, making them highly valuable for sensing applications.[26-32] A subset of such materials, known as mechanochromic luminescent (MCL) systems, demonstrates changes in emission color or intensity when subjected to shear force.[33-37] In crystalline or other solid forms, such luminescence shifts are commonly attributed to molecular packing rearrangements that alter excited-state interactions, although the precise mechanisms behind these color changes remain an area of active investigation.

In this study, we present a synthetically straightforward donor-acceptor (D-A) type acylhydrazone derivative, (E)-N'-(4-(diphenylamino)benzylidene)-4-hydroxybenzohydrazide (DPAhydrzOH), which exhibits multi-stimuli responsiveness, including photoinduced mechanical effects as well as luminescence changes driven by pressure, heat, and chemical vapors. The molecular structure features a bulky diphenylamine donor group that promotes a non-planar packing arrangement, enhancing solid-state luminescence. The acceptor amide group (-NHC=O) facilitates intermolecular hydrogen bonding, which is crucial for reconfigurable supramolecular packing interactions. When illuminated with 405 nm light, **DPAhydrzOH** crystals display photoinduced surface cracking and small-scale movements, attributed to trans-to-cis isomerization within the crystalline lattice. Additionally, these crystals exhibit a striking mechanochromic luminescence shift, transitioning from cyan to green upon the application of shear pressure. This multifaceted behavior underscores the potential of DPAhydrzOH for applications in optoelectronics and stimuli-responsive technologies.

3.2 Experimental

3.2.1. Materials & methods

Materials and Purity: 4-(Diphenylamino)benzaldehyde and 4-hydroxybenzohydrazide were sourced from TCI India and used as received, without any additional purification steps. ACS-grade solvents supplied by Merck were utilized for the synthesis. Spectroscopy-grade solvents were employed during crystallization and spectroscopic studies to maintain high experimental standards.

NMR Analysis: ^{1}H NMR (300 MHz) and ^{13}C NMR spectra of the compound were recorded using a Bruker AVANCE 300 spectrometer. Deuterated solvents, $CDCl_3$ or DMSO-d_6, were used as the medium for NMR studies. Chemical shift values (δ) were reported in parts per million (ppm).

Mass Spectrometry: High-resolution mass spectrometry (HRMS) for the compound was conducted using a QTOF Micro YA263 mass spectrometer in electrospray ionization (ESI) mode. The results confirmed the molecular mass of the compound.

UV–Vis and Fluorescence Studies: Solution and solid-state UV–Vis absorption spectra were recorded on a Shimadzu UV-2401C spectrophotometer. Fluorescence emission measurements were conducted using a HORIBA Jobin Yvon Fluorolomax-4 spectrofluorometer and a Maya 2000 pro Ocean Optics spectrometer. Fluorescence lifetime measurements were carried out using a Modular Time Correlated Single Photon Counting spectrometer (Horiba) equipped with Delta Flex detectors (PPD850).

IR Spectroscopy: Infrared (IR) spectra of the compound were recorded using a Parkin Elmer LX-1 FT-IR spectrometer.

Single Crystal X-ray Diffraction: Single crystal X-ray diffraction data for **DPAhydrzOH** crystals were collected using a Microfocus D8 Venture Bruker APEX 3 diffractometer with a CCD area detector and MoKα radiation (λ = 0.71069 Å). Data reduction was performed using the SAINT program (version 8.38A), and agreement analysis was carried out using XPREP (part of the APEX 3 software suite, version 2017.3–0). Absorption corrections were made using the SADABS program. The structure was solved using SHELXT (version 2018/2) and refined using SHELXL-2014. Non-hydrogen atoms were refined anisotropically, while hydrogen

atoms were calculated and refined isotropically. The crystallographic data were deposited in the Cambridge Crystallographic Data Centre (CCDC) under the deposition number 2338085.

Density Functional Theory (DFT) Calculations: DFT calculations were carried out using the Gaussian 16 (Revision B.01) software package with the B3LYP/gen level of theory. Input molecular coordinates were extracted from the crystal structure (.cif file), and geometry optimization was performed in a vacuum. Frontier molecular orbitals were analyzed using the GaussView program.

3.2.2 Synthesis and chracterization of DPAhydrzOH: A 100 mL round-bottom flask was charged with 4-(diphenylamino)benzaldehyde (0.273 g, 1 mmol) and 4-hydroxybenzohydrazide (0.152 g, 1 mmol) dissolved in 30 mL methanol. A catalytic amount of acetic acid was added to the mixture, which was heated at 90 °C for 4 hours. After cooling, the reaction mixture was filtered, and the filtrate was left to crystallize over three days. Cuboidal, colorless crystals of **DPAhydrzOH** were obtained, yielding 270 mg (66%) upon air drying. **^{1}H NMR** (300 MHz): δ values were recorded as follows: 11.58 (s, 1H, OH), 10.12 (broad, 1H, NH), 8.35 (s, 1H, HC=N), 7.80 (d, J = 9.0 Hz, 2H, ArH), 7.59 (d, J = 8.79 Hz, 4H, ArH), 7.35 (t, J = 9.0 Hz, 2H, ArH), 7.09 (m, J = 8.7 Hz, 2H, ArH), 6.97 (d, 2H, ArH), 6.85 (d, J = 8.7 Hz, 2H, ArH). Melting point: ~ 205 ^{o}C.

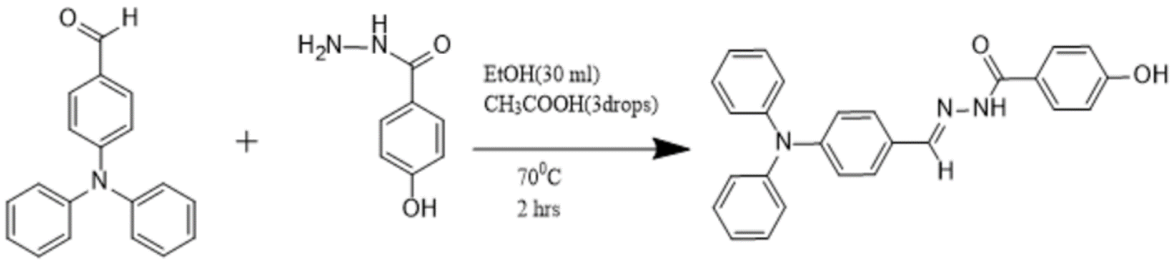

Scheme 1. Synthesis of **DPAhydZOH.**

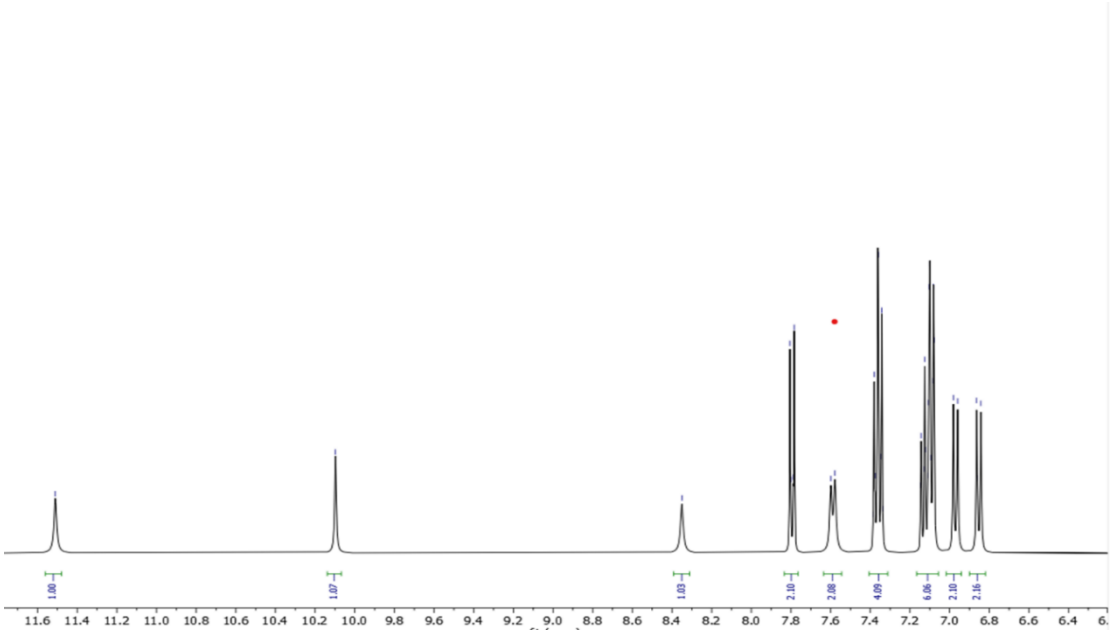

Figure 1. ^{1}H NMR spectra (in DMSO-d_6) of synthesized compound **DPAhydrzOH.**

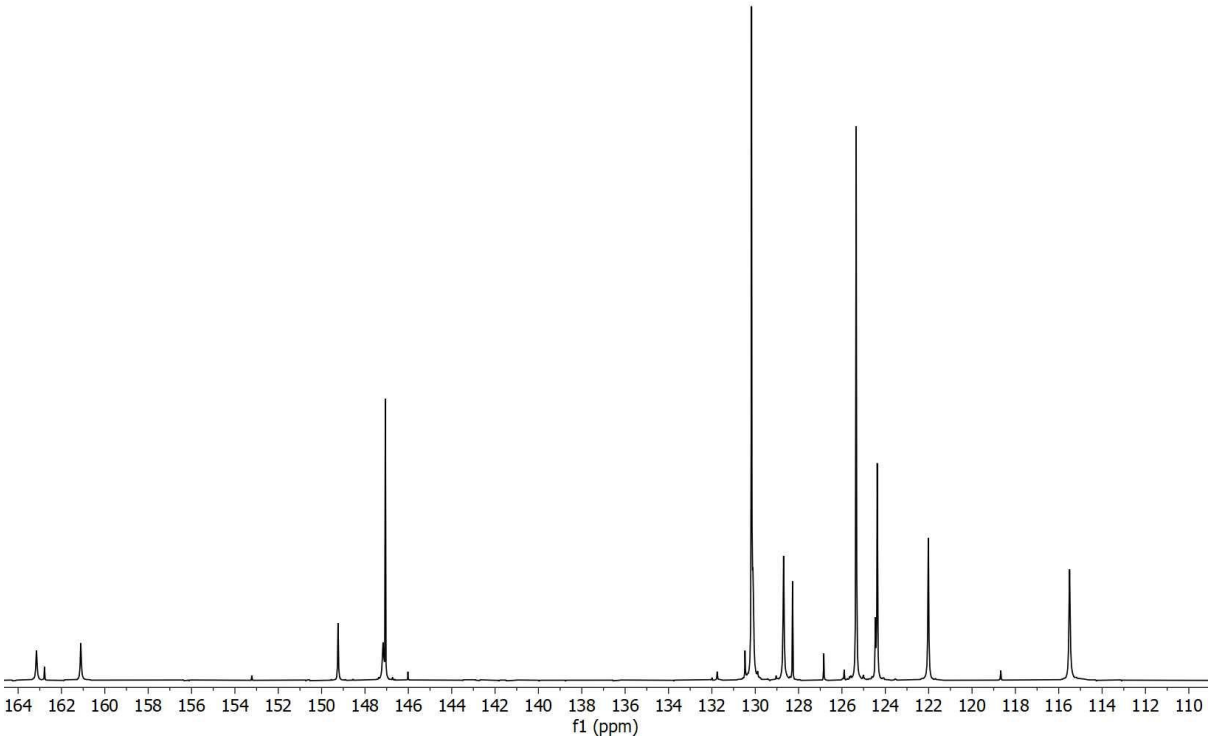

Figure 2. ^{13}C NMR spectra (in DMSO-d_6) of synthesized compound **DPAhydrzOH .**

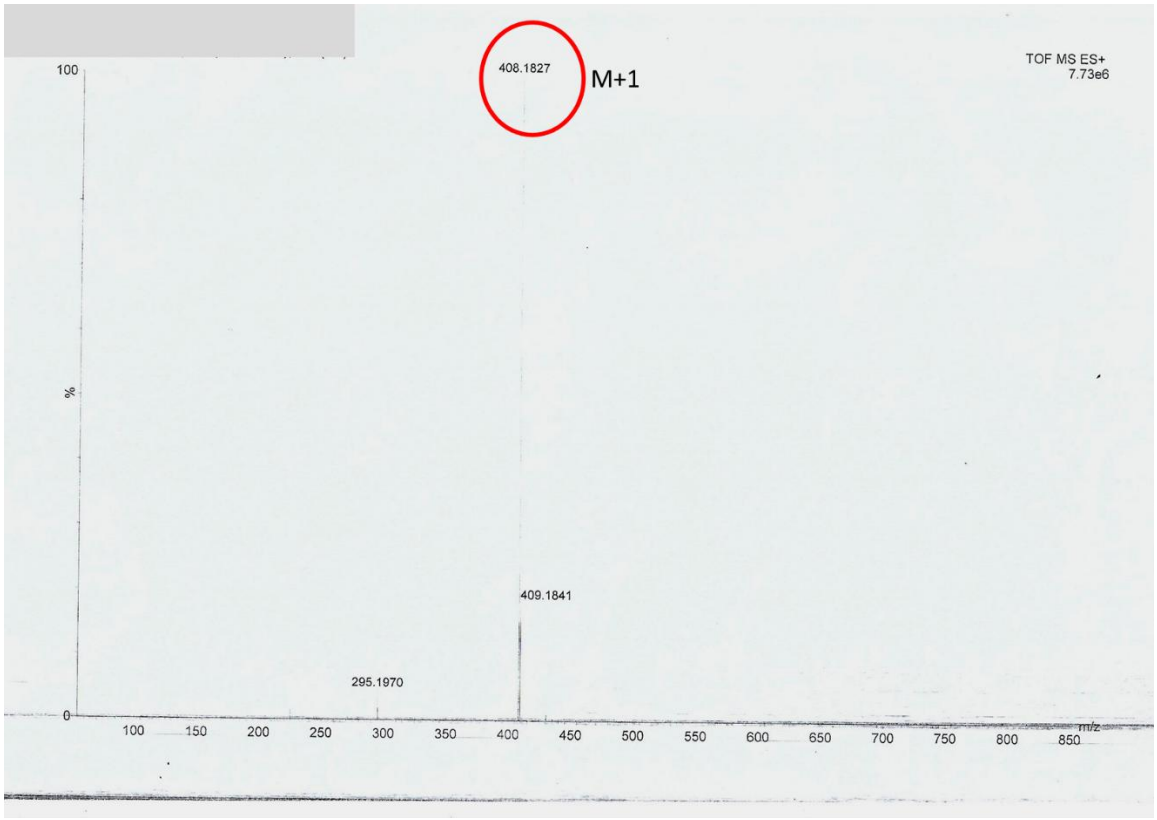

Figure 3. High-resolution mass spectra(HRMS) of the compound **DPAhydrzOH**.

HRMS: The calculated molecular weight for $C_{26}H_{21}N_3O_2$ is 407.1634, with an observed m/z value of 408.1827 (M+H).

3.3 Results and discussions

3.3.1 Photophysical studies

Compound **DPAhydzOH** was synthesized through a Schiff base condensation reaction involving 4-(diphenylamino)benzaldehyde and 4-hydroxybenzohydrazide in the presence of a catalytic quantity of acetic acid. The reaction conditions and procedure are outlined in Scheme S1 (SI). Comprehensive characterization of the synthesized compound was achieved using ^{1}H NMR spectroscopy, mass spectrometry, and IR spectroscopy (Figures 1-3, 8), which confirmed the molecular structure and integrity of the product. UV-Vis absorption spectroscopy of **DPAhydzOH** in methanol (concentration: 1×10^{-5} M) revealed two prominent absorption bands at λmax = 370 nm and 290 nm. The lower energy band at 370 nm was attributed to an intramolecular charge transfer (ICT) transition. This transition arises from the diphenylamine (DPA) donor moiety and the amide-carbonyl acceptor group within the molecule (Figure 4c).

To gain deeper insight into the ICT process and its relationship with the frontier molecular orbitals, density functional theory (DFT) calculations were performed the results of these calculations revealed that the electron density of the highest occupied molecular orbital (HOMO; E = -4.9445 eV) is localized predominantly on the diphenylamine donor, while the lowest unoccupied molecular orbital (LUMO; E = -1.3456 eV) is concentrated on the acylhydrazone carbonyl acceptor group. The calculated HOMO-LUMO energy gap was found to be 3.44 eV (Fig. 4d), confirming the electronic characteristics of the molecule.

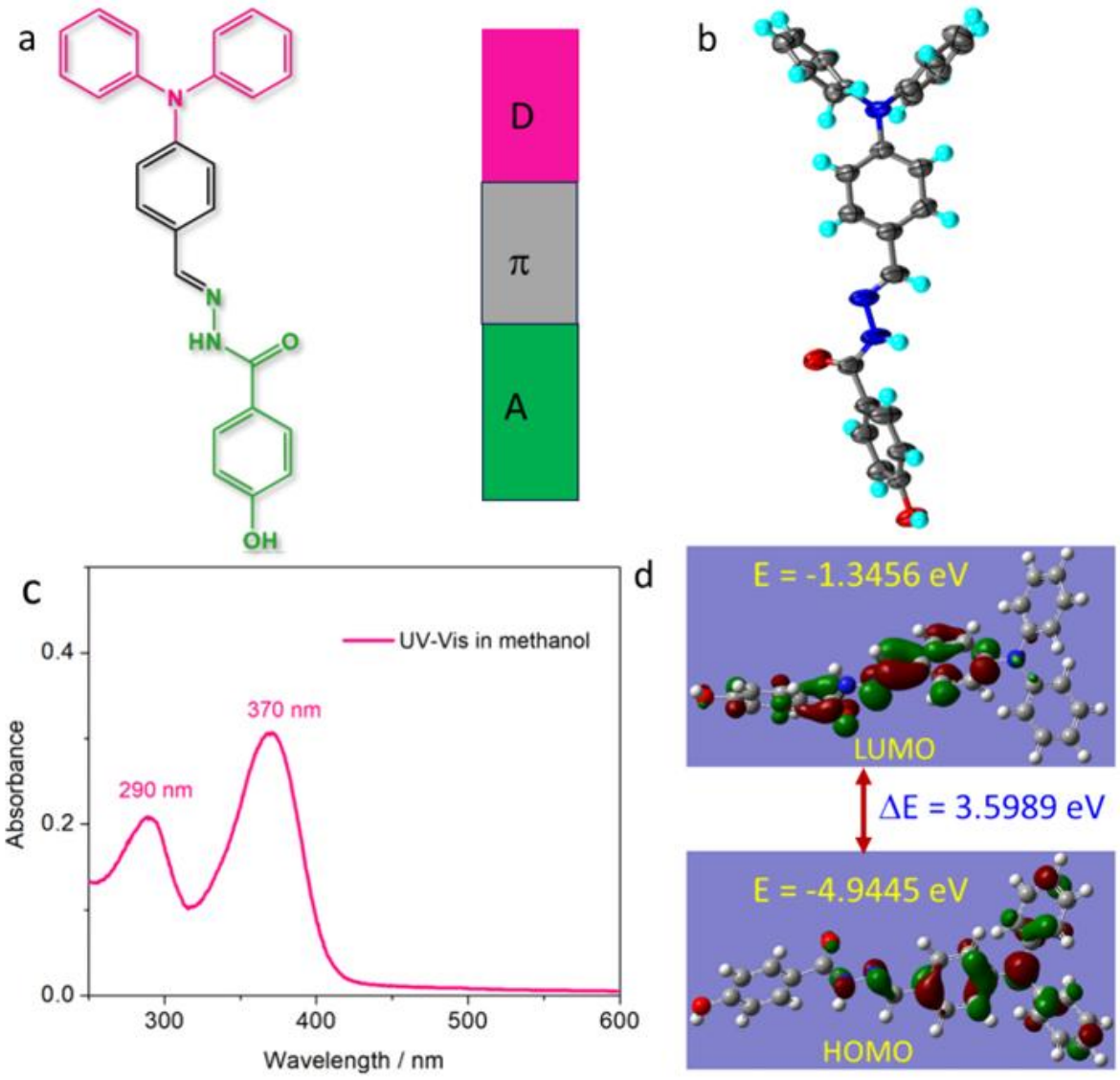

Figure 4. (a) Molecular (donor π-acceptor, D- π -A structure) structure and (b) Crystal structure of the molecule showing trans configuration around C solution absorption data of **DPAHydrzOH** (d) DFT calculated HOMO-LUMO profiles and their energy gap.

Photophysical analysis of **DPAhydzOH** in THF solution (1×10^{-4} M) revealed weak blue fluorescence, with an emission maximum at λ_{max} = 432 nm, a quantum yield (ϕ) of 0.02, and a fluorescence lifetime (τ) of 21.41 ns (Table 1). This fluorescence emission corresponds to the ICT → S_0 transition, characteristic of the ICT fluorescence. Further, as expected from ICT-based fluorescence, a solvatochromic redshift of the fluorescence maxima was observed with increasing solvent polarity (Figures 5 and 6). The diminished emission intensity in THF solution can likely be attributed to higher non-radiative decay ($K_{nr}\uparrow$), which is facilitated by increased rotational freedom of the phenyl rings in solution. Interestingly, **DPAhydzOH** demonstrated moderate aggregation-induced emission (AIE) properties in a solvent mixture of THF (good solvent) and water (anti-solvent). At a water fraction (f_w) of 10%, the emission intensity nearly doubled, accompanied by a redshift in the emission maximum to 457 nm ($\Delta\lambda$ = 25 nm; (Figure 7 and 12). With a further increase in the water fraction to 20%, the emission maximum shifted to 467 nm ($\Delta\lambda$ = 37 nm).

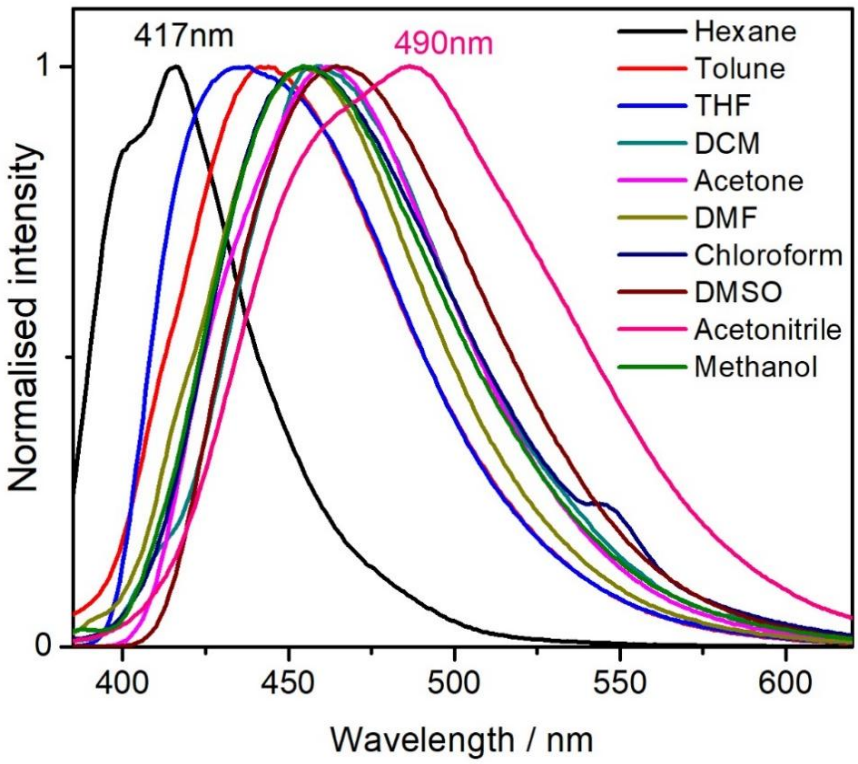

Figure 5. Solvatochromic fluorescence spectra (normalised) of **DPAhydrzOH** in different solvents

Table 1. Life time values of **DPAHydrzOH** in solution

Samples	**Fluorescence Life time values, τ (ns)**
DPAHydrzOH in THF solution λ_{ex} = 370 nm, λ_{em} = 434 nm	τ_1 = 21.41 ±0.006 (100 %) χ^2 = 1.043
DPAHydrzOH Pristine crystal λ_{ex} = 380nm, λ_{em} = 463 nm	τ_1 = 111.97 ± 0.1 (20.12 %) τ_2 = 7.84 ± 0.18 (79.88%) χ^2 = 0.9471955
DPAhydrazOH Ground Powder λ_{ex} = 380nm λ_{em} = 500 nm	τ_1 = 30.04 ± 0.26 (69.23 %) τ_2 = 6.996 ± 12.0 (30.77%) χ^2 = 1.230333

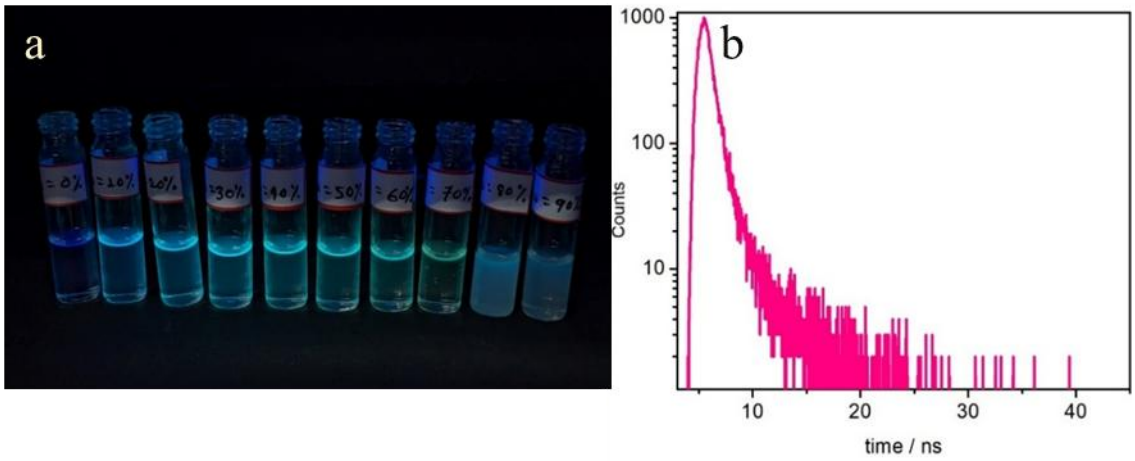

Figure 6.(a) Digital camera snapshots of AIE of **DPAhydrzOH** with increaseing water fraction(f_w) different THF:water ratio. (b) life time plot of **DPAhydrzOH** in THF solution.

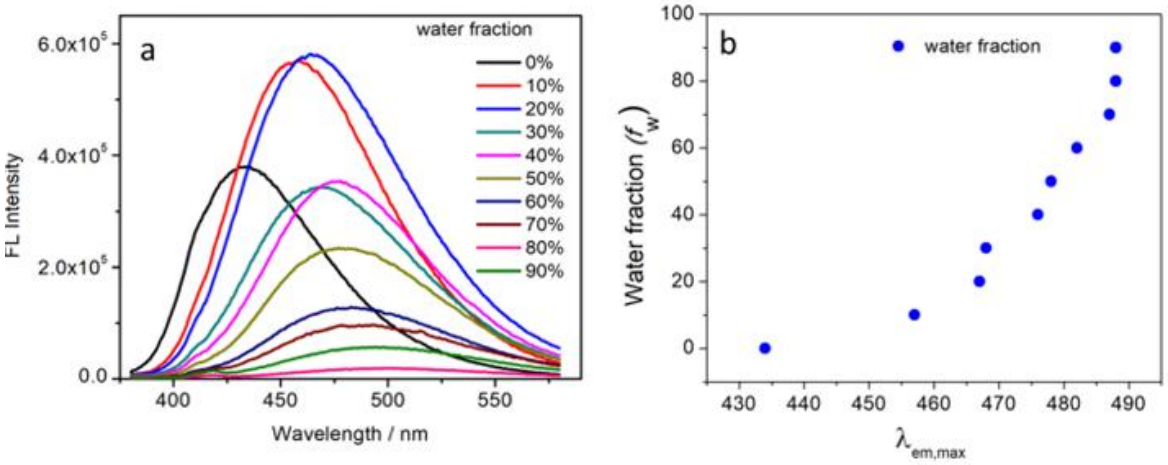

Figure 7. (a) Change in fluorescence spectra during aggregation induced emission in THF: water mixture, (b) Gradual shift of emission maxima with water fraction (f_w).

Although the intensity remained unchanged. However, at higher water fractions, a decrease in emission intensity was observed, along with a small redshift in the emission maximum (Figure 7b). This enhancement in fluorescence upon aggregation can be explained by the restricted molecular motion due to intermolecular interactions, such as hydrogen bonding and van der Waals forces in the aggregated state. These interactions effectively reduce non-radiative decay pathways and enhance radiative emission processes. This hypothesis is supported by the observation of bright blue fluorescence in the solid crystalline state of **DPAhydzOH**, a phenomenon that will be discussed in more detail in subsequent sections.

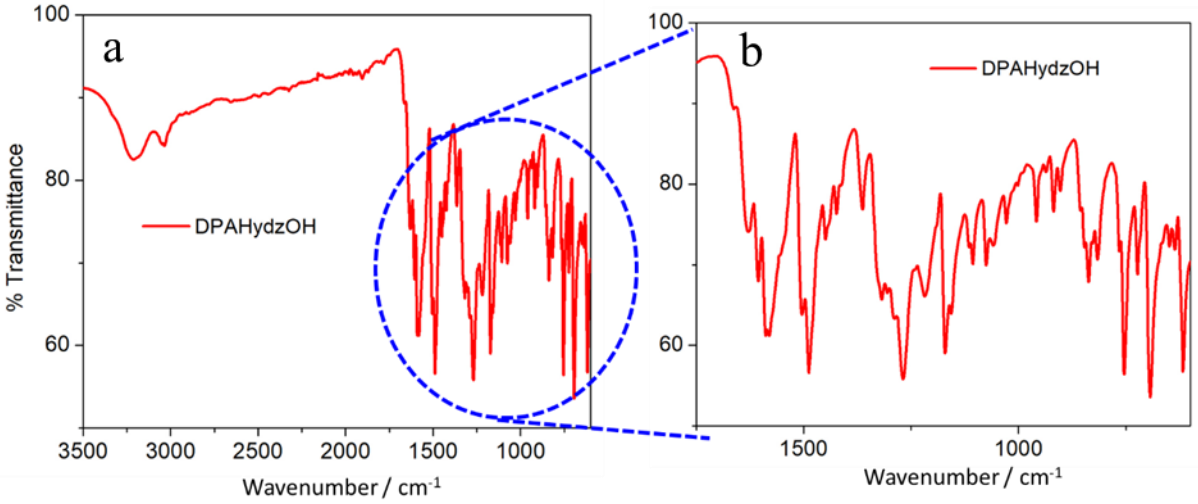

Figure 8. (a) IR spectra of **DPAhydrzOH** (b) Expanded view.

3.3.2 Single crystal X-ray structure Analysis

The solid-state properties of a material are significantly influenced by the molecular packing arrangements and the nature of intermolecular interactions. To explore the structure–function relationship of **DPAhydrzOH**, its crystal structure was analyzed using single-crystal X-ray diffraction. Rectangular plate-shaped single crystals were obtained through the slow evaporation of an ethanol solution of **DPAhydrzOH.** The crystals crystallized in the monoclinic system with a $P2_1$ space group and included one water molecule per unit cell within the lattice. Detailed crystallographic parameters and the CCDC reference number can be found in Table 2. Conformational analysis revealed a non-planar molecular structure with a water molecule embedded within the crystal lattice (Figure 10). The diphenylamine (DPA) donor moiety exhibited a unique out-of-plane orientation relative to the π-phenyl system. This non-planarity reduces the extent of interlayer π–π stacking interactions, which are typically prevalent in planar aromatic systems. The inhibition of such stacking interactions (Figure 9)

contributes to the enhanced solid-state fluorescence of **DPAhydrzOH** compared to its solution-phase fluorescence. This distinctive arrangement is further supported by the presence of various intermolecular forces that stabilize the crystal structure and suppress conformational rotations in the photoexcited state, thereby improving radiative emission and resulting in bright fluorescence in the solid state.

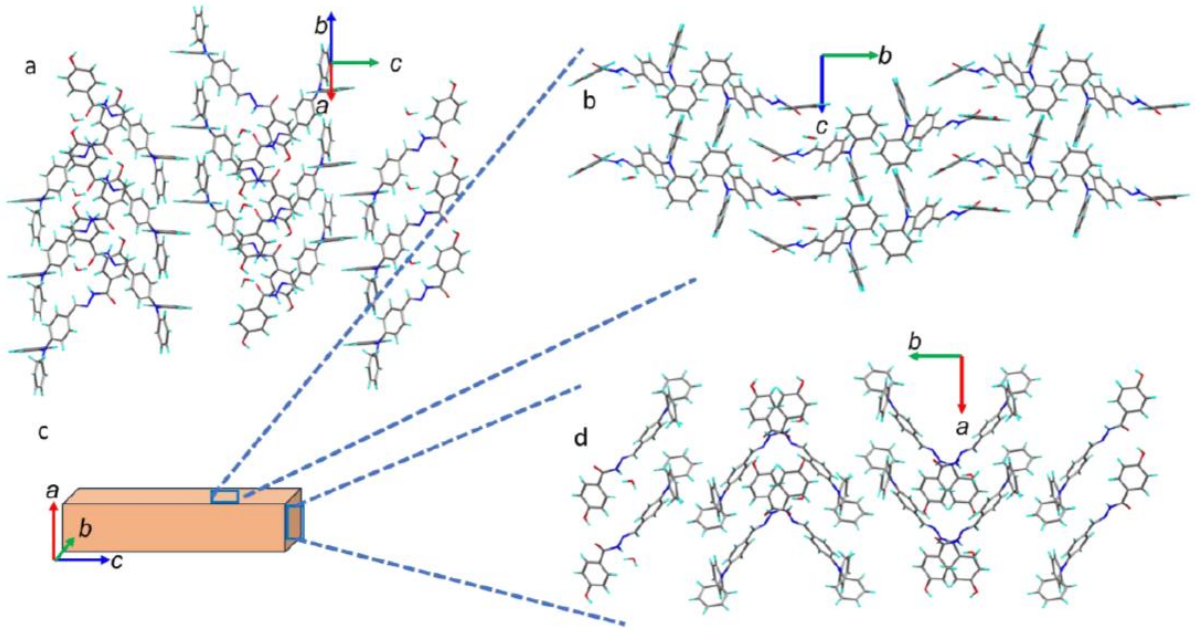

Figure. 9. Packing of **DPAhydrzOH** molecules viewed from different crystallographic directions.

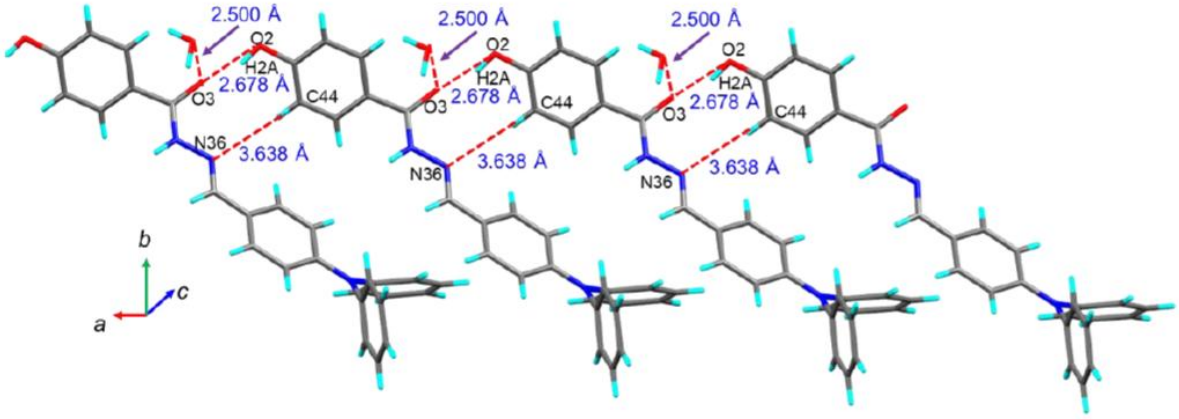

Figure. 10. Various types of H-bonding interaction in the packing structure of **DPAhydrzOH** that stitches the molecules in the crystal lattice.

Further analysis of the packing structure showed that the molecules are interconnected through a network of intermolecular hydrogen-bonding interactions extending across different lattice dimensions. The lattice water molecule plays a pivotal role, acting as a bridge to connect

neighboring molecules through two distinct hydrogen-bonding interactions: N6–H6•••O111 (donor–acceptor distance of 2.783 Å) and O111–H111A•••O3 (donor–acceptor distance of 2.500 Å). Additionally, adjacent molecules are interconnected via hydrogen bonding between the p-hydroxyl group of one molecule and the carbonyl oxygen of another (O1–H1•••O4, with a donor–acceptor distance of 2.761 Å). This interaction extends primarily along the crystallographic a-axis. Moreover, weak hydrogen-bonding interactions are evident between the nitrogen atom of the azomethine C=N group and the phenyl hydrogen of a neighboring molecule (C2–H2•••N7, with a donor–acceptor distance of 3.623 Å).

These hydrogen-bonding interactions serve multiple functions, including stabilizing the crystal lattice and enabling structural reorganization during photoisomerization or stimuli-induced mechanical changes in the solid state. The dynamic and weak nature of these interactions facilitates the rearrangement of molecular packing under external stimuli, providing a framework for potential structural reconfiguration mechanisms. The well-organized hydrogen-bonding network, combined with the unique non-planar molecular geometry, highlights the role of intermolecular forces in the photophysical behavior and structural adaptability of **DPAhydrzOH** in its solid form (Figure 10).

Table 2. Single crystal X-ray parameters of **DPAHydrzOH** at 298 K.

Compound	**DPAHydrzOH**
CCDC deposit No.	2338085
Chemical formula	$C_{52}H_{45}N_6O_5$
M_r	833.94
Crystal system	Monoclinic
Space group	$P\ 2_1$
a / Å	8.2177(17)
b / Å	32.497(7)
c / Å	9.0620(19)
α / °	90
β / °	115.258(6)
γ / °	90
V / Å^3	2188.7(8)

Z_s	2
ρ_{calc} / (g cm^{-3})	1.265
μ / mm^{-1}	0.083
F_{000}	878
θ_{min} / °	2.49
θ_{max} / °	26.81
Reflections collected	9603
Independent reflections	6929
GoF	1.042
Final *R* indices [$I > 2\sigma(I)$]	R_1 = 0.063 wR_2 = 0.1759
R indices (all data)	R_2 = 0.0947 wR_2 = 0.2058

3.3.3. Mechanochromic, Thermochromic and Vapochromic luminescence

The plate-shaped, millimeter-sized single crystals of **DPAhydzOH** exhibit bright cyan-blue fluorescence, with an emission maximum at λ_{max} = 463 nm. This intense fluorescence is attributed to the non-planar packing of the molecules, which arises due to the presence of bulky diphenyl groups within the crystal lattice. Such molecular packing, combined with intermolecular interactions, effectively suppresses non-radiative decay pathways in the solid state, thereby enhancing fluorescence. Interestingly, these crystals display unique mechanochromic luminescence (MCL), thermochromic luminescence, and vapochromic luminescence switching properties (Figure 11a, b), making them multi-stimuli-responsive materials. Mechanochromic luminescence, a phenomenon wherein the luminescence color of a solid changes under mechanical stress or shear pressure, was observed in **DPAhydzOH** crystals. When subjected to mechanical grinding using a mortar and pestle, the pristine cyan-blue fluorescence of the crystals shifts significantly to a yellowish-green emission, with an emission maximum at λ_{max} = 500 nm ($\Delta\lambda$ = ~37 nm, Figure. 11f).

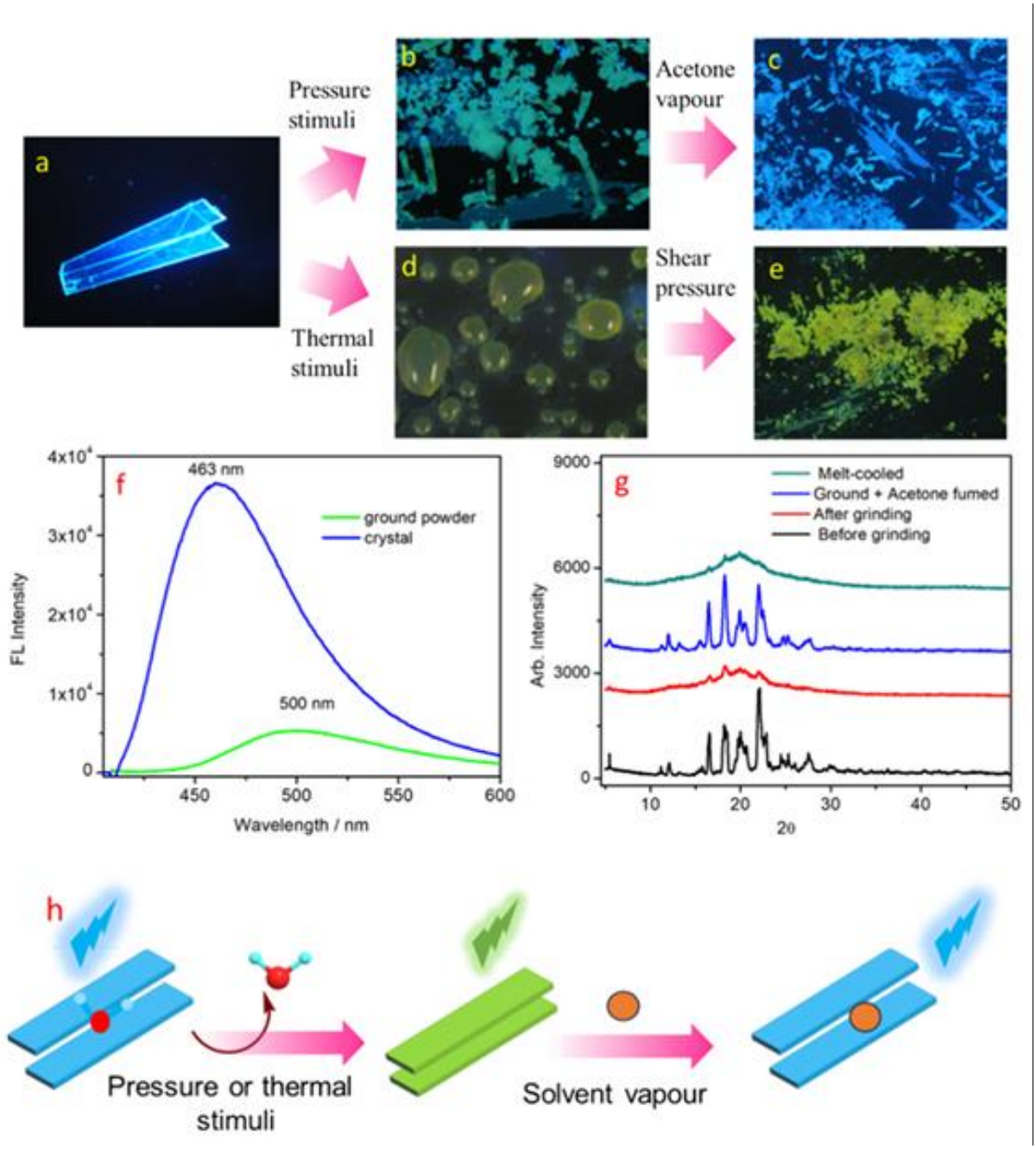

Figure 11 (a-e) Digital images of mechanochromic and thermochromic luminescence switching of the **DPAhydrzOH** crystal from blue to green, (f) emission spectra of crystal and ground powder, (g) pxrd spectra of the melt, before and after grinding and vapour fumed states (h) model representation of possible structural reconfiguration during MCL and thermochromic luminescence switching.

This color transition is hypothesized to result from a structural reorganization within the crystal lattice, induced by the partial expulsion of water molecules. The associated structural changes are believed to alter the excited state relaxation processes, leading to emission in the green spectral region. Fluorescence lifetime measurements of the crystal before and after grinding (Table 1) reveal notable changes, supporting the proposed mechanism.

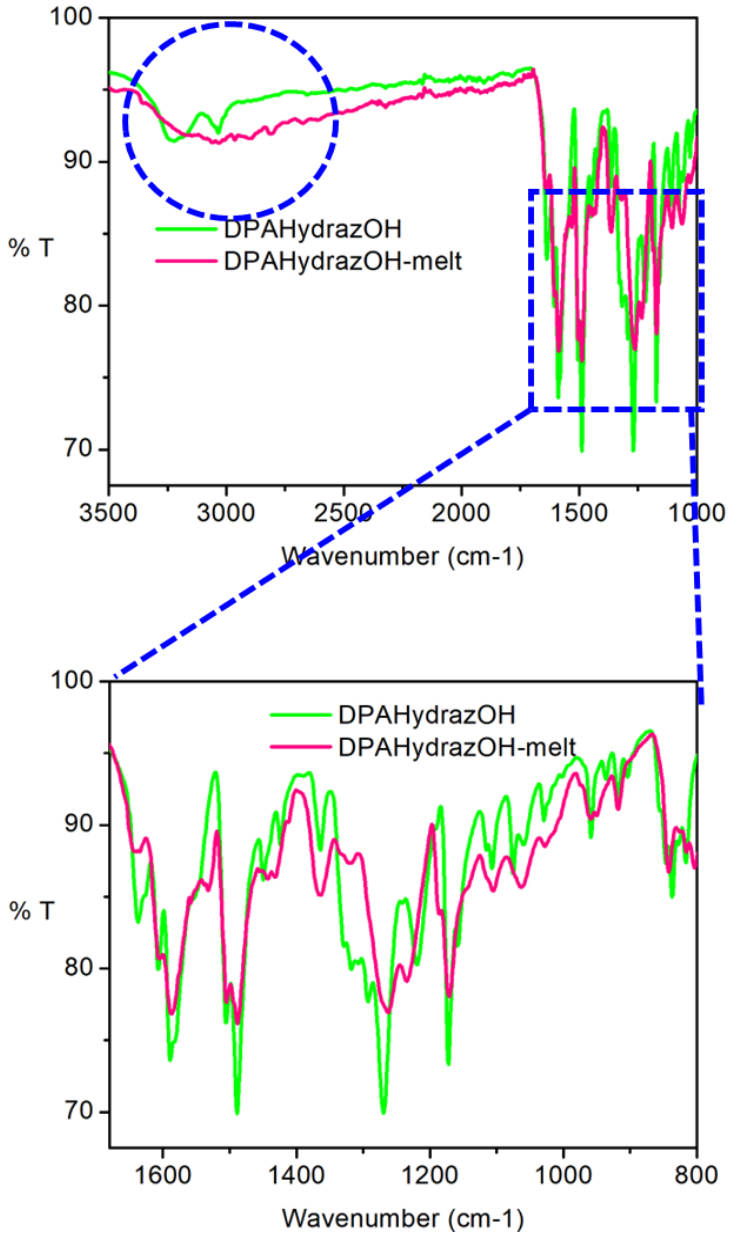

Figure 12. IR spectra of the cyan-blue emissive **DPAHydrazOH** crystal and yellowish green emissive melt solid.

The application of shear pressure is thought to destabilize the lattice water molecules, weakening the hydrogen-bonding interactions and facilitating the rearrangement of adjacent molecules. This rearrangement is responsible for the observed redshift in the emission maximum. Powder X-ray diffraction (PXRD) analysis further corroborates this hypothesis, as the PXRD profile of the ground sample exhibits broadened peaks with significantly reduced intensity (Figure. 11g). These changes indicate a loss of long-range molecular order and crystallinity following the mechanical stress.

Interestingly, the emission shift is reversible. When the ground powder is exposed to acetone vapor at ambient temperature, the emission reverts to the blue spectral region (Figure 11b, c). This reversibility suggests that the disordered molecules can regain their original ordered packing, akin to that of the pristine crystal. PXRD analysis of the solvent-fumed sample confirms this hypothesis, as its profile closely matches that of the unground, pristine crystal (Figure 11g).

Thermal stimuli also induce significant luminescence changes in **DPAhydzOH** crystals. Heating the cyan emissive crystal to approximately 205 °C, until it melts, leads to a transformation into a faint yellowish-green emissive solid. Upon scratching this solid with a spatula, a bright yellowish-green color is observed (Fig. 11d, e). It is assumed that the high temperature facilitates the expulsion of lattice water, resulting in a partially amorphized molecular arrangement. This arrangement is analogous to the structural changes induced by mechanical grinding. Supporting this explanation, the IR spectrum of the annealed, yellowish-green emissive powder differs from that of the pristine crystal and lacks the characteristic lattice water absorption band (Figure 12).

These findings underscore the remarkable multi-stimuli-responsive behaviour of **DPAhydzOH** crystals. The interplay between molecular packing, hydrogen-bonding interactions, and stimuli-induced structural changes enables reversible luminescence switching. This study not only highlights the potential applications of **DPAhydzOH** in sensor technologies and optoelectronic devices but also provides a deeper understanding of the relationship between crystal packing and photophysical properties.

3.3.4 Photomechanical effect in solid state

The photomechanical effect of **DPAhydzOH** in its solid-state form reveals a fascinating interplay between its molecular properties and structural dynamics under light illumination. Solid-state UV–Vis spectra of **DPAhydzOH**, recorded from a drop-cast film, exhibit a charge transfer (CT) absorption band at λ_{max} = 387 nm. This band is slightly red-shifted compared to the spectra observed in solution, indicating an influence of solid-state molecular packing on the optical properties (Figure. 13a). Given that the molecule contains a photoactive C=N group, known for its ability to undergo photoinduced geometric isomerization, we investigated its photomechanical behavior under illumination (Figure 13b).

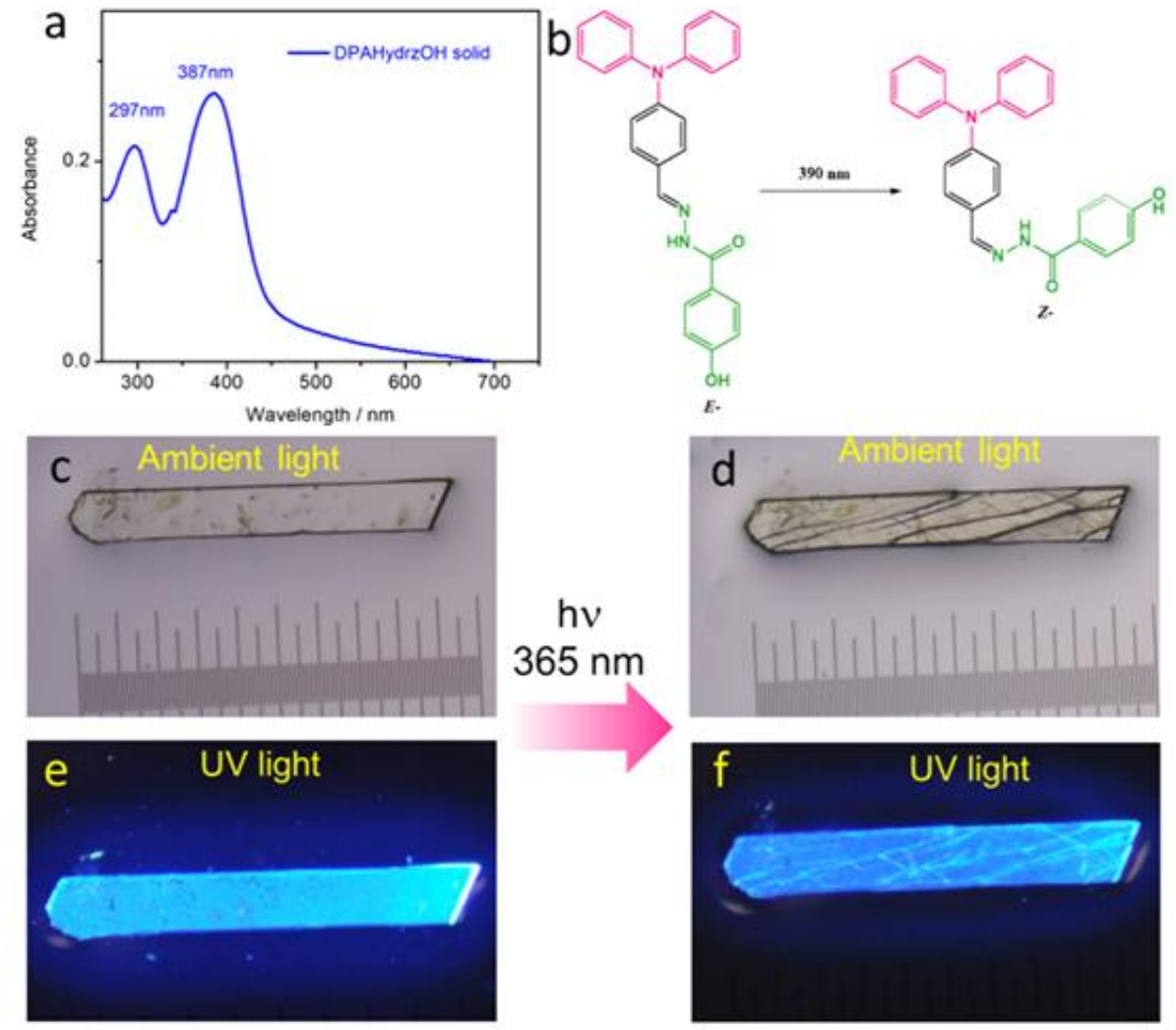

Figure 13 (a) Solid state UV–Vis spectra (drop casted film), (b) Trans- to cis- isomerization of the molecule occur in crystal upon irradiation of 365 nm or 405 nm light, (c-f) photomechanical effect in **DPAHydrzOH** crystal. Images were taken before and after photomechanical effect.

When exposed to UV light at 365 nm or 405 nm, the millimeter-sized crystals of **DPAhydzOH** began to develop surface cracks within 30 seconds. Over a duration of approximately 1 minute, these cracks propagated, ultimately causing the crystal to fragment into multiple pieces (Figs. 13 c–f). In some instances, small yet noticeable movements (2–3 mm) and rotational motions of the crystals were observed under 365 nm illumination. To assess whether the photomechanical response varied with the size and shape of the crystals, we tested samples of diverse dimensions and geometries. Interestingly, all crystals consistently exhibited cracking and slight movement, irrespective of their size or shape, indicating that these effects are intrinsic to the molecular structure and packing arrangement rather than the physical dimensions of the crystal.

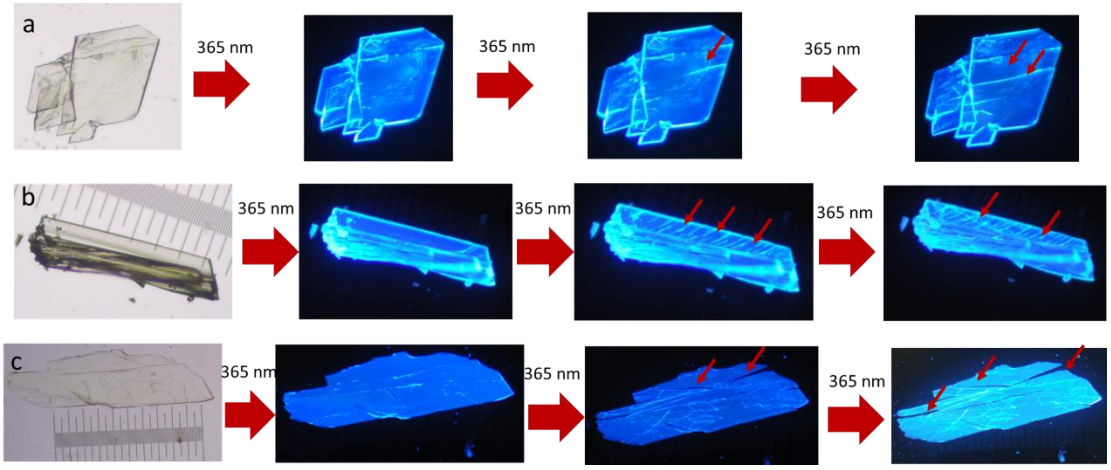

Figure 14. (a, b, c) Phtoinduced mechanical response of differently shaped crystals of **DPAHydrazOH** showing only cracking of the crystals.

The observed photomechanical behavior is attributed to a photoinduced trans-to-cis isomerization of the C=N bond within the crystalline medium (Figure. 13b). This photoisomerization process generates structural stress within the crystal lattice, resulting in the accumulation of strain. The mechanical force imparted by this strain manifests macroscopically as cracking, fragmentation, or movement of the crystal. To better understand the molecular-level mechanism underlying this phenomenon, we recorded the ^{1}H NMR spectra of **DPAhydzOH** crystals after irradiation with 365 nm light. The spectra revealed that 5–6% of the trans-isomer had converted to the cis-isomer during the photoreaction (Figure 16). This relatively low conversion efficiency can be ascribed to the limited molecular rotational freedom and steric constraints present within the dense solid-state environment, which inhibit efficient isomerization. Further insights into the photomechanical effect were gleaned from fluorescence studies. The emission spectra of the fragmented crystals exhibited a slight redshift, with the maxima shifting to λ_{max} = 476 nm (Figure 15). This shift is consistent with the formation of the cis-isomer during photoisomerization and supports the hypothesis of photoinduced molecular rearrangement. Achieving molecular isomerization or conformational changes in a solid medium, such as crystals or polymers, is inherently challenging due to the constrained free volume in these dense environments. However, this difficulty can be mitigated by designing molecules with functional groups that enable weak and reconfigurable supramolecular interactions. **DPAhydzOH** exemplifies such a design, as its weak hydrogen-bonding interactions allow for sufficient lattice adaptability to accommodate molecular rearrangement in response to external stimuli.

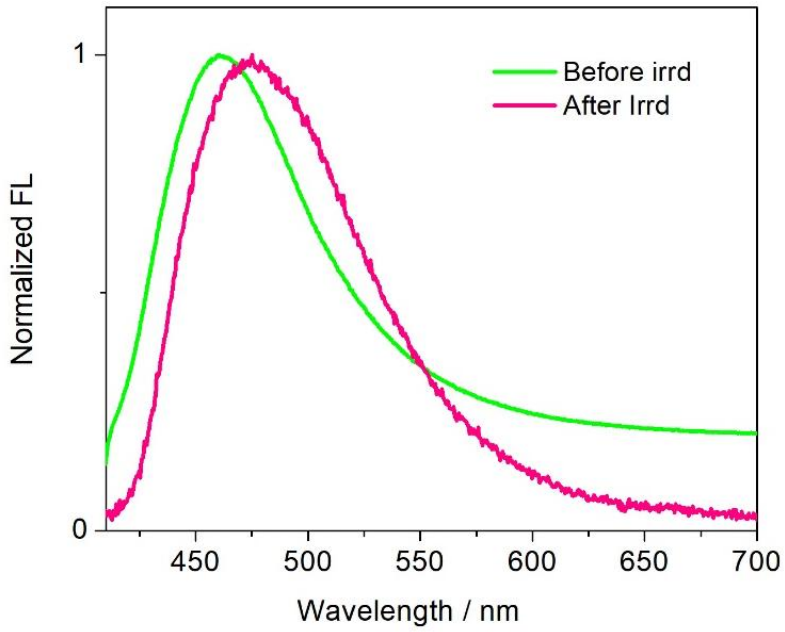

Figure 15. Emission spectra of the *trans*-**DPAHydrzOH** crystal before and after irradiation that leads to photomechanical cracking.

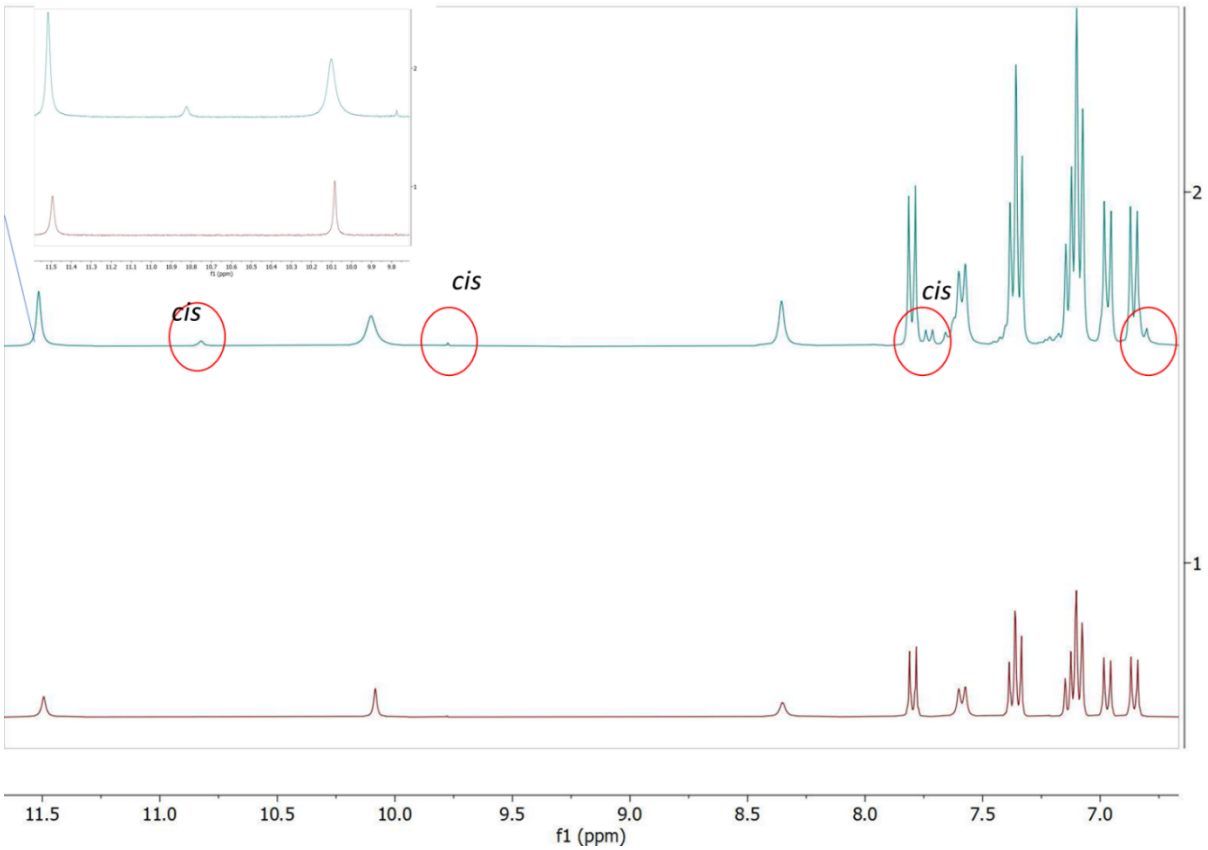

Figure 16. ^{1}H NMR spectra of the compound before and after irradiation with 365 nm light. The red circle denotes peaks from *cis*-**DPAHydrzOH** product.

The ability of **DPAhydzOH** crystals to undergo photoinduced structural changes demonstrates the material's potential for applications in smart technologies, including sensors, actuators, and light-responsive systems.

Overall, this study highlights the importance of rational molecular design in creating materials capable of dynamic responses to external stimuli. The photomechanical effects observed in **DPAhydzOH** provide a compelling framework for the development of advanced functional materials with tailored properties for next-generation applications.

3.4 Conclusion

In conclusion, we have successfully developed a synthetically accessible donor–acceptor type acylhydrazone derivative, **DPAhydrzOH,** which demonstrates exceptional multi-stimuli responsive properties. These include notable mechanochromic luminescence, thermochromic luminescence switching, and photomechanical effects in the solid state. The single-crystal X-ray diffraction analysis revealed that the trans-configuration of **DPAhydrzOH**, along with its non-planar molecular geometry and strong intermolecular interactions, plays a pivotal role in restricting non-radiative decay. This restriction contributes significantly to the bright cyan fluorescence observed in the solid crystals. Further investigations using structural analysis and ^{1}H NMR spectroscopy established that the photomechanical behavior under 390 nm light arises from a trans-to-cis isomerization of the C=N bond within the crystal lattice. On the other hand, the mechanochromic and thermochromic luminescence switching was attributed to stimuli-induced expulsion of lattice water molecules, followed by a reorganization of the molecular packing. These structural changes at the molecular and lattice levels are crucial for the observed stimuli-responsive properties. Such responsive materials offer immense potential for advancing sensor technology, including strain sensors, photo-sensors, and actuators for smart and adaptable devices. The study underscores the importance of rational molecular design and supramolecular engineering in creating versatile materials tailored for cutting-edge technological applications. This work lays the foundation for the future development of multi-functional materials that are not only innovative but also impactful in practical domains.

. ■ **REFERENCES**

1. P. Naumov, D.P. Karothu, E. Ahmed, L. Catalano, P. Commins, J.M. Halabi, M. B. Al-Handawi, L. Li, *J. Am. Chem. Soc*., 2020, **142**, 13256–13272.
2. L. Zhang, H. Liang, J. Jacob, P. Naumov, *Nat. Commun*., 2015, **6**, 7429.
3. P. Giri, A. Mazumder, D. Dey, S. Garani, A. Ravendran, M.K. Panda, *CrystEngcomm.*, 2021, **23**, 5876–5881.
4. M. K. Panda, R. Centore, M. Caus`a, A. Tuzi, F. Borbone, P. Naumov, *Sci. Rep*., 2016, **6**, 29610.
5. R. Medishetty, A. Husain, Z. Bai, T. Runˇ cevski, R.E. Dinnebier, P. Naumov, J. J. Vittal, *Angew. Chem. Int. Ed*., 2014, **53**, 1–6.
6. B. B. Rath, J. J. Vittal, *J. Am. Chem. Soc*., 2020, **142**, 20117–20123.
7. B. B. Rath, G. Gallo, R. E. Dinnebier, J. J. Vittal, *J. Am. Chem. Soc*., 2021, **143**, 2088–2096.
8. S. Ito, J. *Photochem. Photobiol. C: Photochem. Rev*., 2022, **51**, 100481.
9. Y. Sagara, T. Kato, *Angew. Chem*., 2011, **123**, 9294.
10. Y. Lv, Y. Liu, D. Guo, X. Ye, G. Liu, X. Tao, *Chem. Asian J*., 2014, **9,** 2885.
11. S. Nagai, M. Yamashita, T. Tachikawa, T. Ubukata, M. Asami, S. Ito, *J. Mater. Chem. C*., 2019, **7**, 4988.
12. Y. Lv, Y. Liu, X. Ye, G. Liu, X. Tao, *CrystEngComm*., 2015, **17**, 526.
13. S. Yagai, T. Seki, H. Aonuma, K. Kawaguchi, T. Karatsu, T. Okura, A. Sakon, H. Uekusa, H. Ito, *Chem. Mater*., 2016, **28**, 234.
14. P. Xue, J. Ding, P. Wang, R. Lu, *J. Mater. Chem. C*., 2016, **4**, 6688.
15. G. Zhang, J. Sun, P. Xue, Z. Zhang, P. Gong, J. Peng, R. Lu, *J. Mater. Chem. C*., 2015, **3**, 2925.
16. Y. Shu, J. Sun, Y. Yue, K. Ye, R. Lu, *Chemphotochem*., 2022, **6**, 202200006.
17. H. Koshima, H. Uchimoto, T. Taniguchi, J. Nakamura, T. Asahib, T. Asahiac, *CrystEngComm*., 2016, **18** 7305–7310.
18. K. Morimoto, D. Kitagawa, F. Tong, K. Chalek, L. J. Mueller, C. J. Bardeen, S. Kobatake, *Angew Chemie Int Ed*., 2022, **61**, 202114089.
19. K. Yadava, J.J. Vittal, *Cryst. Growth Des*., 2019, **19**, 2542–2547.
20. Yi-X Shi, W. H. Zhang, B. F. Abrahams, J. P. Lang, *Angew. Chem. Int. Ed*., 2019, **58**, 9453–9458.
21. S. Li, B. Lu, X. Fang, D. Yan, *Angew Chem Int Ed*, 2020, **59**, 22623–22630.

22. H. Wang, P. Chen, Z. Wu, J. Zhao, J. Sun, R. Lu, *Angew Chem Int Ed.*, 2017, **56**, 9463–9467.
23. X. Ma, P. Li, J. Wang, M. Yin, Y. Zhang, *Cryst. Growth Des*., 2022, **22**, 4133–4138.
24. P. Giri, A. Panda, M.K. Panda, *Chem. Eur. J*., 2024, **30**, 3836.
25. S. Khan, B. Dutta, S. Naaz, B. Choudhury, P.A. Cazade, E. Kiely, S. Guerin, R. Medishetty, M.H. Mir, *Commun Chem*, 2023, 150.
26. T. Panda, D. Maiti, M.K. Panda, *ACS Appl. Mater. Interfaces*., 2018, **10**, 29100.
27. D. Dey, P. Giri, N. Sepay, A. Husain, M.K. Panda, *Journal of Photochem, Photobiol, A: Chemistry.*, 2023, **437**, 114480.
28. M. K. Panda, T. Panda, P. Asha, A. P. Prakasham, *CrystEngComm*., 2018, **20**, 6046–6053.
29. A. Adak, T. Panda, A. Raveendran, K. S. Bejoymohandas, K.S. Asha, A. P. Prakasham, B. Mukhopadhyay, M.K. Panda, *ACS Omega*., 2018, **3,** 5291–5300.
30. K. Zheng, F. Ni, Z. Chen, C. Zhong, C. Yang, *Angew. Chem. Int. Ed*, 2020, **59**, 9972.
31. S. Jindal, G. Anjum, V.K. Maka, J.N. Moorthy, *Nanoscale*, 2021, **13**, 9668–9677.
32. L. Wen, J. Sun, C. Li, C. Zhu, X. Zhang, Z. Wang, Q. Song, C. Lv, Y. Zhang, *New J. Chem.* 2021, **45**, 11530.
33. Y. Huang, L. Ning, X. Zhang, Q. Zhou, Q. Gong, Q. Zhang, *Chem. Soc. Rev*. 2024, **53**, 1090–1166.
34. P. Shi, R. Zhao, M. Zhang, M. Lin, Y. Duan, T. Han, *Mater. Lett*. 2019, **243**, 38.
35. S. Nakamura, K. Okubo, Y. Nishii, K. Hirano, N. Tohnai, M. Miura, *J. Mater. Chem. C*, 2024, **12**, 2370–2378.
36. Z. Li, X. Wang, L. Han, C. Zhu, H. Xin, Y. Yin, *Adv. Mater*. 2022, **34**, 2107398.
37. J. J. Liu, S. B. Xia, T. Liu, J.M. Liub, F. X. Cheng, *CrystEngComm.*, 2021, **23**, 4320.
38. APEX3, version 2017.3-0, and SAINT, version 8.38A, Bruker AXS Inc., Madison, WI, 2012, URL: https://www.bruker.com.
39. G. M. Sheldrick, SADABS, University of G¨oettingen, G¨ oettingen, Germany, 1996 (part of Bruker APEX3 software package (version 2017.3-0): Bruker AXS, 2017).
40. G. M, Sheldrick, SHELXTL XT – Crystal Structure Solution, version 2014/4, Bruker AXS, 2010-2014.
41. G.M. Sheldrick, SHELXL2014, University of G¨oettingen, Germany, 2014.
42. G.M. Sheldrick, *Acta Crystallogr. A*, 2015, **71**, 3–8.
43. G.M. Sheldrick, *Acta Crystallogr. A*, 2008, **64**, 112–122.
44. Gaussian 16, Revision B.01, M. J. Frisch, G. W. Trucks, H. B. Schlegel, G. E.

Scuseria, M. A. Robb, J. R. Cheeseman, G. Scalmani, V. Barone, G. A. Petersson, H. Nakatsuji, X. Li, M. Caricato, A. V. Marenich, J. Bloino, B. G. Janesko, R. Gomperts, B. Mennucci, H. P. Hratchian, J. V. Ortiz, A. F. Izmaylov, J. L. Sonnenberg, D. Williams-Young, F. Ding, F. Lipparini, F. Egidi, J. Goings, B. Peng, A. Petrone, T. Henderson, D. Ranasinghe, V. G. Zakrzewski, J. Gao, N. Rega, G. Zheng, W. Liang, M. Hada, M. Ehara, K. Toyota, R. Fukuda, J. Hasegawa, M. Ishida, T. Nakajima, Y. Honda, O. Kitao, H. Nakai, T. Vreven, K. Throssell, J. A. Montgomery, J. E. Peralta, F. Ogliaro, M. J. Bearpark, J. J. Heyd, E. N. Brothers, K. N. Kudin, V. N. Staroverov, T. A. Keith, R. Kobayashi, J. Normand, K. Raghavachari, A. P. Rendell, J. C. Burant, S. S. Iyengar, J. Tomasi, M. Cossi, J. M. Millam, M. Klene, C. Adamo, R. Cammi, J. W. Ochterski, R. L. Martin, K. Morokuma, O. Farkas, J. B. Foresman, D. J. Fox, Gaussian, Inc., Wallingford CT, 2016.

CHAPTER-4

Fluorescence Switching in the Solid State Using Functionalized Cyanovinyl Molecules: Synthesis, Computational Insights, and Applications in Secure Data Encryption and Tagging

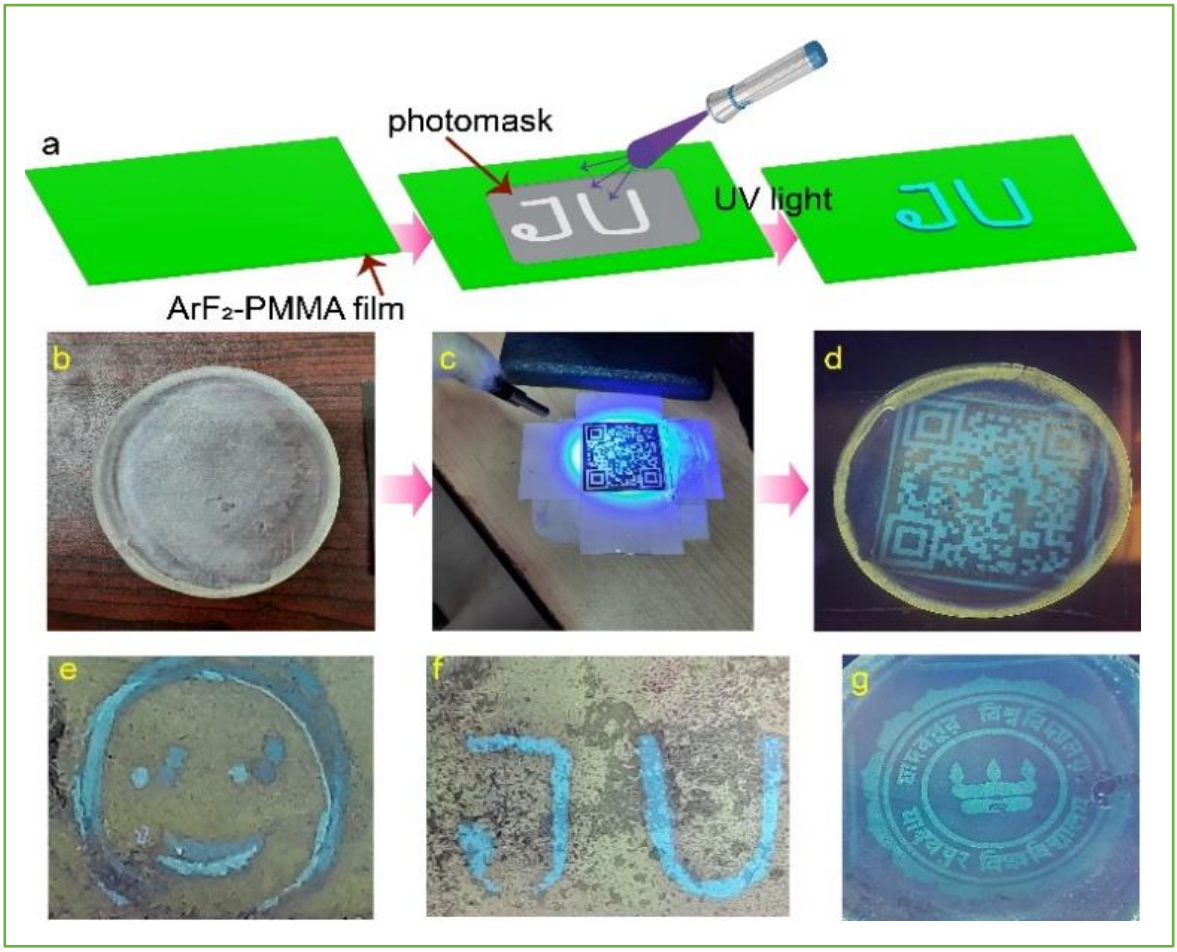

Fluorescence Switching in the Solid State Using Functionalized Cyanovinyl Molecules: Synthesis, Computational Insights, and Applications in Secure Data Encryption and Tagging

4.1 Introduction

In this study, we present cyanovinyl-based luminogens[1-5], **ArF_2** and **$ArCF_3$**, that display remarkable photo-switching behavior in the solid state when exposed to ultraviolet (UV) light. These compounds showcase a unique luminescence switching mechanism, which is drastically influenced by the nature of substituents on the cyanovinyl core. Specifically, altering the substitution from fluorine (-F) in **ArF_2** to trifluoromethyl (**$-CF_3$**) in **$ArCF_3$** produces opposite luminescence responses in the solid state. When crystals of **ArF_2** are illuminated with UV light at 365 nm, the emission color shifts dramatically from green to cyan. Conversely, the crystals of **$ArCF_3$** undergo a distinct transformation from cyan to greenish-yellow emission under the same conditions. This phenomenon of opposing luminescence switching behavior is exceptionally rare in solid-state systems and holds great promise for future technological applications. Utilizing a combination of analytical techniques, including NMR spectroscopy, IR spectroscopy, UV-Vis absorption studies, and computational methods, we investigated the underlying mechanisms responsible for this unique photo-switching behaviour.[6-7] The results indicate that the behavior arises from photoinduced geometric changes such as E/Z isomerization and [2+2] cycloaddition reactions, along with accompanying packing rearrangements in the crystalline lattice. To demonstrate the practicality of these materials, we successfully employed them in photolithographic writing and secret encoding applications. These findings underline the significance of such responsive materials in advancing light-sensitive technologies and their potential integration into innovative systems for data storage, encryption, and optical devices. In recent years, solid-state photoluminescent materials have garnered significant interest due to their wide-ranging applications in light-emitting diodes (LEDs), optical sensors, lasers, and other photonic technologies.[8-10] The remarkable optical properties of these materials are predominantly influenced by their molecular packing arrangements, which are governed by various intermolecular interactions such as π-π stacking, hydrogen bonding, halogen bonding, and other non-covalent interactions. By leveraging external stimuli—such as light, heat, mechanical pressure, or humidity. It is possible to modulate their photoluminescent behavior. This modulation stems from structural changes facilitated by the reconfiguration of these non-covalent interactions. Among these stimuli, light

stands out as a readily accessible and highly tunable option for manipulating the luminescent properties of materials. These light-responsive materials hold immense importance in both fundamental research and technological applications, including tunable lasers, optical waveguiding, solar energy storage, imaging, encoding, data authentication, and tagging [11-17].

Photo-switching materials represent a rare and fascinating class of solids capable of undergoing structural transformations that result in concurrent changes in absorbance or luminescence behavior upon exposure to light.[18-20] Typically, such photo-switching phenomena occur via mechanisms like trans-to-cis isomerization, ring-opening and closing reactions, or proton transfer reactions. These processes are generally more feasible in solution-phase environments due to the larger free volume available for molecular movements. Numerous examples, including azobenzenes, spiropyrans, diarylethenes, fulgides, and others, have been reported to exhibit photo-switching behavior in solution.[21-30] However, despite substantial efforts in developing these photochromic molecules, their practical real-world applications face challenges such as complex multistep synthesis and purification, limited cost-effectiveness, lack of solid-state photo-switching properties, insufficient photo-conversion efficiencies, and poor photostability. Theoretical and computational modelling of photo-switching behavior in solid-state materials has also posed significant challenges due to the intricate interplay of multiple degrees of freedom and the complexities in describing excited-state relaxation processes in condensed-phase environments. Notable attempts, such as modelling crystalochromic [31] materials and exploring conical intersections (CIs) [32-33] in organic molecular crystals, have advanced the understanding of solid-state photophysics and photochemistry. Similarly, efforts to model the mechano-fluorochromic[34] properties of difluoroboron β-diketonates have provided insights into the responsive behavior of such systems.

Despite these advances, achieving photo-switching optical properties in densely packed solid platforms, such as single crystals or polymer matrices, remains particularly challenging. The primary obstacle lies in the limited free volume within these tightly packed environments and the constraints imposed by various intermolecular non-covalent interactions, which inhibit molecular reconfiguration or conformational changes. Addressing these challenges requires the rational design of new molecular systems equipped with photo-active functional groups[35-38] and capable of overcoming these limitations. Solid-state photo-switchable materials with superior properties have the potential to drive innovation across a broad spectrum of

technological applications, and the development of such systems remains a highly sought-after goal in the field.[39-45]

4.2 Experimental

4.2.1. Materials & methods

Materials: The study utilized 4-Acetamido-benzaldehyde and Potassium tert-Butoxide procured from Sigma-Aldrich, employed without additional purification. 3,5-Difluorobenzyl cyanide and 3,5-Bis(trifluoromethyl)phenylacetonitrile were obtained from TCI India and used as received. Tetrabutylammonium hydroxide (TBAH) was purchased from Spectrochem. ACS-grade solvents from Merck were employed for synthesis, while spectroscopy-grade solvents were utilized for spectroscopy studies. The compound **ArF$_2$**, synthesized and comprehensively characterized in a previous report, served as a crucial reagent.

Instruments and Methods: The analysis of nuclear magnetic resonance (NMR) spectra for ^{1}H (300 MHz) and ^{13}C (75 MHz) was performed using Bruker ASCENDTM 500 and Bruker DPX 300 MHz spectrometers, with D6-DMSO as the solvent. Chemical shifts (δ) were recorded in ppm, referenced against tetramethylsilane ($Si(CH_3)_4$) as the standard. High-resolution mass spectra (HRMS) of the compound were generated using the QTOF Micro YA263 mass spectrometer in electrospray ionization (ESI) mode.

UV-Vis and Fluorescence: Solution and solid-state UV-Vis absorption spectra were recorded with a Shimadzu UV-2401C spectrophotometer. Solid-state emission spectra of the crystal samples were obtained using a Horiba Jobin Yvon Fluoromax-4 Spectrofluorometer. Crystals were fixed on a quartz plate with non-fluorescent grease for UV-Vis studies and recorded in front-face mode. For fluorescence studies, **E-ArF$_2$** and **ArCF$_3$** crystals were sandwiched between glass plates inside the sample holder, ensuring optimal data collection.

IR Study: Infrared spectra were recorded using a PerkinElmer LX-1 FT-IR Spectrometer to examine vibrational modes within the samples.

Scanning Electron Microscopy (SEM): SEM images were captured using an FEI INSPECT F50 instrument at 5 kV energy. Samples were prepared by gold-coating to enhance image clarity. This detailed approach reflects the rigorous methodology employed in this study, providing robust characterization of the materials and their properties.

DFT with Localized Basis Set: Density Functional Theory (DFT) calculations were conducted using Orca 5.0.2 software, leveraging the wB97X-D3BJ functional paired with the def2-TVZP basis set to ensure computational efficiency and accuracy. Time-Dependent DFT (TD-DFT) studies employed the default level of approximation, utilizing the TDA and RI approaches without incorporating additional keywords.

Periodic DFT Simulations: Plane-wave DFT calculations were performed using Quantum Espresso software, implementing GBRV pseudopotentials and the vdW-DF-cx exchange-correlation functional, which is particularly suited for systems of this nature. A plane-wave basis set cutoff of 600 eV was utilized, with sampling of the first Brillouin zone carried out using the Monkhorst–Pack k-point mesh method. Experimental XRD coordinates were optimized using the BFGS algorithm—initially with cell parameters fixed to match experimental conditions. For the specific systems studied, including those containing one cyclodimer and one **ArF$_2$**-Z molecule, manual adjustments were applied to prepare input configurations for relaxation processes.

4.2.2 Synthesis & Characterizations:

General synthetic Procedure of ArF$_2$/ArCF$_3$

ArCF$_3$ was synthesized following the similar procedure as reported for **ArF$_2$**.[39] 4-Acetamidobenzaldehyde (0.091g, 5.6×10^{4}mol), 3,5 Bis (trifluromethyl)phenylacetonitrile (0.1 ml, 5.6×10^4 mol), K^+ ^{t}BuO$^-$ (0.094g, 8.4×10^4 mol), TBAH (0.9ml ,8.4×10^4 mol) were mixed with stirring and the resulting mixture was heated at 65 ºC temperature for 5 hours. The precipitate formed was filtered and washed with methanol (5 x 10 mL) and finally dried in air to obtain product as white solid (Yield 0.121 g, 75 %, Scheme 1).

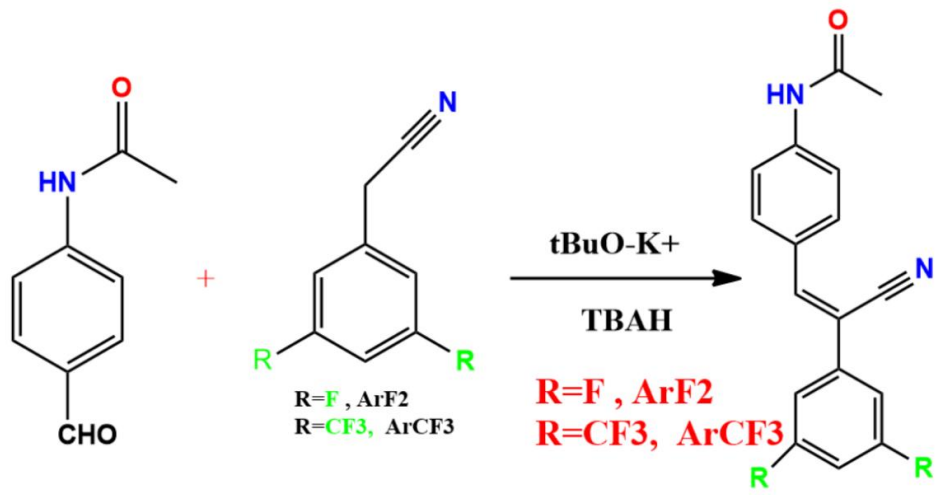

Scheme 1. General synthetic Procedure of **ArF_2/$ArCF_3$**

^{1}H NMR (500 MHz, CDCl3): 10.35 (s, 1H, CONH), 8.34 (d, 3H, J= 8Hz, ArH), 8.33 (s), 8.18 (s, 1H, ArH), 8.00 (d, 2H, ArH), 7.79 (d, 2H, J= 8Hz, ArH), 2.11 (s, 3H, CH_3).

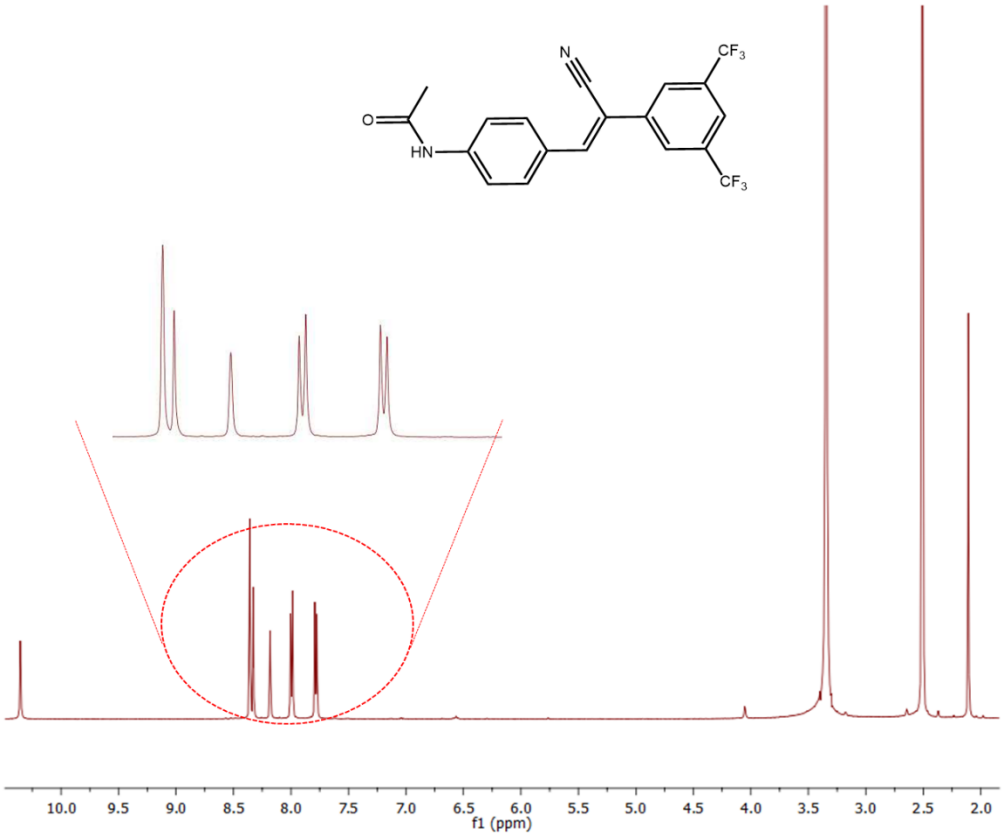

Figure 1. ^{1}H NMR spectra of **$ArCF_3$** in $CDCl_3$

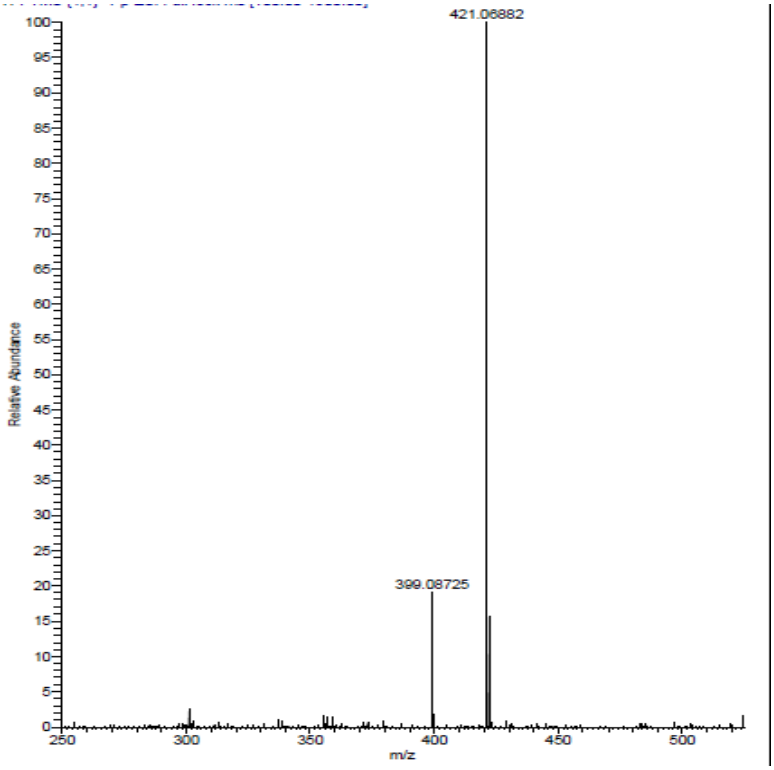

Figure 2. Mass spectra of **ArCF$_3$** showing M+1 peak at 399.08725.

HRMS: calculated for $C_{19}H_{12}F_6N_2O$ is 398.0854, obtained 399.0873 (M+1).

Preparation of ArF$_2$-PMMA and ArCF$_3$-PMMA film:

In a typical procedure, 100 mg of PMMA powder was added to 5 mL of DMF and the solution was heated to 80 C with stirring till a clear slurry was obtained. After that a DMF solution of 5 mg of **ArF$_2$** or **ArCF$_3$** was added to the PMMA slurry and stirred at 80 ºC for 30 minutes. The resultant clear slurry mixture was poured in a Petridish and kept undisturbed at room temperature for 7-8 days to form the film. The film was then peeled out and cut into required size and shape for experiments.

4.3. Results and discussions: The compound **ArF$_2$** was previously synthesized and characterized as described in an earlier report (Ref. 39). On the other hand, the synthesis of **ArCF$_3$** was achieved through a Knoevenagel condensation reaction. This involved the reaction of 4-[Bis(4-methoxyphenyl)-amino]benzaldehyde with 3,5-Bis(trifluoromethyl)-phenyl acetonitrile, using potassium tert-butoxide as a base (outlined in Scheme 1). Comprehensive characterization of all the synthesized compounds was carried out, employing techniques such as ^{1}H NMR, ^{13}C NMR, and mass spectrometry, with detailed data available in figures 1-4.

4.3.1 Photophysical studies in solution: The UV-Vis spectroscopic analysis of **ArF_2** in DMF solution (1×10^{-5} M) reveals a significant absorption band with a maximum peak at λ_{max} = 355 nm. Comparatively, the compound **$ArCF_3$** under identical experimental conditions exhibits a similar absorption band with λ_{max} = 356 nm (Figure 4d). Notably, when **ArF_2** is subjected to gradual irradiation using light at 390 nm, the primary absorption band centered at 355 nm undergoes a steady decrease, accompanied by the appearance of a new blue-shifted band peaking at λ_{max} = 335 nm. This spectral shift is indicative of a photo-induced E- to Z-isomerization process. The presence of a distinct isosbestic point at 335 nm serves as evidence that the transformation involves only two components, the E- and Z- isomers (Figure 3b).

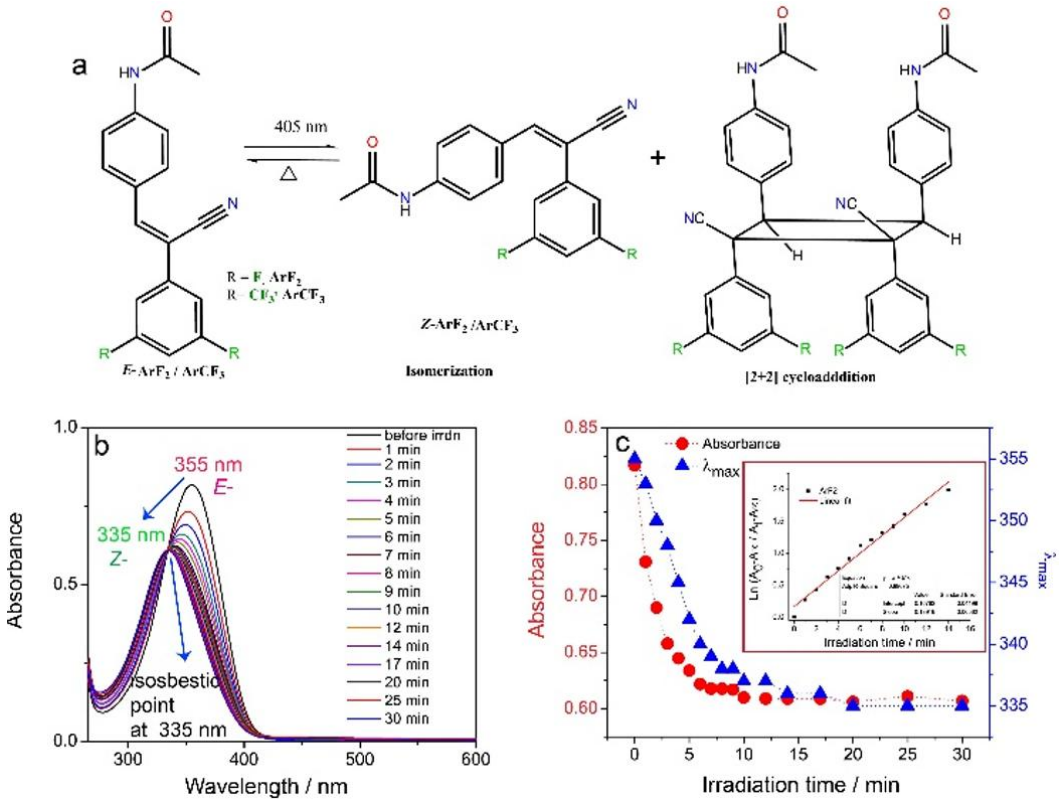

Figure 3. (a) Schematic representation of the photoreaction occurring in **ArF_2/$ArCF_3$** crystals, (b) Absorption spectra of **ArF_2** (DMF solution 1 x 10^{-5} M) upon exposure to 390 nm light, (c) Changes in absorbance with irradiation time.

Upon prolonged irradiation, a photo-stationary state is achieved after 15 minutes, as no further Changes in absorbance are observed. The kinetic analysis of the E- to Z- isomerization process, derived from the plot of ln $[(A_0 - A\infty)/(A_t - A\infty)]$ versus irradiation time (Figure 3c), yields a rate constant of 0.139 min^{-1} (Figure 3c and Figure 7). Similar observations of absorbance changes are evident for **$ArCF_3$** during irradiation experiments (Figure 4d).

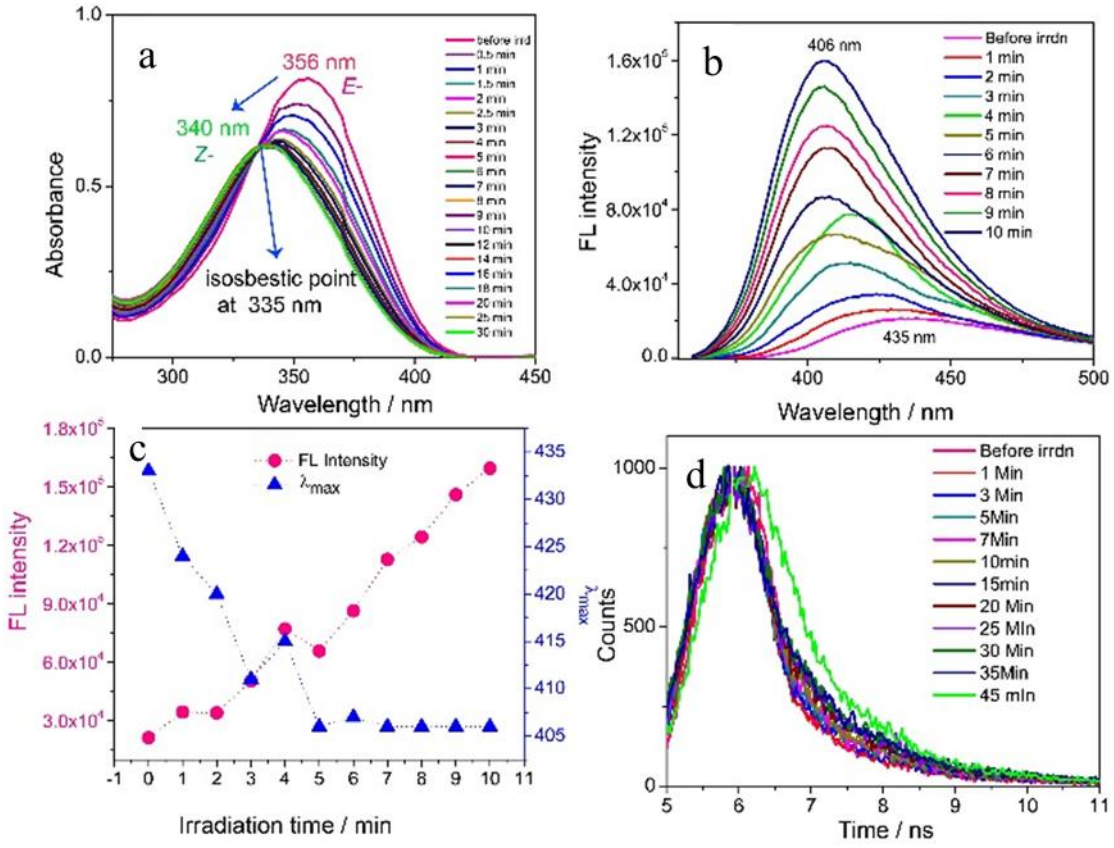

Figure 4. (a) Absorption spectra of **$ArCF_3$** (DMF solution 1 x 10^{-5} M) upon exposure to 390 nm light, (b) Changes in emission spectra of **ArF_2** (in DMF) upon exposure to 390 nm light, (c) Changes in fluorescence intensity and l_{max} with illumination time (for **ArF_2**), (d) Time resolved fluorescence of **ArF_2** (in DMF solution) upon illumination with 390 nm light.

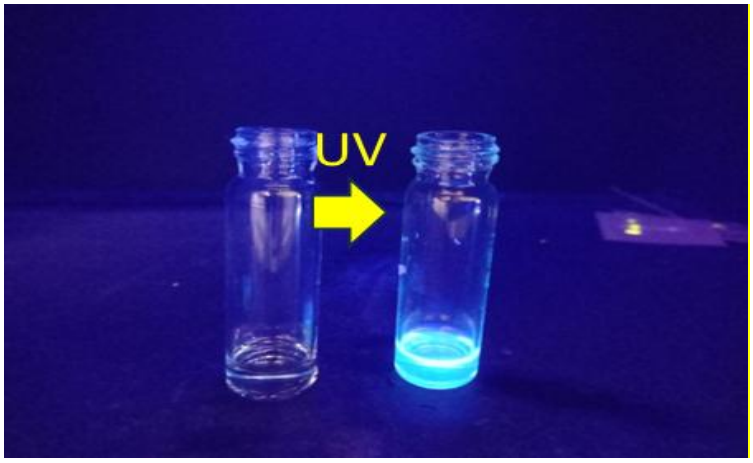

Figure 5. Fluorescence emission of **ArF_2** solution (DMF) before and after irradiation. Image was taken under 365 UV chamber.

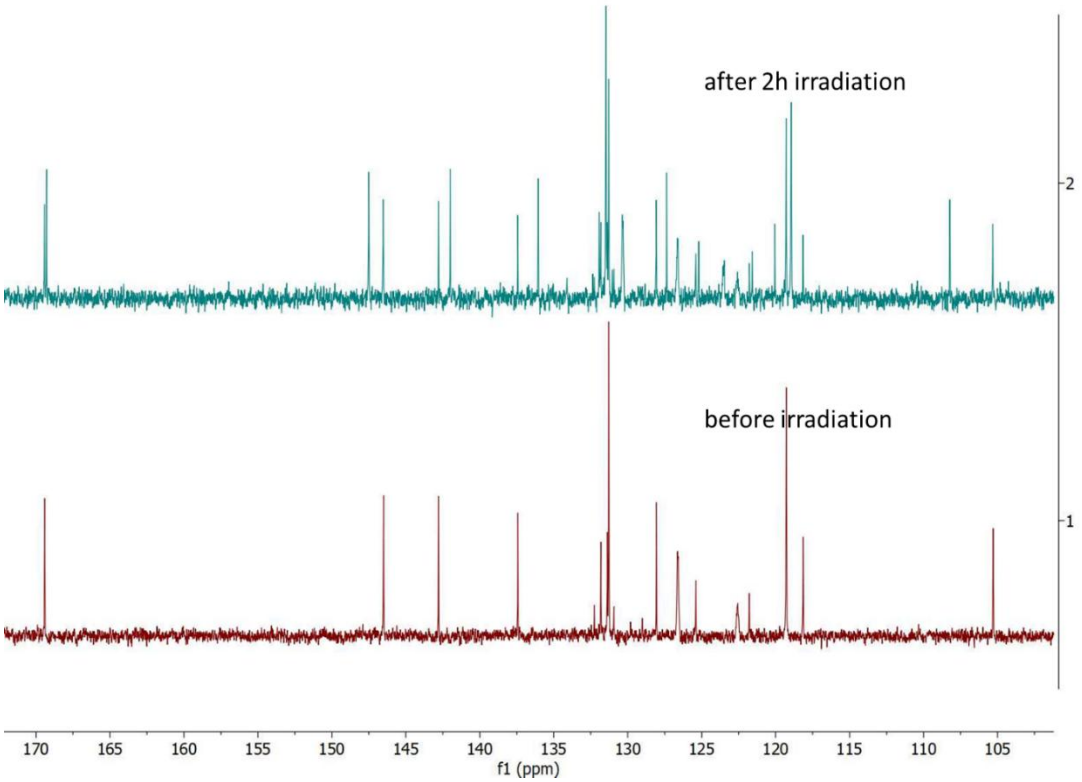

Figure 6. ^{13}C NMR spectra of **ArCF$_3$** in DMSO-d_6 before and after UV irradiation.

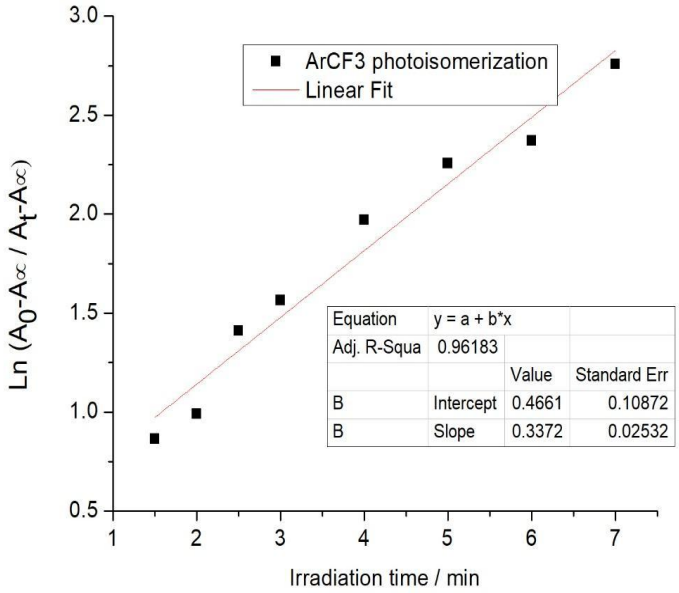

Figure 7. Linear fit plot of Ln (A0-A∞ / At-A∞) vs irradiation time (min) for the calculation of rate constant (K = 0.337 min-1) for E- to Z- isomerization of **ArCF$_3$** solution in DMF.

In terms of fluorescence properties, **ArF$_2$** demonstrates minimal emission in solution phase (in solvents such as methanol, THF, DMF, DMSO) and does not exhibit visible fluorescence when viewed under UV light with the naked eye (Figure 5). However, fluorescence spectral studies reveal that **ArF$_2$** in DMF solution (1×10^{-5} M) emits a broad band with $\lambda_{em,max}$ at 435 nm. With continuous illumination under 365 nm light, the intensity of the emission steadily increases, accompanied by a notable blue shift of $\lambda_{em,max}$ to 406 nm. This enhancement in fluorescence is attributed to the photo-induced transition from *E*- to *Z*- isomerization, which occurs rapidly due to conformational and rotational flexibility inherent to the solution phase. As depicted in Figure 4f, the fluorescence intensity progressively intensifies with irradiation, while $\lambda_{em,max}$ undergoes gradual blue-shifting with increasing exposure time. Interestingly, the photoconverted cyan emissive solution becomes distinctly visible to the naked eye (Figure 5) under UV light at 365 nm, with a quantum yield (ϕ) value of 0.12. Attempts to reverse the Z- to E- isomerization by applying heat or visible light were unsuccessful, although slight fading of emission color was observed when the solution was heated. Time-resolved fluorescence spectroscopy of ***E*-ArF$_2$** solutions in DMF showcases a gradual increase in lifetime values (Table 1), consistent with the ongoing photo-induced transition from E- to Z- isomerization.

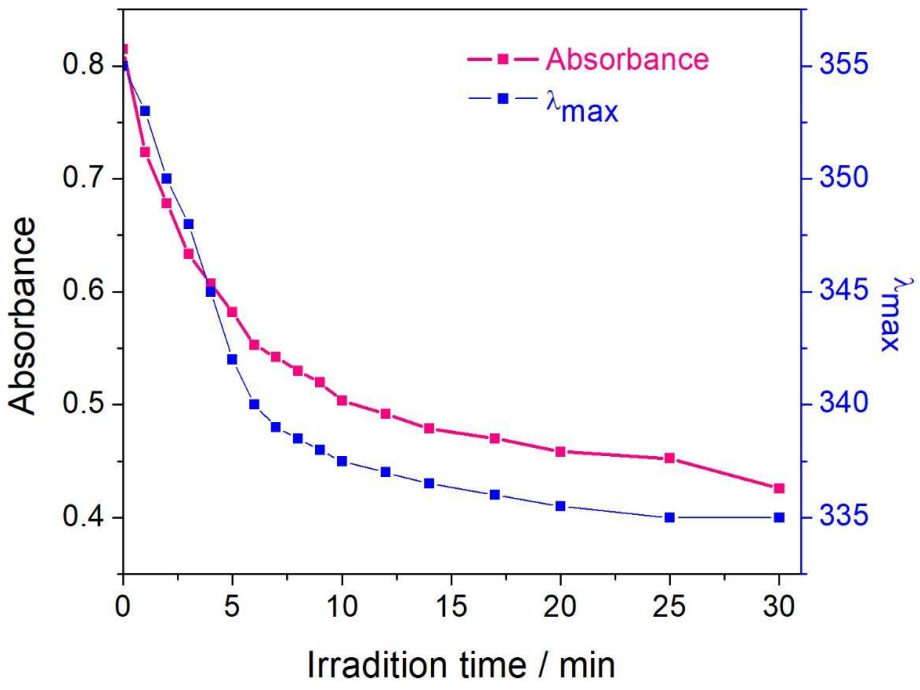

Figure 8. Plot of absorbance vs irradiation time and λ_{max} vs irradiation time of **ArCF$_3$** (DMF, 1 x10^{-5} M)

Similarly, the compound **ArCF$_3$** undergoes E- to Z- isomerization in solution, evident from the rise of a new band at 340 nm in UV-Vis spectra (Figure 4d). However, its fluorescence enhancement is less pronounced, with $\lambda_{em,max}$ observed at 450 nm (Figure 9). The limited fluorescence response is attributed to the structural properties of **ArCF$_3$**, specifically the high rotational and conformational freedom of the **C-CF$_3$** bonds. Such flexibility is known to facilitate non-radiative decay processes in the excited state, thereby reducing the overall radiative decay efficiency.

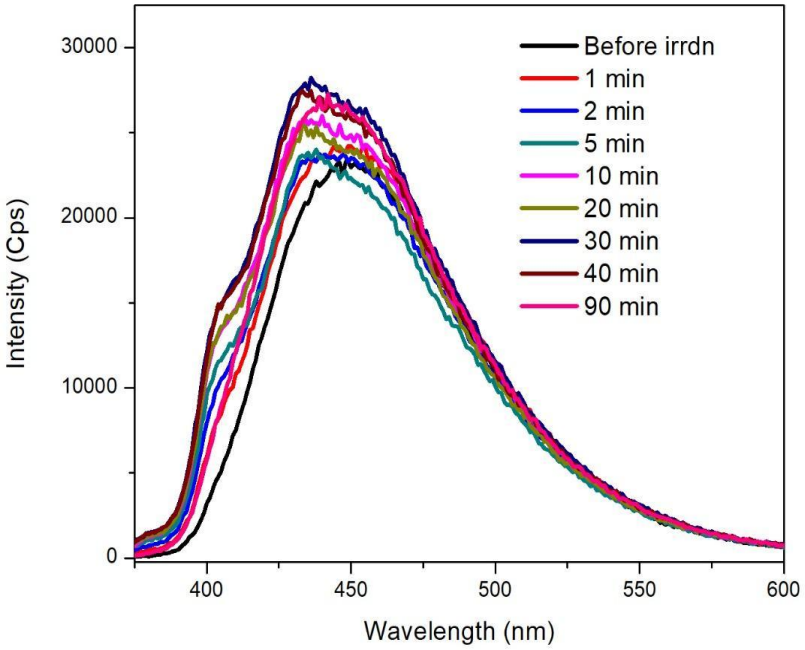

Figure 9. Fluorescence emission change of **ArCF$_3$** (DMF, 1 x 10^{-6} M) upon 405 nm illumination**.**

Table 1. Quantum yield (QY) of the **ArF$_2$** crystals (solid state)

Compound	**Fluorescence maxima**	**QY / %**
ArF$_2$ in DMF	No visible fluorescence	-
ArF$_2$-Green emissive crystal	$\lambda_{em,max}$ = 525 nm	0.24
ArF$_2$-Cyan emissive crystal	$\lambda_{em,max}$ = 490 nm	0.15

Table 2. Fluorescence life time values of **ArF_2**

Samples in DMF solution	**Fluorescence Life time values, τ (ns)**
ArF_2 (0 Min) λ_{ex} = 355nm, λ_{em} = 430 nm	τ_1 = 0.154 ± 0.02 (66.23 %) τ_2 = 1.239 ± 0.02 (33.77 %) χ^2 = 0.9804704
ArF_2 (1 Min) λ_{ex} = 355nm, λ_{em} = 430 nm	τ_1 = 0.183 ± 0.021 (66.36 %) τ_2 = 1.279 ± 0.022 (33.64 %) χ^2 = 0.9730512
ArF_2 (3 Min) λ_{ex} = 355nm, λ_{em} = 430 nm	τ_1 = 0.255 ± 0.027 (60.24 %) τ_2 = 1.346 ± 0.021 (39.76 %) χ^2 = 1.038844
ArF_2 (7 Min) λ_{ex} = 355nm, λ_{em} = 430 nm	τ_1 = 0.295 ± 0.026 (59.06 %) τ_2 = 1.493 ± 0.024 (40.94 %) χ^2 = 1.014237
ArF_2 (10 Min) λ_{ex} = 355nm, λ_{em} = 430 nm	τ_1 = 0.532 ± 0.03 (72.99 %) τ_2 = 1.859 ± 0.042 (27.01 %) χ^2 = 1.035743
ArF_2 (15 Min) λ_{ex} = 355nm, λ_{em} = 430 nm	τ_1 = 0.797 ± 0.017 (81.86 %) τ_2 = 2.62 ± 0.076 (18.14 %) χ^2 = 0.9913272
ArF_2 (25 Min) λ_{ex} = 355 nm, λ_{em} = 430 nm	τ_1 = 0.848 ± 0.017 (83.82 %) τ_2 = 2.951 ± 0.088 (16.18%) χ^2 = 0.9676779
ArF_2 (30 Min) λ_{ex} = 355 nm, λ_{em} = 430 nm	τ_1 = 0.869 ± 0.016 (83.45 %) τ_2 = 3.023 ± 0.919 (16.55%) χ^2 = 0.9709448

Table 3. Fluorescence life time values for **$ArCF_3$**

Samples	**Fluorescence Life time values, τ (ns)**
$ArCF_3$ DMF Solution (before irradiation) λ_{ex} = 355nm, λ_{em} = 450 nm	τ_1 = 0.072 ± 0.017 (24.6%) τ_2 = 0.071 ± 0.017 (75.4%) χ^2 = 1.134312
$ArCF_3$ DMF solution (After irradiation) λ_{ex} = 355nm, λ_{em} = 450 nm	τ_1 = 0.021 ± 0.008 (96.04 %) τ_2 = 1.22 ± 0.069 (3.96 %) χ^2 = 1.074042

4.3.2 Solid-State Optical Properties: Both **ArF_2** and **$ArCF_3$** exhibit intriguing solid-state fluorescence characteristics that can be tuned through light irradiation, presenting a stark contrast to their solution-state optical behaviors. For instance, while the DMF solution of *E*-**ArF_2** does not show visible emission under a UV lamp, the crystals grown from this solution display bright green fluorescence. Previously, it was reported that **ArF_2** crystals exhibit fascinating photomechanical behavior when subjected to UV illumination, driven by *E/Z* isomerization and topochemical [2+2] cycloaddition reactions. Expanding on this, the current study observed that these crystals also undergo fluorescence color changes upon prolonged exposure to UV light. Specifically, when a millimeter-sized block-shaped crystal of **E-ArF_2** (dimensions approximately 1 mm × 0.03 mm × 0.02 mm) was fixed onto a glass slide to prevent actuation (which could result in focus loss under a microscope) and irradiated with 365 nm UV light under a fluorescence microscope, the bright green emission ($\lambda_{em,max}$ = 525 nm, ϕ = 0.21, (Table 2) gradually shifted to cyan emission ($\lambda_{em,max}$ = 467 nm, ϕ = 0.15, (Figure 10a, 10d, Table 2). Similarly, thin acicular-shaped crystals displayed a comparable transition, with their bright green fluorescence fading into cyan, alongside a noticeable reduction in intensity (Figure 10b). It was observed that the rate of this color transformation directly correlates with the intensity of the incident light. Notably, thicker and larger crystals exhibited slower emission changes compared to thinner ones, likely due to limited light penetration in bulkier structures. These solid-state emission changes are primarily attributed to E/Z isomerization and the [2+2] cycloaddition reaction occurring within the crystal lattice. Interestingly, the photoconverted cyan-emissive **ArF_2** crystals could be reverted to their original green-emissive state by heating at 100 °C for 14 hours, driven by thermally induced back reactions (Figure 11).

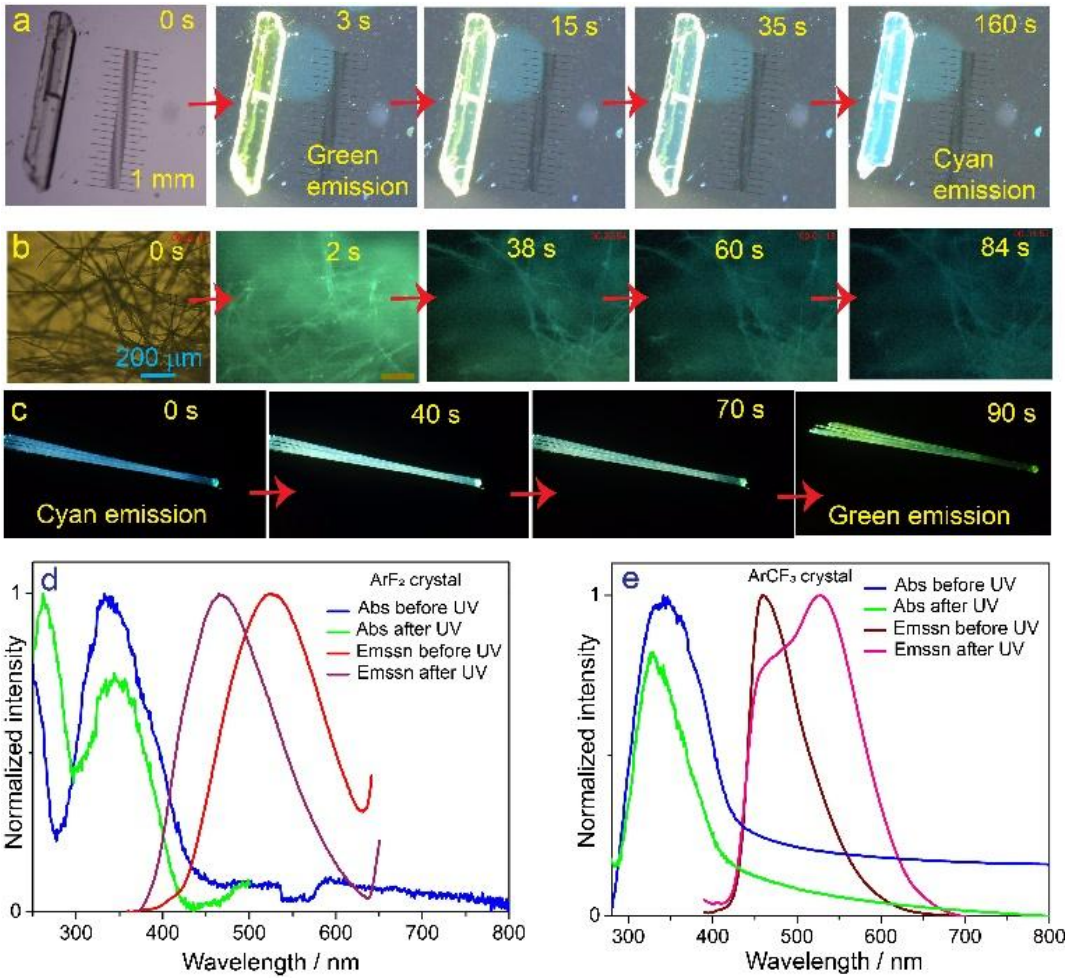

Figure 10. (a) Snapshots of the millimetre shaped **ArF_2** crystal during photo-switching event, (b) snapshots of the thin fibre shaped **ArF_2** crystal during photo-switching event (c) snapshots of the millimeter shaped **$ArCF_3$** crystal during photo-switching event, (d) Solid state fluorescence spectra of **ArF_2** before and after irradiation, (e) Solid state fluorescence spectra of **$ArCF_3$** before and after irradiation.

In contrast, pristine ***E*-$ArCF_3$** crystals exhibit cyan fluorescence ($\lambda_{em,max}$ = 460 nm, ϕ = 0.09, Figure 10e, Table 2). Upon UV irradiation at 365 nm, these crystals rapidly change their emission to a greenish-yellow color ($\lambda_{em,max}$ = 527 nm, ϕ = 0.23), a transformation attributed to photoisomerization and cycloaddition reactions within the lattice. Remarkably, thermal heating of the green-emissive photoconverted **$ArCF_3$** crystals at 100 °C for 3 hours restored their original cyan fluorescence (Figure 11b). This highlights the ability to achieve completely opposite photo-induced luminescence switching behaviors in these solid organic crystals by merely substituting a fluorine atom with a trifluoromethyl (**-CF_3**) group. To date, such molecular systems demonstrating this level of tunable luminescence are rare and represent a

unique advancement in the field. This detailed discussion highlights the novel and contrasting luminescence behaviors of **ArF_2** and **$ArCF_3$** crystals in the solid state.

The solid-state physical properties, particularly the optical characteristics of materials, are significantly influenced by the molecular packing arrangement and intermolecular interactions within the crystal lattice. To explore the mechanism behind fluorescence color switching, detailed structural insights were derived from the single crystal structure of **ArF_2**, which had been previously reported (CCDC No. 2075638).

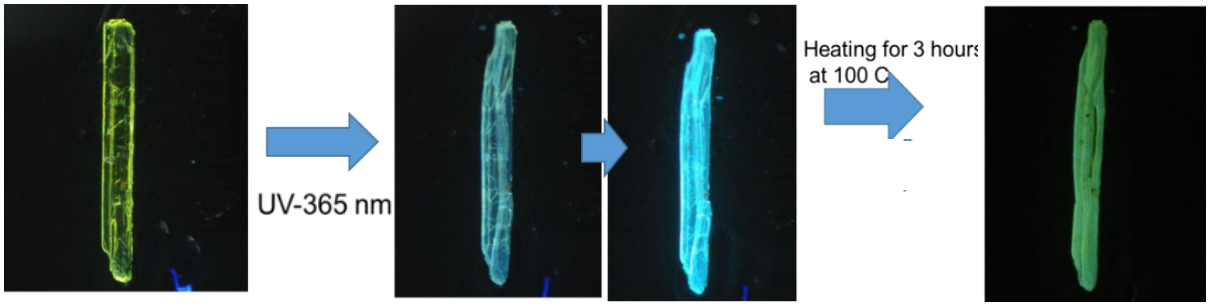

Figure 11a: Snapshots of **ArF_2** crystal during irradiation to cyan emissive crystal followed by thermal heating to the original green emissive crystal.

Conformational analysis of the **ArF_2** molecule revealed an angular deviation of approximately 43° between the planes of its two phenyl rings (Figure 12a). This configuration, combined with strong hydrogen-bonding interactions involving the functional groups -NH-C=O and -CN, helps restrict conformational flexibility or rotational freedom (Figure 12b) in the photo-excited state. Such restrictions effectively minimize non-radiative decay pathways, thereby contributing to fluorescence emission.

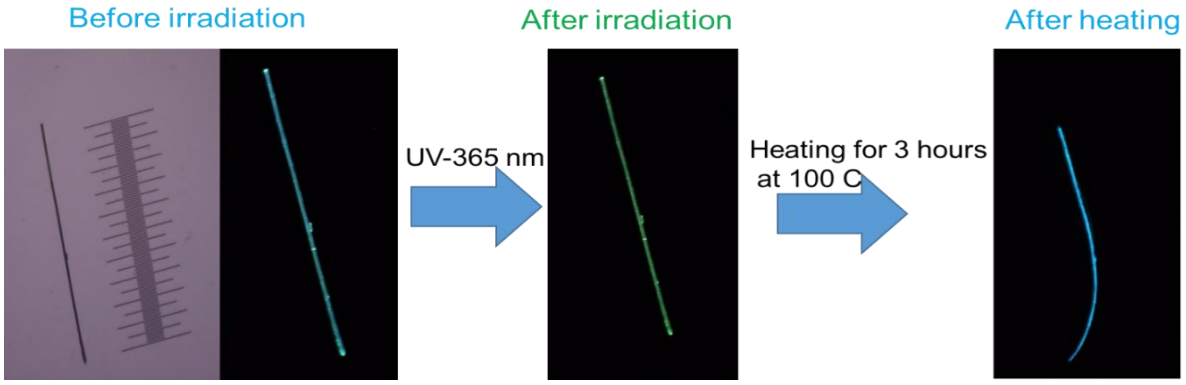

Figure 11b. Snapshots of **$ArCF_3$** crystal during irradiation to greenish-yellow emissive crystal followed by thermal heating to the original cyan emissive form.

The crystal structure further indicates a "head-to-head" stacking pattern of two **ArF$_2$** molecules. Crucially, the cyanovinyl C=C bonds in these molecules are separated by a distance of 3.871 Å, which is shorter than the ideal distance required for Schmidt's topochemical [2+2] photocycloaddition reaction in the solid state. As a result, **ArF$_2$** crystals exhibit susceptibility to undergo this photocycloaddition reaction upon UV irradiation. This observation aligns with subsequent ^{1}H NMR results discussed later.

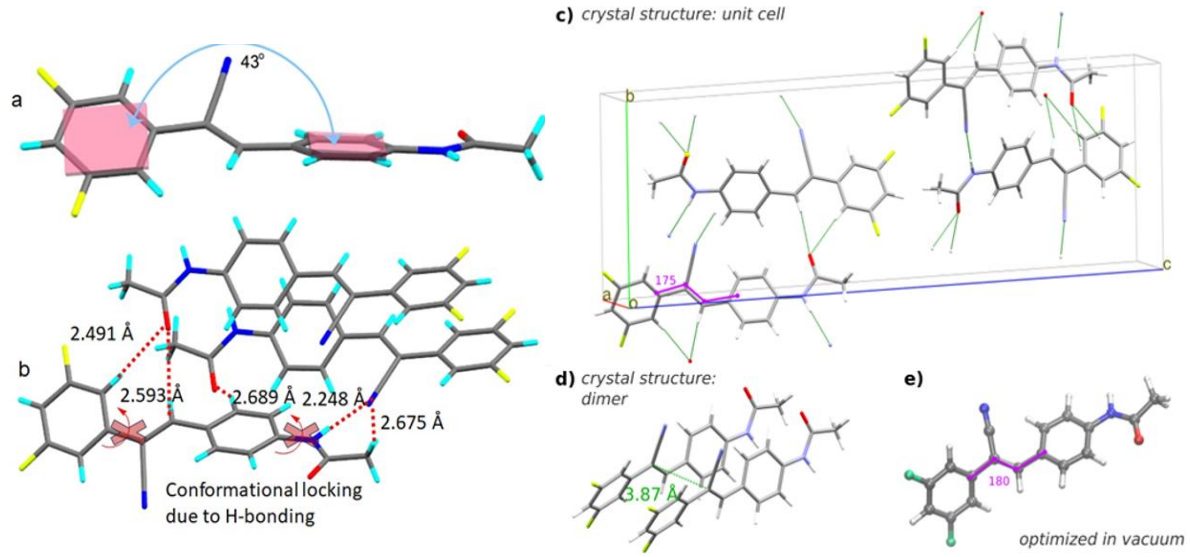

Figure 12. (a) Molecular conformation of the ***E*-ArF$_2$** in the crystal lattice showing the angle between two conjugated phenyl rings, (b) Intermolecular H-bonding interactions that restrict molecular rotation in excited state preventing non-radiative decay. c) **ArF$_2$** crystal unit cell (4 molecules) with short N-N and C-O intermolecular contacts highlighted in green. On one of the molecules, the dihedral expressing the E/Z isomers is highlighted. d) Dimer as resulting from two nearby unit cells and the intermolecular distance (shortest distance can be smaller) e) ***E*-ArF$_2$** as optimized in vacuum**.**

In contrast, **ArCF$_3$** crystals, grown from DMF or DMSO solutions, did not yield high-quality X-ray diffraction data despite extensive efforts, making it challenging to accurately describe their supramolecular arrangement or intermolecular interactions. Nonetheless, it can be reasonably speculated that the bulky trifluoromethyl (**-CF$_3$**) groups likely lead to an anti-parallel molecular stacking arrangement, with a head-to-tail orientation. Experimental irradiation of **ArCF$_3$** crystals using 365 nm UV light followed by dissolution in DMSO-d$_6$ to record ^{1}H NMR spectra confirmed the formation of a [2+2] cycloaddition product. This indicates that the cyanovinyl C=C bonds within the **ArCF$_3$** crystal lie within Schmidt's distance, enabling efficient topochemical cycloaddition reactions. To understand the distinct

fluorescence color switching behavior exhibited by the two crystals, **ArF_2** and **$ArCF_3$**, it is essential to delve into the solid-state reactions occurring within the crystal medium upon light irradiation. Solid-state fluorescence in dense media, such as crystals or polymer matrices, is largely governed by the molecular packing arrangement and the nature of intermolecular noncovalent interactions. These factors exert significant influence on the excited-state structure and dynamics, thus shaping the optical properties of the material.

Given the structural differences between **ArF_2** and **$ArCF_3$**, where the substituents **-F** and **$-CF_3$** play a pivotal role, it is anticipated that the molecular packing and intermolecular interactions in the two crystals differ considerably. These variations could be responsible for the distinct fluorescence behavior observed, with **E-ArF_2** crystals exhibiting bright green emission, while **E-$ArCF_3$** crystals display cyan fluorescence. This divergence in solid-state optical properties may primarily arise from differences in packing arrangements and the specific modes of intermolecular interactions involving functional groups, both of which contribute to alterations in the excited-state emission characteristics of the respective molecules. Although the crystal structure of **E-ArF_2** has been previously reported and extensively analyzed, a definitive structure for **E-$ArCF_3$** crystals could not be resolved due to challenges in obtaining high-quality X-ray diffraction data. Despite this limitation, computational analysis of excited-state pathways for isolated **E-$ArCF_3$** molecules provides some insight, suggesting only minor intrinsic differences. This points to molecular packing and interaction dynamics within the solid-state lattice as the key factors influencing the contrasting fluorescence colors and their switching behavior.

The opposite fluorescence color-switching behaviors of **E-ArF_2** and **E-$ArCF_3$** crystals under UV irradiation at 365 nm can be understood through solid-state reactions and molecular transformations observed in ^{1}H NMR experiments. For **E-ArF_2** crystals, light irradiation triggers both E-/Z- isomerization and [2+2] cycloaddition reactions, resulting in a complex mixture of four distinct species: **E-ArF_2**, **Z-ArF_2** (20%), E- [2+2] ArF2 dimer (31%), and Z-[2+2] **ArF_2** dimer (20%) (Figure 13). The emission shift from green to cyan occurs due to a combination of factors, including the interplay of excited states across multiple species and phenomena like energy transfer and energy funnelling within condensed phases. While the solid-state conversion of **E-ArF_2** to **Z-ArF_2** might logically lead to a red shift, the additional cycloaddition reactions disrupt π-conjugation and introduce alternative emission pathways, ultimately producing a blue-shifted cyan fluorescence.

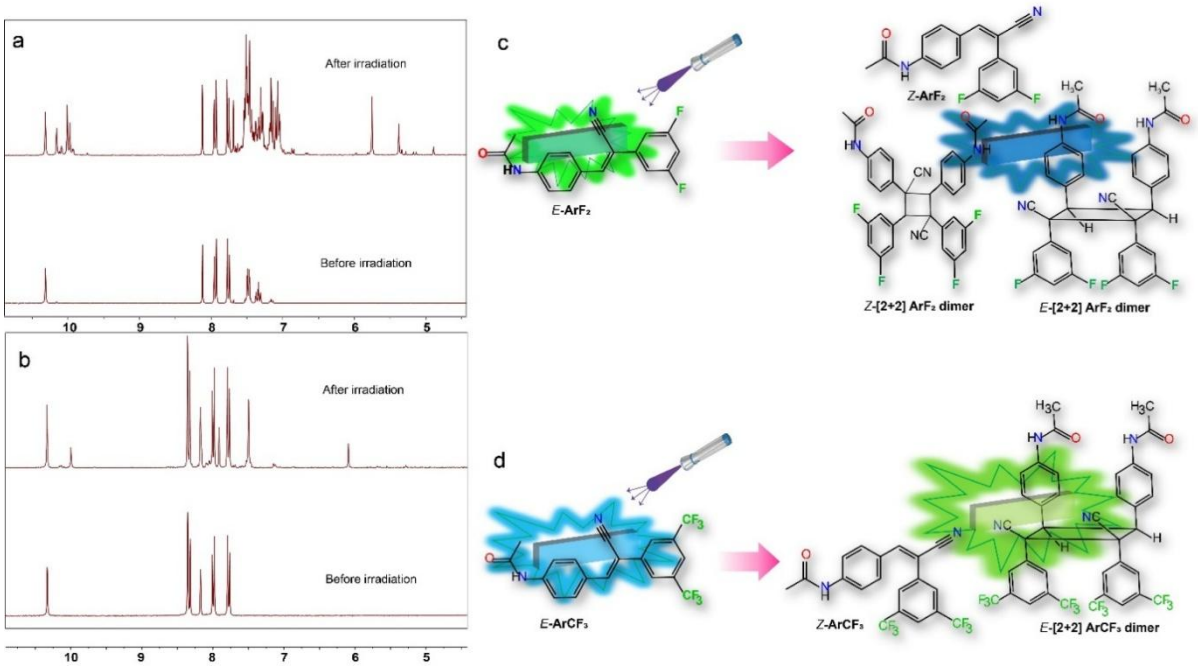

Figure 13. (a) ^{1}H NMR spectra of **ArF$_2$** after irradiation of solid crystals with 365 nm light, showing a mixture of products ***Z*-ArF$_2$**, *E*-[2+2] **ArF$_2$** dimer, *Z*-[2+2] **ArF$_2$** dimer. (b) ^{1}H NMR spectra of **ArCF$_3$** after irradiation of solid crystals with 365 nm light, showing a mixture of products ***Z*-ArCF$_3$**, *E*-[2+2] **ArCF$_3$**. (c, d) Cartoon representation of the solid-state reaction happening in the crystals of **ArF$_2$** and **ArCF$_3$**.

In contrast, the irradiated **E-ArCF$_3$** crystals predominantly yield *E*-[2+2] **ArCF$_3$** dimers (27%) alongside a smaller fraction of **Z-ArCF$_3$** (8%) (Figure 15). The limited **Z-ArCF$_3$** formation is likely due to the bulky trifluoromethyl **(-CF$_3$)** groups, which constrain isomerization by reducing the available free volume in the dense solid medium.

Notably, the formation of *Z*-[2+2] **ArCF$_3$** dimers was absent, likely due to steric hindrance preventing **Z-ArCF$_3$** molecules from aligning within Schmidt's critical distance for cycloaddition. Consequently, while conjugation loss during E-[2+2] **ArCF$_3$** dimer formation causes fluorescence intensity reduction, the original cyan emission red-shifts to green primarily due to the small fraction of **Z-ArCF$_3$** formed within the solid lattice.

These findings highlight how differences in molecular packing, substituents, and interaction dynamics in the crystalline media determine the distinct photo-switching behaviors of the two compounds. Additional computational interpretations further support these observations by elucidating the pathways of molecular transformations and their impact on excited-state properties.

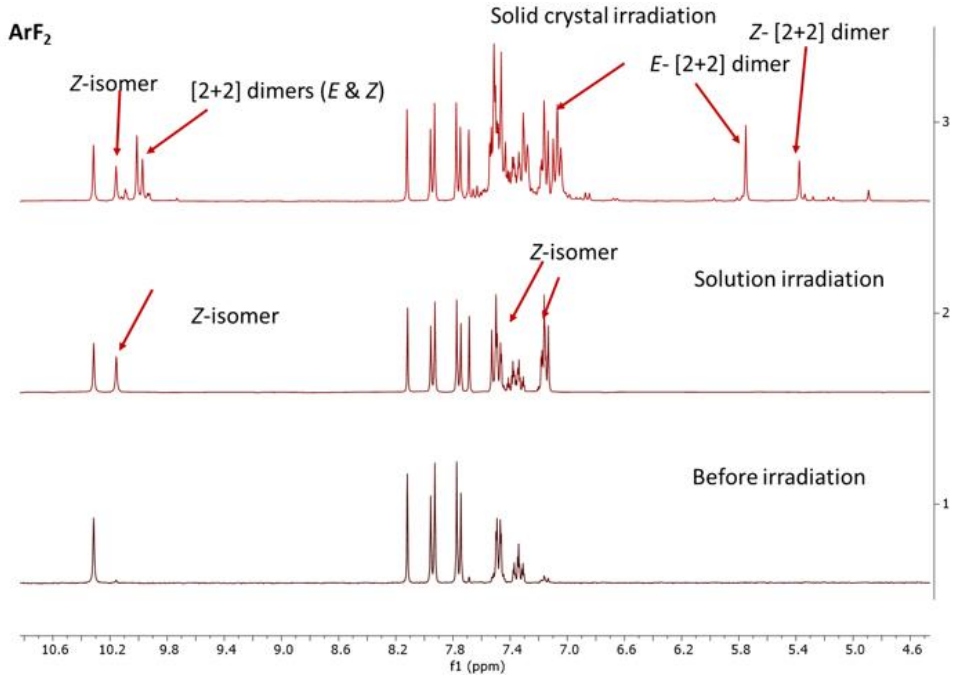

Figure 14. ^{1}H NMR spectra (in DMSO-d_6) of **ArF$_2$**: (i). ^{1}H NMR of **ArF$_2$** before irradiation, (ii). DMSO-d_6 solution was irradiated with UV light for 1 hour and then spectra was recorded, (iii) ***E*-ArF$_2$** crystals were irradiated with UV light for 2 hours and then dissolved in DMSO-d_6 to record ^{1}H NMR spectra.

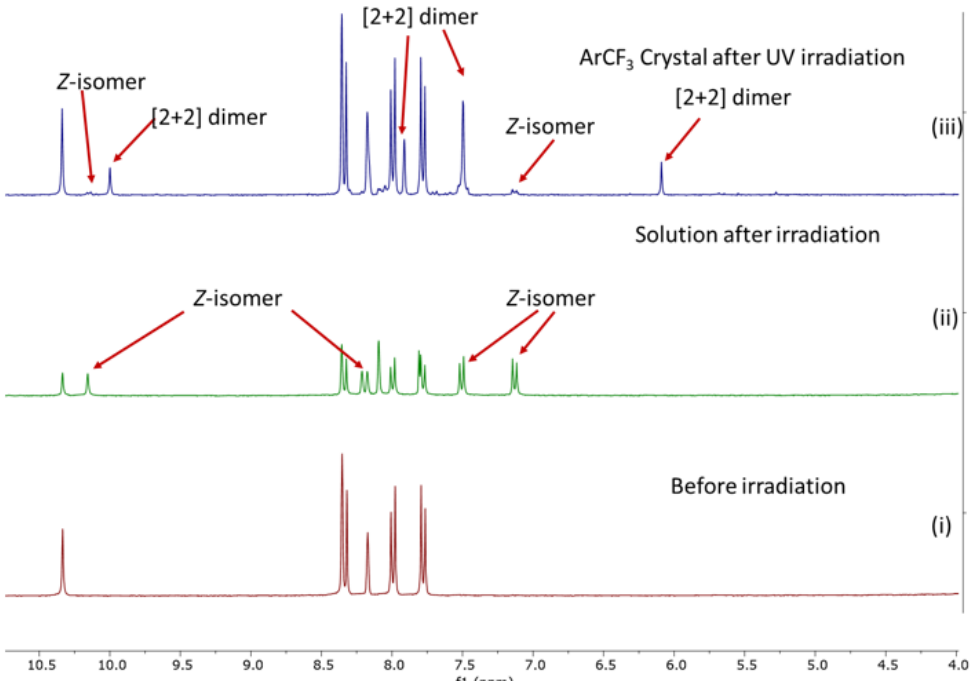

Figure 15. ^{1}HNMR spectra (in DMSO-d_6) of **ArCF$_3$**: (i). **ArCF$_3$** before irradiation, (ii). DMSO-d_6 solution was irradiated with UV light for 1 hour and then spectra was recorded, (iii) **ArCF$_3$** crystals were irradiated with UV light and then dissolved in DMSO-d_6 to record ^{1}H NMR spectra.

4.4 Applications

Following the remarkable photo-switching behavior observed for **ArF_2** and **$ArCF_3$** crystals, efforts were made to investigate whether such properties could be replicated when these dyes are embedded within a polymer matrix. To achieve this, a thin film of **ArF_2**-PMMA was fabricated by incorporating 5% **ArF_2** (by weight) into a Polymethylmethacrylate (PMMA) matrix. The preparation process began with adding PMMA into a DMF solution and heating it to 80 °C to form a clear slurry. This slurry was subsequently poured into a flat-base petri dish and allowed to dry gradually under ambient conditions over a period of 7-8 days, yielding a dry thin film.

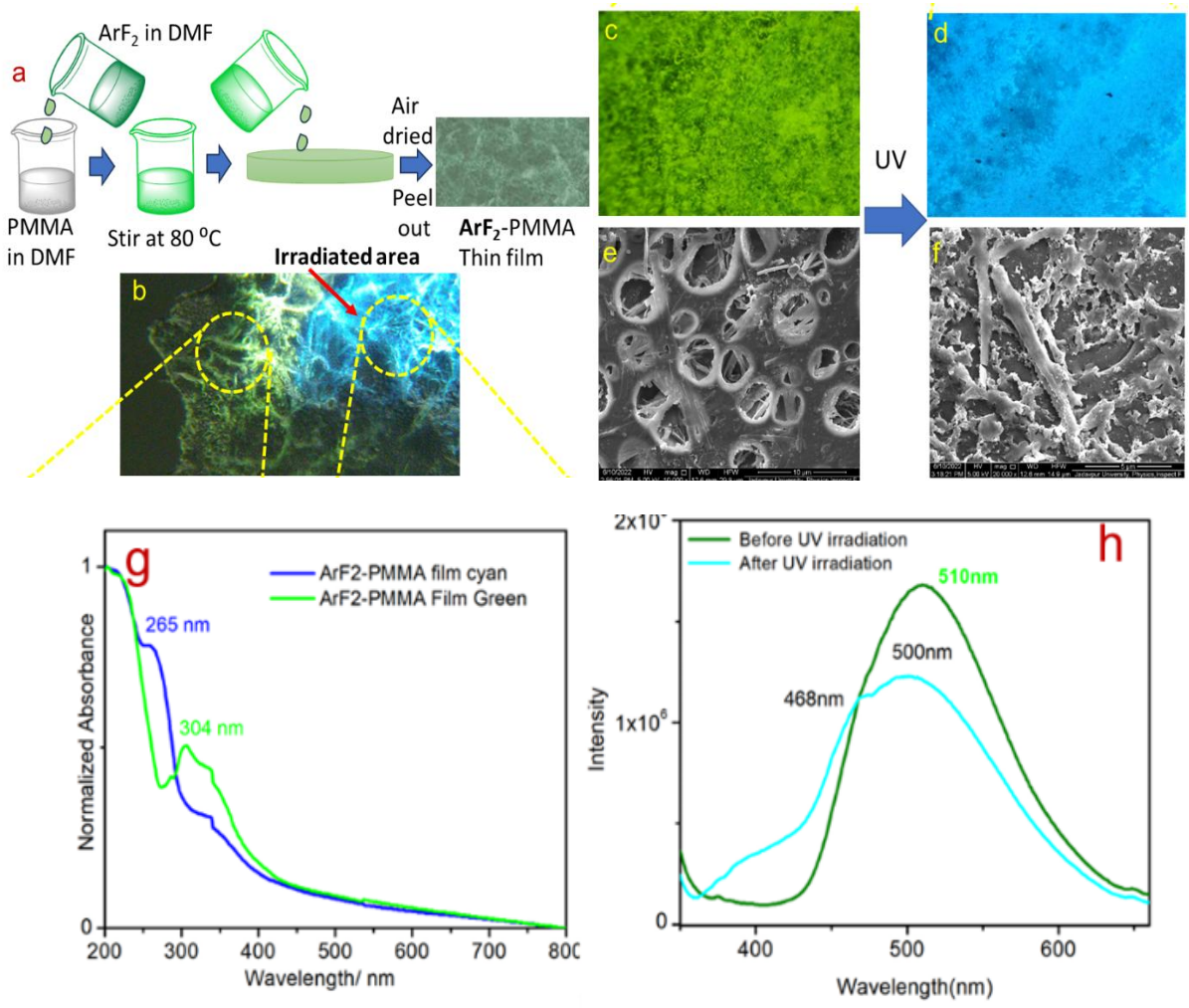

Figure 16. (a) Schematic route for the preparation of **ArF_2**-PMMA thin film, (b) emission of the same film before and (c) after UV illumination, (d) SEM picture of the green emissive film, (e) SEM picture of cyan emissive film, (f) UV-Vis spectra of **ArF_2**-PMMA film before (green) and after (cyan) UV irradiation, (g) Solid state absorption spectra, and (h) solid state emission spectra of green and cyan emissive **ArF2**-PMMA film.

A similar methodology was employed to prepare an **ArCF$_3$**-PMMA film, using 5% **ArCF$_3$** (by weight) in the PMMA matrix. A schematic representation of the film preparation process is shown in Figure 16. Once the films were fully dried, they were carefully peeled off from the petri dishes and subjected to detailed characterization, which included UV-Vis spectroscopy, fluorescence measurements, and IR spectroscopy. This approach not only expanded the scope of photo-switching studies but also provided valuable insights into the optical properties of the embedded dyes. The prepared thin films of **ArF$_2$**-PMMA exhibit fascinating solid-state fluorescence properties. Initially, the green emissive behavior of the film is attributed to the presence of pristine **E-ArF$_2$** microcrystals embedded within the PMMA matrix (Figure 16a, b). Analysis using SEM imaging confirms the existence of micrometer-sized needle-like crystals of **ArF$_2$** distributed throughout the PMMA matrix. Upon illumination with UV light at 365 nm, the green emission of the film gradually transitions to cyan emission (Figure 16b-d,), accompanied by physical damage to the crystal shape. This transformation is driven by *E/Z* isomerization and [2+2] cycloaddition reactions occurring in the dense PMMA matrix.

ArCF$_3$-PMMA films prepared using the same procedure display analogous photo-switching behavior. Initially cyan-emissive, these films shift to greenish-yellow fluorescence upon UV light exposure at 365 nm (Figure 17-18). Remarkably, heating the photo-converted film at 100 °C for 2 hours restores the original cyan emission. This demonstrates that the inherent photo-switching behaviors of both **ArF$_2$** and **ArCF$_3$** in solid-state crystals persist within the PMMA polymer matrix.

UV-Vis spectroscopy of the **ArF$_2$**-PMMA film reveals an absorption band at λ_{max} = 304 nm prior to UV irradiation, which shifts to 265 nm following exposure. Similarly, fluorescence spectra show a distinct shift, with the green emissive peak at 510 nm converting to a shoulder peak at 468 nm after irradiation. IR spectroscopy further validates these observations, displaying noticeable changes in bond stretching frequencies due to the photoreactions of **ArF$_2$** microcrystals within the PMMA matrix (Figure 19).

Such robust retention of photo-switching characteristics in the polymer matrix presents promising opportunities for practical applications, including security printing, photo-lithographic writing, and other photo-responsive technologies.

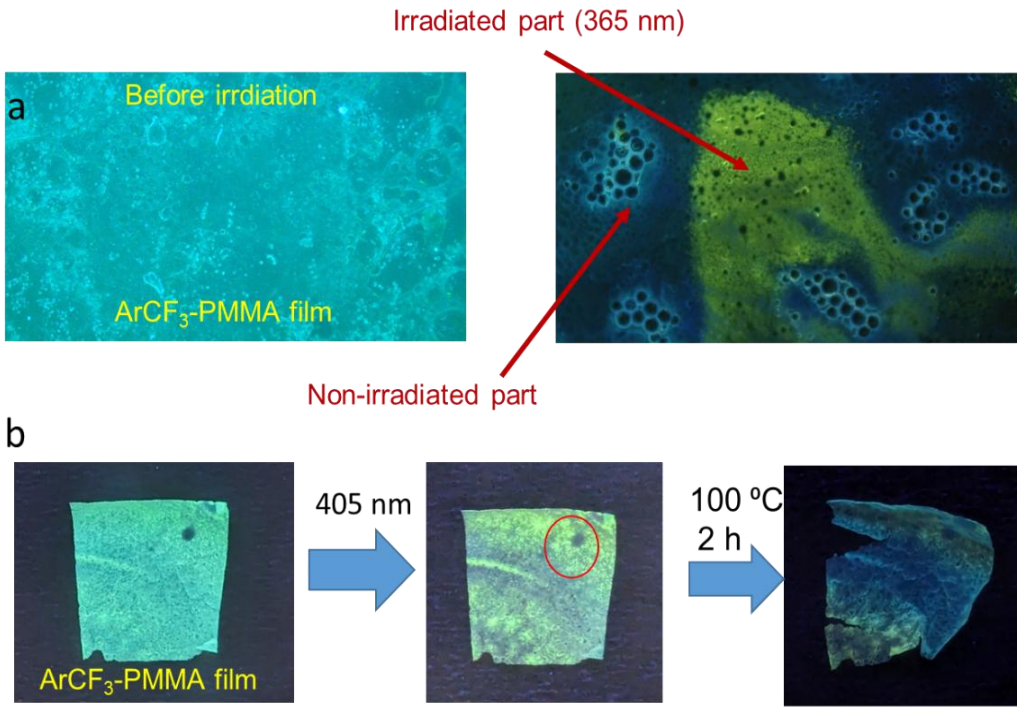

Figure 17. (a) Picture of **ArCF$_3$**-PMMA film before and after irradiation of the by UV light. (b) Reversible fluorescence switching from cyan to greenish yellow and heating back to cyan.

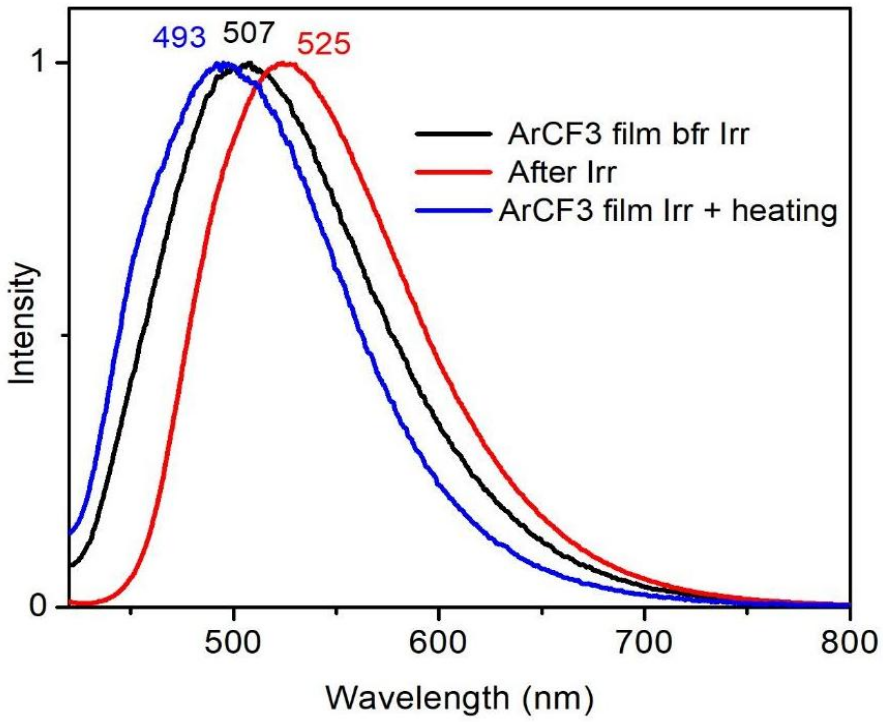

Figure 18. Solid state fluorescence spectra of **ArCF$_3$**-PMMA film showing fluorescence switching from cyan to green upon irradiation and green to cyan upon heating at 100 ºC**.**

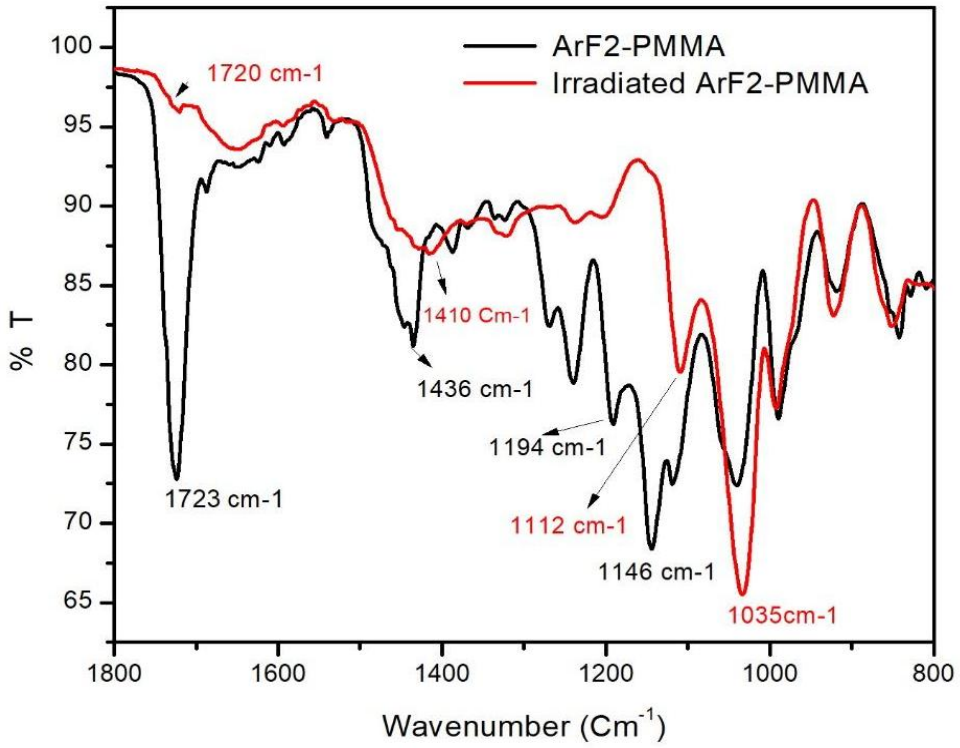

Figure 19. IR spectra of **ArF_2**-PMMA film before and after UV irradiation.

After demonstrating the photo-switching behavior of **ArF_2**-PMMA and **$ArCF_3$**-PMMA films, the study proceeded to explore their potential applications in photolithographic printing for data encryption and security purposes. For this purpose, only the **ArF_2**-PMMA film was utilized throughout the experiments. A schematic representation of the writing/printing process using 365 or 390 nm light is illustrated in Figure 20a. To showcase confidential data encoding, a QR code linking to the lab group's website was successfully printed onto the **ArF_2**-PMMA film using a mask (Figure 20 b-d). This QR code is invisible under ambient light but becomes visible under UV illumination. The intended goal was to read the QR code using electronic devices such as mobile phones or laser readers under UV light.

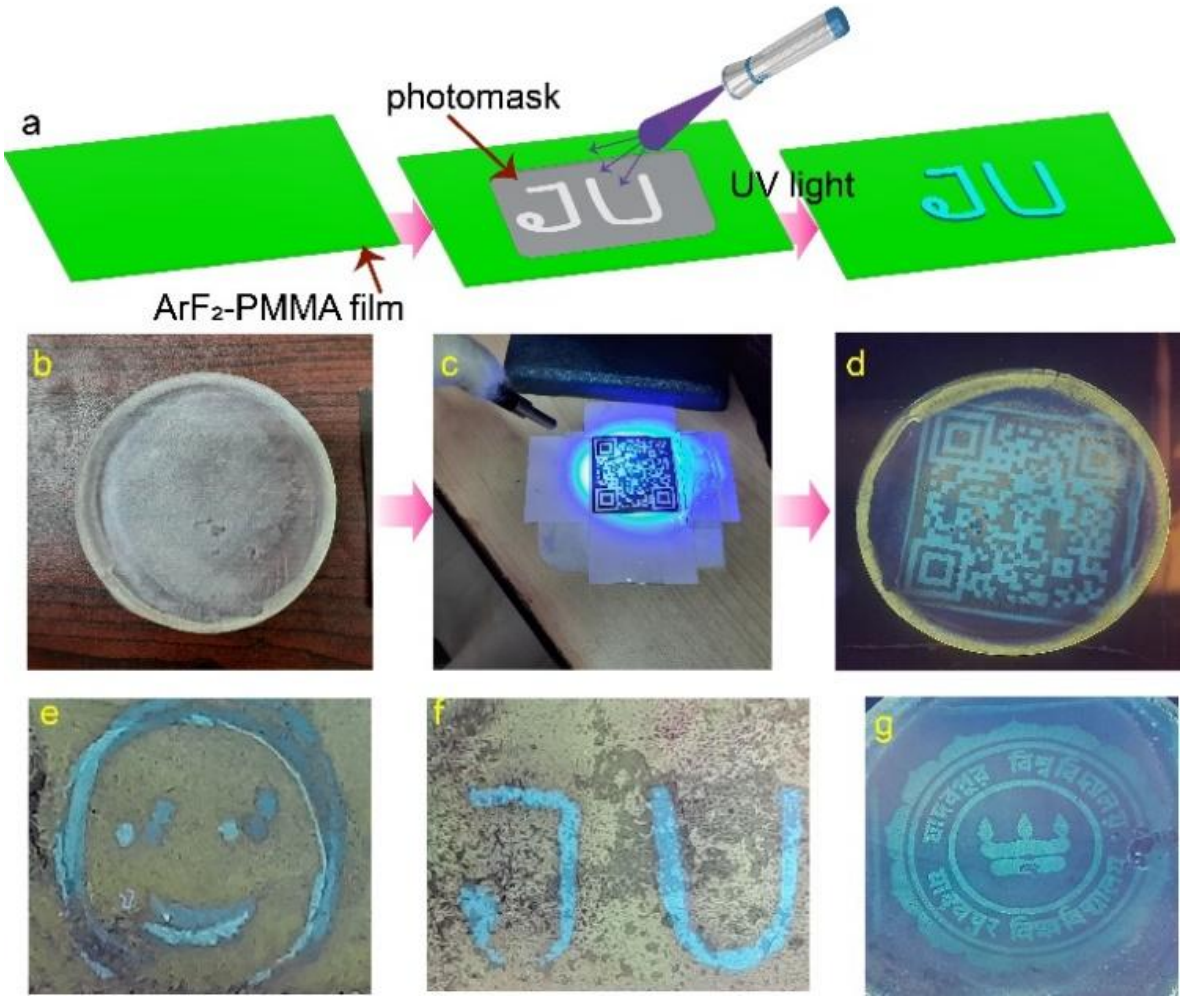

Figure 20. (a) Schematic diagram of photolithographic writing, printing on **ArF_2**-PMMA thin film for the data/logo authentication application, (b-d) QR code printing on **ARF_2**-PMMA film using 390 nm light, (e-j) printing of various complex patterns, (e) smiley, (f) JU (Jadavpur University) and (g) a logo of Jadavpur University.

Although the clarity of the printed QR code is excellent, the poor color contrast between the cyan emission and the background prevented the mobile phone scanner app from successfully decoding the QR code. Further improvements to enhance the color contrast are required for compatibility with mobile scanning applications.

In addition to the QR code, various intricate patterns were printed using the same technique. As illustrated in Figure 20e-g, designs such as smileys, "JU" (representing Jadavpur University), and the university's logo were successfully printed on the film. These patterns, similar to the QR code, are invisible in ambient light but can be observed under UV or blue light. Such capabilities highlight the potential utility of these photo-switching films for secure data communication and applications in security writing.

4.5 Conclusion

This study successfully introduced two innovative photo-switchable fluorescent materials that exhibit remarkable color transitions from green to cyan due to the formation of photo-isomers and distinct cycloaddition products. By strategically varying substituents in the molecular structure, we achieved two distinct solid-state emissive materials with unique photo-switching properties. Unlike existing dyes, these materials are synthesized in a straightforward, one-step process, providing a more cost-effective and efficient approach. Additionally, the fabrication of **ArF$_2$** solids into thin films demonstrated their potential utility for advanced applications such as photolithography, security writing, tangent systems, and logo authentication utilizing UV light. The promising features of these materials, including their ability to encode and decode data securely and facilitate confidential communication, indicate their relevance for data security devices and other advanced technological applications. This research paves the way for further exploration of photo-responsive materials in practical and innovative domains.

■ REFERENCES

1. H. Zhu, S. Zhang, J. Yang, M. Wu, Q. Wu, J. Liu, J. Zhang, L. Kong and J. Yang, *J. Solid State Chem*., 2021, **305**, 122706.
2. Z. Wen, T. Yang, D. Zhang, Z. Wang, S. Dong, H. Xu, Y. Miao, B. Zhao and H. Wang, *J. Mater. Chem. C*., 2022, **10**, 3396.
3. H. Yang, Z. Fu, S. Wang, H. Liu, J. Zhou, K. Wang, X. Wu, B. Yang, B. Zou and W. Zhu, *Mater. Adv*. 2021, **2**, 4859.
4. S. Ito, *CrystEngComm.*, 2022, **24**, 1112.
5. G. Bae, M. Seo, S. Lee, D. Bae and M. Lee, *Adv. Mater. Technol*., 2021, **6**, 2100479.
6. S. Zeng, H. Sun, C. Park, M. Zhang, M. Zhu, M. Yan, N. Chov, Li, S. Li, A. T. Smith, G. Xu, S. Li, Z. Hou, Y. Li, B. Wang, D. Zhang and L. Sun, *Mater. Horiz*. 2020, **7**, 164.
7. G. Giordano, M. Gagliardi, Y. Huan, M. Carlotti, A. Mariani, A. Menciassi, E. Sinibaldi, B. Mazzolai, *Adv. Sci*., 2021, **8**, 2100418.
8. Y. Li, Z. Ma, A. Li, W. Xu, Y. Wang, H. Jiang, K. Wang, Y. Zhao and X. Jia, *ACS. Appl. Mater. Interfaces*., 2017, **9**, 8910.
9. T. Butler, A. S. Mathew, M. Sabat and, C. L. Fraser, *ACS Appl. Mater. Interfaces*., 2017, **9**, 17603.
10. G. Gogoi, D. Kashyap and R. J. Sarma, *Cryst. Growth Des.*, 2018, **18**, 4963.
11. G. Naren, C-W Hsu, S. Li, M. Morimoto, S. Tang, J. Hernando, G. Guirado, M. Irie, F. M. Raymo, H. Sundén & J. Andréasson, *Nat. Commun*., 2019, **10**, 3996.
12. R. M. Snari, R. A. Pashameah, N. M. Alatawi, A. T. Mogharbel, Z. A. Al-ahmed, H. M. Abumelha, N. M. El-Metwaly, *Microsc Res Tech*., 2022, **85**, 3871.
13. Z. Lin, H. Wang, M. Yu, X. Guo, C. Zhang, H. Deng, P. Zhang, S. Chen, R. Zeng, J. Cui and J. Chen, *J. Mater. Chem. C*., 2019, **7**, 11515.
14. C-L Sun, C Wang and R. Boulatov, *Chemphotochem*, 2019, **3**, 268.
15. J. W. Leem, H-J Jeon, Y. Ji, S. M. Park, Y. Kwak, J. Park, K-Y Kim, S-W Kim, and Y L. Kim, *ACS Cent. Sci*., 2022**, 8**, 513.
16. H. Zhang and X. Ji, *ACS Cent. Sci.*, 2022, **8**, 507.
17. D. Hu, W. Xu, G. Wang, K. Liu, Z. Wang, Q. Shi, S. Lin, Z. Liu, and Y Fang, *Adv. Funct. Mater*., 2022, **32**, 2207895.
18. Z. Yu and S. Hecht, *Chem. Commun*., 2016, **52**, 6639.
19. Y. Zhang, K. Zhang, J. Wang, Z. Tian, and A. Q. Li, *Nanoscale*., 2015, **7**, 19342.
20. M. Kathan and S. Hecht, *Chem. Soc. Rev*., 2017, **46**, 5536.

21. M. Dong, A. Babalhavaeji, S. Samanta, A. A. Beharry, and G. A. Woolley, *Acc. Chem. Res.*, 2015, **48**, 2662.
22. D. Bléger, J. Schwarz, A. M. Brouwer, and S Hecht, *J. Am. Chem. Soc*., 2012, **134**, 20597.
23. M. Wegener, M. J. Hansen, A. J. M. Driessen, W. Szymanski, and B. L. Feringa, *J. Am. Chem. Soc*. 2017, **139**, 17979
24. L. Kuroki, S. Takami, K. Yoza, M. Morimoto and M. Irie, *Photochem. Photobiol. Sci*, 2010, **9**, 221.
25. T. Fukaminato, M. Tanaka, T. Doi, N. Tamaoki, T. Katayama, A. Mallick, Y. Ishibashi, H. Miyasaka and M. Irie. Photochem. *Photobiol. Sci*., 2010, **9**, 181.
26. C. W. Hsu, C. Sauvee, H. Sunden and J. Andreasson, *Chem. Sci*, 2018, **9**, 8019.
27. S. Z. Pu, Q. Sun, C. B. Fan, R-J Wang and G Liu, *J. Mater. Chem. C*., 2016, **4**, 3075.
28. A. Abdollahi, H. ASharif, H. Roghani-Mamaqani and A. Herizchic, *J. Mater. Chem. C*, 2020, **8**, 5476.
29. M. Deng, Y. Zhang, Y. Wang and S. Jiang, *J. Mater. Chem. C*, 2020, **8**, 15697.
30. R. Klajn, *Chem.Soc.Rev*, 2014, **43**, 148.
31. Xibo Feng, Axel D. Becke and Erin R. Johnson, *CrystEngComm*, 2021, **23**, 4264.
32. M. Rivera, M. Dommett, and R. C. Otero, *J. Chem. Theory Comput*., 2019, **15**, 2504−2516.
33. M. Rivera, L. Stojanovic, and R. C. Otero, *J. Phys. Chem. A*., 2021, **125**, 1012−1024.
34. L. Wilbraham, M. Louis, D. Alberga, A. Brosseau, R. Guillot, F. Ito, F. Labat, R. Métivier, C. Allain, and I. Ciofini, *Adv. Mater*., 2018, **30**, 1800817.
35. F. Sun, D. Wang, J. *Mater. Chem. C*., 2022, **10**, 13700.
36. A. Gonzalez, E. S. Kengmana, M.V. Fonseca, G.G.D. Han, *Materials Today Advances*., 2020, **6**, 100058.
37. J. W. Chung, Y. You, H. S. Huh, B. K. An, S. J. Yoon, S. H. Kim, S. W. Lee, S. Y. Park, *J. Am. Chem. Soc*., 2009, **131**, 8163.
38. J. W. Chung, S. J Woon, B. K An, S. Y. Park, *J. Phys. Chem. C*., 2013, **117**, 11285.
39. P. Giri, A. Mazumder, D. Dey, S. Garani, A. Raveendran, and M. K. Panda, *CrystEngComm*., 2021, **23**, 5876.
40. G. M. J. Schmidt, *Pure and Appl. Chemistry*., 1971, **27**, 647.
41. A. Najibi, L. Goerigk, *J. Chem. Theor. Comput.*, 2018, **14**, 5725.
42. S. Grimme, S.Ehrlich, L.Goerigk, *J. Comput. Chem*., 2011, **32**, 1456.

43. F. Neese, F. Wennmohs, U. Becker and C. Riplingerm, *J. Chem. Phys*., 2020, **152**, 224108.
44. X. Zhu, K. C. Thompson, T. J. Martinez, *J. Chem. Phys*. 2019, **150**, 164103.
45. K. Berland, C. A. Arter, V. R. Cooper, K. Lee, B. I. Lundqvist, E. Schröder, T. Thonhauser, P. Hyldgaard, *J. Chem. Phys*., 2014., **140**, 18539
46. P. Giannozzi, O. Andreussi, T. Brumme, O. Bunau, M. B. Nardelli, M. Calandra, R. Car, C. Cavazzoni, D. Ceresoli, M. Cococcion., *J. Phys. Condens. Matter.*, 2017, **29**, 465901.
47. K. F. Garrity, J. W. Bennett, K. M. Rabe, D. Vanderbilt, Comput. *Mater. Sci*., 2014, **81**, 446.
48. F. Weigend, R. Ahlrichs, *Phys. Chem. Chem. Phys*., 2005, **7**, 3297.

CHAPTER-5

Influence of Polymorphism and Substituent Variation on the Thermoresponsive and Luminescent Characteristics of Organic Molecular Crystals

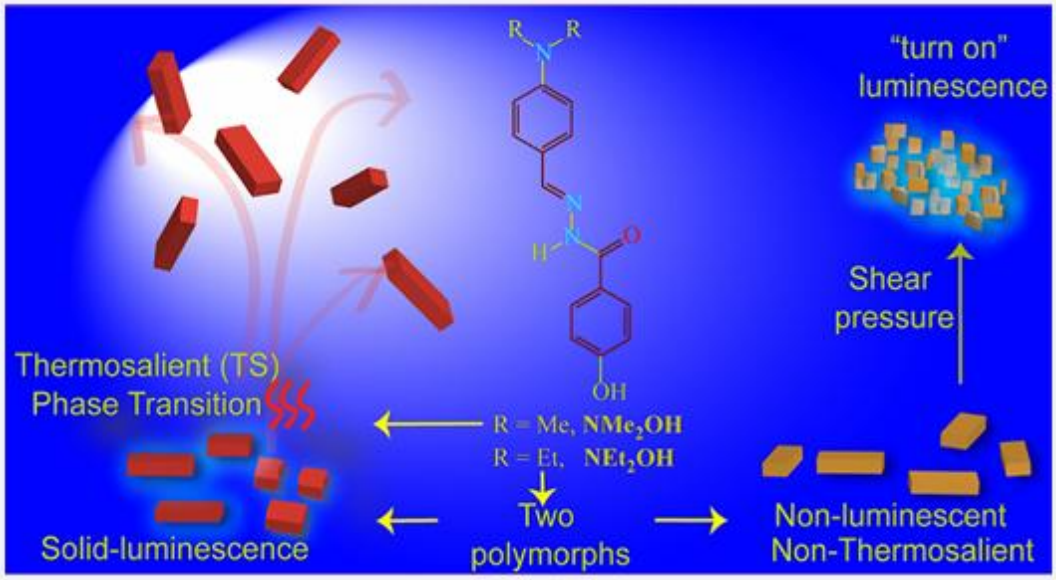

Influence of Polymorphism and Substituent Variation on the Thermoresponsive and Luminescent Characteristics of Organic Molecular Crystals

5.1 Introduction

Smart molecular crystals, which can respond macroscopically to various external stimuli like heat, light, pressure, or humidity, have gained significant attention for applications in actuators, sensors, and optoelectronics.[1-10]Unlike single-stimulus-responsive materials, designing crystals that react differently to multiple stimuli remains a complex challenge. In this study, we introduce a new class of acylhydrazone derivatives that exhibit thermosalient (TS) actuation and solid-state luminescence, with their behavior being tunable through polymorphism and substitutional modifications. For example, **NMe_2OH** crystals demonstrate remarkable TS movement and bright cyan luminescence, while **NEt_2OH** exists in two distinct polymorphs—**NEt_2OH-FL**, which retains TS actuation[11-25] and luminescence, and **NEt_2OH-NFL**, which lacks both. By conducting single-crystal and powder X-ray diffraction studies, we established that differences in molecular conformations and crystal packing dictate these varied responses. Our findings provide a novel approach for tuning stimuli-responsive behavior, paving the way for advanced applications in dynamic materials and smart devices.[26]

Stimuli-responsive materials, which can convert external energy into functional changes, have gained immense attention across various technological fields, including sensors, actuators, optoelectronics, and biomedical tools. These materials provide remarkable versatility due to their ability to undergo macroscopic transformations, such as shape change, mechanical motion, and luminescence switching, when exposed to external stimuli like heat, light, pressure, or mechanical force.

A particularly intriguing subset of these materials is dynamic single crystals, which exhibit striking mechanical effects such as jumping, rolling, bending, and peeling upon activation by external stimuli. The fundamental mechanism behind such behavior is often attributed to the release of internal stress, which accumulates due to stimuli-induced changes in molecular packing and intermolecular interactions.[27-32] As a result, controlling molecular composition, packing structure, and intermolecular forces emerges as a compelling research strategy for fine-tuning dynamic properties.

Among stimuli-responsive materials, multistimuli-responsive crystals—those capable of distinct responses to multiple external inputs—present superior adaptability for multifunctional applications. Although recent studies have reported solid-state luminescence switching triggered by thermal, photonic, or mechanical stimuli, the number of materials that exhibit both macroscopic actuation and color-switching luminescence remains limited [33-37]. The ability to regulate both properties through modifications in chemical composition, molecular packing, and intermolecular interactions highlights polymorphism and functional group variation as key strategies for tailoring multistimuli-responsive behavior.[37-39]

In this study, we introduce a novel class of acylhydrazone derivatives that demonstrate structure-dependent thermal actuation and luminescence switching. By systematically varying N-alkyl substitutions and polymorphic structures, we have developed: **NMe₂OH**, which displays robust thermosalient (TS) actuation and bright solid-state luminescence.[40-44]

NEt₂OH, which exists in two polymorphic forms: **NEt₂OH-FL**, featuring solid-state luminescence and TS effects. **NEt₂OH-NFL**, a nonluminescent and nonthermosalient polymorph, highlighting the influence of crystal structure on functional properties. Our findings provide a strategic approach for fine-tuning molecular crystal behaviour,[45-46] paving the way for advanced materials optimized for technological applications.[47-50]

5.2 Experimental

5.2.1. Materials & methods

For this study, the key reagents—4-hydroxybenzhydrazide, 4-(dimethylamino)benzaldehyde, and 4-(diethylamino)benzaldehyde—were sourced from TCI India and used as received. The solvents employed for synthesis were ACS grade (Merck), while high-purity spectroscopy-grade solvents were used for crystallization and spectroscopic analysis.

Nuclear Magnetic Resonance (NMR) Spectroscopy: ^{1}H NMR (300 MHz) and ^{13}C NMR measurements for **NMe₂OH** and **NEt₂OH** were recorded using a Bruker AVANCE 300 spectrometer. The solvent used was $CDCl_3$, and chemical shifts (δ) are reported in parts per million (ppm).

High-Resolution Mass Spectrometry (HRMS): HRMS spectra for **NMe_2OH** and **NEt_2OH** were obtained using a QTOF Micro YA263 mass spectrometer operating in electrospray ionization mode.

UV–Vis and Fluorescence Spectroscopy: UV–Vis absorption spectra in solution and solid state were measured with a Shimadzu UV-2401C spectrophotometer. Solid-state fluorescence emission spectra were recorded using a HORIBA Jobin Yvon Fluoromax-4 spectrofluorometer. Time-resolved fluorescence measurements were performed on a Horiba time-correlated single-photon counting (TCSPC) spectrometer, equipped with a DeltaFlex detector PPD850.

Infrared (IR) Spectroscopy: IR spectra were collected using a Perkin Elmer LX-1 FT-IR spectrometer to analyze vibrational modes of functional groups.

Scanning Electron Microscopy (SEM): SEM images were obtained from an FEI INSPECT F50 instrument operated at 5–7 kV. Samples were mounted on silicon wafers and coated with gold before imaging.

Powder X-ray Diffraction (PXRD): PXRD patterns were recorded using a Bruker D8 Advanced diffractometer with Cu Kα radiation (λ = 1.5418 Å), operated at 40 kV and 40 mA. A Lynxeye detector was employed, with a scan rate of 0.2 s per step over a 2θ range of 0°–50° at room temperature.

Single-Crystal X-ray Diffraction (SCXRD): Single-crystal XRD data for **NMe_2OH, NEt_2OH-FL,** and **NEt_2OH-NFL** were collected using a Bruker Microfocus D8 Venture diffractometer equipped with a CCD area detector and Mo Kα radiation (λ = 0.71069 Å). Data processing was done using the SAINT program (v. 8.38A), and XPREP (APEX3 software suite, v2017.3-0) ensured data accuracy. Absorption correction was applied using SADABS, while SHELXT (v2018/2) was used for structure solving and SHELXL-2014 for structure refinement. All non-hydrogen atoms were refined anisotropically, while hydrogen atoms were positioned geometrically and refined isotropically. Crystallographic data for **NMe_2OH, NEt_2OH-FL**, and **NEt_2OH-NFL** have been deposited at the Cambridge Crystallographic Data Centre (CCDC) under deposition numbers 2304044, 2359645, and 2304045, respectively.

5.2.2 Synthesis & Characterizations:

The synthesis of **NMe_2OH** was carried out using a modified literature procedure. Briefly, 4-N,N-(dimethylamino)benzaldehyde (0.149 g, 1 mmol) and 4-hydroxybenzohydrazide (0.152 g, 1 mmol) were dissolved in 30 mL of methanol in a 100 mL round-bottom flask. A catalytic amount of glacial acetic acid was added to the reaction mixture, which was then heated at 90°C for 4 hours. The solution was cooled, filtered, and left for crystallization from the mother liquor. After three days, cuboidal-shaped yellow crystals of **NMe_2OH** were obtained, isolated by filtration, and air-dried (yield: 0.201 g, 71%).

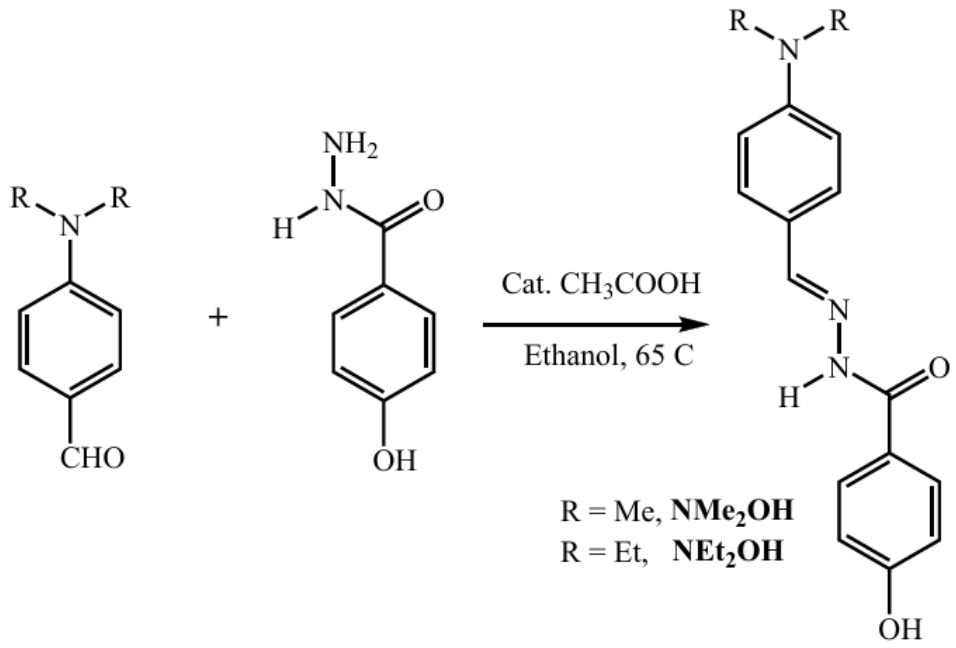

Scheme 1. General synthetic scheme for **NMe_2OH** and **NEt_2OH.**

The synthesis of **NEt_2OH** followed a similar approach. 4-N,N-(diethylamino)benzaldehyde (0.177 g, 1 mmol) and 4-hydroxybenzohydrazide (0.152 g, 1 mmol) were combined in 30 mL of methanol in a 100 mL round-bottom flask. A catalytic amount of glacial acetic acid was added, and the mixture was heated at 90°C for 4 hours. The resulting product was cooled, filtered, and allowed to crystallize from the mother liquor. After three days, yellow crystals of **NEt_2OH** were obtained, isolated via filtration, and air-dried (yield: 212 mg, 68%).

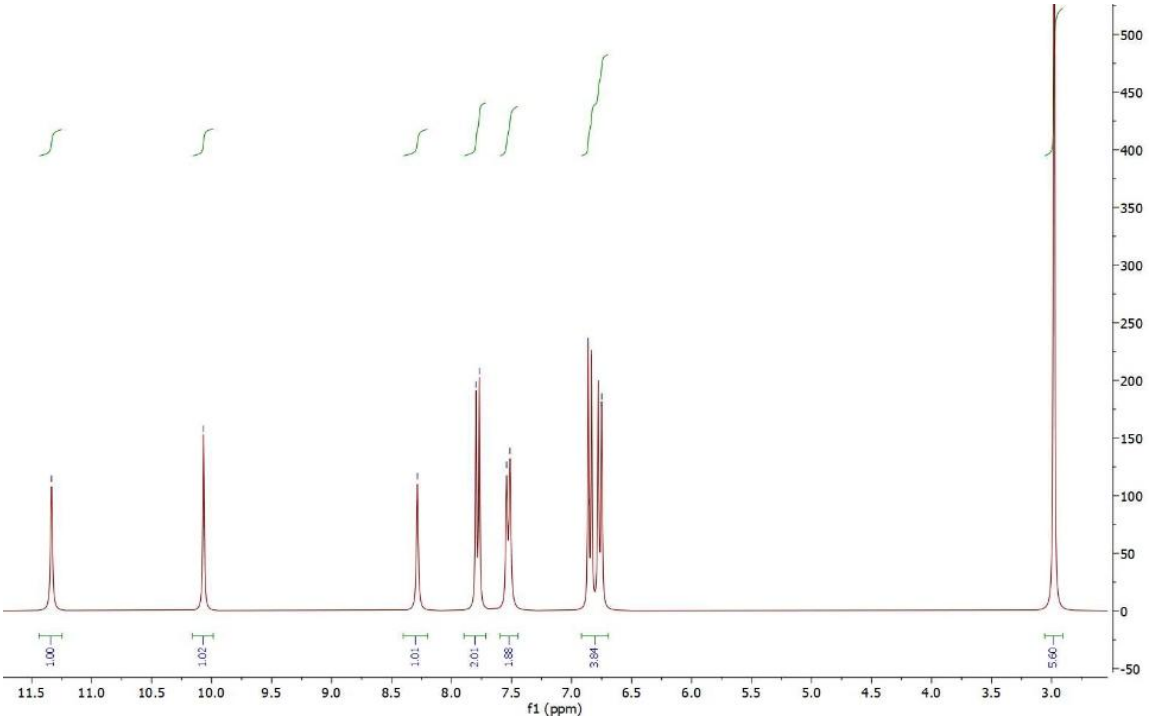

Figure 1. ^{1}H NMR spectra (in DMSO- D_6) of synthesized compound **NMe_2OH**.

The structure was confirmed through ^{1}H NMR (300 MHz, DMSO-d_6) with characteristic peaks at δ 11.40 (s, NH), 10.12 (s, OH), 8.36 (s, HC=N), 7.78 (d, J=9.0 Hz, ArH), 7.52 (d, J=9.0 Hz, ArH), 6.80 (q, J=9.0 Hz, ArH), and 3.00 (s, CH_3). HRMS analysis yielded an m/z value of 284.0849 (M+1), close to the calculated 283.34, with a melting point range of 216–221°C.

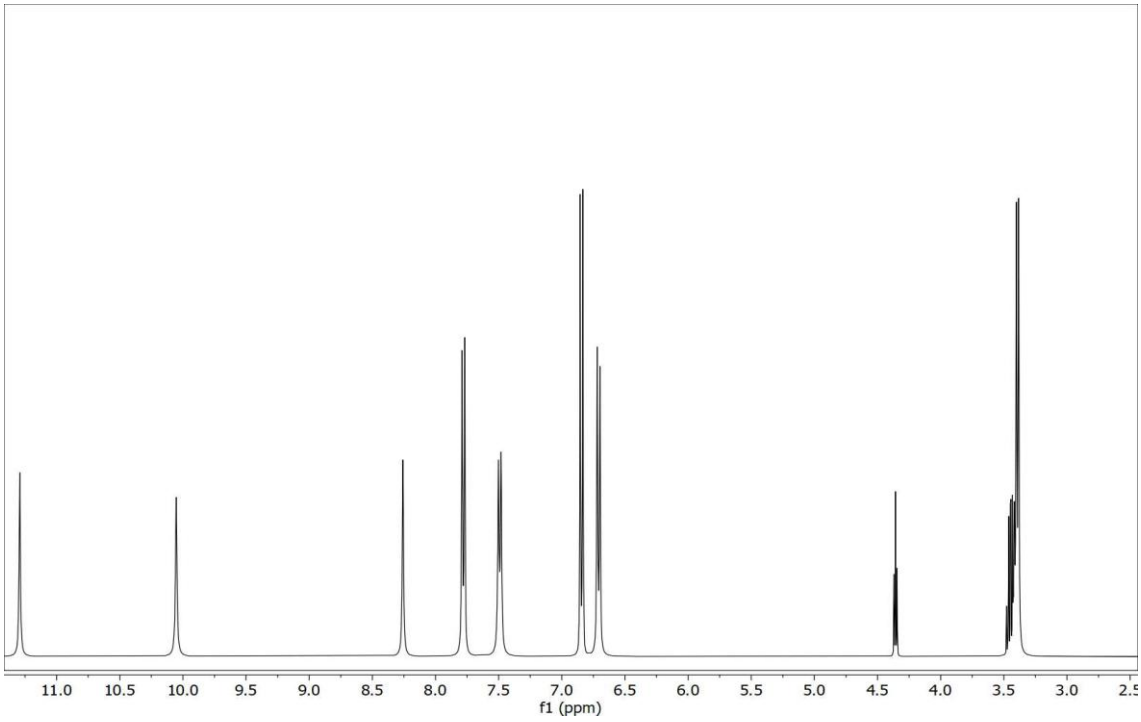

Figure 2. ^{1}H NMR spectra (in DMSO- D_6) of synthesized compound **NEt_2OH**.

The ^{1}H NMR (300 MHz, DMSO-d_6) spectrum of **NEt$_2$OH** displayed peaks at δ 11.29 (s, NH), 10.05 (s, OH), 8.26 (s, HC=N), 7.78 (d, J=6.0 Hz, ArH), 7.49 (d, J=6.0 Hz, ArH), 6.84 (d, J=6.0 Hz, ArH), 6.71 (d, J=6.0 Hz, ArH), 3.41 (m, CH_2CH_3), and 1.15 (m, CH_2CH_3). HRMS analysis yielded m/z = 312.1273 (M+1) compared to the calculated 311.4, with a melting point of 190–196°C. This synthesis method effectively yields structurally distinct crystalline materials with tailored thermal and optical properties.

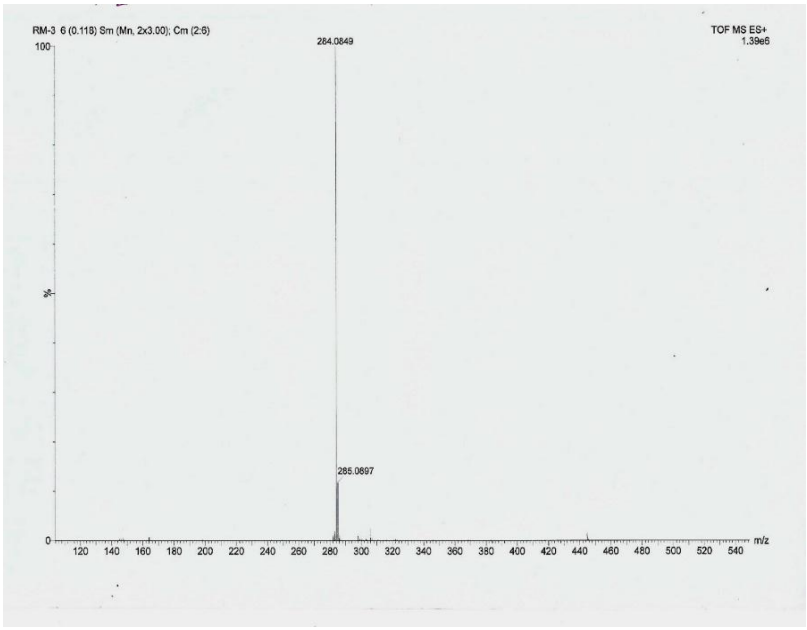

Figure 3. Mass spectra of synthesized compound **NMe2OH** showing M+1 peak at 264.0849.

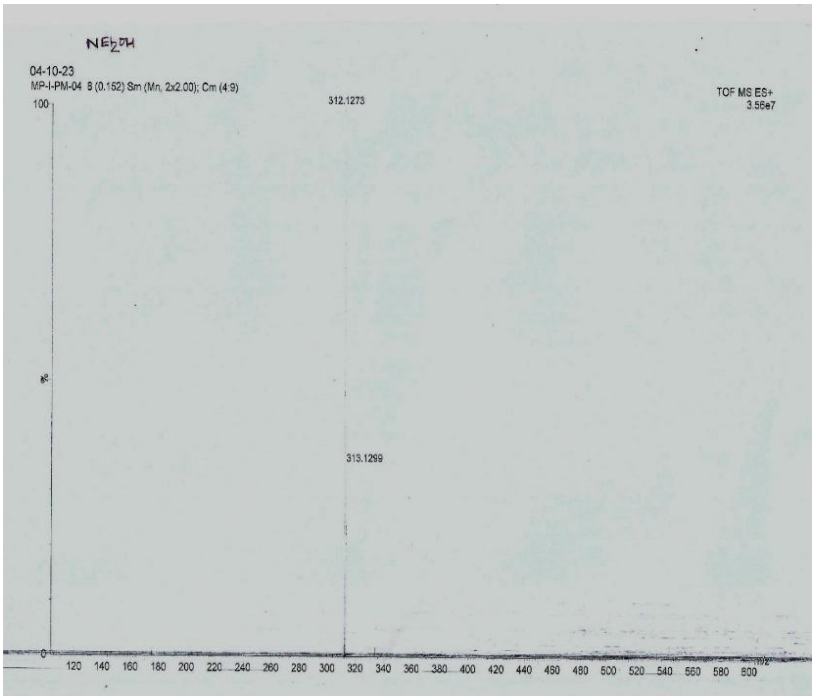

Figure 4. Mass spectra of synthesized compound **NEt$_2$OH** showing M+1 peak at 312.127.

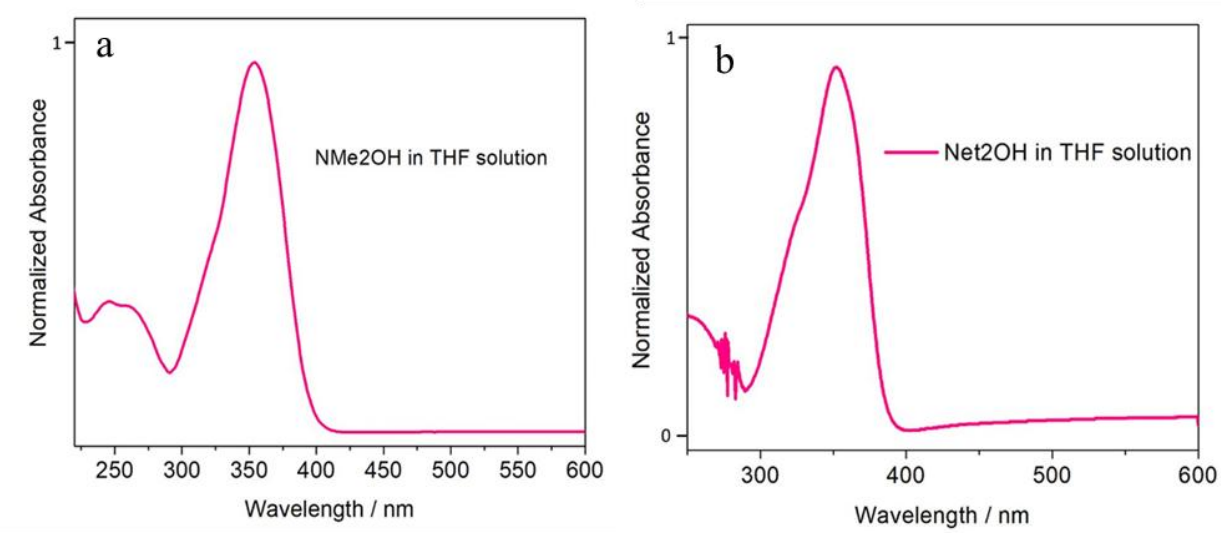

Figure 5. UV-Vis spectra of (a) **NMe_2OH** (b) **NEt_2OH** in THF solution (1 x 10-5 M).

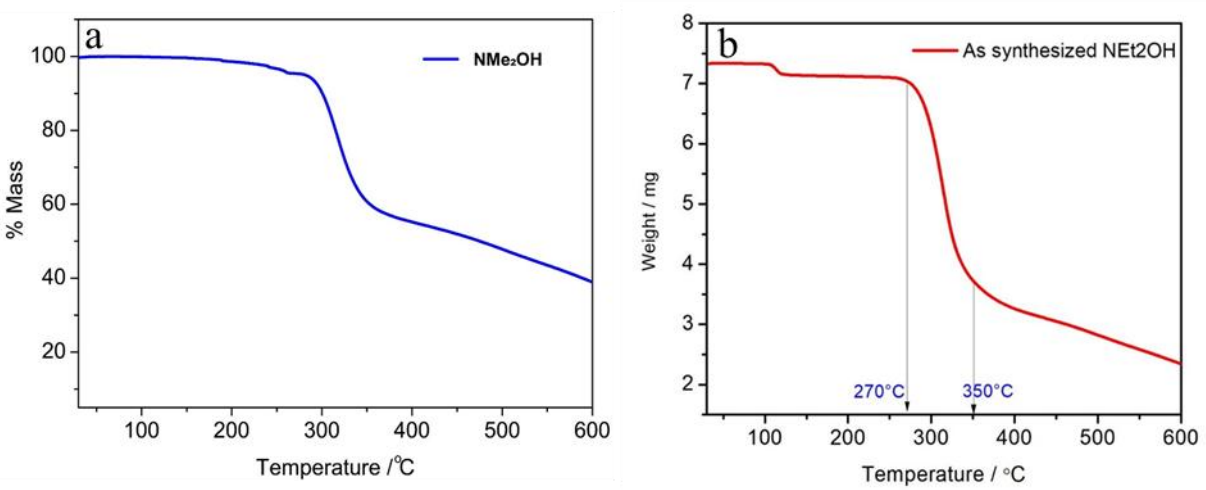

Figure 6. TGA thermograms of as-synthesized (a) **NMe_2OH** (b) **NEt_2OH**.

Crystallization Procedure: NMe_2OH crystals were obtained by slow evaporation of a methanol solution at room temperature. In this case, the crystals obtained from the mother liquor were all cyan emissive **NEt_2OH-FL**. Recrystallization of as-synthesized **NEt_2OH-FL** from methanol solution provided both **NEt_2OH-FL** and **NEt_2OH-NFL** crystals, which were segregated under a fluorescence microscope. Even though the structural data of **NMe_2OH** and **NEt_2OH-NFL** have been reported earlier, we had to collect our X-ray data as a process of polymorph screening.

5.3 Results and discussions:

The compounds **NMe_2OH** and **NEt_2OH** were synthesized via a Schiff base condensation reaction between 4-hydroxybenzhydrazide and either 4-(dimethylamino)benzaldehyde or 4-(diethylamino)benzaldehyde in methanol, with a catalytic amount of acetic acid facilitating the reaction. Both compounds were characterized using ^1H NMR and mass spectrometry, confirming their structural integrity. Thermogravimetric analysis revealed that the synthesized materials exhibit thermal stability up to approximately 250°C.

5.3.1 Solid-State Optical Properties:

Yellow, cuboidal-shaped single crystals of **NMe_2OH** were successfully obtained from methanol. However, despite multiple attempts, no alternative polymorphs of **NMe_2OH** could be isolated. The UV–Vis spectra of **NMe_2OH** and **NEt_2OH** in THF solution (1×10^{-5} M) revealed absorption bands with λ_{max} at 354 nm and 352 nm, respectively. Under fluorescence microscopy at 365 nm excitation, **NMe_2OH** crystals exhibited a bright cyan-blue emission with λ_{max} at 468 nm, which remained unchanged upon exposure to pressure or thermal stimuli.

In contrast, **NEt_2OH** crystallized from methanol resulted in two distinct polymorphs with varying crystal structures and fluorescence behavior. The prismatic-shaped **NEt_2OH-FL** crystals emitted cyan fluorescence ($\lambda_{em,max}$ = 480 nm) under UV light, whereas the **NEt_2OH-NFL** polymorph was non-emissive (figure 7). These differences in crystal habits and emission properties allowed for their easy separation using fluorescence microscopy, facilitating further experimental studies.

To analyze their stimuli-responsive luminescence, the polymorphs were subjected to thermal, pressure, and light stimuli to monitor emission variations. Similar to **NMe_2OH**, the fluorescence of **NEt_2OH-FL** crystals remained unaffected by shear pressure, indicating minimal alteration in molecular packing. However, annealing **NEt_2OH-FL** at 150°C resulted in the loss of solid-state luminescence, which did not recover upon cooling to room temperature, suggesting an irreversible structural transformation due to thermal exposure. Interestingly, when shear pressure was applied (using a mortar and pestle) to the thermally treated nonfluorescent **NEt_2OH-FL**, the emission partially reappeared at $\lambda_{em,max}$ = 490 nm, emitting with reduced intensity compared to the original crystal.

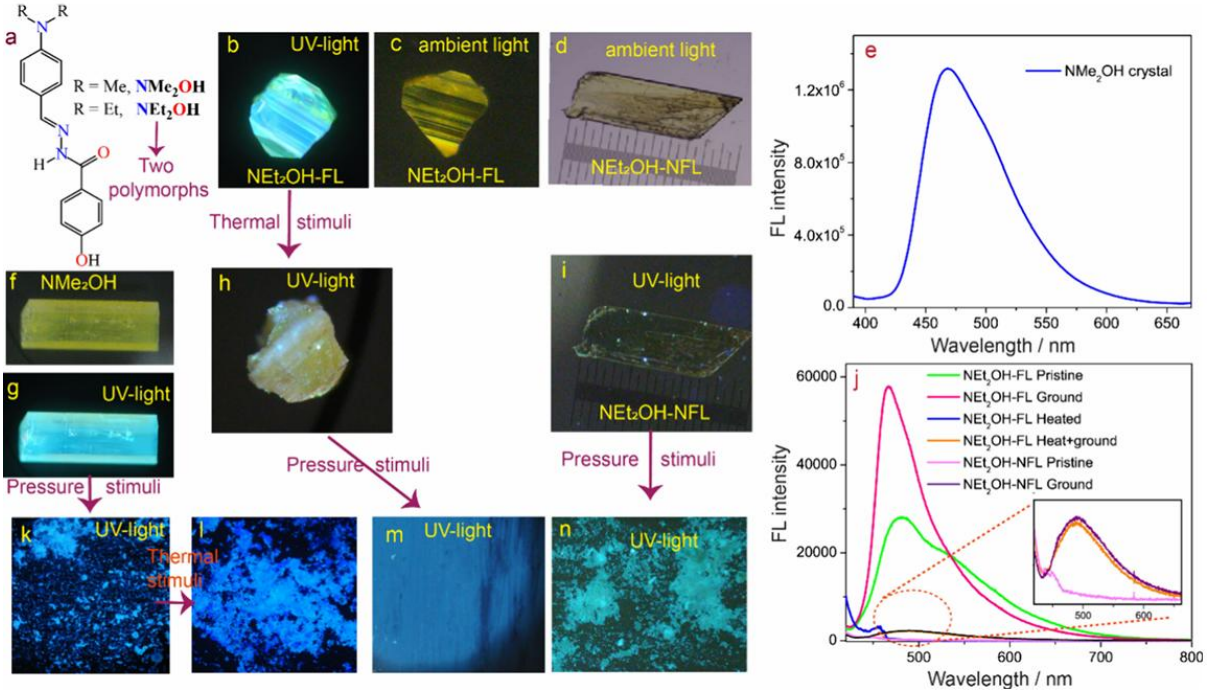

Figure 7. Schematic illustration of stimuli-responsive luminescence switching of the crystals. (a) Molecular structure of the compounds; (b, c) Optical images of **NEt_2OH-FL** crystal under UV light and visible light; (e) solid-state fluorescence spectra of **NMe_2OH**;(f,g,k,l) optical images of **NMe_2OH** crystal under UV light and visible light and its stimuli-responsive luminescence behavior; (h,m) stimuli-responsive behavior of **NEt_2OH-FL** crystal; (i,n) stimuli-responsive behavior of **NEt_2OH-NFL** crystal; (j) solid-state fluorescence spectra of **NEt_2OH-FL** and **NEt_2OH-NFL** under different stimuli.

Table 1 Solid state Fluorescence life time values of the crystals.

Samples (solid state)	**Fluorescence life time values τ (ns)**
NMe_2OH λ_{ex} = 370nm λ_{em}= 468nm	τ_1 = 2.84 ± 0.018 (100 %) χ^2 = 1.09
NEe_2OH-FL λ_{ex} = 370nm λ_{em}= 480nm	τ_1 = 1.45 ± 0.066 (60.12%) τ_2 = 10.63 ± 0.522 (39.88%) χ^2 = 1.19
NEe_2OH-NFL ground λ_{ex} = 370nm λ_{em}= 470nm	τ_1 = 0.43 ± 0.013(94.5%) τ_2 = 2.63 ± 0.107 (5.5%) χ^2 = 1.08

On the other hand, the **NEt₂OH-NFL** crystals, which were inherently non-emissive, displayed a luminescence "turn-on" effect when subjected to mechanical grinding, emitting a cyanish-green fluorescence at $\lambda_{em,max}$ = 491 nm. Powder X-ray diffraction (PXRD) analysis of ground **NEt₂OH-NFL** exhibited shifts in 2θ peak positions and the appearance of new diffraction peaks, indicating significant lattice reconfiguration under mechanical stress. These observations highlight the crucial role of molecular packing and intermolecular interactions in determining the stimuli-responsive luminescence properties of these polymorphic crystals. The solid-state luminescence properties of the crystals are significantly influenced by their molecular conformation, packing arrangement, and intermolecular interactions. To identify the structural features responsible for these distinct luminescence behaviors, X-ray crystallographic analysis was conducted on all studied crystals.

5.3.2 X-Ray crystallographic analysis:

The conformational analysis of molecular structures within their respective lattices revealed variations in orientation and electronic conjugation, which play a crucial role in determining their luminescent properties.

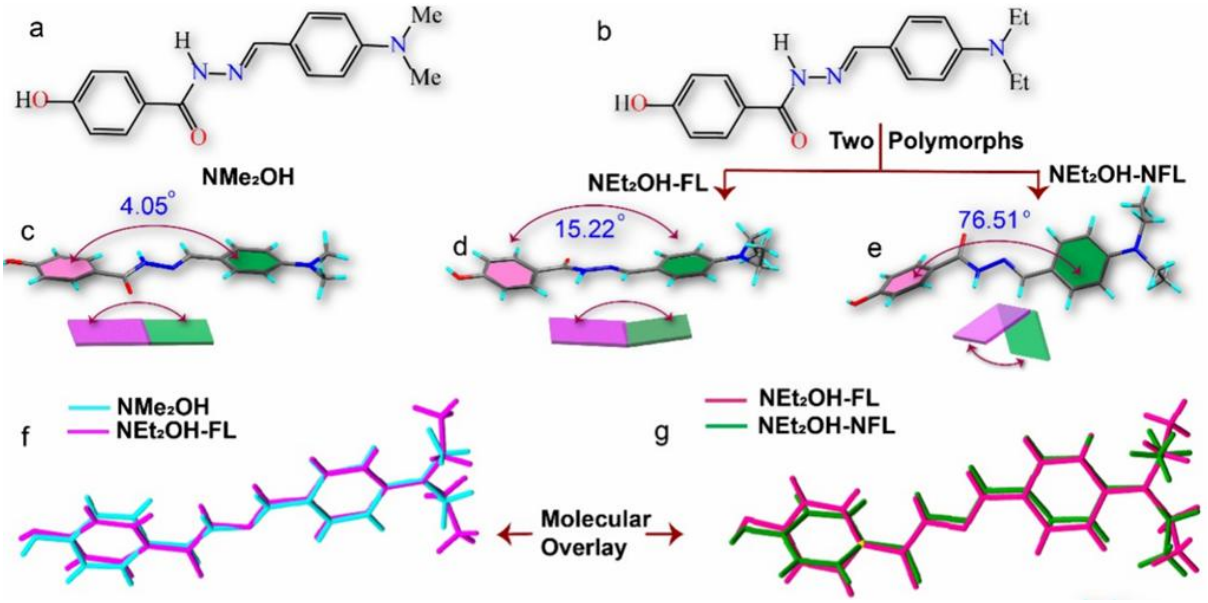

Figure 8. (a, b) Molecular structures of **NMe₂OH** and **NEt₂OH.** (c) Crystal structure of **NMe₂OH** Article showing the interplanar angle between two terminal phenyl rings. (d) Interplanar angle in **NEt₂OH** lattice molecules. (e) Interplanar angle in **NEt₂OH-FL** and **NEt₂OH-NFL**. (f) Overlay of **NMe₂OH-NFL** lattice molecules (g) Overlay of **NEt₂OH-FL**.

The **NMe_2OH** crystals, obtained from methanol solution, crystallized in a monoclinic system with a $P2_1$ space group (cell parameters: a = 6.1510 Å, b = 18.1218 Å, c = 13.3714 Å, $\alpha = \gamma = 90°$, $\beta = 95.413°$). Structural analysis showed that the terminal aromatic rings of the **NMe_2OH** molecule are almost coplanar (4.05°), enabling effective electronic conjugation. This planar molecular configuration (Figure 8) enhances electronic communication within the crystal lattice and is likely responsible for its intense cyan luminescence in the solid state. Within the lattice, molecules are stabilized by both strong and weak hydrogen bonding interactions, which limit rotational movement and promote radiative emission. Lattice water molecules form hydrogen bonds between antiparallel molecular orientations, with interaction distances of 3.006 Å and 3.041 Å, extended along the crystallographic a-axis. Additionally, π–π stacking interactions between aromatic rings (centroid-to-centroid distance: 3.927 Å) and strong hydrogen bonding interactions involving the phenoxy O–H group and acyl oxygen (O1–H1···O4 at 2.684 Å, 159.7° and O3–H3···O2 at 2.702 Å, 170.4°) contribute to the "herringbone" packing arrangement observed in the crystal structure. Overall, the specific packing arrangement and intermolecular forces within **NMe_2OH** crystals play a vital role in maintaining their luminescent characteristics, offering insights into their potential applications in functional materials.

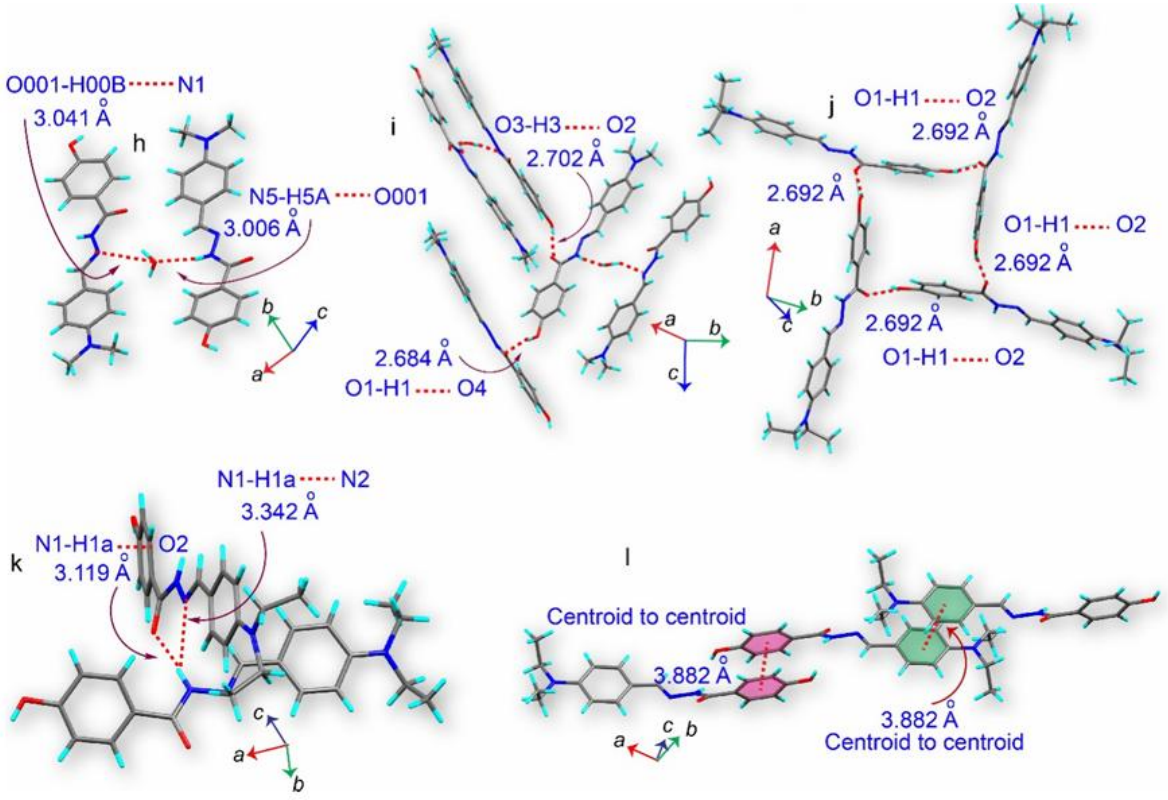

Figure 9. Noncovalent interactions in (h,i) **NMe_2OH** and **NEt_2OH,** (j,k) **NEt_2OH-FL**, and (l) **NEt_2OH-NFL** crystals.

Apart from the above interactions, several other H-bonding interactions (Figures 9) connect and stabilize the molecules in the crystal lattice (N6−H6···O3, 3.174 Å, 129°, O1−H1···N4, 3.242 Å, 129.4°. The compound **NEt₂OH-FL** crystallizes in the tetragonal system with the space group $I4_1/a$, exhibiting cell parameters of 22.3869 Å, 22.3869 Å, and 14.9090 Å. Its lattice contains disordered methanol solvent molecules, influencing its structural properties. A key distinction between the two polymorphs of **NEt₂OH** (**NEt₂OH-FL** and **NEt₂OH-NFL**) lies in their molecular conformations and intermolecular interactions, which appear to be the primary factors governing their luminescence behavior. The **NEt₂OH-FL** molecule adopts a nearly planar configuration, with an interplanar angle of approximately 15.22°, which enhances electronic conjugation within the structure and supports strong solid-state luminescence. Overlay diagrams comparing **NMe₂OH**, **NEt₂OH-FL**, and its non-emissive counterpart **NEt₂OH-NFL** reinforce the importance of molecular conformation in dictating luminescence properties. Although **NMe₂OH** and **NEt₂OH-FL** differ in substitution, both maintain a similar planar structure (Figure 8f), which explains their enhanced solid-state fluorescence.

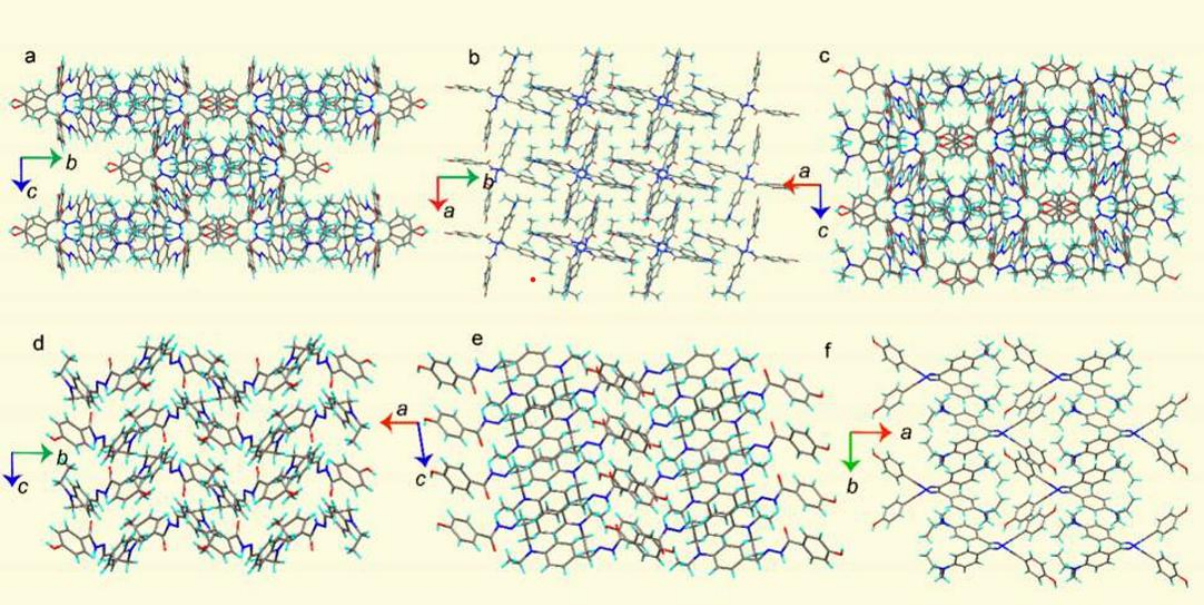

Figure 10. Packing structure of (a−c) **NEt₂OH-FL** crystal and (d−f) **NEt₂OH-NFL** crystal from different crystallographic directions.

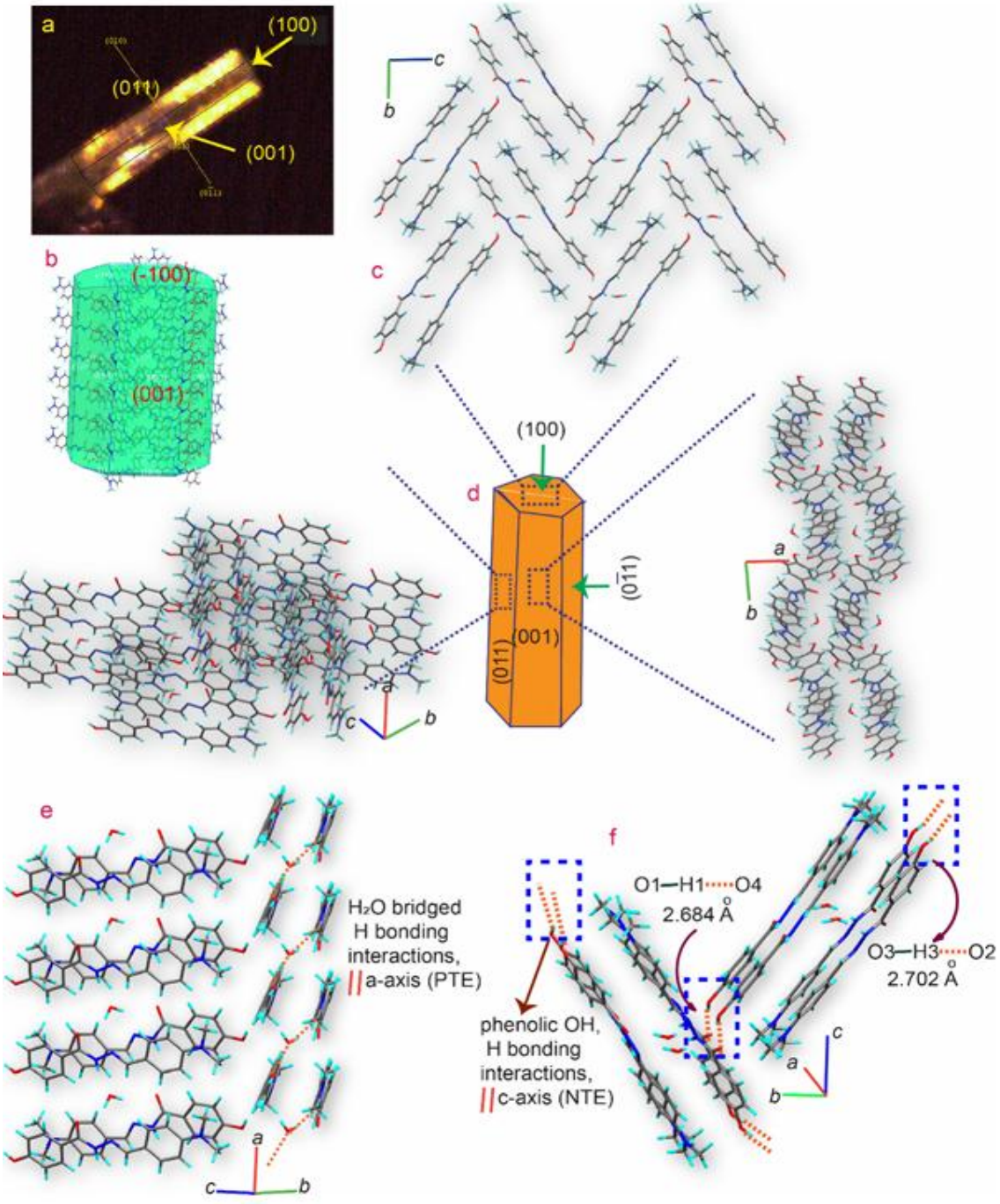

Figure 11. (a) Face indexing of **NMe_2OH** morphology of the **NMe_2OH** crystal. (b) BFDH crystal. (c, d) Packing diagrams of the **NMe_2OH** crystal from different crystallographic directions. (e) Water-bridged H-bonding interactions that stich the molecules along the crystallographic a-axis. (f) H-bonding interaction involving phenolic −OH group extended roughly along the crystallographic c axis.

Table 2. Single crystal X-ray structure parameters of **NMe_2OH**, **Net_2OH-FL** and **Net_2OH-NFL** at 298 K.

Compound	**NMe_2OH-G**	**Net_2OH-FL**	**Net_2OH-NFL**
CCDC deposit No.	2304044	2359645	2304045
Chemical formula	$C_{32}H_{34}N_6O_4$, H_2O	$C_{18}H_{21}N_3O_2$, 0.5 CH_3OH	$C_{18}H_{21}N_3O_2$
M_r	584.67	327.408	311.38
Crystal system	Monoclinic	Tetragonal	Monoclinic
Space group	$P\,2_1$	$I\,4_1/a$	$P\,2_1/c$
a / Å	6.1510(6)	22.3869(19)	14.8532(3)
b / Å	18.1218(17)	22.3869(19)	12.5608(2)
c / Å	13.3714(12)	14.9090(18)	9.33010(10)
α / °	90	90	90
β / ° γ / °	95.413(3) 90	90 90	97.9650(10) 90
V / Å^3	1483.8(2)	7472.0(16)	1723.91(5)
Z	2	16	4
ρ_{calc} / (g cm^{-3})	1.309	1.164	1.200
μ / mm^{-1}	0.090	0.079	0.080
F_{000}	620	2801.79	664
θ_{min} / °	2.25	2.450	2.74
θ_{max} / °	27.12	29.252	27.05
Reflections collected	100361	51130	25906
Independent reflections	6472	3384	3772
GoF	1.052	1.2845	1.035
Final R indices [$I > 2\sigma(I)$]	$R_1 = 0.0339$ $wR_2 = 0.0972$	$R_1 = 0.0626$ $wR_2 = 0.1849$	$R_1 = 0.0727$ $wR_2 = 0.1969$
R indices (all data)	$R_2 = 0.0348$ $wR_2 = 0.0960$	$R_2 = 0.0999$ $wR_2 = 0.2741$	$R_2 = 0.0839$, $wR_2 = 0.2149$

In contrast, the **NEt₂OH-NFL** polymorph adopts a markedly different molecular orientation, resulting in no detectable luminescence. This observation suggests that planarity plays a crucial role in the optical characteristics of the crystals. Additionally, strong hydrogen bonding interactions further stabilize the **NEt₂OH-FL** lattice. The O1−H1···O2 interaction (2.692 Å, 157.71°) forms a tetrameric H-bonded network, linking acyl oxygen (O) with phenolic OH groups from neighboring molecules (Figure 9j). The crystal also contains weaker bifurcated hydrogen bonds, where the amide N−H interacts with imine nitrogen (N) and acyl oxygen (O2) at distances of 3.342 Å (135.39°) and 3.119 Å (152.39°), respectively (Figure 9k). These structural elements contribute to the distinct properties exhibited by the two polymorphs, reinforcing the role of molecular packing and noncovalent interactions in tuning solid-state luminescence behavior. The compound **NEt₂OH-NFL** crystallizes in a monoclinic system with $P2_1/c$ space group and cell parameters of 14.8532 Å, 12.5608 Å, and 9.33010 Å along with angles 90°, 97.9650°, and 90°. Unlike its luminescent counterpart **NEt₂OH-FL**, the **NEt₂OH-NFL** molecule adopts a highly puckered structure, with an interplanar angle of approximately 76.51° (Figure 8e, g). This distorted conformation leads to poor electronic communication within the molecule, which is likely responsible for its non-luminescent nature. Additionally, the structure features moderately strong π–π stacking interactions between two antiparallel molecules, with a centroid-to-centroid distance of 3.882 Å (Figure 9l). These interactions further suppress luminescence by restricting efficient electronic transitions. However, applying shear pressure to **NEt₂OH-NFL** crystals can lead to molecular rearrangement, enhancing intramolecular planarity. This pressure-induced conformational shift is expected to disrupt π–π stacking interactions between phenyl rings, effectively altering the crystal's electronic properties. This structural modification likely explains the luminescence "turn-on" effect observed upon mechanical grinding of **NEt₂OH-NFL** crystals. Packing analysis reveals that molecules within **NEt₂OH-NFL** are interconnected through two distinct hydrogen bonding interactions. One interaction involves amide N-H with acyl oxygen (N1−H4···O2 at 2.864 Å, 132.66°), extending along the crystallographic c-axis, while the second phenolic OH-imine nitrogen interaction (O1−H1···N2 at 2.804 Å, 166.01°) further stabilizes molecular packing (figure 12). The arrangement of molecules along different crystallographic directions is illustrated in figure 10, showcasing the interplay of noncovalent interactions that dictate structural properties. This detailed structural insight highlights the impact of molecular conformation and packing forces on the crystal's stimuli-responsive behavior, paving the way for further investigations into mechanically triggered luminescent switching mechanisms.

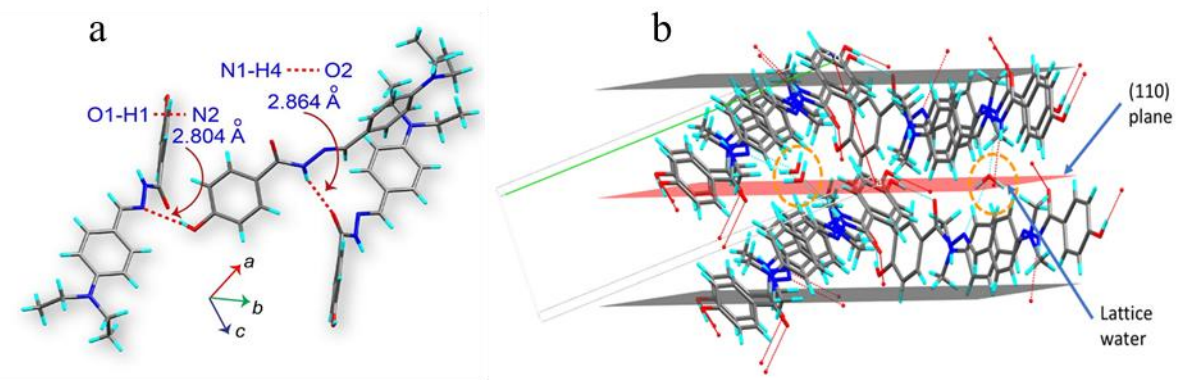

Figure 12. (a) H-bonding interactions in **NEt_2OH-NFL** crystal. (b) H-bonding interactions involving lattice water molecules in **NMe_2OH** crystal.

Table 3. Noncovalent intermolecular interactions in the crystals

	D–H•••A	**D–A distance / Å**	**<DHA angle /^{0}**
NMe_2OH			
	O1–H1 ••• O4	2.684(2)	159.7
	C112–H11A•••O1	3.433(3)	151.4
	O1–H1 ••• N4	3.242(2)	129.4
	C7–H7•••O3	3.290(3)	127.2
	C23–H23•••O001	3.300(3)	147.6
	C27–H27•••N1	3.610(3)	169.0
	N5–H5A•••O001	3.006(2)	167(3)
	N6–H6•••O3	3.174(3)	129(3)
NEt_2OH-NFL			
	O1–H1••• N2	2.8037(19)	166.0
	N1–H4••• O1	3.178(2)	137.3
	N1–H4••• O2	2.8642(18)	132.7
	C2–H2 •••N1	3.517(2)	147.8

5.3.3 Thermosalient property:

While investigating the thermal effects on the luminescence properties of the crystals, an unexpected discovery emerged—certain crystals exhibited motion, jumping, splitting, and cracking upon heating on a hot surface. This intriguing behavior prompted a deeper exploration into the thermos-responsive actuation of these crystals. To systematically study this Phenomenon, each crystal was placed on a hot plate under an optical microscope, and its behavior was observed at specific temperature points. Among the tested compounds, **NMe_2OH** and **NEt_2OH-FL** crystals demonstrated remarkable thermosalient (TS) behavior, a phenomenon in which a crystal jumps, moves, or alters its shape due to the rapid release of stored elastic energy during a thermal phase transition.

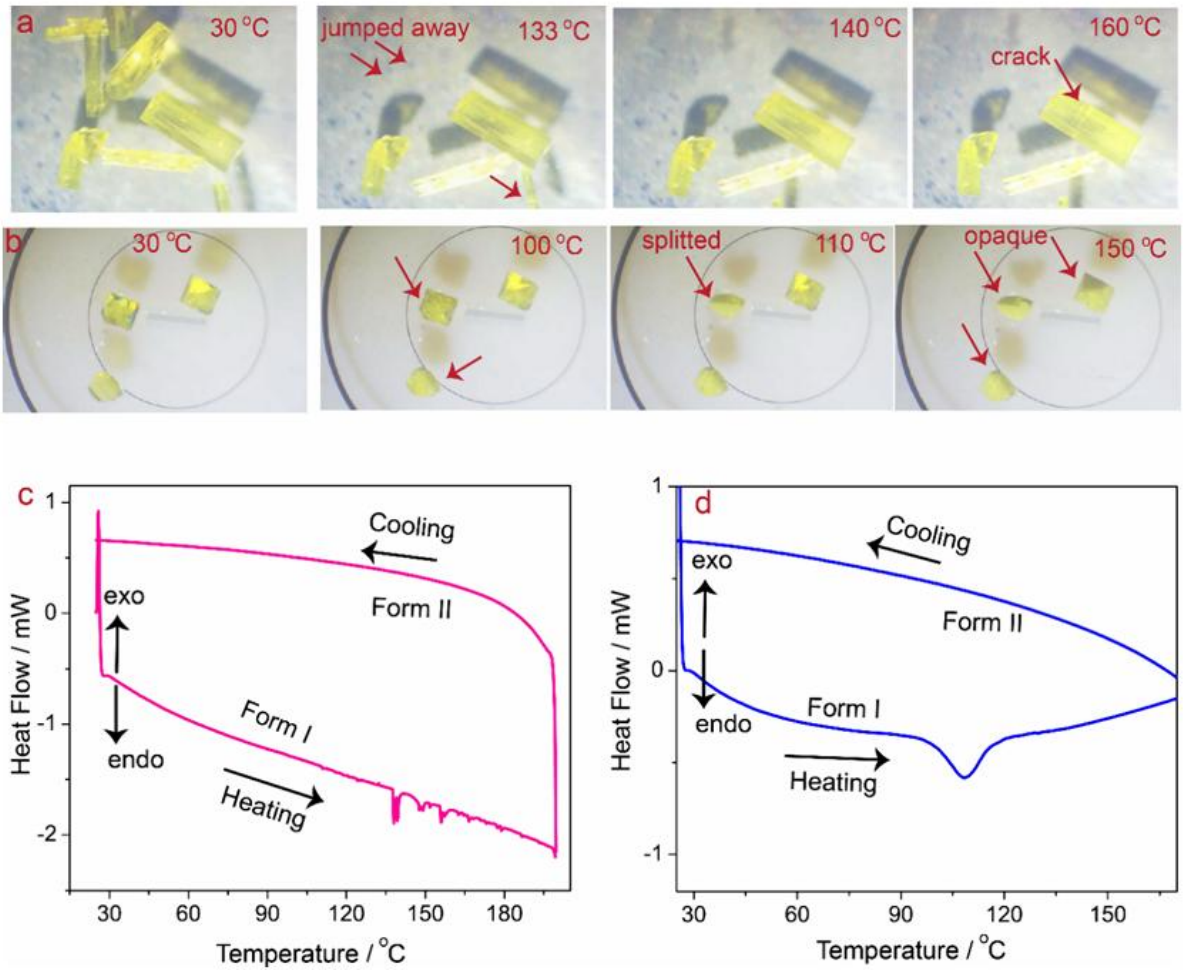

Figure 13. Digital camera snapshots of TS motions in (a) **NMe_2OH** crystal and (b) **NEt_2OH-FL** crystal. (c) DSC thermogram of **NMe_2OH** crystals and (d) **NEt_2OH-FL** crystals.

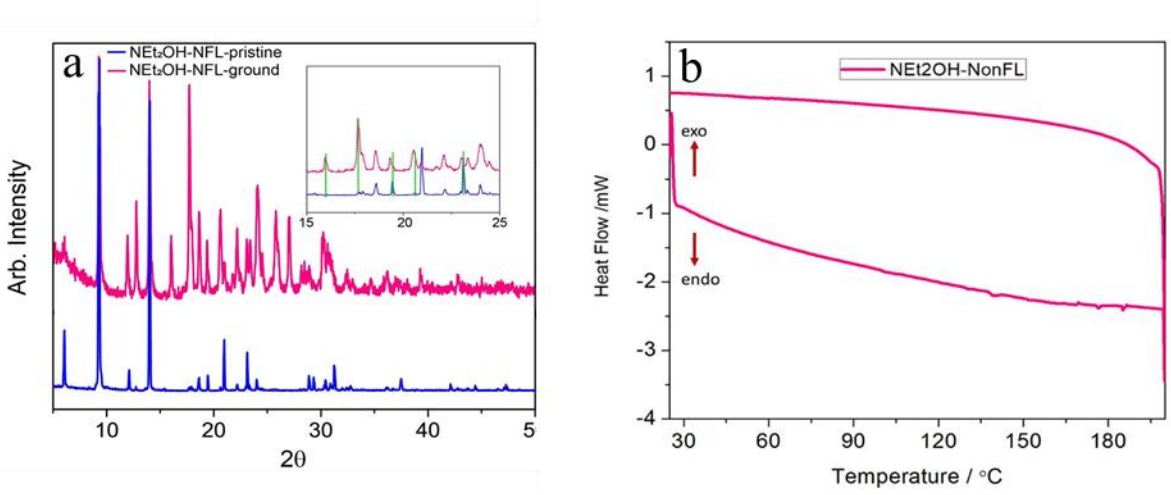

Figure 14: (a) PXRD profile of the **NEt₂OH-NFL** crystal before and after shear mechanical pressure. (b) DSC profile of **NEt₂OH-NFL** crystal.

When **NMe₂OH** crystals were positioned on a wider (001) face and heated up to 160°C, they abruptly jumped within a temperature range of approximately 130–145°C (Figure 13). Notably, a 0.4 × 0.2 × 0.1 mm crystal exhibited a jumping distance of about 10 cm, nearly 25 times greater than its actual length. In certain instances, instead of jumping, the crystal displayed cracking and minor movements, highlighting variations in mechanical response.

This mechanical effect was observed only once per heating-cooling cycle, indicating that the transition was irreversible. Interestingly, the size of the crystal played a crucial role, as smaller crystals jumped at lower temperatures, whereas larger ones required higher temperatures to exhibit similar behavior. To gain a comprehensive understanding of this size-dependent kinematic behavior, a detailed analysis was conducted on 15 crystals of various dimensions, confirming that crystal size significantly influences its thermosalient activity (figure 18). These observations provide key insights into stimuli-responsive materials and their potential applications in smart actuation systems, dynamic molecular devices, and high-performance materials that harness the mechanical effects of thermal stimuli. When examining the thermosalient (TS) behavior of crystals, it was observed that smaller crystals exhibited more pronounced jumping behavior, whereas larger crystals tended to split or crack upon heating. After undergoing a TS transition or jumping, the crystals became opaque and developed multiple surface cracks, indicating a significant loss in crystallinity. Scanning Electron Microscopy (SEM) images provided further evidence, clearly revealing surface defects and fractures formed during the crystal-to-crystal TS phase transition (Figure 15).

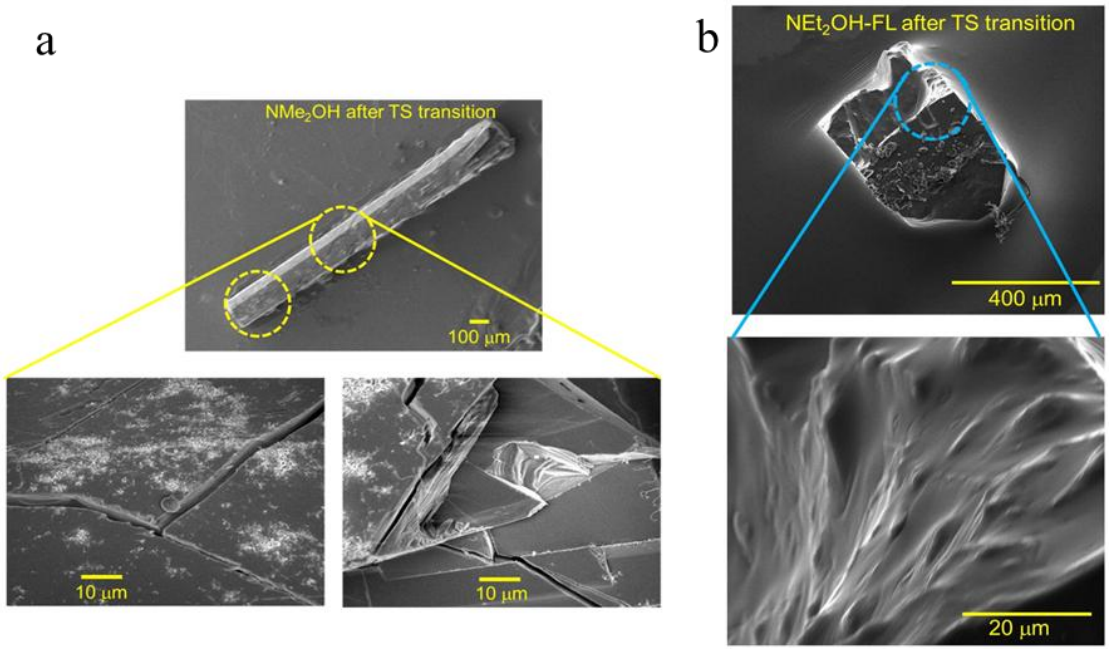

Figure 15: (a) SEM images of the **NMe₂OH** crystal (b) **NMe₂OH-FL** showing cracks and defects on the crystal surface after TS transition.

This cracking and structural disruption increases the mosaicity of the crystal, leading to substantial degradation in the crystallinity of the high-temperature form-II phase. This loss of crystallinity was confirmed through Variable Temperature Powder X-ray Diffraction (VT-PXRD) studies (Figure 16).

Despite repeated attempts, obtaining the crystal structure of the high-temperature form-II phase proved challenging, as the drastic reduction in crystalline order hindered successful characterization. Additionally, Differential Scanning Calorimetry (DSC) thermograms of **NMe₂OH** crystals exhibited distinct endothermic peaks within the 137–150°C range, which correspond to the TS phase transition from form-I to form-II (Figure 13c). The process was found to be irreversible, further emphasizing the profound structural changes occurring upon thermal excitation. These findings contribute valuable insights into thermal actuation mechanisms in molecular crystals, reinforcing the influence of molecular conformation and packing arrangements on stimuli-responsive properties.

The two polymorphs of the ethyl-substituted derivative (**NEt₂OH-FL** and **NEt₂OH-NFL**) exhibit markedly different thermomechanical behaviors. While the fluorescent polymorph **NEt₂OH-FL** shows strong thermosalient (TS) actuation upon heating, the nonfluorescent polymorph **NEt₂OH-NFL** remains unresponsive to thermal stimuli. Under controlled heating on a hot plate equipped with an optical microscope, prismatic-shaped **NEt₂OH-FL** crystals

(dimensions: 0.50 × 0.40 × 0.30 mm, form-I) displayed splitting and jumping movements, reaching distances of approximately 5 cm, before turning into an opaque solid at 107°C (form-II, Figures 13b, 15). The Differential Scanning Calorimetry (DSC) thermogram for **NEt₂OH-FL** confirmed the TS transition with an endothermic peak at 108°C. Similar to **NMe₂OH-** crystals, a dimension-dependent kinematic study of **NEt₂OH-FL** revealed that smaller crystals tend to jump more easily, whereas larger ones typically splinter, jump briefly, or crack during TS transition (Figure 13). Scanning Electron Microscopy (SEM) images of splintered crystals showed fractured surfaces and structural defects, emphasizing the mechanical stress endured during thermal activation.

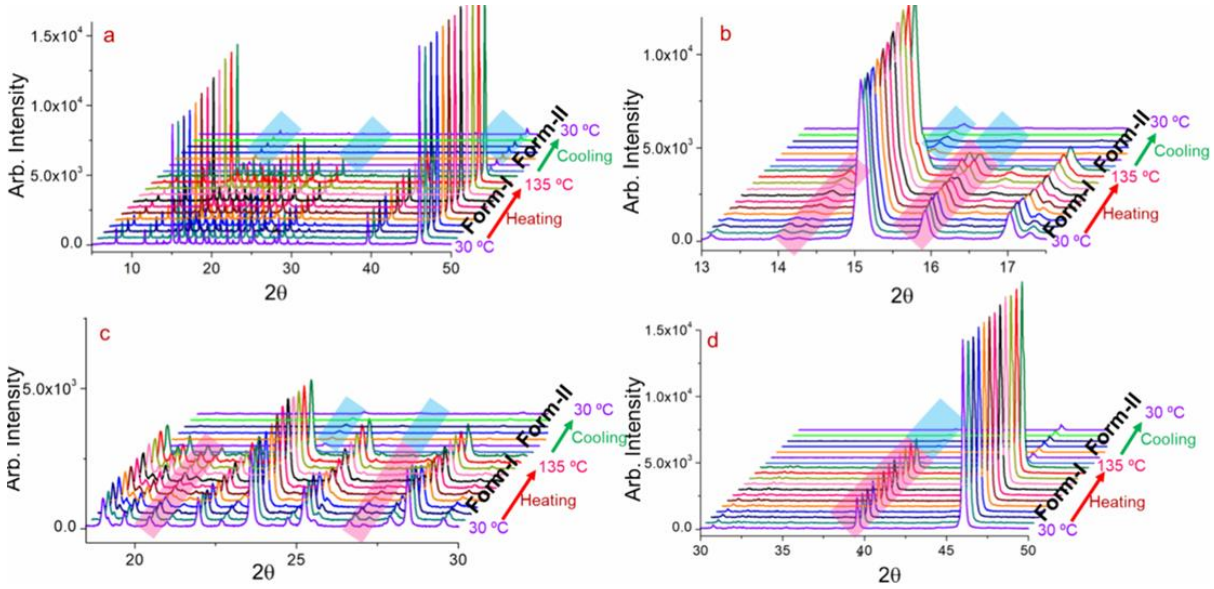

Figure 16: VT-PXRD profiles of **NMe₂OH** crystal. (a) Full profile. (b−d) Expanded view showing the change (pink shades are for form-I and blue shades are for form-II) in the PXRD profile upon heating and phase transition. The data were taken at 25, 50, 90, 100, 105, 110, 115, 120, 125, 130 °C, and finally at 135 °C on heating followed by cooling, and final data were collected at 30 °C to complete the cycle. Note that the peak intensity drastically decreased (panel a) during cooling, suggesting the loss of crystallinity after TS phase transition.

In sharp contrast, **NEt₂OH-NFL** crystals do not exhibit thermoresponsive actuation or any mechanical effects when subjected to thermal stimuli. This inert behavior is attributed to its unfavorable molecular packing, which restricts the release of stored elastic energy. The DSC thermogram of **NEt₂OH-NFL** further supports this observation, confirming the absence of TS phase transitions (Figure 14b). These findings underscore the critical role of molecular packing and structural conformation in determining thermomechanical responses, providing valuable insights for designing functional materials with tunable actuation properties.

The variable-temperature powder X-ray diffraction (VT-PXRD) analysis was conducted to investigate the structural changes occurring during the thermosalient (TS) transition. At 30°C, the PXRD pattern of **NMe₂OH** displayed sharp diffraction peaks, indicating high crystallinity. The experimental PXRD data closely matched the simulated PXRD pattern derived from single-crystal structure analysis. However, upon heating the sample to 135°C, a noticeable shift in diffraction peaks was observed, reflecting lattice deformation during the transition.

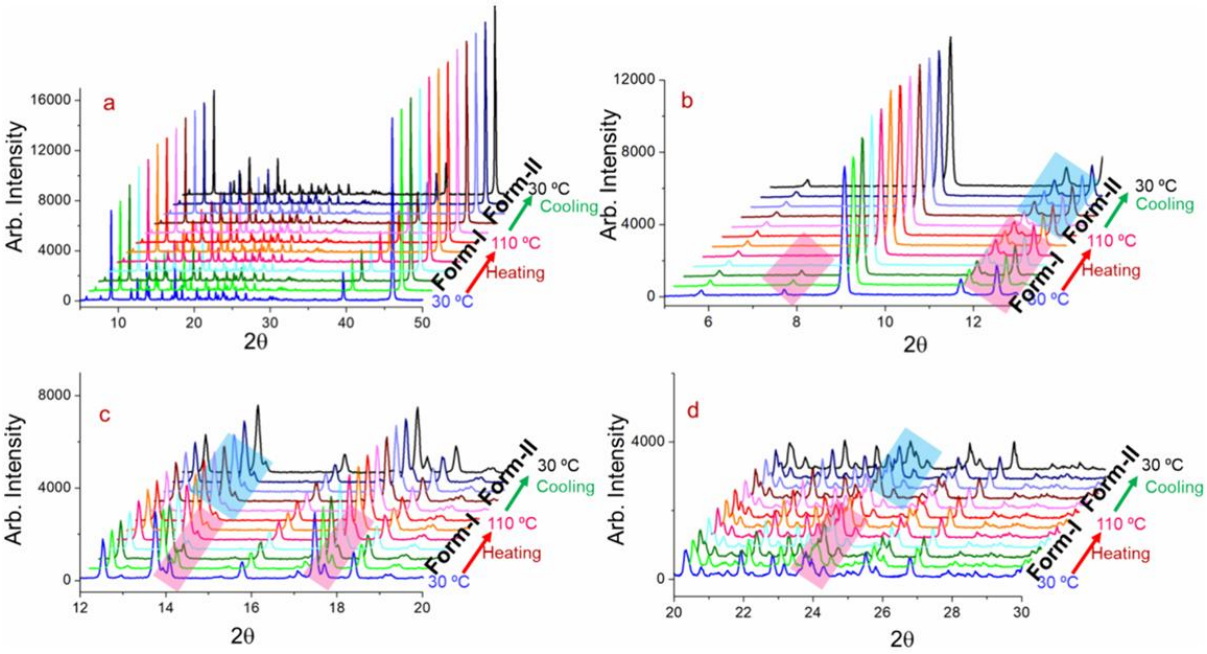

Figure 17: VT-PXRD profiles of **NEt₂OH-FL** crystal. (a) Full profile. (b–d) Expanded view showing the change (pink shades are for form-I and blue shades are for form-II) in the PXRD pattern upon heating and phase transition. The data were taken at 30, 50, 90, 100 °C and finally at 110 °C on heating followed by cooling, and the final data were collected at 30 °C to complete the cycle.

In the pre-phase transition region (form-I), the peak intensity remained nearly unchanged. However, following the TS transition, a significant reduction in peak intensity was recorded, confirming the poor crystallinity of the high-temperature form-II phase. This aligns with previous findings that TS phase transitions are closely associated with anisotropic thermal expansion of the unit cell axes. The VT-PXRD results further validate that **NMe₂OH** form-I crystals undergo anisotropic expansion upon heating to the phase transition temperature. Specifically: The diffraction peak at 2θ = 6.45° (at 30°C) for the (001) plane shifted to 6.56° at 130°C, indicating negative thermal expansion (NTE) along the crystallographic c-axis. The peak at 2θ = 14.3° (30°C) for the (100) plane shifted to 14.2° at 130°C, demonstrating positive thermal expansion (PTE) along the a-axis, which is the longitudinal axis of the crystal.

Additionally, the peak at 2θ = 15.03° (30°C) for the (110) plane shifted to 14.94° at 130°C, suggesting an increase in interplanar distance.

Further packing analysis revealed that neighboring molecules in the lattice are bridged by water molecules through hydrogen bonding interactions that are orthogonal to the (110) planes (Figure 18). Thus, the increase in interplanar distance can be attributed to the rupturing of hydrogen bonds upon heating, leading to packing reconfiguration during the TS phase transition. Additionally, the overall peak shifts and transformations observed in the PXRD pattern support the occurrence of the TS phase transition at 135°C, reinforcing the role of molecular packing and intermolecular interactions in governing thermomechanical responses.

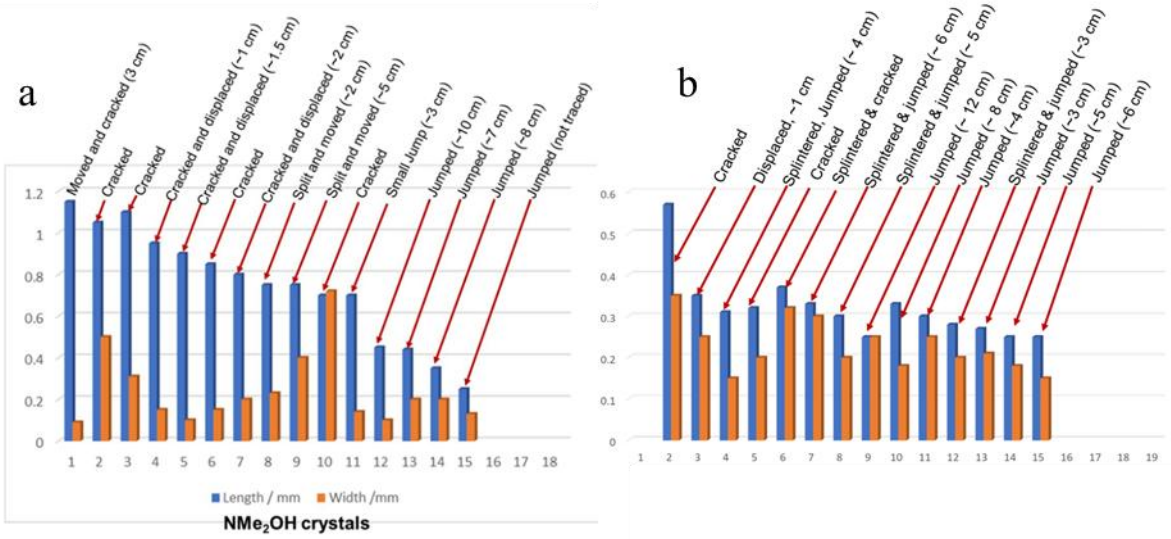

Figure 18. Size-dependent kinematic statistics of thermosalient effect in (a) **NMe_2OH** and (b) **NEt_2OH-FL** crystals.

The PXRD pattern of **NEt_2OH-FL** undergoes significant changes upon heating from 30°C to 120°C, indicating lattice deformation and subsequent phase transition from form-I to form-II. As shown in Figures 17, the diffraction peak at 2θ = 7.70° (corresponding to the (200) plane at 30°C) disappears at higher temperatures, highlighting structural reconfiguration. Additionally, the peak at 2θ = 11.72° for the (002) plane shifts to 11.62° at 110°C, confirming positive thermal expansion along this direction.

Several other notable peak shifts were observed, including at 2θ = 13.77°, 14.07°, 17.4°, and 18.3°, further supporting the lattice distortion that drives the TS phase transition of **NEt_2OH-FL** from form-I to form-II. In contrast, **NEt_2OH-NFL** did not exhibit any thermal phase transition, suggesting its structural stability under heat. Consequently, only room-temperature

PXRD data were collected for **NEt₂OH-NFL** and compared with the simulated confirming its absence of thermally induced structural transformations.

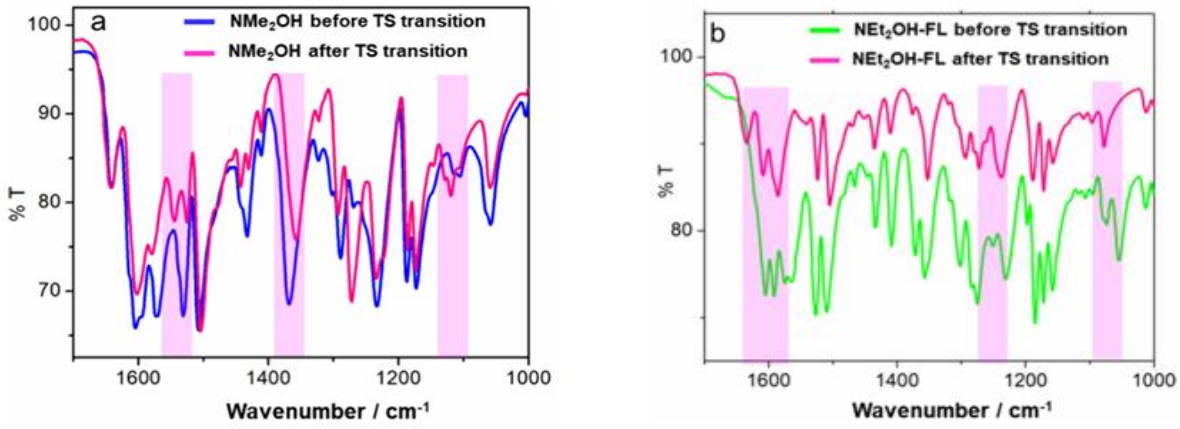

Figure 19: IR spectra of (a) **NMe₂OH** before and after TS transition and (b) **NEt₂OH-FL** before and after TS transition.

These findings reinforce the crucial role of molecular packing and intermolecular interactions in determining thermal phase transitions. To investigate how intermolecular interactions in the crystal lattice are influenced by the TS phase transition, IR spectroscopy was conducted before and after heating. The **NMe₂OH** crystals were subjected to 150°C for 30 minutes, then cooled to room temperature, and their IR spectra were recorded. As shown in Figures 19a, the stretching frequencies of the C=O (amide-I) bond remained largely unchanged, while a slight shift was observed for the C=N bond, shifting from 1605 cm^{-1} to 1601 cm^{-1}. Additionally, the N–H in-plane bending mode (amide-II) shifted from 1531 cm^{-1} to 1545 cm^{-1}, indicating significant reconfiguration of noncovalent interactions post-transition. Furthermore, the lattice water absorption frequencies at 3544 cm^{-1} and 3474 cm^{-1} disappeared, suggesting loss of water molecules from the lattice (figure 12). The phenolic O–H stretching frequency also red-shifted from 3358 cm^{-1} to 3289 cm^{-1}, signifying weakening of hydrogen bonding interactions upon the TS transition.

Similar trends were observed for **NEt₂OH-FL** crystals, which exhibited drastic changes in stretching frequencies following their TS phase transition. As seen in figure 19b, the C=O stretching vibration (amide-I) shifted from 1605 cm^{-1} to 1608 cm^{-1}, while the C=N stretching mode experienced a blue shift, moving to 1635 cm^{-1} post-transition. The N–H bending (amide-II) mode also exhibited a minor shift from 1527 cm^{-1} to 1524 cm^{-1}. These spectral variations point to changes in bond strengths and molecular packing, highlighting the reorganization of noncovalent interactions as the crystal undergoes thermal-induced structural transformation.

This detailed IR spectroscopy analysis provides critical insights into the role of hydrogen bonding and packing interactions in driving stimuli-responsive behavior in molecular crystals.

5.3.4 Theoretical findings

To better understand how noncovalent interactions contribute to lattice stabilization, Hirshfeld surface analysis and 2D fingerprint mapping were performed for all studied crystals. The percentage contribution of various intermolecular interactions, including O···H, N···H, C···H, and H···H, are presented in Table 4.

As illustrated in figure 20, **NMe₂OH** crystals exhibit a substantial fraction of hydrogen bonding interactions (O–H and N–H), accounting for 23.9% of the total intermolecular forces. These hydrogen bonds play a crucial role in stabilizing the lattice structure and facilitating packing reconfiguration during the TS phase transition. For the two polymorphic forms of **NEt₂OH**: **NEt₂OH-FL** shows O···H and N···H contributions of 14.4% and 7.4%, respectively. **NEt₂OH-NFL**, on the other hand, has significantly lower values, with O···H at 14.6% and N···H at 6.6% Table 4).

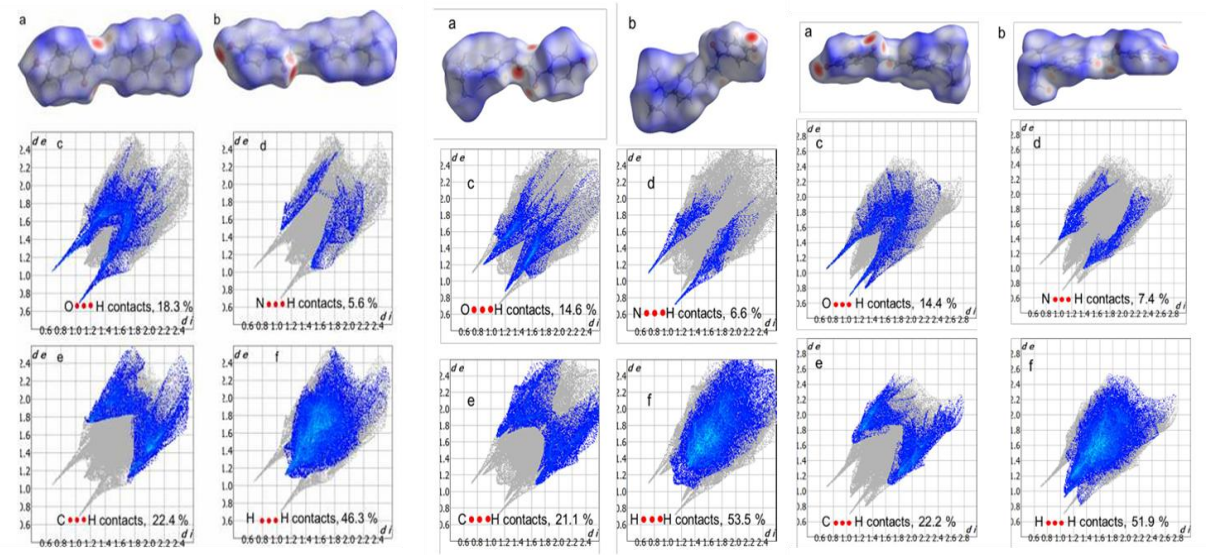

Figure 20: (a,b) Hirshfeld surface and (c–f) 2D fingerprint plots of **NMe₂OH** (Left) **NEt₂OH-NFL** (middle), **NEt₂OH-FL** (right) showing percentages of various interactions present in the crystal lattice.

These findings highlight the impact of intermolecular interactions on crystal stability and reveal how hydrogen bonding influences thermomechanical behavior. The differences between **NEt₂OH-FL** and **NEt₂OH-NFL** emphasize the role of molecular packing and bonding strength in determining their stimuli-responsive properties.

Table 4. Percentage (%) of intermolecular interactions present in **NMe_2OH**, **Net_2OH-NFL** and **Net2OH-FL** crystals derived from Hirshfeld surface analysis.

Interactions	NMe_2OH	NEt_2OH-NFL	NEt_2OH-FL
% O•••H	18. 3	14.6	14.4
% N•••H	5.6	6.6	7.4
% C•••H	22.4	21.1	22.2
% H•••H	46.3	53.5	51.9

5.3.5 Probable Mechanism of jumping

The mechanistic model proposed in Figure 21 provides a comprehensive understanding of luminescence switching and thermosalient (TS) effects in molecular crystals. Single-crystal overlay analysis confirms that the lattice molecules in **NMe_2OH** and **NEt_2OH-FL** crystals adopt a nearly planar conformation (Figure 8f), enabling both solid-state luminescence and TS phase transition. While molecular planarity enhances electronic conjugation, ensuring fluorescence, it must also prevent strong π–π stacking interactions, which can suppress radiative emission.

Interestingly, the molecular conformation and packing arrangement of **NMe_2OH** and **NEt_2OH-FL** satisfy both conditions, allowing for efficient luminescence in the solid state. Additionally, their planar structures facilitate robust lattice packing, enabling the effective propagation of small structural changes that occur during TS phase transition. The presence of solvent molecules H_2O in **NMe_2OH** and disordered MeOH in **NEt_2OH-FL**—also plays a significant role in molecular packing and structural rearrangement during the transition event.

In contrast, **NEt_2OH-NFL** crystals exhibit a puckered molecular conformation, resulting in strong π–π stacking interactions within the solid-state lattice. This packing arrangement effectively quenches radiative emission, preventing solid-state luminescence (Figure 21). However, applying shear pressure to **NEt_2OH-NFL** crystals can induce conformational changes, disrupting the π–π stacking interactions. This structural modification leads to the activation of luminescence ("turn-on" effect) upon mechanical grinding (Figure 19a). These findings highlight the interplay between molecular geometry, packing forces, and noncovalent interactions in determining stimuli-responsive behavior in crystalline materials. The model serves as a valuable framework for designing functional materials with tunable optical and mechanical properties, offering insights into stimuli-induced structural transformations at the molecular level.

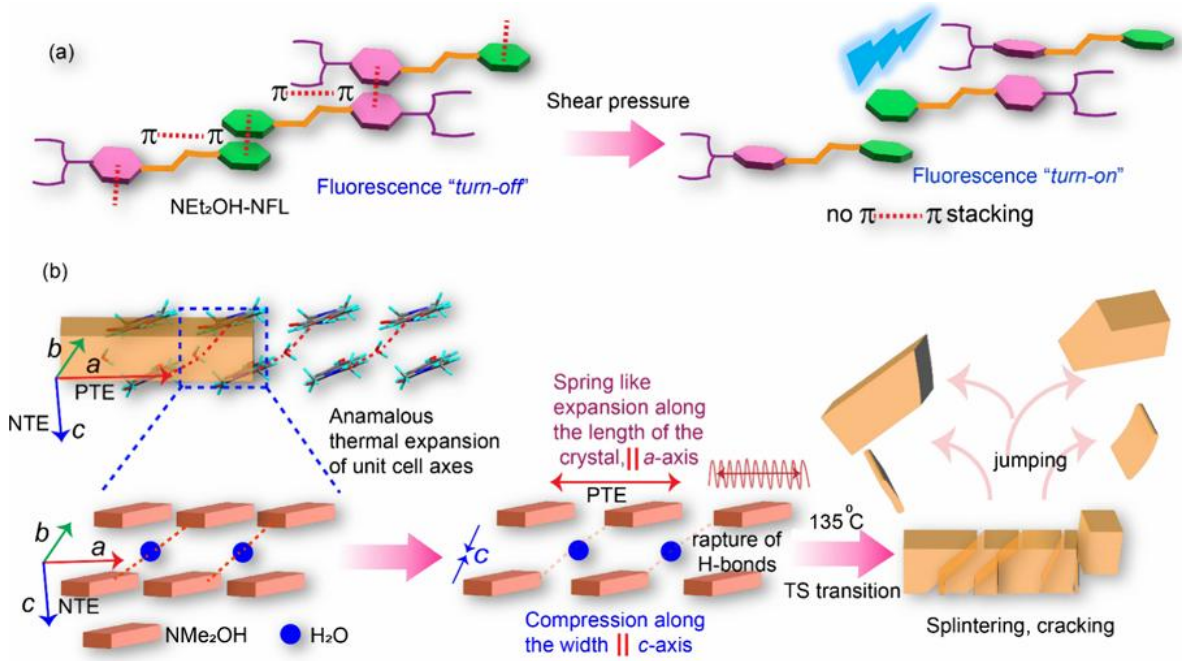

Figure 21. (a) Mechanistic model of luminescence turn on in **NEt₂-NFL** crystal; (b) TS effect in **NMe₂OH** crystal.

The thermosalient (TS) effect refers to the kinematic behavior exhibited by certain molecular crystals when they undergo a thermal phase transition, resulting in jumping, splitting, or cracking due to the sudden release of accumulated internal stress. It is well established that anisotropic thermal expansion of different unit cell axes plays a crucial role in this process.

To investigate the TS mechanism in **NMe₂OH** and **NEt₂OH-FL** crystals, a detailed structural study on noncovalent interactions was conducted. However, due to the presence of disordered solvent molecules in the **NEt₂OH-NFL** lattice, a systematic study was not feasible. Thus, the mechanistic model in figure 21a is based primarily on observations from **NMe₂OH** crystals. The Variable temperature PXRD (VT-PXRD) analysis confirmed that, with increasing temperature, **NMe₂OH** crystals experience positive thermal expansion (PTE) along the a-axis, which is attributed to weakening and eventual rupture of water-bridged hydrogen bonding interactions (Figures 11,12 and 17). Additionally, IR spectra of **NMe₂OH** indicated a weakening of the phenolic O–H bond post-TS transition, suggesting a strengthening of other hydrogen bonding interactions involving this functional group.

Given that both **NMe₂OH** and **NEt₂OH-FL** undergo TS phase transitions, it is likely that their mechanisms share fundamental similarities, with noncovalent interactions and thermal expansion-driven lattice distortions being key contributors. These findings reinforce the role of

molecular packing and anisotropic expansion in governing thermosalient behavior, offering valuable insights for designing stimuli-responsive materials.

The hydrogen bonding interactions in the crystal lattice are aligned roughly parallel to the c-axis, which plays a crucial role in the negative thermal expansion (NTE) along this direction. This structural reconfiguration occurs as a response to thermal stimuli, specifically involving the phenolic O–H bond. During the TS phase transition, the accumulated internal stress, generated due to anisotropic thermal expansion, is suddenly released when minor structural rearrangement occurs. This abrupt energy dissipation leads to a spring-like rapid shape change, ultimately manifesting as kinematic motion (Figure 21b).

These findings provide valuable insight into thermal-actuated mechanical effects in molecular crystals, reinforcing the significance of intermolecular interactions and packing geometry in governing stimuli-responsive properties.

5.4 Conclusion

In this study, we have demonstrated that the thermal actuation and luminescence properties of crystalline materials can be effectively tuned through polymorphism and systematic substitutional variations. By developing three distinct acylhydrazone-based molecular crystals, we have uncovered remarkably different thermal responses and solid-state luminescence switching behaviors. Among these materials, **NMe$_2$OH** and **NEt$_2$OH-FL** crystals exhibited prominent thermosalient (TS) actuation and bright luminescence, whereas **NEt$_2$OH-NFL** behaved differently, remaining non thermosalient and nonfluorescent. Detailed X-ray crystallographic analysis revealed that these variations in stimuli-responsive properties arise from differences in molecular conformation, crystal packing, and intermolecular interactions. Our findings present a viable strategy for designing small-molecule organic crystals with tailored physical properties, opening new possibilities for advanced technological applications, including smart actuators, sensors, and dynamic optoelectronic devices.

■ REFERENCES

1. P. Naumov, S. Chizhik, M. K. Panda, N. K. Nath, E. Boldyreva, *Chem. Rev*., 2015, **115**, 12440−12490.
2. D. Das, T. Jacobs, L. J. Barbour, *Nat. Mater*. 2010, **9**, 36−39.
3. I. E. Claassens, L. J. Barbour, D. A. Haynes., *J. Am. Chem. Soc*. 2019, **141**, 11425−11429.
4. Z. Wen, T. Yang, D. Zhang, Z. Wang, S. Dong, H. Xu, Y. Miao, B. Zhao, H. J. Wang. *Mater. Chem. C*., 2022, **10**, 3396.
5. P. Sudhakar, T. P. Radhakrishnan, *J. Mater. Chem. C*., 2019, **7**, 7083−7089.
6. D. Yan, Z. Wang, Z. Zhang, *Acc. Chem. Res*., 2022, **55**, 1047−1058.
7. K. Chen, J. Wang, Y. Feng, H. Liu, X. Zhang, Y. Hao, T. Wang, T. Huang, H. J. Hao, *Mater. Chem. C*., 2021, **9**, 16762−16770.
8. M. Mrinalini, S. Prasanthkumar, *ChemPlusChem*., 2019, **84**, 1103−1121.
9. Z. Zhang, N. Xu, Z. Huang, J. Lai, J. Liu, G. Deng, X. Wang, W. Zhao, *Adv. Devices Instrum.*, 2023, **4**, 0019.
10. L. Lan, L. Li, P. Naumov, H. Zhang, *Chem. Mater*. 2023, **35**, 7363− 7385.
11. P. Naumov. D. P. Karothu, E. Ahmed, L. Catalano, P. Commins, J. M. Halabi, M. B. Al-Handawi, L Li, *J. Am. Chem. Soc*., 2020, **142**, 13256−13272.
12. W. M. Awad, D. W. Davies, D. Kitagawa, J. Mahmoud Halabi, M. B. Al-Handawi, I. Tahir, F. Tong, G. Campillo-Alvarado, A. G. Shtukenberg, T. Alkhidir, Y. Hagiwara, M. Almehairbi, L. Lan, S. Hasebe, D. P. Karothu, S. Mohamed, H. Koshima, S. Kobatake, Y. Diao, R. Chandrasekar, H Zhang, C. C. Sun, C. Bardeen, R. O. Al Kaysi, B. Kahr, P. Naumov, *Chem. Soc. Rev.*, 2023, **52,** 3098− 3169.
13. D. P. Karoth, J. M. Halabi, L. Li, A. Colin-Molina, B. Rodríguez-Molina, P. Naumov, *Adv. Mater*., 2020, **32**, 1906216.
14. Y Su, S. Bhunia, S. Xu, A. Chen, C. M. Reddy, T. Cai, *Chem. Mater*., 2021, **33**, 4821−4829.
15. B. B. Rath, J. J. Vittal, *Chem. Mater*., 2021, **33**, 4621−4627.
16. R. Samanta, S. Ghosh, R. Devarapalli, C. M. Reddy, *Chem. Mater*., 2018, **30**, 577−581.
17. B. B. Rath, J. J. Vittal, *Acc. Chem. Res*., 2022, **55**, 1445−1455.
18. R Centore, M. Causa, *Crystal Growth & Des.*, 2018, **18**, 3535−3543.
19. S. Bhandary, M. Belis, A. M. Kaczmarek, K. V. Hecke, *J. Am. Chem. Soc*., 2022, **144**, 22051−22058.

20. S. Bhandary, M. Belis, R. Shukla, L. Bourada, A. M. Kaczmarek, K. V. Hecke, *J. Am. Chem. Soc.*, 2024, **146**, 8659−8667.
21. R. Chinnasamy, B. Munjal, R. Suryanarayanan, A. M. P. Peedikakkal, M. K. Mishra, S. Ghosh, *Crystal Growth & Des.*, 2022, **22**, 615−624.
22. S. Khan, B. Dutta, S. Naaz, B. Choudhury, P. A. Cazade, E. Kiely, S. Guerin, R. Medishetty, M. H. Mir., *commun. Chem.*, 2023, **6**, 150.
23. F. Tong, D. Kitagawa, I. Bushnak, R.-O. Al-Kaysi, C. J. Bardeen, *Angew. Chem., Int. Ed*. 2021, **60**, 2414−2423.
24. T. J. Gately, C. Cook, R. Almuzarie, I. Islam, Z. Gardner, R. J. Iuliucci, R. O. Al-Kaysi, G. J. O. Beran, C. J. Bardeen, *Crystal Growth & Des*., 2022, **22**, 7298−7307.
25. S. Chuskit, T. Sethi, P. Harsha, D. Das, *Crystal Growth & Des*., 2023, **23**, 1336−1342.
26. S. Dai, J. Zhong, X. Yang, C. Chen, L. Zhou, X. Liu, X. Sun, K. Ye, H. Zhang, L. Li, P. Naumov, R. Lu. *Angew. Chem., Int. Ed.*, 2024, **136**, 202320223.
27. S. Ito, *CrystEngComm*., 2022, **24**, 1112.
28. S. Ito, *J. Photochem. Photobiol. C: Photochem. Rev*., 2022, **51**,100481.
29. P. Commins, M. B. Al-Handawi, C. Deger, S. Polavaram, I. Yavuz, R. Rezgui, L. Li, K. N. Houk, P. Naumov, *J. Am. Chem. Soc*., 2024, **146**, 16540.
30. P. Shi, R. Zhao, M. Zhang, M. Lin, Y. Duan, T. Han, *Mater. Lett*., 2019, **243**, 38.
31. Z. Li, X. Wang, L. Han, C. Zhu, H. Xin, Y. Yin, *Adv. Mater*., 2022, **34**, 2107398.
32. L. Yu, C. Yang, *J. Mater. Chem. C*., 2021, **9**, 17265.
33. Z. Jiang, H. Zhao, W. Wu, K. Chen, H. Yu, T. Wang, X. Huang, N. Wang, L. Zhou, H. Hao, *J. Mater. Chem. C*., 2023, **11**, 4375−4383.
34. Y. Hao, L. Gao, X. Zhang, R. Wei, T. Wang, T. Wang, X. Huang, H. Yu, H. Hao, *J. Mater. Chem. C*., 2021, **9**, 8294− 8301.
35. K. Naim, S. C. Sahoo, P. P. Neelakandan, *ACS Applied Mater & Interfaces*., 2022, **14**, 22650−22657.
36. M. Lakshmipathi, A. I. Sk, P. K. Kundu, S. Tothadi, S. Ghosh, *Cryst. Growth Des.*, 2023, **23**, 4939−4945.
37. Y. J. Ma, G. Xiao, X. Fang, T. Chen, D. Yan, *Angew. Chem. Int. Ed*., 2023, **62**, 202217054.
38. X. Wei, B. Li, Z. Yang, R. Zhong, Y. Wang, Y. Chen, Z. Ding, G. Men, Z. Yan, H. Zhang, B. Yang, W. Xu, S. Jiang, *Chem. Sci*., 2021, **12**, 15588−15595.
39. Y. H. Yang, Y. S. Chen, Y. T. Chuang, J. S. Yang, *J. Am. Chem. Soc.*, 2024, **146**, 8131−8141.

40. M. K. Panda, T. Runcevski, S. C. Sahoo, A. A. Belik, N. K. Nath, R. E. Dinnebier, P. Naumov, *Nat. Commun.*, 2014, **5**, 4811.
41. APEX3, version 2017.3−0, and SAINT, version 8.38A, Bruker AXS Inc., Madison, WI, 2012, \URL: https://www.bruker.com
42. G. M. Sheldrick, SADABS; University of Gottingen: Gottingen, Germany, 1996 (part of Bruker APEX3 software package (version 2017.3-0): Bruker AXS, 2017).
43. G. M. Sheldrick, SHELXTL XT−Crystal Structure Solution, version 2014/4, Bruker AXS, 2010−2014.
44. G. M. Sheldrick, SHELXL 2014; University of Gottingen: Germany, 2014.
45. G. M. Sheldrick, *Acta Crystallogr. A.*, 2015, **71**, 3−8.
46. G. M. Sheldrick, *Acta Crystallogr. A.*, 2008, **64**, 112−122.
47. H. Lin, C. Doebelin, R. Patouret, R. D. Garcia-Ordonez, M. R. Chang, V. Dharmarajan, C. R. Bayona, M. D. Cameron, P. R. Griffin, T. M. Kamenecka, Bioorg. *Med. Chem. Lett.*, 2018, **28**, 1313−1319.
48. H. Liu, *Crystallographica Acta*., 2010, **66**, 1582.
49. A. Subashini, P. Priyadharsani, K. Thamaraiselvi, V. Veeramani, P. Rose, R. Philip, H. S. Evans, K. Ramamurthi, R. J. Ramesh Babu, *Mater. Sci. Mater. Electron*., 2019, **30**, 2638.
50. A Subashini, K. Ramamurthi, H. Stoeckli-Evans, *Acta Crystallogr, Sect. E: Struct. Rep*. 2012, **68**, 1152.